Derivatised Phenanthroline Transition Metal chelates: Targeted Chemotherapeutic Agents

Submitted in the fulfilment of the requirements for the degree of

Doctor of Philosophy

By

Leigh André Hunter

BSc (Honours) (University of KwaZulu–Natal)

July 2023

School of Chemistry and Physics

College of Agriculture, Engineering and Science

University of KwaZulu-Natal

Pietermaritzburg

Declaration

COLLEGE OF AGRICULTURE, ENGINEERING AND SCIENCE

I, Leigh A. Hunter, declare that

1. The research reported in this thesis, except where otherwise indicated, is my original research.

2. This thesis has not been submitted for any degree or examination at any other university.

3. This thesis does not contain other persons' data, pictures, graphs or other information, unless specifically acknowledged as being sourced from other persons.

4. This thesis does not contain other persons' writing, unless specifically acknowledged as being sourced from other researchers. Where other written sources have been quoted, then:
   a. Their words have been re-written but the general information attributed to them has been referenced
   b. Where their exact words have been used, then their writing has been placed in italics and inside quotation marks, and referenced.

5. This thesis does not contain text, graphics or tables copied and pasted from the Internet, unless specifically acknowledged, and the source being detailed in the thesis and in the References sections.

Signed: ..... [redacted]. Date: 16/04/2024

Leigh A. Hunter

I hereby certify that this is correct.

Signed: .... [redacted].....

Prof. M.P. Akerman
Supervisor

Acknowledgements

Firstly, I would like to express my gratitude to Prof. M. P. Akerman for his time and readiness to help and guild me through this work. His enthusiasm and persistence throughout my work kept me motivated.

I would like to thank Prof O. Q. Munro, Dr K. Akerman and Dr C. W. Wilson for their help and guidance in both the synthetic and experimental aspects of my project.

My studies would have been inconceivable without the financial support of the National Research Foundation (NRF) and the facilities provided by the University of KwaZulu-Natal (UKZN).

I would also like to acknowledge the technical staff of UKZN PMB chemistry department for all the help received with regards to collection of structural data and day-to-day assistance.

Lastly, I would like to thank all my friends, family and colleagues for the support and motivation they have provided me with throughout my research.

List of Abbreviations

5,6-dmp	5,6-dimethyl-1,10-phenanthroline
AIDS	Acquired immunodeficiency syndrome
app	Apparent
AR	Analytical reagent
ATR	Attenuated Total Reflection
B3LYP	Becke-3-parameter-Lee-Yang-Parr
BBOF	Broadband Observe + Fluorine
BEOV	Bis(ethylmaltolato) oxovanadium
BMOV	Bis(maltolato) oxovanadium
BSA	Bovine serum albumin
bp	Base Pair
bpy	2,2'-bipyrine
Cal or Calc	Calculation
chrysi	Chrysene-9,10-diimine
Cont.	Continued
COSY	Correlation Spectroscopy
CSD	Cambridge Structural Database
ct	Calf Thymus
C_t	Concentration
CT	Computerised tomography
Diff.	Difference
DFT	Density Functional Theory
DMSO	Dimethyl sulfoxide
DNA	Deoxiribose nucleic acid
dppz	Dipyrido[3,2-a:20,30-c] phenazine
dpq	Dipyrido[3,2-d:2',3'-*f*]quinoxaline
DTP	Developmental Therapeutics Program
EB or EtBr	Ethidium bromide
ECP	Effective core potential
EDTA	Ethylenediaminetetraactetic acid
en	Ethane-1,2-diimine
EPR	Electron paramagnetic resonance
ES	Electrospray
Exp.	Experimental
FBS	Fetal bovine serum
FT	Fourier transform
GI_{50}	Growth inhibition concentration
GIAO	Gauge Including Atomic Orbitals
HIV	Human immunodeficiency virus
HSA	Human serum albumin
HMBC	Heteronuclear multiple-bond correlation

HOMO	Highest occupied molecular orbital
HSQC	Heteronuclear single quantum coherence
IC_{50}	Total growth inhibition concentration
Intest.	Intestine
IR	Infrared
L1	Ligand 1 - *N*-(quinolin-8-yl)-1,10-phenanthroline-2-carboxamide
L2	Ligand 2 - *N*-(pyridin-2-ylmethyl)-1,10-phenanthroline-2-carboxamide
LanL2DZ	Los Alamos National Laboratory 2-double-zeta
LC_{50}	Lethal inhibition concentration
LSD1	Lysine-specific histone demethylase
LUMO	Lowest unoccupied molecular orbital
max	Maximum
MLCT	Metal-to-ligand Charge Transfer
MRI	Magnetic Resonance Imaging
MTT	3-(4,5-dimethylthiazol-2-yl)-2,5-diphenyltetrazolium bromide
NCI	National Canser Institute
NECSA	South African Nuclear Energy Corporation
NMR	Nuclear Magnetic Resonance
NSCLC	Non-Small Cell Lung cancer
NTeMBI	Nuclear Technologies In Medicine And The Biosciences Initiative
PBS	Phosphate Buffered Saline
PDTA	Propylenediamine tetra-acetic acid
PET	Positron Emission Tomography
phen	1,10-phenanthroline
phi	Phenanthrene-9,10-diimine
pico	Picolylamine
PTI	Photon Technology International
quino	Quinoline
RMSD	Root Mean Square Deviation
RNA	Ribonucleic acid
RNU	Rowett Nude
SD	Standard Deviation
SPECT	Single photon emission computing tomography
TAE	Tris-acetate Ethylenediaminetetraactetic acid
TD	Time Dependent
TMS	Tetramethylsilane
topo	Topoisomerase
UKZN	University of KwaZulu-Natal
UFS	University of Free State
UV	Ultraviolet
UV/vis	Ultraviolet/Visible

List of Figures

List of Tables

Abstract

The derivatisation of 1,10-phenanthroline at the 2-position afforded two classes of compounds with two different bridging groups in this study. The first group comprised two amide-bridged tetradentate N_4-donor ligands and were chelated to copper(II), nickel(II) and palladium(II). The ligand chelation occurred with concomitant deprotonation of the amide N-H, resulting in a monoanionic ligand and monocationic complexes when coordinated to the divalent metal ions. The ligands *N*-(quinolin-8-yl)-1,10-phenanthroline-2-carboxamide, HL1, and *N*-(pyridin-2-ylmethyl)-1,10-phenanthroline-2-carboxamide, HL2, were characterised by NMR, IR and UV/vis spectroscopy as well as mass spectrometry. The second class of compounds were imine-bridged copper(II) chelates. These chelates were synthesised *via* a templating condensation reaction between various salicylaldehyde derivates and 1,10-phenanthrolin-2-ylmethanaminium chloride, yielding eight additional copper(II) chelates. The metal chelates were characterised by IR, UV/vis and EPR spectroscopy, and mass spectrometry. HL1, [Cu(L4)(NO_3)] and [Cu(L7)](NO_3) were further studied by X-ray diffraction. The copper(II) chelates exhibit two different solid-state structures with the nitrate counter ion coordinated to the metal centre in [Cu(L4)(NO_3)], but in the outer coordination sphere for [Cu(L7)](NO_3). The paramagnetic copper(II) chelates were studied with EPR spectroscopy, which confirmed the square planar coordination geometries of these chelates in solution.

The metal chelates were designed to be chemotherapeutic agents, exerting their cytotoxicity through DNA intercalation and, for the copper(II) chelates, DNA cleavage through the catalytic production of ROS. The ability of the copper(II) chelates to catalyse the production of hydroxyl radical *in situ* in the presence of ascorbic acid and hydrogen peroxide was studied *via* a hydroxyl radical assay using Rhodamine B as an analogue for the aromatic DNA bases. Competitive binding studies determined the affinity of the metal chelates towards ct-DNA, [Cu(L1)](PF_6) has the highest binding constant: 5.91×10^6 M^{-1}.

DFT calculations were performed on the ligands and metal chelates to determine the geometry-optimised structures, vibrational frequencies, ^1H and ^{13}C NMR chemical shifts and electronic transitions. The B3LYP/6-311G (d,p) level of theory was used for the ligands, copper(II) and nickel(II) chelates and the B3LYP/LanL2DZ level of theory for the palladium(II) chelates. The TD-DFT method was used for the energy calculations. The experimental and calculated results were compared where possible, and a reasonable correlation was found.

The cytotoxicity of five amide-based chelates was evaluated against four human cancer cell lines, namely A549, TK-10, HT29 and U251, using an MTT assay. The screened chelates exhibited favourable anticancer activity with the mean IC_{50} values against the four cancer cell lines ranging from *ca*. 12 to 35 µM. Importantly, it was found that the combination of the copper(II) ion and the ligand was essential for enhanced cytotoxicity. The complex

[Cu(L1)](PF_6) was identified as the lead drug candidate based on the high DNA affinity and cytotoxicity. This compound was most cytotoxic towards the glioblastoma cell line U251 with an IC_{50} value of 7.59 μM. The imine-based chelates were screened against three human cancer cell lines: MDA-MB, HELA, and SHSY5Y, and a healthy human cell line, HEK293. The selectivity index of these chelates for neoplastic versus the healthy cell line was calculated. The imine-based chelates showed a high selectivity towards the triple-negative breast cancer MDA-MB, an order of magnitude more toxic to the tumour cell than the healthy one. This selectivity index is significantly improved over that of cisplatin. A gel mobility shift assay investigated the interactions between the copper(II) chelates and plasmid DNA.

The *in vivo* biodistribution of [Cu(L1)](PF_6) was determined using the copper-64 radiolabelled analogue of [Cu(L1)]Cl and microPET-CT scanning. The initial biodistribution studies suggested that the complex has good serum stability and showed that there was no significant accumulation in any organs. The subsequent study involved a xenograft model using the A549 cell line and showed significant uptake and retention of the complex in the tumour. The cytotoxicity of the chelate when synthesised with the non-radioactive isotopes of copper and the uptake of the radiolabelled equivalent in a tumour model suggest that this complex could have application as a “theranostic agent”.

Table of Contents

Chapter 1: Introduction and Literature Survey

1.1 Introduction

This thesis looks at the potential of novel metal chelates for controlling the proliferation of tumour cells. The ligands are derived from 1,10-phenathroline to form tetradentate species. These ligands will be coordinated to a range of divalent metal ions including copper(II), palladium(II) and nickel(II), the main emphasis being copper(II). The palladium and nickel species are used as a control to determine the role of the biologically redox-active copper(II) in the mechanism of action. The use of metal complexes in medicine has increased in recent years due to the many favourable properties of metal chelates.[1] There are several examples of metal chelates currently in clinical use as chemotherapeutic agents for cancer treatment, the most well-known being cisplatin and its derivatives.[2] Cisplatin, and indeed most anticancer agents, have severe side effects, a limited range of therapeutic efficacy, and reported drug resistance in secondary tumours.[3] These limitations are the driving force to develop new transition-metal chelates with mechanisms of action that differ from the currently available compounds.[4] To provide context for the current study, the literature survey will look at known examples of metal-based chemotherapeutics and their mechanisms of action.

The metal chelates that were designed for this thesis draw on the fact that copper(II) complexes are considered promising alternatives to current cancer treatments.[4] Copper(II) is generally more biocompatible than platinum(II). Evidence of this is found in the fact that copper(II) is central to cell physiology as a catalytic co-factor in enzymes, mitochondrial respiration and free radical scavenging.[4] The literature survey will expand on these roles of copper as well as how copper(II) complexes can interact with DNA *via* different modes when compared to platinum(II) complexes. Instead of cross-linking the DNA through the guanine base pairs, copper(II) complexes can be designed to intercalate between the base pairs of the DNA helix. In this process, the copper-based compounds alter the uniformity of the DNA structure.[5] A further advantage of copper, and one of the key reasons it was selected as the central metal ion for this study, is that it is a redox-active metal. This means that it can catalyse the production of hydroxyl radicals which are able to cleave DNA.[6] The chemistry of this process will be discussed in the literature survey.

The ligand systems that will be coordinated to the metal ions in this work are phenanthroline derivatives. The ligand systems were selected for their planarity and high aromaticity, which is ideal for DNA binding.[4,5] To provide context for the current study, some of the chemistry of phenanthroline will be reviewed. Literature has already shown that the pairing of copper(II) and phenanthroline can be favourable when designing antitumour agents.[7] This concept is further developed in the current study with the ligands being designed to also include hydrogen

bonding regions which should improve the interactions between the metal complexes and their intended cellular target: DNA.

In addition to the motivation above, a burgeoning field of research is the application of the radioactive isotope copper-64 Positron Emission Tomography (PET) imaging. The specific decay mode of copper-64 will be reviewed with an emphasis on what makes it suitable for the design of PET imaging agents.

1.2 Metals in Medicine

1.2.1 The Applications of Late Transition Metals in Medicine

The field of medicinal inorganic chemistry is relatively new compared to classical organic medicines. Still, primitive use of metals in the pharmaceutical field has been found to date back to the ancient Egyptians and Chinese.[8] Egyptians used copper and aluminium sulfates to prepare "potions" because of their sterilising effects. 15th and 16th Century European physicians used gold flakes in their treatments, but in modern science, metallic gold has not yet shown medicinal value.[9]

1.2.1.1 The Applications of Gold in Medicinal Chemistry

Gold cyanide, $[Au(CN)_2]^-$, showed significant success as a bactericide in 1890 by Koch[10,11], who showed it was active towards pulmonary tuberculosis. Building on this knowledge, Forestier[12,13] believed that gold-containing compounds could be used to treat rheumatoid arthritis.[11] This sparked a growing interest in gold-based drugs that has led to compounds used to treat arthritis and cancer. Many gold drugs have also shown promise in treating AIDS, malaria, and American trypanosomiasis.[14] In the treatment of AIDS, gold cyanide has been reported to hinder the production of HIV in $CD4^+$ T cells at similar dosages used in other ailments. This is significant as these are the white blood cells targeted by the virus and have an important role in the immune system. Similarly, gold coordinated to thioglucose ligands have demonstrated an ability to prevent HIV from binding to the surface of MT-4 cells, another white blood cell, therefore hindering the virus' activity.[14]

Auranofin and its derivatives (Figure 1.2.1), reported by Sannella, *et al.*[15], stunt *Plasmodium falciparum*'s growth: the parasite responsible for malaria. The gold compounds interfere with the redox balance of the parasites' cells by inhibiting the role of the thioredoxin reductase enzyme, leading to oxidative stress and eventually killing the parasite.[15]

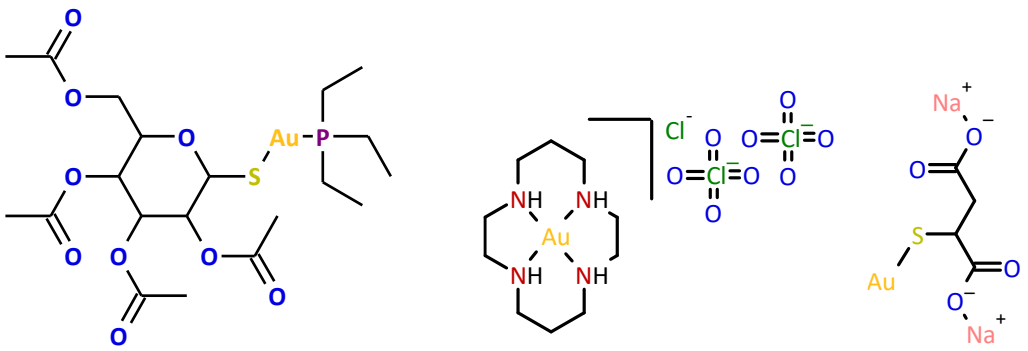

(a) (b) (c)

Figure 1.2.1: Structures of (a) Auranofin, (b) AuCyclam, and (c) Myochrysine, examples of gold-based drugs.

The gold complexes in Figure 1.2.1 have also been shown to have antitumor activity (except for Auranofin being primarily used to effectively treat rheumatoid arthritis)[11], resulting in further research into metal chelate anticancer research.[16] Gold(III) complexes demonstrated significant potential as anticancer agents; however, the low stability of gold(III) plays a major role in the design of the gold(III) complexes. Gold has a high reductive potential and is susceptible to reduction under physiological conditions.[17] It thus requires strong sigma-donor ligands for stability.

A more recent application of gold in medicine is the use of gold nanoparticles to increase the antitumor activity of well-known organic chemotherapeutic compounds. This was achieved by loading the organic compounds onto polymer-gold nanoparticles.[11,18] The uptake and retention of the organic compounds in the tumour tissue increased when they were loaded onto the gold nanoparticles, enhancing tumour size reduction. Two examples of such compounds are doxorubicin and bortezomib, shown in Figure 1.2.2:

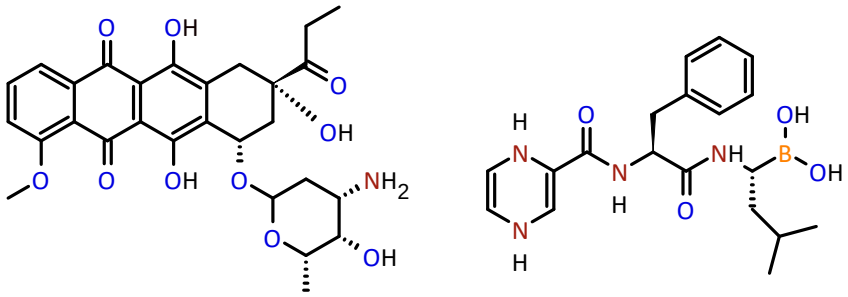

(a) (b)

Figure 1.2.2: Structures of (a) doxorubicin and (b) bortezomib, examples of commercial chemotherapeutics that have been appended to gold nanoparticles to increase tumour uptake and retention.[11]

1.2.1.2 Cisplatin and Platinum-Derived Chemotherapeutics

Another heavy metal used for cancer treatment is platinum. Adjacent to gold in the periodic table, platinum(II) and gold(III) are isoelectronic and share some common features.[8] Platinum

is the central metal ion in cisplatin as well as derivatives thereof such as carboplatin and oxaliplatin (Figure 1.2.3). These commercially available platinum drugs, which are used for cancer treatment, have been developed following Rosenberg's serendipitous discovery of the anti-bacterial properties of cis-diamminedichloroplatinum(II) in 1964.[19] While studying the effects of electric fields on bacteria, Rosenberg noticed the stunted growth of cells on platinum electrodes and concluded that platinum-containing compounds are responsible. Platinum drugs all interact with the DNA of the target cells, resulting in controlled cell death (apoptosis).[8] More specifically, it interacts with adjacent guanine base pairs in a GG intrastrand cross-link, thus distorting the DNA structure, and, ultimately, forcing the cell to undergo apoptosis.[2]

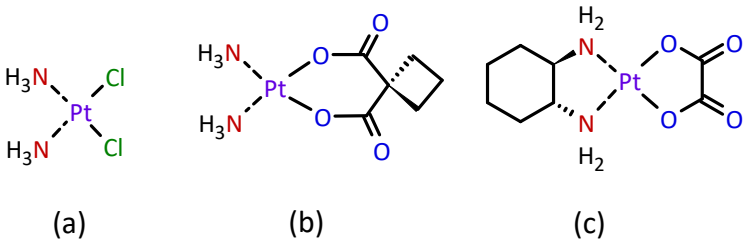

Figure 1.2.3: Structure of (a) cisplatin; (b) carboplatin; and (c) oxaliplatin, examples of platinum-based chemotherapeutics.[13,20,21]

The above diagram (Figure 1.2.3) shows that each of the cisplatin derivatives has the characteristic square planar geometry as a result of the d^8 electronic configuration of the platinum(II) ion. The low-spin d^8 configuration with a square planar coordination geometry has vacant dx^2-y^2 orbitals. Since the derivatives have the same core structures, they bind to DNA *via* a similar mode to that of cisplatin, hence there is a similarity in function.[8,20] Many more derivatives of cisplatin are currently in clinical trials, again with similar core structures to the above derivatives. Changing the ancillary ligands has been shown to lower the toxicity levels as well as target more types of cancer cells when compared to cisplatin.[8,20] The following mechanism illustrates the mode of action for cisplatin:

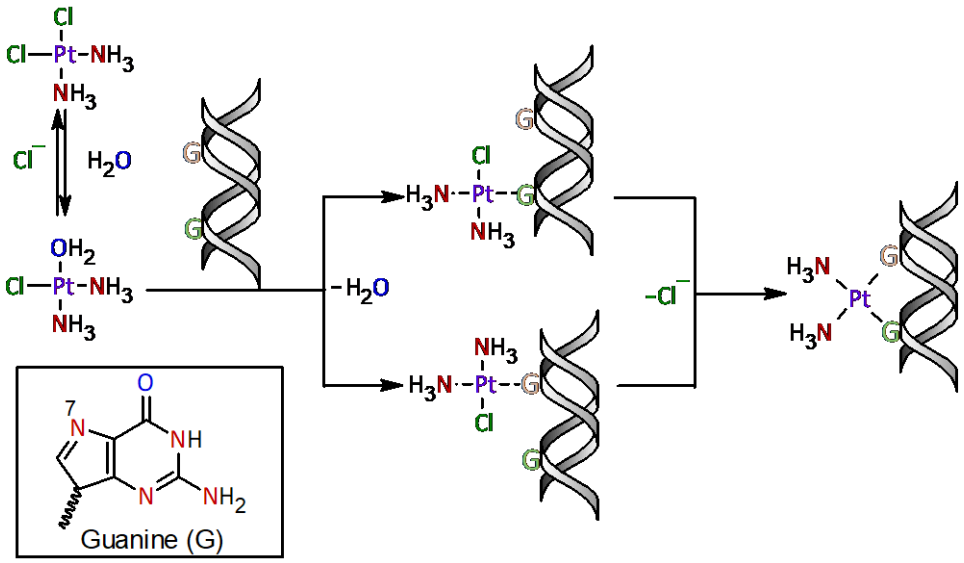

Figure 1.2.4: Mechanism of cisplatin binding to DNA *via* GG intrastrand cross-linking, including guanine structure with N7 labelled. The diagram was recreated based on information reported by Kostova.[22]

Figure 1.2.4 shows cisplatin loses a chloride ligand which is then replaced with an aqua ligand when it enters a cell; this aqua ligand then dissociates. The ligand exchange reaction is a consequence of the lower chloride concentrations inside the cell. The platinum metal centre binds to the DNA structure at a guanine N7 site, the most electron-rich position of the DNA.[3,22] The second chlorido ligand then dissociates, and the platinum binds to another guanine N7 site on the other side of the major groove of the DNA structure. This cross-linking forces the DNA into a 'twisted' structure which renders the DNA incapable of replication and triggers cell apoptosis.[3,22]

The mechanism of action of cisplatin is of great interest and is used in the design of newer platinum chelates. A study by Ang *et al.*[23] reports a range of platinum(II) compounds which are coordinated to ethane-1,2-diamine (en) and various methyl-substituted 1,10 - phenanthroline (M_p) ligands, as shown in Figure 1.2.5. They then showed the high affinity of these complexes towards G-quadruplex DNA (G-DNA) through different characterisation techniques. The planarity and electron-rich properties of the 1,10-phenanthroline ligands aided in the DNA interaction of the Pt(II) complexes.[23] The substitution of the 1,10-phenanthroline ligand increased the platinum complex's selectivity towards G-DNA when compared to cisplatin.[23] This efficacy of phenanthroline-derived metallodrugs was one of the driving forces for the ligand design in this work.

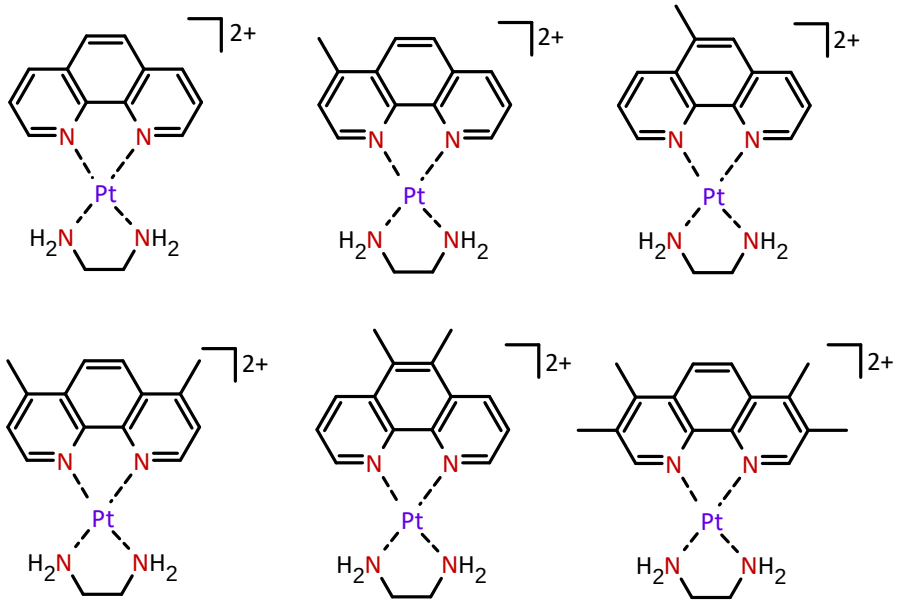

Figure 1.2.5: Structures of $[Pt(II)(en)(M_p)]^{2+}$ complexes.[23]

1.2.1.3 Rhodium-Based Chemotherapeutics

Rhodium-based chemotherapeutics have a different DNA binding mode when compared to platinum metallodrugs. This is due to the differing cooridination geometry of the rhodium chelates.[5] The rhodium(III) chelate in Figure 1.2.6 has an octahedral coordination geometry with three planar aromatic bidentate ligands coordinated. This allows the rhodium chelate to intercalate between the base pairs of the DNA structure.

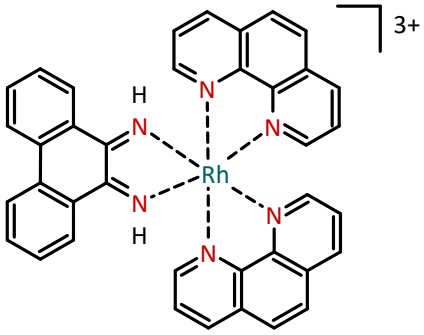

Figure 1.2.6: Structure of Δ-$[Rh(phen)_2phi]^{3+}$: an example of a DNA intercalator.

The phenanthrene-9,10-diimine (phi) ligand, is the planar region of the metal complex that intercalates the DNA.[5] There are many derivatives of the above rhodium complex, with different planar ligands that intercalate between the DNA base pairs and also different non-intercalating derivatives. The metal centre, rhodium(III) in this case, can be switched out with other late transition metals, which changes the complexes' intercalating ability, based on the metal centre's properties.[5] The complex in Figure 1.2.6 was altered to determine whether planarity affected the intercalating ability of the complex. Figure 1.2.7 shows the altered rhodium complex:

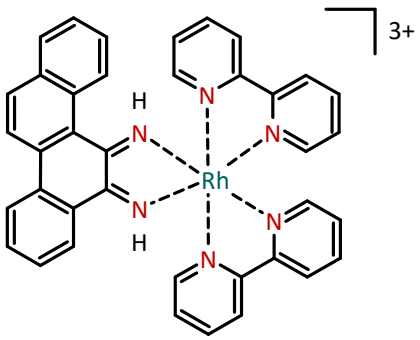

Figure 1.2.7: Structure of Δ-[Rh(bpy)$_2$chrysi]$^{3+}$. This compound was designed to study the influence of aromaticity on intercalation efficacy.

The [Rh(bpy)$_2$chrysi]$^{3+}$ complex (Figure 1.2.7) has an extended planar aromatic region, the chrysene-9,10-diimine (chrysi) ligand, compared to the phi ligand in the [Rh(phen)$_2$phi]$^{3+}$ complex. This increase in planarity leads to greater DNA intercalative ability as the additional fused phenyl ring increases the π-region of the ligand. This increase in aromaticity improves the favourable π-interactions between the DNA base pairs and the rhodium chelate, stabilising the DNA/drug conjugate.[5]

The [Rh(bpy)$_2$chrysi]$^{3+}$ complex is approximately 2.1 Å wider than the [Rh(bpy)$_2$phi]$^{3+}$ complex making it, theoretically, less suitable for intercalation based on steric arguments. Despite this, the [Rh(bpy)$_2$chrysi]$^{3+}$complex still has a superior DNA binding affinity. This is because thermodynamically speaking, the energetic cost of steric clash is offset by the energetic benefit of the π-stacking of the aromatic ligand within the DNA.[5] The [Rh(bpy)$_2$chrysi]$^{3+}$ and the [Rh(bpy)$_2$phi]$^{3+}$ complexes have an added characteristic of photoactivated DNA strand cleavage.[5]

A study by Yang, *et al.*[24] presents a rhodium(III) complex (Figure 1.2.8), which is the first metal-based compound to inhibit the Lysine-Specific Histone Demethylase 1 (LSD1) enzyme. This enzyme is responsible for various cancers when overactive. By inhibiting the LSD1 enzyme, the proliferation of neoplastic tissue can be slowed or stopped entirely.[24] The complex selectively targets the LSD1 enzyme with no observed interaction with other vital enzymes *in vivo*.[24]

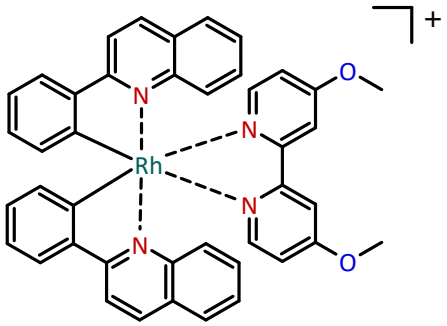

Figure 1.2.8: Structure of a $[Rh(C^N)_2(N^N)]^+$ complex, which is the first example of a metal-based LSD1 enzyme inhibitor.

1.2.1.4 Ruthenium-Based Chemotherapeutics

A metal adjacent to rhodium on the Periodic Table is ruthenium, which is also used in medicinal inorganic chemistry. Ruthenium complexes are used as molecular light switches to detect DNA as well as in the treatment of cancer.[5] Ruthenium-dppz complexes, which are luminescent, first interact with DNA by either groove binding or groove intercalation; this induces a decay in the luminescence of the complexes. This decay can be monitored to determine the presence of DNA.[5] Figure 1.2.9 shows the structure of a ruthenium-dppz complex:

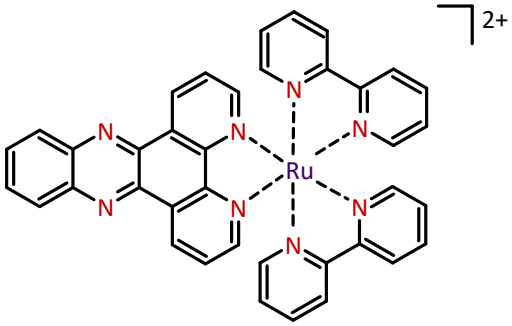

Figure 1.2.9: Structure of $[Ru(bpy)_2dppz]^{2+}$ used as a molecular light switch to detect DNA.

NAMI-A (Figure 1.2.10), has been shown to lower the metastasis of certain cancers by interacting with cells that separate from the primary tumour. Even though NAMI-A does not reduce the primary tumour size, the reduction in metastasis rates reduces the spread of cancer; it is often the metastases that become life-threatening.[21,25]

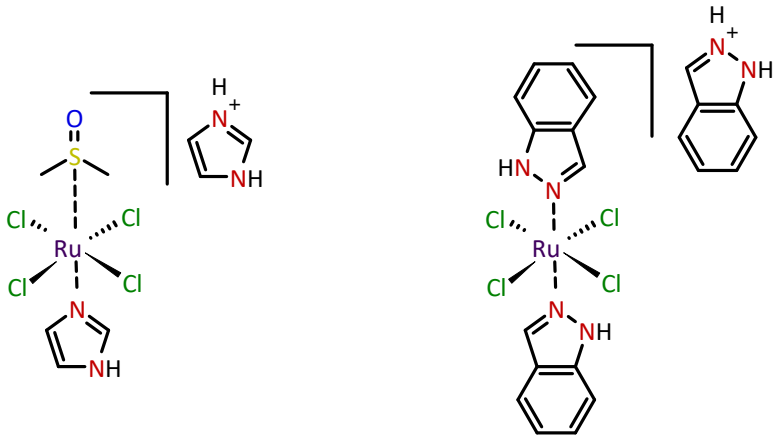

Figure 1.2.10: Structures of [left] NAMI-A, and [right] KB1019 showing the octahedral geometry of the Ru(III) metal centre and the four chlorido ligands coordinated in equatorial positions.[21]

Other ruthenium complexes with similar structural properties to that of NAMI-A have similar reactivity and increased metastasis resistance.[25] NAMI-A had become the first ruthenium-based drug to enter phase I clinical trials in 1999.[26] The toxicity profile for NAMI-A was determined in this phase of clinical trials, and when compared to the toxicity profile for platium-based antitumour drugs, NAMI-A showed a lower renal toxicity and no hematological toxicity.[25] Phase I showed that NAMI-A was more effective towards Non-Small Cell Lung Cancer (NSCLC) and was approved for phase II clinical trials. Phase II clinical trials for NAMI-A were not as successful as phase I due to the lower than expected efficacy of the drug towards NSCLC *in vivo*.[25] KB1019, a NAMI-A derivative, has also entered into phase I clinical trials and has shown to have antitumour activity with overall moderate to low toxicity, similar to NAMI-A. However, the two compounds have different modes of action, with NAMI-A being antimetastic and KB1019 being cytotoxic, with KB1019 also being effective toward colorectal cancer.[25]

Lai, *et al.*[27] synthesised a series of ruthenium(II) benzimidazole complexes as possible anti-angiogenic agents. Anti-angiogenic agents inhibit the growth of blood vessels (vasculation) around a tumour, this prevents essential oxygen and nutrient uptake in tumours. By reducing or hindering the vasculation of a tumour, the size and growth rate of the tumour are decreased.[27] Figure 1.2.11 shows the structures of these ruthenium(II) benzimidazole complexes:

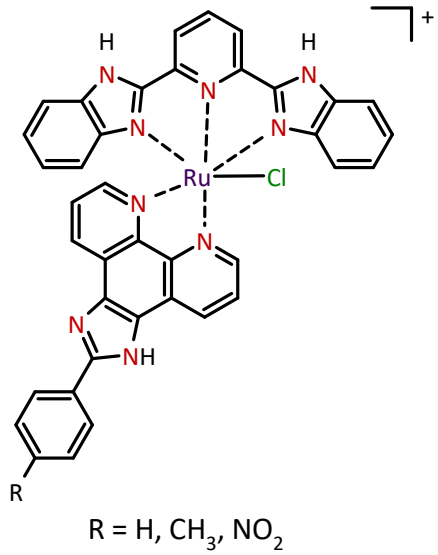

Figure 1.2.11: Structure of ruthenium(II) benzimidazole complexes synthesised by Lai, *et al.*[27] as anti-angiogenic compounds.

1.2.2 The Applications of Early Transition Metals in Medicinal Chemistry

Metals in the first row of the d-block of the Periodic Table have also found applications in medicine. These metals include vanadium, iron and copper. The applications of each of these metals is discussed.

1.2.2.1 The Applications of Vanadium in Medicinal Chemistry

In the 1970's it was discovered that two oxidation states of vanadium, vanaduim(IV) and vanadium(V), could imitate the function of insulin, i.e., glycogen synthesis and glucose oxidation and uptake.[28,29] The combination of organic ligands with vanadium reduces the toxicity of the metal ion as well as increases solubility and lipophilicity.[30] An example of these compounds is bis-(maltolato) oxovanadium(IV), BMOV, and bis-(ethylmaltolato) oxovanadium(IV), BEOV, shown in Figure 1.2.12 below. BMOV and BEOV have been shown to be considerably more active than vanadium sulfate, a known insulin-mimetic agent.[28]:

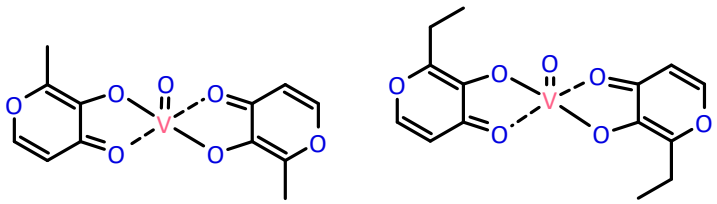

Figure 1.2.12: Structures of [left] BMOV, and [right] BEOV. These are examples of vanadium(IV) insulin-mimetic.

Vanadium complexes have a unique mechanism of action when compared to Pt-based compounds, making them ideal for treatment of Pt-resistant cancers.[29,31] Vanadium complexes inhibit tumour growth *via* a two-fold mechanism, firstly, inducing cell apoptosis

and halting proliferation, and secondly, by hindering the metastatic ability of a tumour.[31] Notably, vanadium-based complexes have been shown to enhance the effectiveness of oncolytic viruses, which are compounds that attack cancer cells and reduce the size of tumours, but require assistance from other compounds.[32] The combination of vanadium complexes and oncolytic viruses increase the overall antitumour ability of the vanadium complexes.[32] Examples of oncolytic viruses include the Herpes simplex virus and the measles virus.

1.2.2.2 The Applications of Iron in Medicinal Chemistry

Iron, a vital metal for oxygen transport in blood and muscles, has found various pharmacological applications, some of which can be dated back to the time of Hippocrates. Iron, in the form of iron(II) dextran (Figure 1.2.13), has been shown to treat restless legs syndrome since the condition is thought to be associated with low levels of iron-containing proteins in the brain. A downfall with using iron in treating restless legs syndrome is the low absorbance if taken orally. Intravenous iron has been shown to be more effective, but if a high dose of iron is taken, it can lead to iron-toxicity-related organ damage.[33]

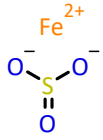

Figure 1.2.13: Structure of iron(II) Dextran, an example of an iron-based pharmaceutical.

One of the most widespread applications of iron in medicinal inorganic chemistry is in the treatment of malaria. Iron complexes are effective in malaria treatment. The most relevant example of this is ferroquine. Figure 1.2.14 shows the structure of the iron(II) antimalarial agent ferroquine:

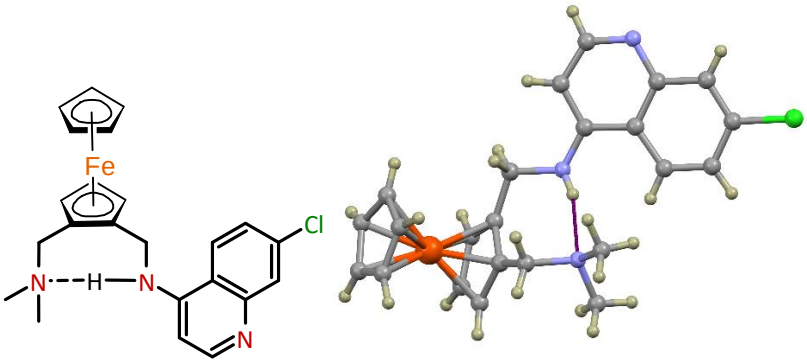

Figure 1.2.14: Structure of ferroquine showing the intramolecular hydrogen bond between the secondary and tertiary amine groups.[34]

The ferroquine complex is derived from chloroquine, which has been appended with the ferrocene moiety. Chloroquine is a well-known drug used in malaria treatment, targeting the parasites responsible for malaria (*Plasmodium falciparum* and *Plasmodium vivax*).[35,36] The

mechanism of how chloroquine attacks the parasites is not fully understood, however, it has been shown to inhibit haemoglobin digestion in the parasites food vacuole.[36] The developed resistance towards chloroquine has necessitated the development of more compounds for malaria treatment, and ferroquine and its analogues have shown great promise.[36]

Iron has also been shown to have anticancer properties, which are attributed to the redox activity of iron(II/III) in the body. Iron acts as a catalyst for the formation of highly reactive hydroxyl radicals from superoxide and hydrogen peroxide.[37] The reaction is known as the Fenton reaction and is shown below in Scheme 1:

$$Fe^{3+} + O_2^{\cdot -} \rightarrow Fe^{2+} + O_2$$

$$Fe^{2+} + H_2O_2 \rightarrow Fe^{3+} + OH^{\cdot} + OH^-$$

$$\text{Net reaction: } O_2^{\cdot -} + H_2O_2 \rightarrow OH^{\cdot} + OH^-$$

Scheme 1: Fenton reaction of iron and hydroden peroxide.[37]

The anticancer properties of the iron-based chelates have shown great potential, which can be attributed to the biologically accessible reduction potential of iron and the type of ligand cooridinated to the metal centre.[37] A study by Lee, *et al.*[38] demonstrated the potential of iron(III) *N,N'*-Bis(salicylidene)-1,2-phenylenediamine, [Fe^{III}(salophene)(Cl)], as an alternative anticancer agent for multi-drug-resistant leukemia.[37,38] Cytotoxicty studies have shown [Fe^{III}(salophene)(Cl)] to have a higher cytotoxicity than cisplatin. Based on this result, a further study by Vanco, *et al*.[39] illustrated the effects of changing the co-ligand from chlorido to arole-derived liagnds. Table 1.2.1 below summarises the cytotoxicities of the iron-based salophene chelates, their structures and cisplatin's cytotoxicity towards the human breast cancer cell line, MCF-7:[38,39]

Table 1.2.1: Structures of [Fe^{III}(salophene)(Cl)], [Fe^{II}(salophene)(imidazole)], and [Fe^{III}(salophene)(5-methyltetrazole)]; and the corresponding IC_{50} (μM) concentrations towards MCF-7 cell line.

	IC_{50} (μM)		IC_{50} (μM)
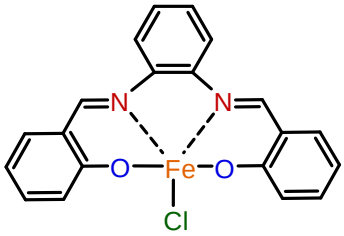 [Fe^{III}(salophene)(Cl)]	5	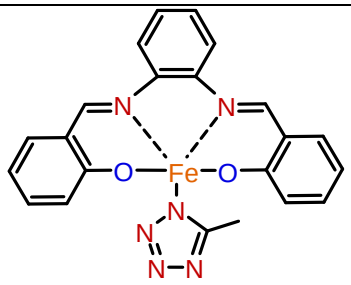 [Fe^{III}(salophene)(5-methyltetrazole)]	0.38
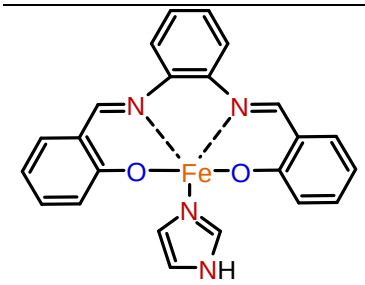 [Fe^{II}(salophene)(imidazole)]	0.70	Cisplatin	20

[Fe^{III}(salophene)(Cl)] has a much lower IC_{50} towards MCF-7 when compared to cisplatin. The azole-based iron chelates, [Fe^{II}(salophene)(imidazole)] and [Fe^{III}(salophene)(5-methyltetrazole)], have even higher cytotoxicities towards MCF-7 cells with the IC_{50} values below 1 μM, illustrating their potential as anticancer agents.[36,38,39]

1.2.2.3 The Applications of Copper in Medicinal Chemistry

Copper is another metal that has found application in medicinal chemistry and is the main focus of the present study. The use of copper in medicine can be traced back to ancient Iran and the Romans, approximately 5000 – 10000 years ago.[40] Copper is found in all plants and animals and is an essential element, involved in different processes in growth and development.[41-43] These processes, which are controlled by enzymes and proteins containing copper, include DNA synthesis, energy metabolism, and respiration. At high concentrations, however, copper is toxic and, in some cases, lethal, especially to lower-order organisms. Wilson disease is a genetic disorder where the body has elevated levels of copper, which leads to other disorders like epilepsy, rheumatoid arthritis, and diabetes.[40]

The toxicity of copper to lower organisms, such as bacteria, fungi, and viruses, is attributed to the ability of copper to yield reactive oxygen species, displace other essential metal ions, and damage RNA and DNA.[44] The inhibition of growth of bacteria by copper metal has made it ideal for contact surfaces, like door handles and breweries, where contamination can cause adverse outcomes.[45] Figure 1.2.15 shows a brewery system manufactured from copper metal.

The application of copper-based drugs as anticancer agents has been researched from as early as the 1960s.[46]

Figure 1.2.15: Brewery system manufactured with copper metal.[47] The antimicrobial properties of copper make it ideal for the construction of items prone to contamination.

The coordination of organic drugs to metal ions has been shown to increase the activity of the drugs in some cases.[45] One class of drugs that shows an activity increase with copper(II) coordination is non-steroidal anti-inflammatory drugs.[45] A review by Psomas[45] illustrated a range of copper(II) complexes with non-steroidal anti-inflammatory drugs and the effects of the metal centre on the drugs' activity.[45]

A study by Almendras, *et al.*[48] showed positive effects on the antiplasmodial activity of 2-hydroxy-benzaldehyde-ferrocenyl-sulfonylhydrazone (HL) when coordinated to copper(II). The structure of this complex is shown in Figure 1.2.16.

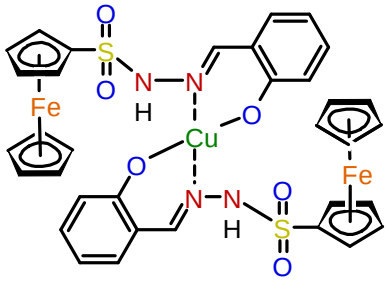

	IC_{50} (µM)
HL	105.03
$[Cu(L)_2]$	11.87
Chloroquine	0.0159

Figure 1.2.16: Structure of copper(II) di-2-hydroxy-benzaldehyde-ferrocenyl-sulfonylhydrazone, with table insert of the antiplasmodial activity, in IC_{50} (µM), of the ligand, complex and chloroquine.

The *in vitro* studies of this complex showed a reasonable increase in the antiplasmodial activity compared to 2-hydroxy-benzaldehyde-ferrocenyl-sulfonylhydrazone. The activity, however, was not greater than chloroquine, a widely used antiplasmodial agent, which could be attributed to the low solubility of the complex.[48]

A study by Lee, *et al.*[49] shows two copper(II) salicylaldehyde semicarbazone complexes with higher cytotoxicity towards certain cancer cell lines than cisplatin, making them potential chemotherapeutic agents. The semicarbazone copper(II) chelates have been shown to induce

apoptosis in human leukaemia MOLT-4 cells. Figure 1.2.17 shows the structure of these copper(II) chelates.

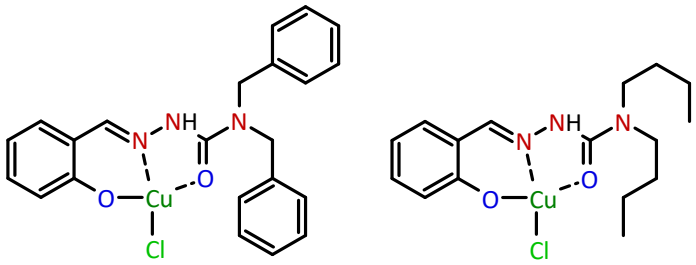

Figure 1.2.17: Structures of two salicylaldehyde-*N,N*-disubstituted semicarbazone complexes which have been shown to inhibit the growth of MOLT-4 cells.

The mechanism of how these semicarbazone copper(II) complexes induce apoptosis is yet to be conclusively determined. However, the most likely mechanism is through DNA binding and cleavage, based on the DNA cleavage and DNA binding activity studies.[49]

The antineoplastic activity of a group of copper(II) thiosemicarbazone complexes has been studied over several decades.[50] Studies demonstrate that the presence of copper(II) in the complexes increased the activity significantly.[50] These thiosemicarbazone chelates severely inhibit the enzyme ribonucleotide diphosphate reductase, which is responsible for the synthesis of DNA nucleotide precursors.[51] Figure 1.2.18 shows the structure of a thiosemicarbazone and the copper(II) complex thereof.[51] Further studies of copper(II) thiosemicarbazones have illustrated additional anticancer effects of the complexes; examples of these complexes are shown in Figure 1.2.19, below.

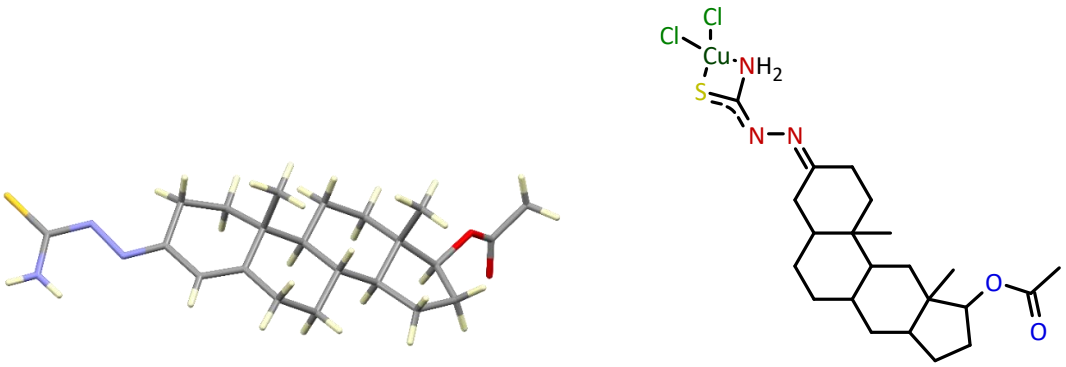

Figure 1.2.18: X-ray structure of 17-13-hydroxyandrost-4-one acetate thiosemicarbazone and the corresponding copper(II) chelate.[51]

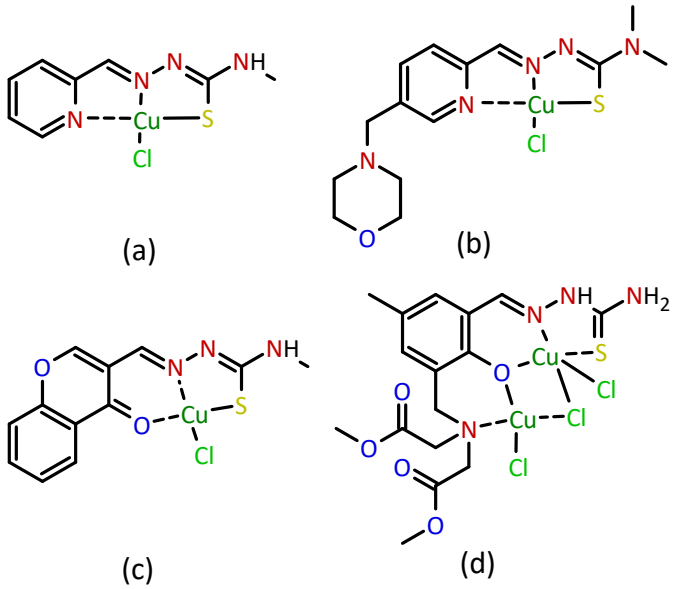

Figure 1.2.19: Structures of copper(II) thiosemicarbazones; (a) *N*-methyl-2-(pyridin-2-ylmethylene)hydrazinecarbothioamide copper(II)[52]; (b) 4*N*dimethyl-3-thiosemicarbazide copper(II)[53]; (c) *N*-methyl-*N*'-[(4-oxo-4*H*-1-benzopyran-3-yl)methylidene]carbamohydrazonothioic copper(II)[54]; and (d) dimethyl 2,2'-((3-((carbamothioylhydrazono)methyl)-2-hydroxy-5-methylbenzyl)imino)diacetate copper(II).[55]

The compounds shown in Figure 1.2.19 all have more significant anticancer activity when compared to cisplatin; Table 1.2.2 summarises these copper(II) chelates' and cisplatin's IC_{50} values against selected tumour cell lines:

Table 1.2.2: IC_{50} values of structures in Figure 1.2.19 and cisplatin.

Compounds	**Cell line**		
	Hep-G2 (hepatoblastoma)	**A2780 (ovarian cancer)**	**A549 (lung carcinoma)**
N-methyl-2-(pyridin-2-ylmethylene)hydrazinecarbothioamide copper(II)	6.81 µM[52]		
4*N*dimethyl-3-thiosemicarbazide copper(II)		0.012 µM[53]	
N-methyl-*N*'-[(4-oxo-4*H*-1-benzopyran-3-yl)methylidene]carbamohydrazonothioic copper(II			7.71 µM[54]
dimethyl 2,2'-((3-((carbamothioylhydrazono)methyl)-2-hydroxy-5-methylbenzyl)imino)diacetate copper(II)			4.30 µM[55]
cisplatin	17.23 µM[52]	0.44 µM[53]	15.10 µM[54,55]

N-methyl-2-(pyridin-2-ylmethylene)hydrazinecarbothioamide copper(II) (Figure 1.2.19 (a)) induces apoptosis in tumour cells *via* two modes of action. Firstly, the inhibition of the cell cycle through blocking the nuclear transcription process, and secondly, by attacking the cellular mitochondria.[52]

The complex in Figure 1.2.19(b) induces apoptosis in the cell by the following mechanism, (although the mechanism is dependent on the thiosemicarbazone ligand). Under reducing conditions in a cell, the copper(II) undergoes a reversible reduction, causing oxidative stress, while the thiosemicarbazone ligand inhibits proteins necessary for the cell cycle.[53] A study by Kalaiarasi, *et al.*[54] found that *N*-methyl-*N*'-[(4-oxo-4*H*-1-benzopyran-3-yl)methylidene]carbamohydrazonothioic copper(II), Figure 1.2.19(c), has a high affinity for DNA, binding *via* an intercalative mode and has a moderate binding affinity for serum albumins *viz.* bovine (BSA) and human (HSA). The complex was found to have both anticancer and antimicrobial properties.[54] The complex in Figure 1.2.19(d) shows a higher cytotoxicity compared to cisplatin, but it has a lower selectivity towards cancerous cells.[55]

A study by Saha, *et al.*[56] showed the addition of a thiosemicarbazide *via* a Schiff base to Ketoprofen (a known non-steroidal anti-inflammatory drug) significantly increased their antiproliferative activity, especially towards breast cancer cells.[56] The structure of one of these thiosemicarbazone complexes is shown in Figure 1.2.20 below.[56]

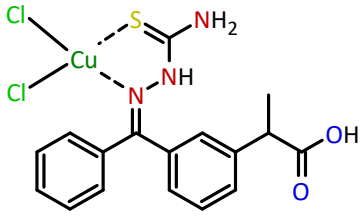

Figure 1.2.20: Thiosemicarbazone copper(II) complex which was shown by Saha, *et al.*[56] to effectively control the growth of breast cancer cells.

Copper(II) complexes with aroylhydrazone ligands have shown anticancer activity, as noted in the study by Hou, *et al.*[57] The copper(II) complex shown in Figure 1.2.21 was investigated for anticancer properties. It was found to induce apoptosis and reduce the activity of anti-apoptosis proteins, this combination makes it an effective anticancer compound.

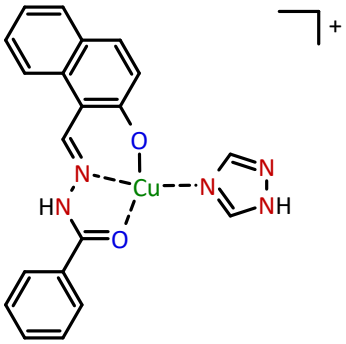

Figure 1.2.21: Structure of *(E)-N'*-((2-hydroxynaphthalen-1-yl)methylene)benzohydrazide) (1*H*-1,2,4-triazole) copper(II).[57]

The presence of the co-ligand, 1*H*-1,2,4-triazole, played a role in the cytotoxicity of the copper(II) aroylhydrazone complex. The copper(II) aroylhydrazone complex on its own did show some anticancer activity; however, the addition of the triazole co-ligand increased this activity greatly by initiating the reactive oxygen species-mediated pathway for apoptosis.[57] Table 1.2.3 summarises the IC_{50} values of the aroylhydrazone ligand (HL), the copper(II) chelate, $[Cu(L)(H_2O)_2]$, and the copper(II) chelate with a 1*H*-1,2,4-triazole co-ligand, [Cu(L)(1*H*-1,2,4-triazole)], and how the cytotoxicity of these compounds compare to cisplatin.

Table 1.2.3: IC_{50} (µM) values of HL, $[Cu(L)(H_2O)_2]$, [Cu(L)(1*H*-1,2,4-triazole)], and cisplatin towards the liver cancer cell line: Bel-7402.[57]

Compound	IC_{50} (µM)
HL	39.35
$[Cu(L)(H_2O)_2]$	9.62
[Cu(L)(1*H*-1,2,4-triazole)]	1.65
cisplatin	11.71

Apoptosis-inducing cancer treatment has limitations with respect to apoptosis-resistant cancers, and research into different mechanisms of action is of great importance. Gou, *et al.*[58] showed that dithiocarbazate copper(II) complexes could be used to treat pancreatic cancer, which exhibits apoptotic-resistant anticancer properties. In addition to the anticancer activity, the mixed copper(II)/(I) dithiocarbazate complexes, which are fluorescent, can also be used in bioimaging for cancer.[58] Figure 1.2.22 shows the structure of one such dithiocarbazate copper complex.

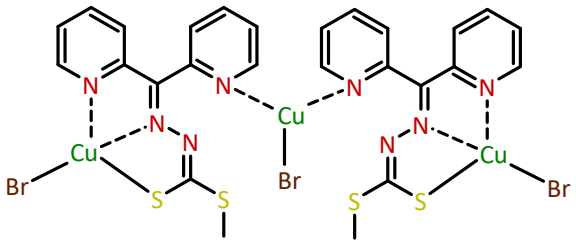

Figure 1.2.22: Structure of $[Cu^{II}_2Cu^{I}$(2-(di(pyridine-2-yl)methylene)hydrazinecarbodithioate))$(Br)_3]$ a dithiocarbazate copper compound with promising anti-proliferative properties and applications in bioimaging.[58]

The complex is trinuclear with mixed oxidation states of copper, 1+ and 2+. This is reported to give it an advantage in treating pancreatic cancer. The non-apoptotic pathway used by this complex is ferroptosis, which involves inducing high oxidative stress in the cell and peroxidation of the lipid membranes in the cell.[58] The bioimaging properties were also investigated and showed promising results *in vivo* when used with confocal fluorescence.[58]

A study by Kamah, *et al.*[59] showed copper(II) forming a six-coordinate chelate, a less common coordination geometry for copper(II), with 1,2-propylenediamine-*N,N,N,N*-tetraacetic acid (PDTA), $[Cu(PDTA\text{-}H_2)(H_2O)_2]H_2O$. This complex was shown to have substantial *in vitro* anticancer activity towards ovarian tumour TG cell line, as shown in Figure 1.2.24.[59]

Figure 1.2.23 shows the structure of the copper(II) complex.

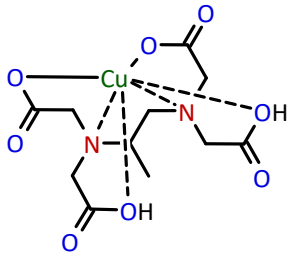

Figure 1.2.23: Structure of [Cu(PDTA-H_2)], H_2O's omitted for clarity.

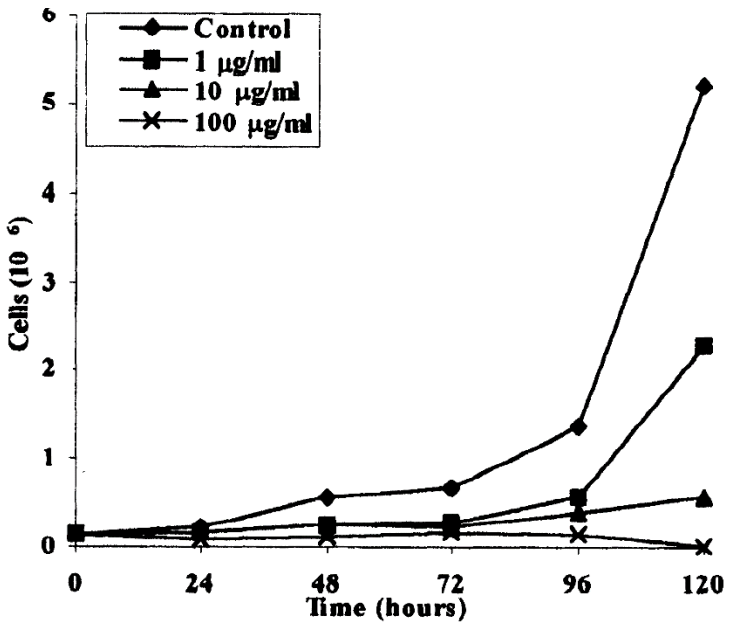

Figure 1.2.24: Graph showing the effects on cell growth when exposed to [Cu(PDTA-H_2(H_2O)$_2$]H_2O at various concentrations. Image reproduced from Kamah, *et al.*[59]

The anticancer activity of [Cu(PDTA-H_2)(H_2O)$_2$]H_2O is observed across all concentrations until 72 hours after initial dose, illustrating the intense interaction with the ovarian tumour TG cell line. The higher concentration (100 µg/ml) is shown to have an overall negative growth rate after 120 hours. The examples above highlight the potential of copper(II) as an anticancer agent.

1.3 DNA Interactions

1.3.1 Background

DNA is anticipated to be the primary cellular target for the compounds synthesised in this work. A discussion of the structure and various types of DNA interactions has, thus, been included. The double helix structure of DNA has many different components making it susceptible to interactions with a range of compounds not naturally present in the cell.[5] The DNA structure has grooves and spaces present, which are ideal areas for interactions to take place.[5] There are two main types of DNA structure, both with different orientations, i.e. left-handed and right-handed (or A-DNA and B-DNA). Additionally a third type has also been discovered (Z-DNA), which is rarely found, with Figure 1.3.1 illustrates the three forms of DNA:

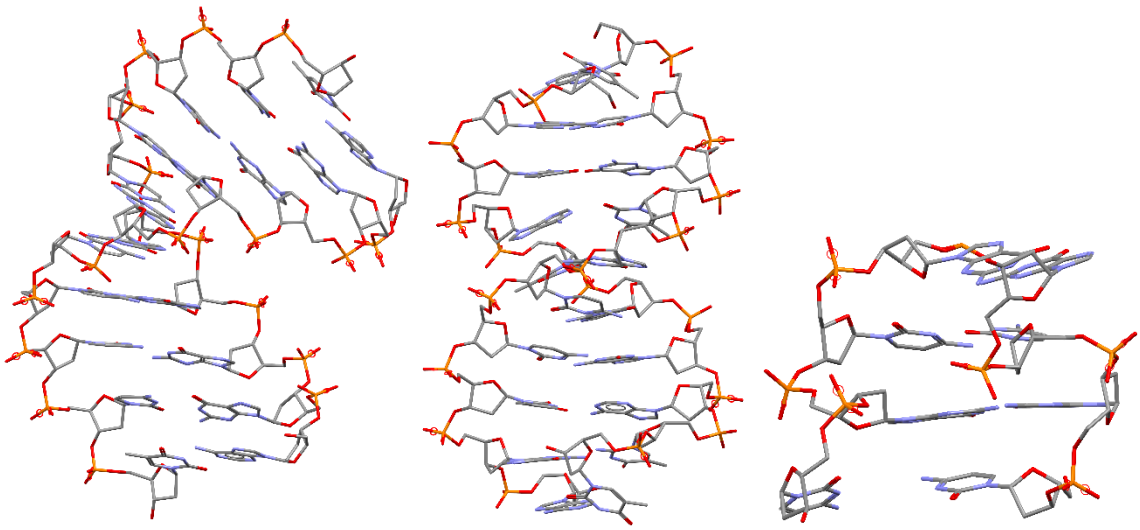

Figure 1.3.1: Structures of the three types of DNA (a) A-DNA; (b) B-DNA; and (c) Z-DNA. Image reproduced from Sammes and Yahioglu.[60]

The A- and B-DNA types are the most common in a cell, whereas the Z-DNA type is rarely found. The Z-DNA has a step-like double helix structure, while the A- and B-DNA types have the typical double helix shape. A-DNA is a combination of RNA and DNA base pairs, while B-DNA is a sequence of only DNA base pairs.[60]

The primary functions of DNA include transcription, regulation and replication, all of which control the synthesis of proteins that modulate the function of the cell.[60] Disrupting any of these processes can result in the cell undergoing apoptosis; this also occurs when the cell has reached the end of its lifespan.[60] The structure of DNA changes when the cell is about to divide; this process is controlled by two enzymes which are responsible for the supercoiling and uncoiling of DNA.[61] These enzymes are topoisomerase I and topoisomerase II (topo I and topo II) and if the function of these two enzymes is inhibited the cell can no longer replicate

its DNA, resulting in cell apoptosis.[61] Several commercially available drugs deactivate the topoisomerase I and II enzymes; these include topotecan, camptothecin and etoposide. These drugs work by binding to the DNA helix and interrupting the topo enzymes. Figure 1.3.2 illustrates the topo I enzyme bound to DNA as well as the enzyme being blocked by topotecan.

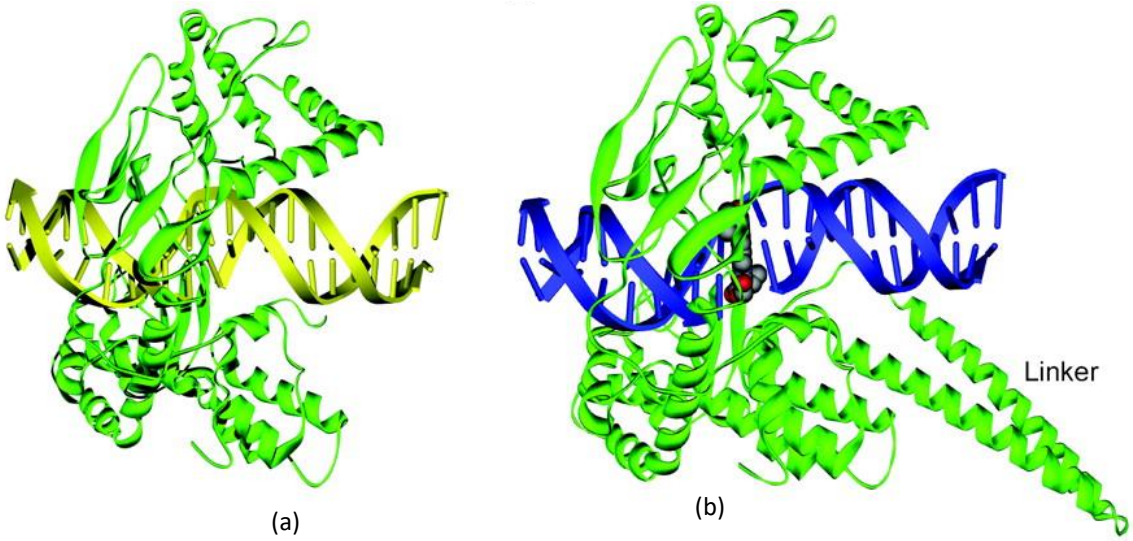

Figure 1.3.2: DNA (yellow and blue) segment with the topo I enzyme (green) bound (a) without, and (b) with topotecan interacting with the DNA structure. The linker section of topo I in (b) is absent in (a). Image obtained from Staker, *et al*.[62]

There are many ways in which a complex can interact with the DNA structure. These include groove binding, covalent binding, intercalation and lastly, phosphate-backbone association, a rare form of binding whereby an amine-containing complex hydrogen bonds to the oxygen atoms of the sugar-phosphate structure.[63] There are also bimodal systems where the complexes interact with the DNA *via* a combination of groove binding, covalent binding and intercalation. Complexes bind to DNA *via* external electrostatic association which is similar to groove binding and phosphate-backbone association. An electrostatic association between a compound and a DNA strand is a weak force that 'holds' the ligand close to the DNA chain.[64] This binding mode cannot affect the DNA structure due to a lack of interactions with the base pairs of the DNA chain. Since the DNA chain has a partially negatively charged phosphate backbone, cations are attracted to the DNA chain and promote further interactions.[49] The metal chelates synthesised in this work have been designed to have a positive overall charge to increase their attraction to the DNA helix.

1.3.2 Groove Binders

Groove-binding is an intermolecular interaction between the DNA helix and a drug; this binding mode does not alter the DNA structure.[60] The different binding sites of a DNA helix (major and minor grooves) have different properties due to the surface area of the two grooves (major – larger surface area, minor – smaller surface area). The structure of the DNA

binding agent will determine which binding site it will favour: major versus minor grooves. Figure 1.3.3 shows the major and minor grooves of DNA into which metal chelates can bind.

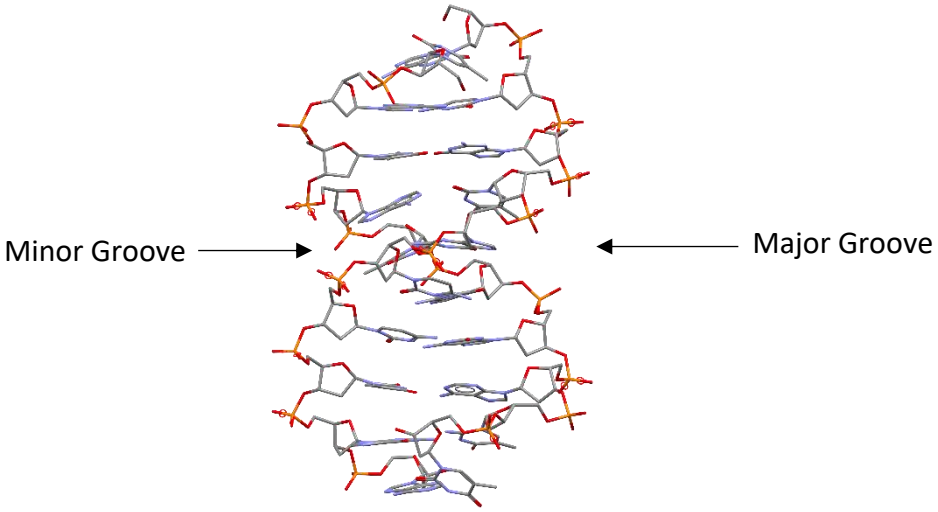

Figure 1.3.3: Section of a DNA helix illustrating the major and minor groove binding sites.[60]

There are several examples of metallodrugs that are DNA groove binders, these include ruthenium complexes as well as zinc and cobalt porphyrins. An example of a ruthenium complex is $[Ru(3,4,7,8\text{-tetramethyl-phen})_3]^{2+}$. Due to its ligand structure, it was thought to have intercalating properties, but instead was found to be a groove binder. The zinc and cobalt porphyrin complexes are, unexpectedly, groove binders. While the copper, nickel, and metal-free variants have intercalating properties. This unique property can be attributed to the zinc and cobalt complexes having axial ligands, primarily neutral amine ligands.[60,65,66] Figure 1.3.4 shows the structures of these groove-binding chemotherapeutics.

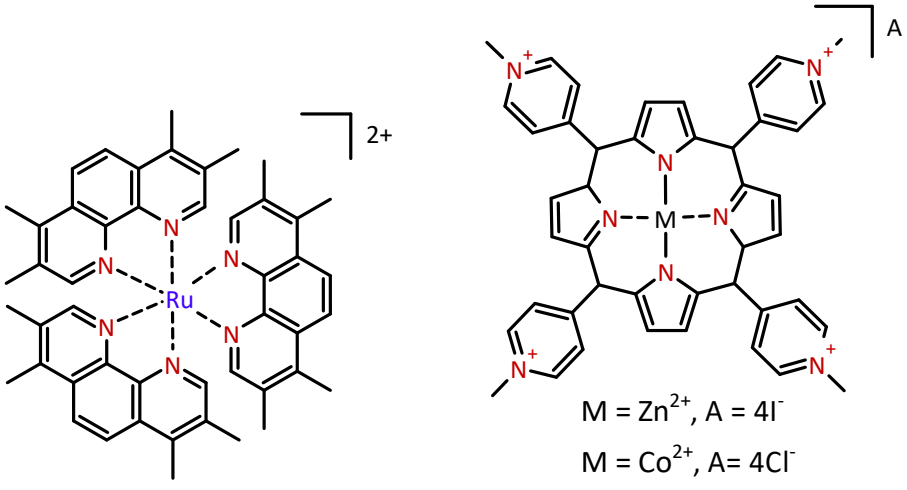

Figure 1.3.4: Examples of metal-based DNA groove binders.

1.3.3 Covalent Binders

As mentioned in section 1.2, cisplatin and its derivatives bind to the DNA structure through dative covalent bonds. This mode of interaction causes the DNA structure to unwind, inhibiting transcription and inducing cell apoptosis because the DNA is unable to repair its structure.[3] The covalent bonds can be either intra- or inter-strand, with respect to the DNA double helix, or form a single bond with the DNA and one with a protein or ligand.[3] There are limitations to the use of cisplatin and its derivatives, i.e. resistance and dose-limiting toxicity levels. Research into the applications of platinum(IV), instead of platinum(II), has afforded complexes with two extra ligands since the coordination geometry of the d^6 metal ion is octahedral. These changes can be used to introduce additional properties such as increased lipophilicity, fluorescent ligands for tracing the complexes, and tumour-targeting species.[3] Some platinum-containing covalent binders are multi-nuclear and can bond to the DNA at multiple sites, making it more difficult for the DNA to repair itself. Multiple ligands, therefore, lower the resistance potential. The overall positive charge of these compounds increases hydrophilicity and thus the cellular uptake. This also allows for faster DNA binding due to electrostatic attractions; further decreasing the resistance potential. [3]

Covalent DNA binders have also been synthesised from other d-block metals (example titanium) with cobalt used to deliver DNA binding compounds to cancerous cells.[67]. Figure 1.3.5 shows examples of these complexes:

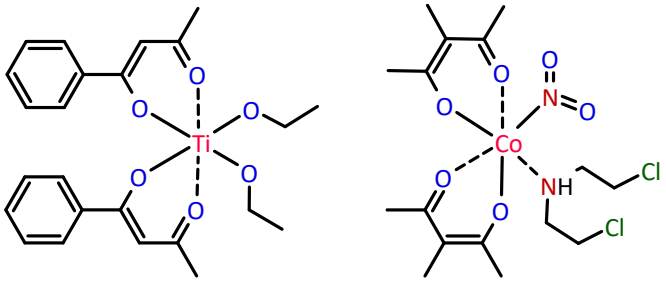

Figure 1.3.5: Structure of Budotitane, which is a covalent DNA binder based on titanium(IV), and a cobalt complex with a nitrogen mustard ligand.[63]

One of the first non-platinum metallodrugs to go into clinical trials was Budotitane. Budotitane hydrolyses the ethoxy groups before binding to the DNA base pairs, unlike cisplatin, the hydrolysis reaction is an extracellular process.[3]

Cobalt complexes that deliver DNA binding compounds (eg. 8-hydroquinoline or nitrogen mustard ligands) have either higher cellular uptake or are more stable in serum *in vivo* when compared to the free DNA binders.[68] The coordination to cobalt(III) reduces the cellular resistance of these compounds and provides stability *in vivo*.[69] The liberation of the active moiety is facilitated by the reduction of Co(III) to Co(II) by either the hypoxic regions of the cell or externally by ionising radiation.[63]

1.3.4 DNA Intercalators

DNA intercalation is the insertion of a compound into the DNA structure, between the base pairs.[6] There are many different types of DNA intercalators, both organic and inorganic. The organic intercalators, eg. adriamycin and daunomycin, are often naturally formed compounds used to control the DNA structure.[70] The intercalation of DNA is dependent on the type of ligand bound to the metal ion. The complex also has to be in a specific orientation relative to the DNA for it to intercalate. If the complex is in an orientation that is not suited to intercalation, then the complex may only groove-bind or externally associate itself electrostatically with the DNA.[60] Inorganic DNA intercalators usually include a planar aromatic organic ligand coordinated to a metal ion.[60]

DNA intercalation is a common mechanism of action for chemotherapeutic agents, and is the anticipated DNA binding mode for the metal chelates synthesised in this work. Analysis of commercially available DNA intercalators shows that they have several structural features in common. These include a planar aromatic region, a hydrogen bonding region and an overall positive charge.

The planar aromatic structure is important for two reasons. Firstly, it allows the molecule to fit in the limited space between the DNA base pairs. Secondly, it leads to favourable π-π interactions with the aromatic DNA bases. The overall positive charge leads to favourable electrostatic interactions with the negatively charged phosphate backbone of the DNA helix, increasing the binding affinity. Additionally, the ability of the chemotherapeutic agent to hydrogen bond to the DNA helix stabilises the DNA-drug conjugate, effectively locking the drug in position. The structure of topotecan, a known DNA intercalator, is shown in Figure 1.3.6, highlighting these common structural features.

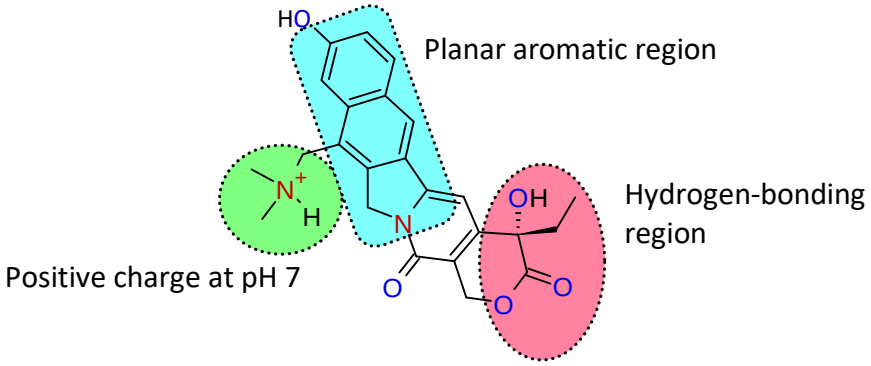

Figure 1.3.6: Structure of topotecan, highlighting the key structural features of DNA intercalators. These features were considered in the design of the compounds in this work.

Metalloporphyrins are examples of metal-based DNA intercalators.[64] Porphyrins have good electrochemical and spectroscopic properties, making them ideal for the characterisation and identification of biological activities.[71] The porphyrin structure is a planar, tetradentate ligand, which means, depending on the electron configuration of the metal ion, the metal ion to

which the porphyrin is coordinated often has no axial ligands coordinated.[71] Figure 1.3.7 shows the structure of a gold(III) tetraarylporphyrin, an effective DNA intercalator and chemotherapeutic agent:[72]

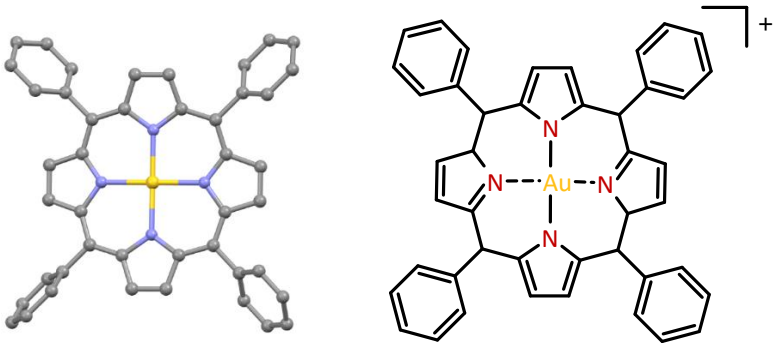

Figure 1.3.7: The X-ray and chemical structures of a cationic Au(III) porphyrin complex. Note that this complex has the planar geometry and overall positive charge often associated with DNA intercalators. The anions and H-atoms of the X-ray structure have been omitted for clarity.[72]

Coordination of the gold(III) ion by the tetradentate and dianionic tetraarylporphyrin ligand yields a monocationic complex ideal for DNA intercalation. This porphyrin complex and its analogues are stable with regards to reductive demetallation under physiological conditions.[72] The cytotoxicity of the porphyrin complexes are approximately 100-fold greater than that of cisplatin against both cisplatin- and multidrug-resistant cancer cell lines.[72]

A study by Ramakrishnan, *et al.*[4] illustrated the different abilities of four ligands to intercalate DNA. The four ligands were 2,2'-bipyridine (bpy); 1,10-phenanthroline (phen); 5,6-dimethyl-1,10-phenanthroline (5,6-dmp); and dipyrido[3,2-d:2',3'-*f*]quinoxaline (dpq).[4] The ligands were coordinated to copper(II) ions bridged by 2-hydroxy-*N*-[2-(methylamino)ethyl]benzamide ligands (Figure 1.3.8).

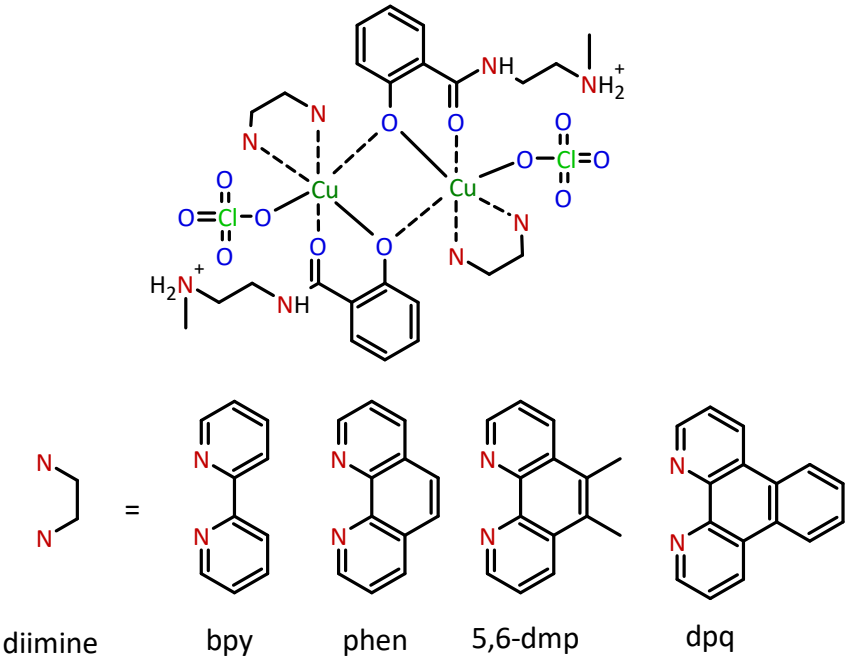

Figure 1.3.8: The different divalent ligands used in the study by Ramakrishnan, *et al.*[4]

Similar to the compounds presented in this work, these chelates were designed to intercalate and cleave DNA. It was found that the order of DNA cleavage ability for the above complexes was dpq > phen > bpy > 5,6-dmp.[4] This finding shows that the planarity of the ligand plays a significant role in DNA binding and cleavage. All four of these copper(II) complexes produce hydroxyl radicals in addition to intercalating DNA.[4] The study also presented a DNA viscosity test for each of the complexes; the viscosity test determines the nature of the DNA-drug interaction.[4] The original viscosity of supercoiled DNA is measured, and after each complex has interacted with the sample, the viscosity is measured again. If the viscosity stays the same or is reduced slightly in a particular experiment, this indicates that the complex interacts with the DNA helix via major groove binding and intercalation. If the viscosity is significantly reduced, the complex interacts via minor groove binding.[4] The dpq complex was the only complex to interact with the DNA helix *via* minor groove binding; the remaining complexes interacted *via* major groove binding and intercalation.[4]

A study by Chen, *et al.*[73] illustrated that copper(II) complexes with dpq and dipyrido[3,2-a:20,30-c] phenazine (dppz) can be used for light-induced DNA cleavage.[73] The complexes undergo groove binding and are then irradiated with natural or UV light.[73] This process forms singlet oxygen.[73] The singlet oxygen acts similarly to hydroxyl radicals. The singlet oxygen is highly reactive towards the DNA backbone, attacking the electron-rich double bonds of the DNA base pairs.[73] Figure 1.3.9 illustrates the structures of the copper(II) chelates synthesised by Chen, *et al.*[73] to act as DNA intercalators and cleaving agents.

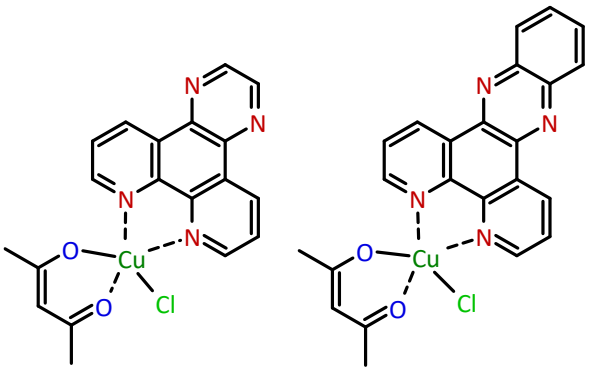

Figure 1.3.9: The structures of the copper(II) complexes used for photo-induced DNA cleavage, the dpq-based complex is on the left, and the dppz-based complex is on the right.

It was found that the dppz ligand made the complex more effective both in terms of DNA intercalating ability and singlet oxygen formation.[73] This was attributed to the extended aromatic structure of the dppz compared to the dpq ligand. The use of the acetylacetonate (acac) in the complex was for the planarity of the square pyramidal geometry and to balance the charge of the copper(II) ion to yield a neutral complex. Figure 1.3.10 illustrates the effect the different complexes, and the different light sources, have on tumour cells.[73]

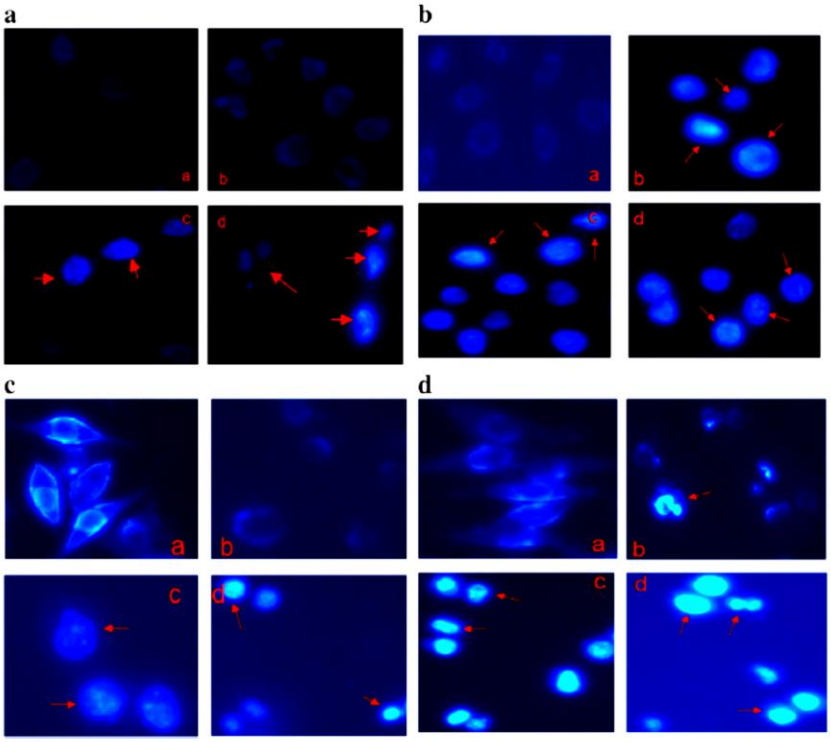

Figure 1.3.10: The features of apoptosis in cancer cells treated with the complexes, images a and b are using natural light, c and d using UV light. The images a and c on the left are treated with the dpq complex, and the b and d are treated with the dppz complex. Figure reproduced from Chen, *et al.*[73]

The arrows on the images indicate the cells that are going through or have been through apoptosis.[73] This diagram illustrates the increase in the dppz complex's cytotoxicity compared to the dpq complex by showing the number of cells undergoing apoptosis after treatment with the copper(II) chelates.

1.4 Hydroxyl Radicals and DNA Cleavage

The biologically accessible reduction potential of the copper(I)/copper(II) couple can catalyse the production of hydroxyl radicals under the right conditions, which, in a cell, can induce both single and double-stranded DNA cleavage. The latter is particularly difficult for cells to repair and usually leads to cell apoptosis.[6] The 1,10-phenanthroline ligand has been well studied, and it has been shown that in combination with a reducing agent, a metal and molecular oxygen, hydroxyl radicals are produced.[6] The hydroxyl radical attacks the double-stranded DNA chain and breaks down the base pairs and helix' backbone' of the DNA.[6]

Five metal-ligand combinations were tested by Que, *et al.*[6] with 1,10-phenanthroline as the ligand and cobalt, cadmium, nickel, zinc and copper (all divalent metal ions) as the metal centres. It was found that the copper(II) complex was the only one that produced the hydroxyl radicals, and therefore, was the most useful complex for control of the proliferation of tumour cells. The redox-active copper(II) centre is the catalyst for the hydroxyl radical formation.

The most common cellular reducing agents are ascorbate, 2-mercaptoethanol, and naturally occurring thiyls.[6] The following reaction scheme (Scheme 2) illustrates the hydroxyl radical formation:

$$HS\text{-}R\text{-}S^- + Cu(phen)^{2+} \rightarrow HS\text{-}R\text{-}S^{\cdot} + Cu(phen)^{1+}$$
$$HS\text{-}R\text{-}S^{\cdot} + O_2 \rightarrow S\text{-}S\text{-}R + H^+ + O_2^{-\cdot}$$
$$2O_2^{-\cdot} + 2H^+ \rightarrow H_2O_2 + O_2$$
$$Cu(phen)^{1+} + H_2O_2 \rightarrow OH^{\cdot} + OH^- + Cu(phen)^{2+}$$
$$OH^{\cdot} + DNA \rightarrow Fragments$$

Scheme 2: The reaction equations for the formation of hydroxyl radicals for DNA degradation catalysed by copper(II).

Hydroxyl radicals cause DNA chain degradation as they attack the electron-rich aromatic base pairs. It has been shown that radicals are the cause of DNA damage through experimentation with radical scavengers.[6] The scavengers absorb radicals, and when the hydroxyl radical producing copper(II) chelates are incubated with DNA and the scavengers, the DNA is virtually undamaged. This supports the hypothesis that radicals are the leading cause of DNA degradation in the mechanism of these copper-based complexes.[6]

The reason the other four metals mentioned above were inactive for the hydroxyl radical formation is due to the highly stable complexes formed with the 1,10-phenanthroline ligand and the differing reduction potentials. It was found that the copper(II) was inactive (for hydroxyl radical formation) when placed with ligands such as EDTA, triethyltetraamine, and neocuproine.[6] This shows that the pairing of copper(II) and a 1,10-phenanthroline derivative has a unique ability to produce hydroxyl radicals.

1.5 Radiochemistry

Many different types of metals are being used in medicine in conjunction with organic ligands for both the detection and treatment of diseases.[74] Some metals used in medicinal inorganic chemistry are radioactive and are used as diagnostic agents; such metals include technetium-99m (^{99m}Tc), gallium-68 (^{68}Ga) and indium-111 (^{111}In).[8] Diagnostic agents are introduced into the patient and are used for the early detection of diseases. In some cases, these drugs are used for radiotherapy. In the early stages of research, these radioactive isotopes can also monitor the biodistribution of compounds *in vivo*.[8] Technetium-99m is found in many metalloradiopharmaceuticals having different diagnostic imaging properties; an example of a ^{99m}Tc-based pharmaceutical agent is [^{99m}Tc(sestamibi)]$^{+}$ (trade name of Cardiolite), which is used to image breast and myocardium cancers.[8] Figure 1.5.1 shows the structure of Cardiolite.

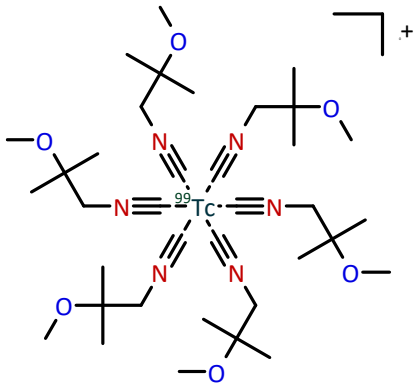

Figure 1.5.1: Structure of Cardiolite.[8]

Another two metalloradiopharmaceutical agents used in diagnostics are ^{68}Ga citrate, and ^{111}In pentetreodtide, as shown in Figure 1.5.2.[8]

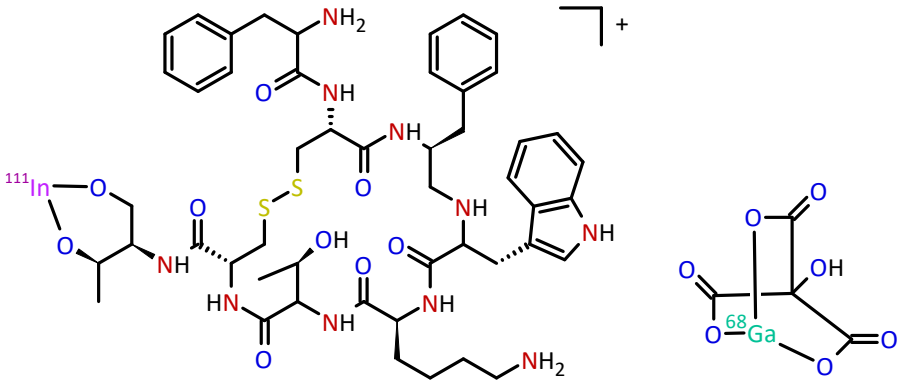

Figure 1.5.2: Structure of (a) ^{111}In pentetreodtide on the left; and (b) ^{68}Ga citrate on the right.

^{68}Ga has a half-life of 68 minutes, which makes it a suitable isotope for imaging.[75] A study by Smith, *et al.*[75] showed a range of ^{68}Ga complexes used as imaging agents for mitochondrial dysfunction in heart disease. The study illustrated that the retention of the second generation

^{68}Ga complexes had improved, and the uptake had increased.[75] The complexes are shown in Figure 1.5.3, below.

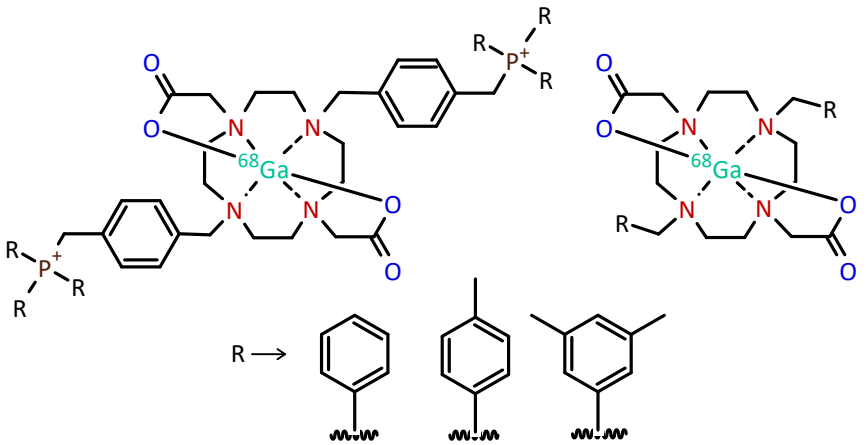

Figure 1.5.3: Structure of ^{68}Ga complexes used in cardiovascular radioimaging.[75]

Imaging of the cardiovascular system is conventionally done *via* Single Photon Emission Computing Tomography (SPECT) using ^{99m}Tc lipophilic complexes. This method of imaging has its downfalls - namely low sensitivity and low resolution.[75] The ^{68}Ga complexes in Figure 1.5.3 use Positron Emission Tomography (PET) for imaging rather than SPECT (due to the specific decay properties) and have proven to be potential radiotracers.[75]

A study by Gyuricza *et al.*[76] showed ^{68}Ga being used in conjunction with a peptide to enhance the imaging properties due to the high affinity of the peptide for the $\alpha_v\beta_3$ integrin receptor that is overproduced in some cancers.[76] The ^{68}Ga peptide is shown below in Figure 1.5.4:

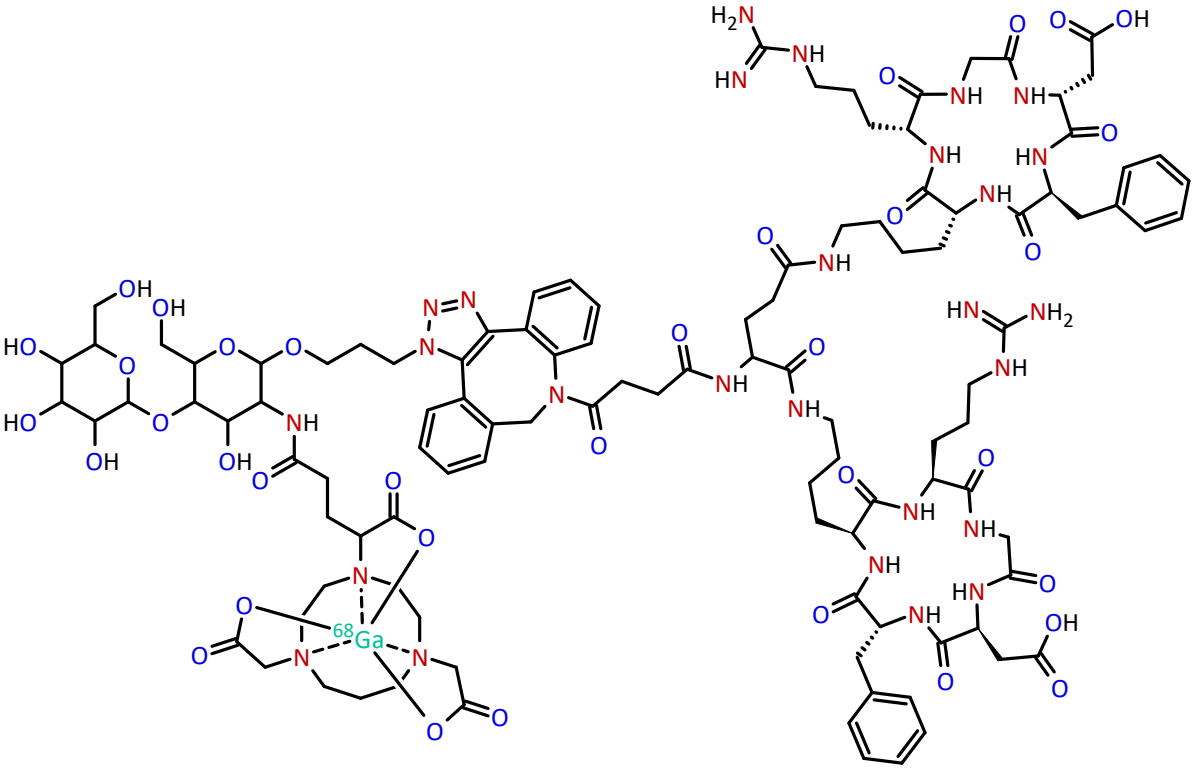

Figure 1.5.4: Structure of a ^{68}Ga peptide complex used for tumour imaging.

The stability of the ^{68}Ga peptide in Figure 1.5.4 and the hydrophilic properties make the complex ideal for cancer diagnosis and tumour imaging.[76]

In addition to the anticancer properties of natural copper (a mix of the non-radioactive ^{63}Cu and ^{65}Cu isotopes), the metal also has radioactive properties ideal for imaging and radiotherapy. Copper has five radioactive isotopes with half-lives ranging from 9.9 minutes to 61.9 hours. ^{62}Cu is mainly used for diagnosis and ^{64}Cu is used for both diagnosis and therapy.[77] The dual properties of ^{64}Cu make the radioactive isotope a potential anticancer agent when coordinated to ligands that aid in the process. ^{64}Cu has a half-life of 12.7 hours and decays *via* β emission and electron capture.[77] A study by Philpott, *et al.*[78] used a ^{64}Cu-labelled antibody to illustrate the distribution of the antibody for breast and colorectal cancers. With the distribution characterisation from this technique, cancer treatment could be optimised for the best results.[77,78]

The imaging properties of ^{64}Cu have also been used in a study by Paterson *et al.*[79] and another by Torres, *et al.*[80] The structures of these compounds are shown in Figure 1.5.5:

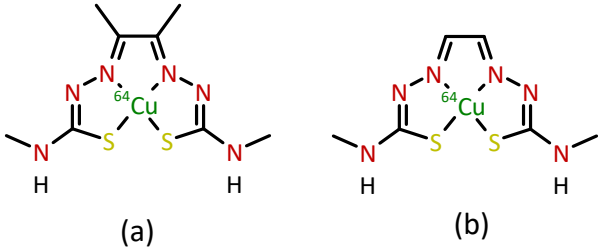

Figure 1.5.5: Structures of (a) diacetylbis(4-methyl-3-thiosemicarbazonato)copper(II)[79]; (b) glyoxalbis(N4-methyl-3-thiosemicarbazonato) copper(II) which have been radiolabelled with ^{64}Cu for tumour imaging studies.[80,81]

The complex in Figure 1.5.5(a) has been used in neck and head tumour imaging due to the high uptake of the complex in the brain. The complex has also shown potential for imaging other brain disorders such as Parkinson's disease and amyotrophic lateral sclerosis due to the ability of the complex to pass through the blood-brain barrier.[79,82]

The structure in Figure 1.5.5(b) has shown great potential as an imaging agent for Alzheimer's disease. This is due to the high uptake of the complex in the brain, attributed to the lipophilicity of the complex. The complex passes into the brain and dissociates, allowing the ^{64}Cu ion to be mobile. Copper metabolism in the brain is then monitored *via* PET imaging which can illuminate the extent of the plaque buildup for patients with Alzheimer's disease; this is an alternative non-invasive diagnostic method.[80-82]

The radiochemical properties of a ^{64}Cu complex were studied by Gao, *et al.*[83], which showed the complex has a high affinity and specificity towards melanoma.[83] Figure 1.5.6 shows the structure of this complex.

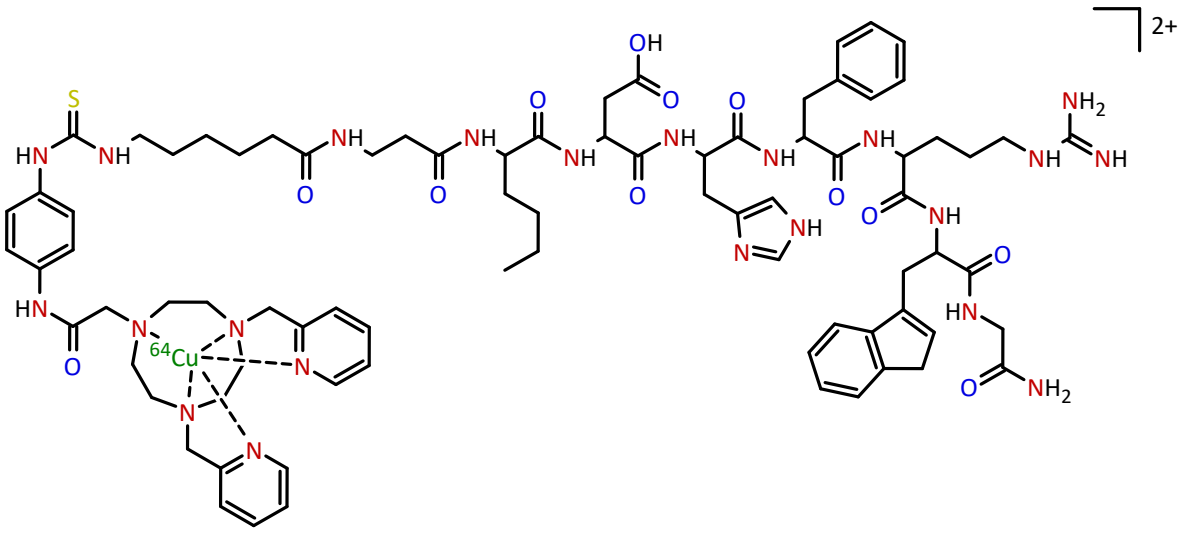

Figure 1.5.6: Structure of NAP-NS1 peptide conjugated with p-SCN-Ph-bis(2-pyridyl-methyl)-1,4,7triaza-cyclononane) and radiolabelled with ^{64}Cu.[83]

The complex in Figure 1.5.6 has the dual functionality of being used as a diagnostic agent, through the radiolabelled ^{64}Cu, and a treatment for melanoma. The latter is possible because of the cytotoxicity of the conjugate as a result of the high affinity and specificity of the NAP-NS1 peptide towards the melanocortin-1 receptor. Excretion of any radioactive complex is of great concern, and the structure in Figure 1.5.6 is excreted *via* the kidneys relatively fast due to the hydrophilic nature.[83]

1.6 Ligands and Metal Chelates

The ligands synthesised in this work are derivatives of 1,10-phenanthroline. Therefore, this bidentate ligand and its derivatives as well as their metal chelates will be discussed briefly. 1,10-phenanthroline can be derivatised to form a variety of different ligands. Most of the derivatisation is on the C5-C6 double bond because this site is the most susceptible to electrophilic addition.[60] 1,10-phenanthroline is shown in Figure 1.6.1 with the atom numbering scheme.

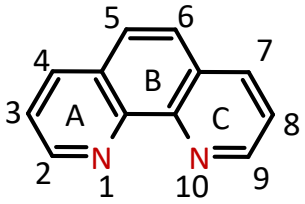

Figure 1.6.1: The structure of 1,10-phenanthroline, showing the atom numbering scheme.

The ligand itself has many functions, such as anticancer properties, due to its intercalation ability, the ligand also acts as a DNA 'nicking' agent.

Nicking is a process whereby the ligand removes a base pair from the DNA chain and, in turn, causes the cell to terminate.[60] The nicking happens in the presence of free radical hydroxyl groups, which are formed inside a cell in the presence of a copper ion. The phenanthroline ligand helps transport the copper(II) ion into cells where the production of the free radicals for the nicking process occurs,[60] as shown in Figure 1.6.2.

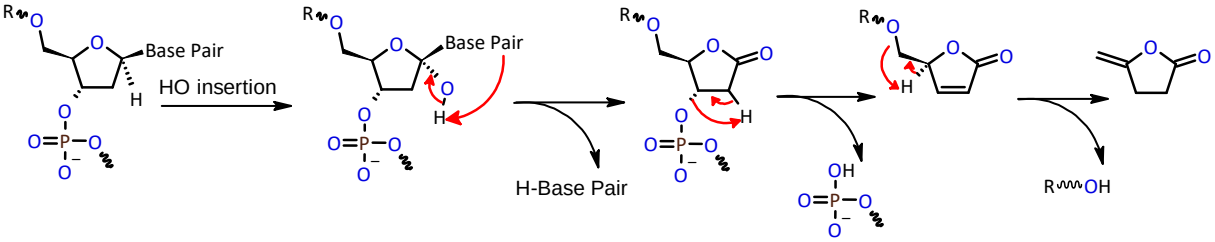

Figure 1.6.2: The reaction between the OH ion and a portion of the DNA.

Phenanthroline has been coordinated to europium(III), a lanthanide element. It was found that this complex has luminescent properties and is used in various assays and a selection of diagnostic probes.[60] The different derivatives of phenanthroline give rise to different properties in the luminescence; these are due to interactions between the complex and the aqueous solution. In a DNA assay, the probe, with a Eu^{3+} complex attached to it, interacts with a single DNA chain and a sensitiser so that a group is added into the DNA chain when the two single DNA chains merge.[60] This process causes the DNA helix to insert a group into the DNA chain, and the cell then undergoes apoptosis. This process is similar to intercalation, and is illustrated in Figure 1.6.3 below.

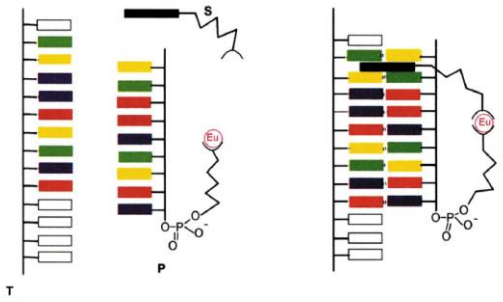

Figure 1.6.3: The interaction between the base pair of a DNA chain and the ligands.[60]

Reed, *et al.*[84] derivatised phenanthroline to form ligands closely related to those in this work. Phenanthroline (phen) is linked to an aromatic substituent *via* an amide bridge and is then coordinated to platinum(II). Figure 1.6.4 illustrates the structure of this ligand, which has the 1,10-phenanthroline attached to a pyridine ring *via* an amide bond.

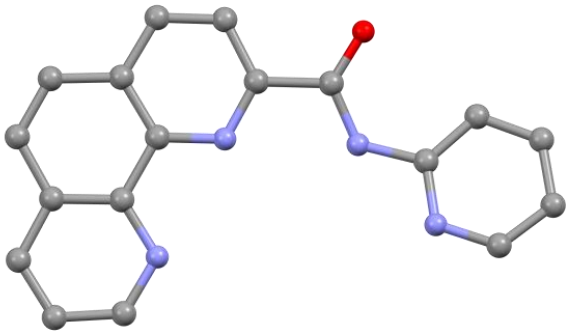

Figure 1.6.4: X-ray structure of a derivatised phenanthroline ligand closely related to those in this work. Hydrogen atoms have been omitted for clarity. [18]

The above ligand was coordinated to platinum(II), yielding an unusual dinuclear chelate, as shown below (Figure 1.6.5).

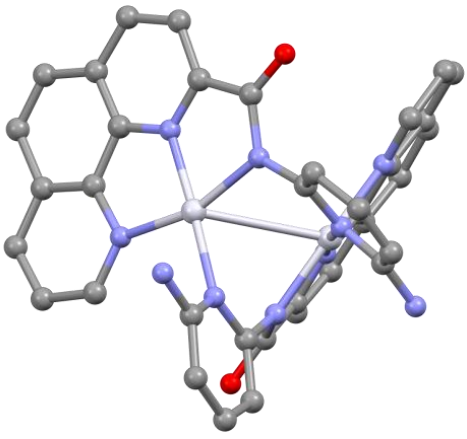

Figure 1.6.5: X-ray structure of a dimeric platinum(II) chelate derived from a phenanthroline-based ligand.[84]

This derivatised phenanthroline ligand was designed by Reed *et al.*[84] to have an extended aromatic nature, which makes it ideal for forming π-π interactions with guanine residues in the DNA helix.[84] Platinum(II) was used because of its high affinity for nitrogen and its usual

preference for a square planar geometry, which would maintain the planarity of the chelate.[84] These platinum(II) complexes were shown to intercalate DNA forming a stable DNA-chelate conjugate which induces cell apoptosis.[84]

The combination of copper(II) and two 1,10-phenanthroline ligands has been extensively studied for anticancer activities. Zhang, *et al.*[85] showed it to be highly effective towards human leukaemic HL60 cells, inhibiting the growth by up to 90%.[85] The low association of the second 1,10-phenanthroline ligand in physiological conditions, prompted a study by Pitié, *et al.*[86] to link the two phen ligands. The addition of a bridge between the two phen ligands has been shown to improve the overall effectiveness of the copper(II)-phen complexes as antitumour agents when compared to the non-bridged copper(II)-phen complex.[87] Figure 1.6.6 shows the structural features of the bridged copper(II)-phen complexes.

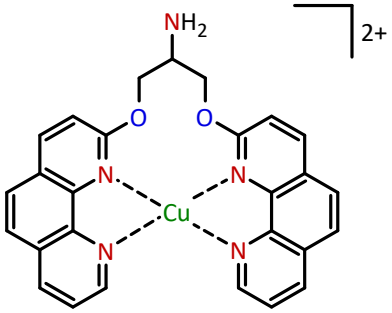

Figure 1.6.6: Structure of 2-Amino-1,3-bis(1',10'-phenanthrolin-2'-yloxy)propane copper(II). It was shown that linking the two phenanthroline ligands rendered the compound more stable and cytotoxic than the bis(phen) chelate.[86]

1.7 Summary

Heavy transition metals have shown to be beneficial in medicine to treat a range of illnesses. Gold chelates such as Auranofin, which is primarily used for the treatment of rheumatoid arthritis, have also been shown to have antiparasitic properties towards the *Plasmodium falciparum*, which is responsible for malaria. Gold chelates, such as the gold(III) tetraarylporphyrins, have been shown to have antitumor properties and are being further studied. Platinum, rhodium, and ruthenium chelates have antitumor properties, with multiple platinum chelates already being commercially available for cancer treatment. Rhodium chelates interact with DNA by intercalating between the base pairs when the metal ion is combined with an extended aromatic ligand. This process induces cell apoptosis. Ruthenium chelates like NAMI-A have become the first ruthenium-based chelates to enter phase I of clinical trials specifically for cancer treatment.

Light transition metals have also been shown to have anticancer properties, with multiple modes of action. Vanadium complexes are able to induce apoptosis and reduce the metastatic ability of cancer. Iron-based ferroquine has antimalarial properties. Additionally, iron complexes have anticancer properties as they are able to catalyse the formation of the highly reactive hydroxyl radicals in the Fenton reaction. These hydroxyl radicals react with the DNA structure and can induce DNA cleavage.

Metal chelates are capable of different types of DNA interactions which are dependent on the structural properties of the complex. For example, cisplatin binds to the DNA helix through a dative covalent bonds which cross-link the DNA strands, preventing replication. DNA groove binders can occupy either the minor or major grooves of DNA; however, this interaction does not alter the DNA structure. The DNA binding mode of interest in the present study is intercalation, which involves a planar compound inserting between the base pairs of the DNA structure, rendering the DNA structure unable to be replicated.

The metal of interest for this work is copper(II) due to the various applications in cancer treatment and diagnosis. Copper(II) chelates have been shown to be effective anticancer agents with a unique mechanism of action that is able to overcome issues of drug resistance. It is the biologically accessible reduction potential of the copper(II) ion which is able to catalyse the production of hydroxyl radicals in the presence of thiyls. The hydroxyl radicals react with the DNA structure and causing strand breaks which lead to apoptosis. The coordination of copper(II) to 1,10-phenanthroline derivatives has been shown to yield compounds that have antitumor properties and are potential chemotherapeutic agents.

One of the radioactive isotopes of copper (^{64}Cu) has shown potential as a diagnostic agent when chelated to different ligands. These radiolabeled copper(II) chelates have been shown to be effective in non-invasive imaging of brain disorders such as Parkinson's and Alzheimer's

disease. The diagnostic properties of radiolabeled ^{64}Cu chelates adds to the medicinal applications of the compounds.

1.8 Aims and Objectives

The fused ring system of phenanthroline was selected for derivatisation to produce the two groups of ligands and complexes in this work. The novel amide-based ligands will be coordinated to various metal ions, including copper(II), due to the ability of copper to catalyse the production of hydroxyl radicals. Nickel(II) is used as a control to determine if the copper(II) chelates have higher cytotoxicity due to their redox activity, and palladium(II), to determine if the metal-ligand combination affects cytotoxicity. Figure 1.8.1 and Figure 1.8.2 show the proposed novel amide-based ligands and the corresponding metal chelates.

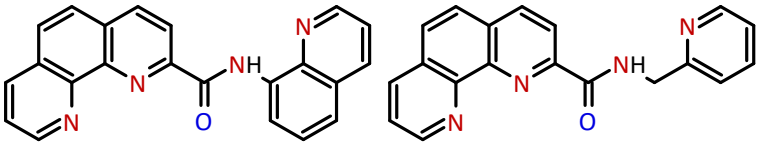

(a) HL1 (b) HL2

Figure 1.8.1: Structure and abbreviation of (a) HL1; and (b) HL2.

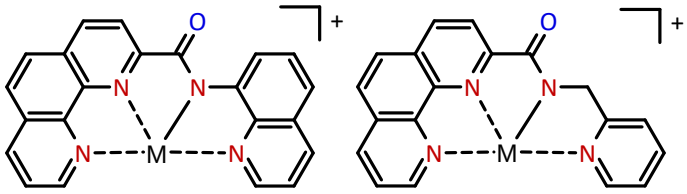

M = Cu(II), Ni(II), Pd(II)

Figure 1.8.2: Structures of the novel amide-based metal chelates proposed for the current study.

Chelation of the proposed amide-based ligands to divalent metal ions with concomitant deprotonation of the amide nitrogen atom will lead to a monocationic chelate. The overall positive charge, coupled with the extended aromatic region and hydrogen bonding ability of the amide oxygen, should render these chelates effective chemotherapeutic agents.

The second group of imine-based ligands were selected for this work and will be coordinated to copper(II). These imine-based chelates will have similar properties to the above amide-based complexes, but the change in structure will allow for the facile incorporation of various functional groups. These functional groups will change the electronic properties, lipophilicity and hydrogen bonding ability of the chelates. The effects of these changes on their cytotoxic properties can then be evaluated. Figure 1.8.3 shows an overview of the imine-chelates.

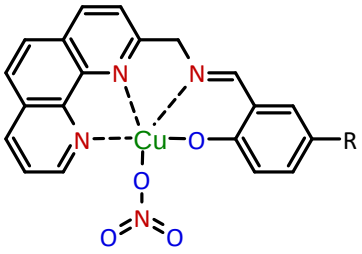

R = H, HL3
Cl, HL4
Br, HL5
CH_3, HL6
OCH_3, HL7
Naph, HL8
t-Butyl, HL9
NO_2, HL10

Figure 1.8.3: Structures of the proposed imine-based copper(II) chelates.

The following objectives for the project have been identified from the literature review:

1. To synthesise two novel amide-based ligands derived from 1,10-phenanthroline, as proposed in Figure 1.8.1, and to fully characterise the ligands. Ligands with these design elements have not been well studied prior to this work
2. To coordinate the amide-bridged ligands to copper(II), nickel(II) and palladium(II) and to fully characterise the chelates by various spectroscopic techniques. The palladium and nickel ions will serve as controls to see whether the redox activity of the copper is an aspect of the cytotoxicity.
3. To synthesise and fully characterise the proposed imine-bridged ligands derived from 1,10-phenanthroline and coordinate these to copper(II).
4. The compounds have been designed to act as DNA binding agents, and therefore, their affinity for DNA will be measured.
5. The ability of the copper(II) complexes to catalyse the production of hydroxyl radicals will be explored and their role in cytotoxicity will be evaluated.
6. The cytotoxicity of each metal chelate will be determined by screening them against a panel of human tumour cell lines to identify any lead compounds.
7. The biodistribution of the most active compound identidied from the *in vitro* screening will be determined through the radiolabelled copper-64 analogue.
8. The tumour uptake and retention of the lead drug candidate in a xenograft model will be determined using the radiolabelled analogue.

The goal of this work is to produce novel transition metal chelates that produce hydroxyl radicals and/or intercalate DNA, resulting in cytotoxic compounds. Before the chelates can be tested for their potential as chemotherapeutic agents, the first step will be synthesising the novel ligands and their metal chelates and determining their physical properties. Once the physical properties of the compounds have been analysed, the cytotoxicity of the compounds will be measured *in vitro*. The collection and interpretation of this information will determine if the proposed complexes are viable chemotherapeutic agents.

1.9 References

1. Gasser, G., *CHIMIA* **2015,** *69* (7-8), 442.
2. Crispini, A.; Pucci, D.; Sessa, S.; Cataldi, A.; Napoli, A.; Valentini, A.; Ghedini, M., *New J. Chem.* **2003,** *27*, 1497 - 1503.
3. Guo, Z.; Sadler, P. J., *Angewandte Chemie International Edition* **1999,** *38* (11), 1512-1531.
4. Ramakrishnan, S.; Shakthipriya, D.; Suresh, E.; Periasamy, V. S.; Akbarsha, M. A.; Palaniandavar, M., *J. Inorg. Chem.* **2011,** *50*, 6458-6471.
5. Zeglis, M.; Pierre, V. C.; Barton, J. K., *Chem. Commun.* **2007,** *44*, 4565 - 4579.
6. Que, B. G.; Downey, K. M.; So, A. G., *Biochem.* **1980,** (19), 5987-5991.
7. Alessio, E., *Bioinorganic Medicinal Chemistry*. Wiley-VCH Verlag GmbH & Co. KGaA: Weinheim, Germany, 2011.
8. Mjos, K. D.; Orvig, C., *Chem. Rev.* **2014,** *114* (8), 4540-4563.
9. Jones, C. J.; Thornback, J., *Medicinal applications of coordination chemistry*. Royal Society of Chemistry: Cambridge, 2007.
10. Benedek, T. G., *J Hist Med Allied Sci* **2004,** *59* (1), 50-89.
11. Faa, G.; Gerosa, C.; Fanni, D.; Lachowicz, J. I.; Nurchi, V. M., *Current Medicinal Chemistry* **2018,** *25* (1), 75-84.
12. Forestier, J., *The Lancet* **1934,** *224* (5795), 646-648.
13. Englinger, B.; Pirker, C.; Heffeter, P.; Terenzi, A.; Kowol, C. R.; Keppler, B. K.; Berger, W., *Chemical Reviews* **2019,** *119* (2), 1519-1624.
14. Dabrowiak, J. C., Gold Compounds for Treating Arthritis, Cancer and Other Diseases. In *Metals in Medicine*, pp 191-217.
15. Sannella, A. R.; Casini, A.; Gabbiani, C.; Messori, L.; Bilia, A. R.; Vincieri, F. F.; Majori, G.; Severini, C., *FEBS Letters* **2008,** *582* (6), 844-847.
16. Messori, L.; Orioli, P.; Tempi, C.; Marcon, G., *Biochemical and Biophysical Research Communications* **2001,** *281* (2), 352-360.
17. Shi, P.; Jiang, Q.; Zhao, Y.; Zhang, Y.; Lin, J.; Lin, L.; Ding, J.; Guo, Z., *JBIC Journal of Biological Inorganic Chemistry* **2006,** *11* (6), 745-752.
18. Khandekar, S. V.; Kulkarni, M. G.; Devarajan, P. V., *J Biomed Nanotechnol* **2014,** *10* (1), 143-53.

19. Rosenberg, B.; Van Camp, L.; Krigas, T., *Nature* **1965,** *205* (4972), 698-699.
20. Kelland, L., *Nat Rev Cancer* **2007,** *7* (8), 573-84.
21. Kenny, R. G.; Marmion, C. J., *Chemical Reviews* **2019,** *119* (2), 1058-1137.
22. Kostova, I., *Recent patents on anti-cancer drug discovery* **2006,** *1*, 1-22.
23. Ang, D. L.; Kelso, C.; Beck, J. L.; Ralph, S. F.; Harman, D. G.; Aldrich-Wright, J. R., *JBIC Journal of Biological Inorganic Chemistry* **2020,** *25* (3), 429-440.
24. Yang, C.; Wang, W.; Liang, J. X.; Li, G.; Vellaisamy, K.; Wong, C. Y.; Ma, D. L.; Leung, C. H., *J Med Chem* **2017,** *60* (6), 2597-2603.
25. Alessio, E.; Messori, L., *Molecules* **2019,** *24* (10), 1995.
26. Rademaker-Lakhai, J. M.; van den Bongard, D.; Pluim, D.; Beijnen, J. H.; Schellens, J. H., *Clin Cancer Res* **2004,** *10* (11), 3717-27.
27. Lai, H.; Zhao, Z.; Li, L.; Zheng, W.; Chen, T., *Metallomics* **2015,** *7* (3), 439-447.
28. Basu, A., *Sci. Revs. Chem. Commun.* **2015,** *5* (2), 77-87.
29. Crans, D. C.; Yang, L.; Haase, A.; Yang, X., *Met Ions Life Sci* **2018,** *18*.
30. Thompson, K. H.; Orvig, C., *Coordination Chemistry Reviews* **2001,** *219-221*, 1033-1053.
31. Kioseoglou, E.; Petanidis, S.; Gabriel, C.; Salifoglou, A., *Coordination Chemistry Reviews* **2015,** *301-302*, 87-105.
32. Selman, M.; Rousso, C.; Bergeron, A.; Son, H. H.; Krishnan, R.; El-Sayes, N. A.; Varette, O.; Chen, A.; Le Boeuf, F.; Tzelepis, F.; Bell, J. C.; Crans, D. C.; Diallo, J. S., *Mol Ther* **2018,** *26* (1), 56-69.
33. Ondo, W. G., *Sleep Medicine* **2010,** *11* (5), 494 - 496.
34. Biot, C.; Taramelli, D.; Forfar-Bares, I.; Maciejewski, L. A.; Boyce, M.; Nowogrocki, G.; Brocard, J. S.; Basilico, N.; Olliaro, P.; Egan, T. J., *Molecular Pharmaceutics* **2005,** *2* (3), 185-193.
35. Gasser, G.; Ott, I.; Metzler-Nolte, N., *Journal of Medicinal Chemistry* **2011,** *54* (1), 3-25.
36. Dive, D.; Biot, C., *ChemMedChem* **2008,** *3* (3), 383-391.
37. Basu, U.; Roy, M.; Chakravarty, A. R., *Coordination Chemistry Reviews* **2020,** *417*, 213339.
38. Lee, S.-Y.; Hille, A.; Kitanovic, I.; Jesse, P.; Henze, G.; Wölfl, S.; Gust, R.; Prokop, A., *Leukemia Research* **2011,** *35* (3), 387-393.

39. Vančo, J.; Šindelář, Z.; Dvořák, Z.; Trávníček, Z., *Journal of Inorganic Biochemistry* **2015,** *142*, 92-100.
40. Cristina, M.; Maura, P.; Francesco, T.; Carlo, S., *Anti-Cancer Agents in Medicinal Chemistry* **2009,** *9* (2), 185-211.
41. Linder, M. C., Introduction and Overview of Copper as an Element Essential for Life. In *Biochemistry of Copper*, 1 ed.; Springer US: 1991; pp 1-13.
42. Chellan, P.; Sadler, P. J., *Philosophical Transactions of the Royal Society A: Mathematical, Physical and Engineering Sciences* **2015,** *373* (2037), 20140182.
43. Crisponi, G.; Nurchi, V. M.; Fanni, D.; Gerosa, C.; Nemolato, S.; Faa, G., *Coordination Chemistry Reviews* **2010,** *254* (7), 876-889.
44. Halliwell, B.; Gutteridge, J. M. C., [1] Role of free radicals and catalytic metal ions in human disease: An overview. In *Methods in Enzymology*, Academic Press: 1990; Vol. Volume 186, pp 1-85.
45. Psomas, G., *Coordination Chemistry Reviews* **2020,** *412*, 213259.
46. Padhyé, S.; Kauffman, G. B., *Coordination Chemistry Reviews* **1985,** *63*, 127-160.
47. Wiel, B. v. d., Free Brewery Stock Photo. brewery-1422239, Ed. Getty Images International: freeimages.com, Vol. 3996 x 2859.
48. Almendras, I.; Huentupil, Y.; Novoa, N.; Roussel, P.; Melis, D. R.; Smith, G. S.; Arancibia, R., *Inorganica Chimica Acta* **2019,** *496*, 119050.
49. Lee, W. Y.; Yan, Y. K.; Lee, P. P. F.; Tan, S. J.; Lim, K. H., *Metallomics* **2012,** *4*, 188-196.
50. Zhang, H.; Thomas, R.; Oupicky, D.; Peng, F., *J Biol Inorg Chem* **2008,** *13* (1), 47-55.
51. Murugkar, A.; Unnikrishnan, B.; Padhye, S.; Bhonde, R.; Teat, S.; Triantafillou, E.; Sinn, E., *Met Based Drugs* **1999,** *6* (3), 177-182.
52. Deng, J.; Yu, P.; Zhang, Z.; Wang, J.; Cai, J.; Wu, N.; Sun, H.; Liang, H.; Yang, F., *European Journal of Medicinal Chemistry* **2018,** *158*, 442-452.
53. Ohui, K.; Afanasenko, E.; Bacher, F.; Ting, R. L. X.; Zafar, A.; Blanco-Cabra, N.; Torrents, E.; Dömötör, O.; May, N. V.; Darvasiova, D.; Enyedy, É. A.; Popović-Bijelić, A.; Reynisson, J.; Rapta, P.; Babak, M. V.; Pastorin, G.; Arion, V. B., *Journal of Medicinal Chemistry* **2019,** *62* (2), 512-530.
54. Kalaiarasi, G.; Rajkumar, S. R. J.; Dharani, S.; Lynch, V. M.; Prabhakaran, R., *Inorganica Chimica Acta* **2018,** *471*, 759-776.

55. Zaltariov, M. F.; Hammerstad, M.; Arabshahi, H. J.; Jovanović, K.; Richter, K. W.; Cazacu, M.; Shova, S.; Balan, M.; Andersen, N. H.; Radulović, S.; Reynisson, J.; Andersson, K. K.; Arion, V. B., *Inorganic Chemistry* **2017,** *56* (6), 3532-3549.
56. Saha, D. K.; Padhye, S.; Padhye, S., *Met Based Drugs* **2001,** *8* (2), 73-77.
57. Hou, L.; Jia, X.; Wu, Y.; Li, J.; Yao, D.; Gou, Y.; Huang, G., *Journal of Molecular Structure* **2021,** *1239*, 130469.
58. Gou, Y.; Chen, M.; Li, S.; Deng, J.; Li, J.; Fang, G.; Yang, F.; Huang, G., *Journal of Medicinal Chemistry* **2021,** *64* (9), 5485-5499.
59. Kamah, S.; Vilaplana, R.; Moreno, J.; Akdi, K.; García-Herdugo, G.; González-Vílchez, F., *Met Based Drugs* **2000,** *7* (4), 219-224.
60. Sammes, P. G.; Yahioglu, G., *Chem. Soc. Rev.* **1994,** *1*, 327-334.
61. Besterman, J. M.; Elwell, L. P.; Cragoe, E. J., Jr. ; Andrews, C. W.; Cory, M., *J. Biol. Chem.* **1989,** *265* (4), 2324-2330.
62. Staker, B. L.; Hjerrild, K.; Feese, M. D.; Behnke, C. A.; Burgin, A. B.; Stewart, L., *Proceedings of the National Academy of Sciences* **2002,** *99* (24), 15387-15392.
63. Pages, B. J.; Ang, D. L.; Wright, E. P.; Aldrich-Wright, J. R., *Dalton Transactions* **2015,** *44* (8), 3505-3526.
64. R.J.Fiel; J.C.Howard; E.H.Mark; Gupta, N. D., *Nucleic Acids Res.* **1979,** *6* (9), 3093-3118.
65. Ishikawa, Y.; Yamakawa, N.; Uno, T., *Molecules* **2008,** *13* (12), 3117-3128.
66. Ishikawa, Y.; Yamakawa, N.; Uno, T., *Bioorganic & Medicinal Chemistry* **2007,** *15* (15), 5230-5238.
67. Teicher, B. A.; Abrams, M. J.; Rosbe, K. W.; Herman, T. S., *Cancer Research* **1990,** *50* (21), 6971-6975.
68. Renfrew, A. K.; Bryce, N. S.; Hambley, T. W., *Chemical Science* **2013,** *4* (9), 3731-3739.
69. Ahn, G.-O.; Ware, D. C.; Denny, W. A.; Wilson, W. R., *Radiation Research* **2004,** *162* (3), 315-325.
70. Barton, J. K.; Danishefsky, A. T.; Goldberg, J. M., *J. Am. Chem. Soc.* **1984,** *106*, 2172-2176.
71. Liu, Y.; Chen, T.; Wong, Y.-S.; Mei, W.-J.; Huang, X.-M.; Yang, F.; Liu, J.; Zheng, W.-J., *Chem. Biol. Interact.* **2010,** *1*, 349-356.
72. Che, C.-M.; Sun, R. W.-Y.; Yu, W.-Y.; Ko, C.-B.; Zhu, N.; Sun, H., *Chem. Commun.* **2003,** (14), 1718-1719.

73. Chen, G.-J.; Qiao, X.; Qiao, P.-Q.; Xu, G.-J.; Xu, J.-Y.; Tian, J.-L.; Gu, W.; Liu, X.; Yan, S.-P., *J. Inorg. Biochem.* **2011,** *105*, 119-126.

74. Kaluderovic, G. N.; Gomez-Ruiz, S.; Maksimovic-Ivanic, D.; Paschke, R.; Mijatovic, S., *Bioinorg. Chem. Appl.* **2012,** *2012*, 705907-705909.

75. Smith, A. J.; Osborne, B. E.; Keeling, G. P.; Blower, P. J.; Southworth, R.; Long, N. J., *Dalton Transactions* **2020,** *49* (4), 1097-1106.

76. Gyuricza, B.; Szabó, J.; Arató, V.; Szücs, D.; Vágner, A.; Szikra, D.; Fekete, A., *Pharmaceutics* **2021,** *13*, 796.

77. Gutfilen, B.; Souza, S. A.; Valentini, G., *Drug Des Devel Ther* **2018,** *12*, 3235-3245.

78. Philpott, G. W.; Schwarz, S. W.; Anderson, C. J.; Dehdashti, F.; Connett, J. M.; Kurt R. Zinn, C.; Meares, F.; Cutler, P. D.; Welch, M. J.; Siegel, B. A., *J Nucl. Med.* **1995,** *36*, 1818 - 1824.

79. Paterson, B. M.; Cullinane, C.; Crouch, P. J.; White, A. R.; Barnham, K. J.; Roselt, P. D.; Noonan, W.; Binns, D.; Hicks, R. J.; Donnelly, P. S., *Inorganic Chemistry* **2019,** *58* (7), 4540-4552.

80. Torres, J. B.; Andreozzi, E. M.; Dunn, J. T.; Siddique, M.; Szanda, I.; Howlett, D. R.; Sunassee, K.; Blower, P. J., *Journal of Nuclear Medicine* **2016,** *57* (1), 109-114.

81. Fodero-Tavoletti, M. T.; Villemagne, V. L.; Paterson, B. M.; White, A. R.; Li, Q. X.; Camakaris, J.; O'Keefe, G.; Cappai, R.; Barnham, K. J.; Donnelly, P. S., *Journal of Alzheimer's Disease* **2010,** *20* (1), 49-55.

82. Singh, N. K.; Kumbhar, A. A.; Pokharel, Y. R.; Yadav, P. N., *Journal of Inorganic Biochemistry* **2020,** *210*, 111134.

83. Gao, F.; Sihver, W.; Bergmann, R.; Walther, M.; Stephan, H.; Belter, B.; Neuber, C.; Haase-Kohn, C.; Bolzati, C.; Pietzsch, J.; Pietzsch, H.-J., *Journal of Labelled Compounds and Radiopharmaceuticals* **2019,** *62* (8), 495-509.

84. Reed, J. E.; White, A. J. P.; Neidle, S.; Vilar, R., *Dalton Trans.* **2009,** (14), 2558-2568.

85. Zhang, S.; Zhu, Y.; Tu, C.; Wei, H.; Yang, Z.; Lin, L.; Ding, J.; Zhang, J.; Guo, Z., *Journal of inorganic biochemistry* **2004,** *98* (12), 2099-2106.

86. Pitié, M.; Donnadieu, B.; Meunier, B., *Inorganic Chemistry* **1998,** *37* (14), 3486-3489.

87. Pitié, M.; Boldron, C.; Gornitzka, H.; Hemmert, C.; Donnadieu, B.; Meunier, B., *European Journal of Inorganic Chemistry* **2003,** *2003* (3), 528-540.

Chapter 2: Experimental

2.1 General Methods

All reactions were carried out under standard atmospheric conditions (298 K, 1 atm) unless otherwise specified. A double manifold vacuum line, cannula techniques and Schlenkware were used for reactions which required inert and anhydrous conditions. All solvents were of analytical reagent (AR) grade and were dried before use. Tetrahydrofuran and acetonitrile were dried with CaH_2 and filtered using cannula techniques. All reagents were purchased from Sigma-Aldrich and were used as received. All solvents were purchased from Merck. The synthesis of ligand precursors, with the exception of 1,10-phenanthrolin-2-ylmethanaminium chloride, follow the literature procedure reported by Corey, *et al.*[1] The purity of the chelates were confirmed with ^{13}C NMR, elemental analysis, or low-resolution mass spectrometry.

2.2 Instrumentation

Electronic spectra were recorded with a Shimadzu UV-1800 (with a fixed slit width = 1 nm) double-beam spectrophotometer using various solvents in a 1.0 cm path length quartz cuvette. FTIR spectra were recorded using a Cary 630 FTIR spectrometer equipped with an ATR Diamond 1-bounce reflectance accessory. Data were collected over 15 scans with a resolution of 4 cm^{-1}. NMR data were recorded in DMSO-d_6 using a 400 MHz Bruker Avance III spectrometer equipped with a 9.4 T magnet and 5 mm BBOF probe. The residual solvent signals were used as the reference: 2.50 ppm for ^{1}H and 39.52 ppm for ^{13}C NMR, all spectra were recorded at 303 K. ^{13}C NMR experiments were done with proton decoupling. The ^{1}H and ^{13}C NMR spectra were assigned using 2D COSY data as well as HSQC and HMBC data as required. High-resolution mass spectra were recorded by direct injection into a Waters Acquity-LCT Premier mass spectrometer using electrospray ionisation in positive mode. Low-resolution mass spectra were recorded by direct injection into a Shimadzu LCMS single-quadrupole mass spectrometer using electrospray ionisation in positive mode. Emission spectra were recorded on a Photon Technology Int. (PTI) fluorescence spectrometer controlled by PTI's Felix32© Version 1.1 software. Steady-state emission spectra were recorded using PTI's XenoFlash™ 300 Hz pulsed light source. Detection was by means of PTI's Model 814 analogue/photon-counting photomultiplier detector. Elemental analysis data were collected using a Thermo Scientific Flash 2000 Organic Elemental CHNS–O Analyser.

2.3 Synthesis of Ligand Precursors

2.3.1 Synthesis of 1,10-phenanthroline-1-oxide

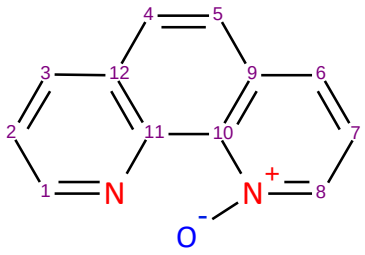

Figure 2.3.1: Structure of 1,10-phenanthroline-1-oxide showing the carbon numbering scheme.

To a solution of 1,10-phenanthroline monohydrate (2.06 g, 0.0114 mol) dissolved in glacial acetic acid (12 mL) was added an aqueous solution of hydrogen peroxide (30%, 1.2 mL). The reaction mixture was heated to 70 – 80 °C for three hours, after which a second aliquot of hydrogen peroxide was added (30%, 1.2 mL) and the solution heated for a further three hours at the same temperature to ensure complete oxidation.[1] The solution was cooled to room temperature and the solution adjusted to pH 10 using a saturated solution of sodium hydroxide. The aqueous solution was extracted with chloroform (3 × 20 mL portions), the organic fractions were combined and dried over anhydrous magnesium sulphate. The chloroform was removed using rotary evaporation under reduced pressure yielding a yellow solid (0.832 g, 37%).[2]

The following characterisation data were recorded: ^{1}H NMR (400 MHz, DMSO-d_6, 303 K) [δ, ppm]: 9.11 (dd, 1H, J_1 = 4.5 Hz, J_2 = 1.7 Hz, 8); 8.67 (dd, 1H, J_1 = 6.3 Hz, J_2 = 0.9 Hz, 3); 8.48 (dd, 1H, J_1 = 8.2 Hz, J_2 = 1.9, 6); 8.00 (q, 2H, 4, 5); 7.95 (d, 1H, 1); 7.78 (dd, 1H, J_1 = 8.1 Hz, J_2 = 4.3 Hz, 7); 7.64 (dd, 1H, J_1 = 8.5 Hz, J_2 = 6.4 Hz, 2). ^{13}C NMR (100 MHz, DMSO-d_6, 303 K) [δ, ppm]: 149.34 (C-8); 142.14 (C-10); 140.78 (C-3); 136.54 (C-6); 133.66 (C-11); 130.71 (C-9); 129.35 (C-4); 127.42 (C-5); 125.02 (C-12); 124.31 (C-1); 124.21 (C-2); 123.85 (C-7). IR (powder, cm^{-1}): 3228 (s, ν(C–H), aromatic hydrogens); 1433, 1246 (s, ν(N-O), N^{+}-O^{-}). ES+: 197.0717 *m/z* (M+1), [calculated: 197.0715 *m/z*]. Melting point (°C): 175 – 178 (lit. 176 – 179).[1]

2.3.2 Synthesis of 1,10-Phenanthroline-2-carbonitrile

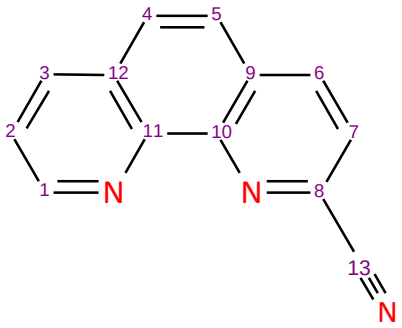

Figure 2.3.2: Structure with carbon numbering scheme of 1,10-phenanthroline-2-carbonitrile.

To a solution containing 1,10-phenanthroline-1-oxide (1.61 g, 8.20 mmol) and potassium cyanide (1.57 g, 24.1 mmol) dissolved in water (25 mL) was added (drop-wise) benzoyl chloride (1.5 mL, 12.9 mmol) with continuous stirring at room temperature.[1] The solution was stirred for an additional 15 minutes during which time a precipitate formed. The precipitate was collected *via* suction filtration, washed with water, and dried, yielding a tan solid (1.59 g, 95%).[1]

The following characterisation data were recorded: ^{1}H NMR (400 MHz, DMSO-d_6, 303 K) [δ, ppm]: 9.17 (dd, 1H, J_1 = 4.4 Hz, J_2 = 1.7 Hz, 1); 8.76 (d, 1H, 6); 8.57 (dd, 1H, J_1 = 8.2 Hz, J_2 = 1.7 Hz, 3); 8.13 (m, 2H, 4, 5); 7.87 (dd, 1H, J_1 = 8.2 Hz, J_2 = 4.5 Hz, 7); 7.49 (t, 1H, 2). ^{13}C NMR (100 MHz, DMSO-d_6, 303 K) [δ, ppm]: 150.7 (C-1); 145.7 (C-10); 144.4 (C-11); 138.1 (C-6); 136.6 (C-3); 132.8 (C-8); 132.2 (C-9); 129.8 (C-4); 128.4 (C-2); 126.7 (C-12); 126.1 (C-5); 124.3 (C-7); 117.8 (C-13). IR (powder, cm^{-1}): 3067 (s, ν(C-H), aromatic hydrogens); 2229 (s, ν(C≡N)). ES+: 206.0715 *m/z* (M+1), [calculated: 206.0718 *m/z*]. Melting point (°C): 230 – 232 (lit. 233 – 234).[1]

2.3.3 Synthesis of 1,10-phenanthroline-2-carboxylic acid

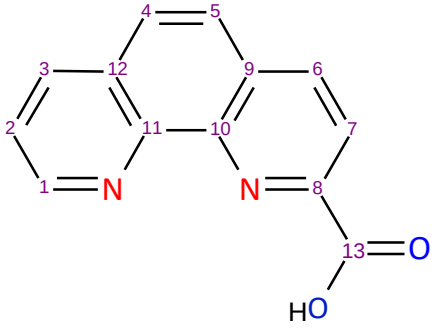

Figure 2.3.3: Structure of 1,10-phenanthroline-2-carboxylic acid showing the carbon numbering scheme.

A solution containing 1,10-phenanthroline-2-carbonitrile (1.00 g, 4.87 mmol) dissolved in ethanol (rectified, 10 mL) was added to a solution of sodium hydroxide

(0.8 g, 20.0 mmol) dissolved in water (5 mL) and the mixture heated to reflux for two hours.[1] The resulting solution was cooled to room temperature and acidified with concentrated hydrochloric acid (5 mL).[1] The resulting precipitate was collected and recrystallised from ethanol yielding a light tan solid (0.809 g, 74%).[1]

The following characterisation data were recorded: ^{1}H NMR (400 MHz, DMSO-d_6, 303 K) [δ, ppm]: 9.40 (d, 1H, 1); 9.26 (d, 1H, 6); 8.90 (d, 1H, 3); 8.54 (d, 1H, 7); 8.38 (m, 2H, 4, 5); 8.33 (t, 1H, 2). ^{13}C NMR (100 MHz, DMSO-d_6, 303 K) [δ, ppm]: 165.7 (C-13); 148.8 (C-8); 148.5 (C-11); 147.3 (C-1); 142.3 (C-6); 139.9 (C-10); 138.7 (C-3); 130.4 (C-9); 129.2 (C-12); 128.5 (C-5); 127.1 (C-4); 124.7 (C-2); 123.7 (C-7). IR (powder, cm^{-1}): 3467 (broad s, ν(O-H)); 3019 (broad s, ν(C-H)); 1742 (s, ν(C=O)). ES+: 247.0484 *m/z* (M + Na^{+}). Melting point
(°C): 207 – 210 (lit. 209 – 210).[1]

2.3.4 Synthesis of 1,10-phenanthrolin-2-ylmethanaminium chloride

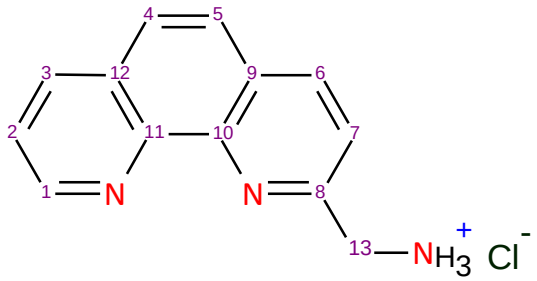

Figure 2.3.4: Structure of 1,10-phenanthrolin-2-ylmethanaminium chloride showing the atom numbering scheme.

To a solution of 1,10-phenanthroline-2-carbonitrile (2.120 g, 10.33 mmol) dissolved in methanol/HCl (40 mL/10 mL) palladium on carbon (5%, 2.200 g, 1.033 mmol) was added and the mixture placed under H_2 atmosphere (one atm) and stirred for 24 hours. The solution was filtered through a celite plug, and the filtrate reduced under vacuum. The solid was dissolved in H_2O (*ca.* 150 mL) and basified with a concentrated KOH solution (*ca.* 50 mL) to *ca.* pH 12 and the product extracted with chloroform (3 × 100 mL) and the organic layers combined. The organic phase was dried with $MgSO_4$ (anhydrous), filtered, and the solvent removed under vacuum. The resulting solid was dissolved in ethanol (30 mL) and concentrated HCl (3 mL) was added, the amine hydrochloride salt was collected by filtration, and dried in an oven at 40°C. (1.068 g, 49.4%).

The following characterisation data were recorded: ^{1}H NMR (400 MHz, DMSO-d_6, 303 K) [δ, ppm]: 9.09 (dd, 1H, J_1= 4.3 Hz, J_2= 1.8 Hz, 1); 8.46 (dd, 1H, J_1= 8.1 Hz, J_2= 1.8 Hz, 3); 8.43 (d, 1H, 6); 7.95 (d, 1H, 5); 7.92 (d, 1H, 4); 7.86 (d, 1H, 7); 7.74 (dd, 1H, J_1= 8.1 Hz, J_2= 4.3 Hz, 2); 4.14 (s, 2H, 13). ^{13}C NMR (100 MHz, DMSO-d_6, 303 K) [δ, ppm]: 163.21 (C-8); 149.65 (C-1); 145.34 (C-11); 144.59 (C-10); 136.47 (C-6); 136.09 (C-3); 128.52 (C-9); 127.08 (C-12); 126.50 (C-5); 125.75 (C-4); 123.02 (C-2); 121.36 (C-7); 48.17 (C-13). IR (powder, cm^{-1}): 3364

(broad s, ν(N-H)); 2849 (broad s, ν(C-H)); 1264 (s, ν(C-N)). ES+: 210.1028 *m/z* ([M-Cl]$^+$) , [calculated: 210.1031 *m/z*].

2.4 Synthesis of Ligands

2.4.1 Synthesis of N-(quinolin-8-yl)-1,10-phenanthroline-2-carboxamide

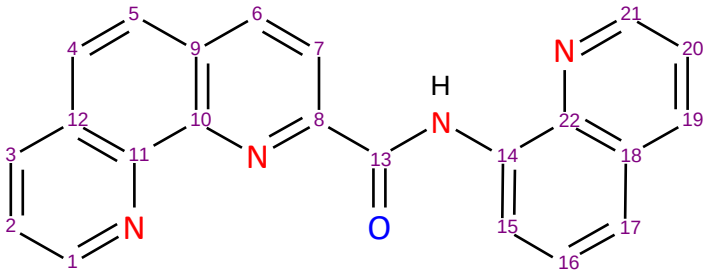

Figure 2.4.1: Structure with numbering scheme of N-(quinolin-8-yl)-1,10-phenanthroline-2-carboxamide (HL1).

A solution of 1,10-phenanthroline-2-carboxylic acid (0.300g, 1.340 mmol) in thionyl chloride (20 mL) was heated to reflux for six hours under inert conditions.[3] The thionyl chloride was removed under vacuum and the precipitate washed with tetrahydrofuran (3 × 20 mL) using a canunla, this too was removed under vacuum. To the resulting solid was added *via* canula 8-aminoquinoline (0.194 g) dissolved in tetrahydrofuran (20 mL) and the solution stirred for 48 hours at room temperature under inert conditions.[3] The ligand precipitated from solution and was collected by gravity filtration yielding a light brown powder (0.273 g, 0.779 mmol, 58%).

The following characterisation data were recorded: ^{1}H NMR (400 MHz, DMSO-d_6, 303 K) [δ, ppm]: 12.63 (s, 1H, N-H); 9.32 (dd, 1H, J_1 = 4.4 Hz, J_2 = 1.7 Hz, 1); 9.13 (dd, 1H, J_1 = 4.3 Hz, J_2 = 1.8 Hz, 21); 8.98 (dd, 1H, J_1 = 7.7 Hz, J_2 = 1.3 Hz, 15); 8.81 (d, 1H, 6); 8.59 (d, 1H, 3); 8.57 (dd, 1H, J_1 = 8.1 Hz, J_2 = 1.9 Hz, 7); 8.49 (dd, 1H, J_1 = 8.3 Hz, J_2 = 1.6 Hz, 19); 8.16 (m, 2H, 4, 5); 7.90 (dd, 1H, J_1 = 8.3 Hz, J_2 = 4.3 Hz, 2); 7.75 (11 peaks, 3H, 20, 17, 16). ^{13}C NMR (100 MHz, DMSO-d_6, 303 K) [δ, ppm]: 162.9 (C-13); 151.2 (C-12); 149.8 (C-1); 149.5 (C-21); 145.6 (C-5); 144.6 (C-9); 139.1 (C-10); 138.9 (C-19); 137.1 (C-3); 136.9 (C-22); 134.5 (C-14); 130.7 (C-6); 129.5 (C-4); 129.3 (C-8); 128.5 (C-18); 127.6 (C-16); 126.8 (C-7); 124.4 (C-2); 122.9 (C-20); 122.8 (C-17); 121.1 (C-11); 116.7 (C-15). IR (powder, cm^{-1}): 3339, 1557 (s, ν(N-H)); 1671 (s, ν(C=O), C=O stretching). UV (λ_{max}, ε, DMSO) [nm, M^{-1} cm^{-1}]: 273, 24704; 322, 12959. ES+: 351.1247 *m/z* (M+1), [calculated: 351.1246 *m/z*].

2.4.2 Synthesis of N-(pyridin-2-ylmethyl)-1,10-phenanthroline-2-carboxamide

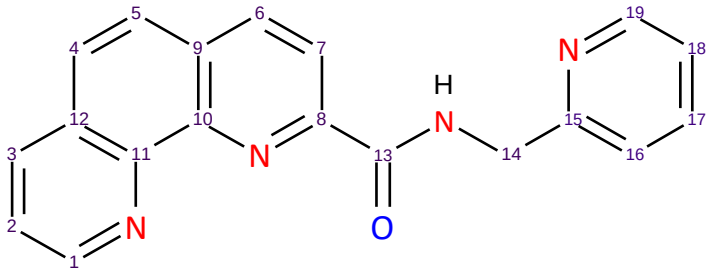

Figure 2.4.2: Structure of N-(pyridin-2-ylmethyl)-1,10-phenanthroline-2-carboxamide showing the atom numbering scheme (HL2).

A solution of 1,10-phenanthroline-2-carboxylic acid (0.300 g, 1.34 mmol) in thionyl chloride (20 mL) was refluxed for six hours under inert conditions.[3] The thionyl chloride was removed under vacuum and the resulting solid washed with tetrahydrofuran (3 × 20 mL) using a canula and was similarly removed under vacuum. To the resulting solid was added *via* canula 2-picolylamine (0.20 mL, 1.94 mmol) dissolved in tetrahydrofuran (20 mL) and the solution stirred for 48 hours at room temperature under inert conditions.[3] The ligand precipitated from solution, was collected *via* centrifugation, and washed twice with tetrahydrofuran, yielding a light tan powder (0.383 g, 1.22 mmol, 91%).

The following characterisation data were recorded: ^{1}H NMR (400 MHz, DMSO-d_6, 303 K) [δ, ppm]: 11.26 (t, 1H, N-H); 9.42 (d, 1H, 6); 9.23 (d, 1H, 7); 8.92 (d, 1H, 1); 8.62 (d, 1H, 19); 8.57 (d, 1H, 2); 8.53 (d, 1H, 3); 8.43 (m, 2H, 4, 5); 7.89 (dd, 1H, J_1 = 7.7 Hz, J_2 = 1.7 Hz, 17); 7.53 (d, 1H, 16); 7.42 (dd, 1H, J_1 = 7.7 Hz, J_2 = 4.9 Hz, 18); 4.97 (d, 2H, 14).^{13}C NMR (100 MHz, DMSO-d_6, 303 K) [δ, ppm]: 165.14 (C-13); 163.64 (C-8); 153.07 (C-10); 149.32 (C-11); 148.61 (C-19); 146.33 (C-6); 144.13 (C-7); 139.07 (C-1); 137.46 (C-17); 136.49 (C-15); 129.92 (C-9); 129.08 (C-12); 125.61 (C-7); 125.24 (C-6); 124.37 (C-3); 123.44 (C-18); 123.21 (C-2); 122.73 (C-16); 41.72 (C-14). IR (powder, cm^{-1}): 3401 (broad s, ν(N-H)); 2850, 2815 (d, ν(C-H)); 1669 (s, ν(C=O)). UV (λ_{max}, ε, DMSO) [nm, M^{-1} cm^{-1}]: 274, 18916; 328, 1829. ES+: 315.1242 *m/z* (M+1), [calculated: 315.1246 *m/z*].

2.5 Synthesis of Amide-based Metal Chelates

2.5.1 Synthesis of N-(quinolin-8-yl)-1,10-phenanthroline-2-carboxamide copper(II) hexafluorophosphate(V)

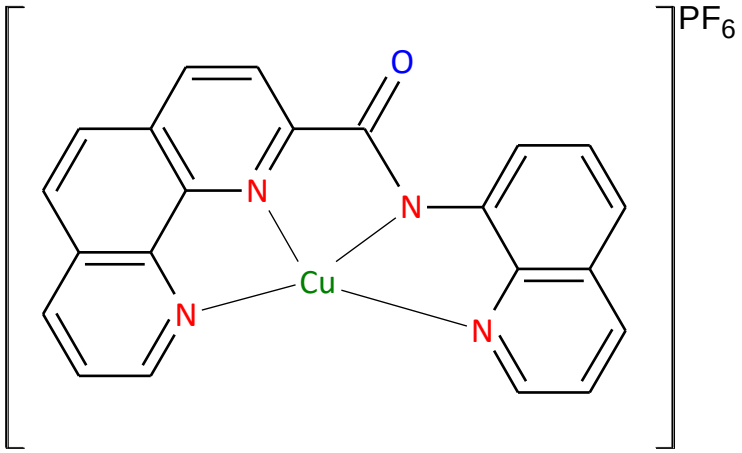

Figure 2.5.1: Structure of [Cu(L1)](PF$_6$).

To a solution of HL1 (300 mg, 0.856 mmol) dissolved in methanol (30 mL) was added a solution of $Cu(NO_3)_2 \cdot 3H_20$ (207 mg, 0.857 mmol) dissolved in methanol (30 mL) and the mixture refluxed for two hours. The reaction mixture was cooled to room temperature and the precipitate was collected *via* gravity filtration and recrystalised from ethanol, yielding a green powder (273 mg, 0.575 mmol, 67%) of [Cu(L1)](NO_3). The following characterisation data were recorded: ES+: 412.0377 *m/z* (M^+), [calculated: 412.0385 *m/z*]. Elemental analysis: Calculated for $C_{22}H_{13}CuN_5O_4$: C, 55.64; H, 2.76; N, 14.75. (Found: C, 54.72; H, 2.76; N, 11.83).

The hexafluorophosphate salt was synthesised for X-ray crystallographic studies, using the following method. To a solution of [Cu(L1)](NO_3) (200 mg, 0.421 mmol), dissolved in a minimum of methanol, was added a saturated aqueous solution of potassium hexafluorophosphate(V) (10 mL) and the solution refluxed for two hours. The reaction mixture was cooled to room temperature and the precipitate was collected *via* gravity filtration and washed with water (2 × 10 mL), yielding a green powder (110 mg, 0.198 mmol, 47%). The following characterisation data were recorded: IR (powder, cm^{-1}): 1620, 1605 (d, ν(C=O)); 3597 (s, ν(C-H)); 827 (s, ν(P-F_6)). UV (λ_{max}, ε, DMSO) [nm, M^{-1} cm^{-1}]: 263, 39156; 390, 6872.

2.5.2 Synthesis of N-(pyridin-2-ylmethyl)-1,10-phenanthroline-2-carboxamide copper(II) nitrate(V)

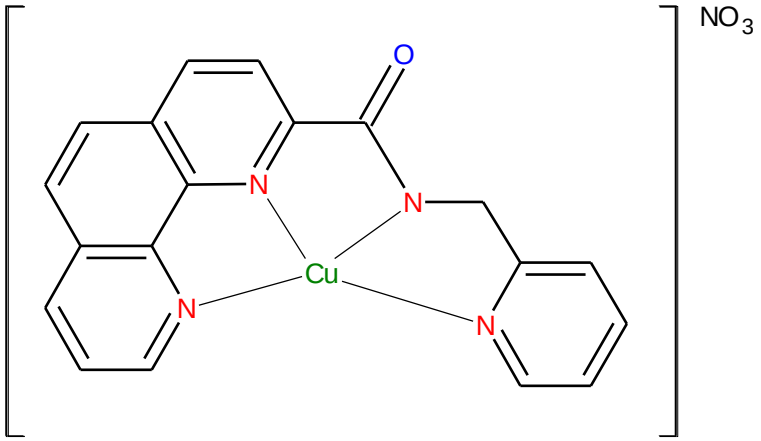

Figure 2.5.2: Structure of [Cu(L2)](NO_3).

To a solution of HL2 (300 mg, 0.954 mmol) dissolved in methanol (30 mL) was added a solution of $Cu(NO_3)_2 \cdot 3H_20$ (231 mg, 0.956 mmol) dissolved in methanol (30 mL) and the mixture refluxed for two hours. The resulting solution was cooled to room temperature, and the precipitate was collected *via* gravity filtration and washed with methanol (2 × 10 mL), yielding a light green powder (320 mg, 0.729 mmol, 76%).

The following characterisation data were recorded: IR (powder, cm^{-1}): 3044 (s, $\nu(C\text{-}H_{methylene})$); 1633 (s, $\nu(C{=}O)$); 734 (s, $\nu(C\text{-}H_{aromatic})$). UV ($\lambda_{max}$, ε, DMSO) [nm, M^{-1} cm^{-1}]: 276, 26742. ES+: 376.0377 *m/z* (M^+), [calculated: 376.0385 *m/z*].

2.5.3 Synthesis of N-(quinolin-8-yl)-1,10-phenanthroline-2-carboxamide nickel(II) hexafluorophosphate(V)

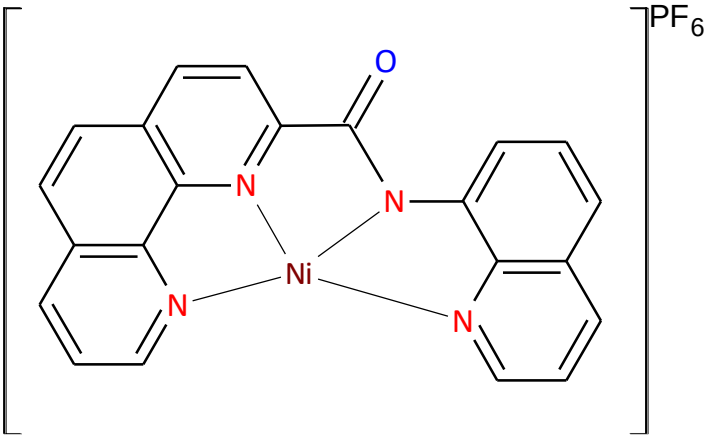

Figure 2.5.3: Structure of [Ni(L1)](PF_6).

To a solution of HL1 (300 mg, 0.856 mmol) dissolved in methanol (30 mL) was added a solution of $Ni(NO_3)_2{\cdot}6H_2O$ (249 mg, 0.858 mmol) dissolved in methanol (30 mL) and the mixture refluxed for two hours. The resulting solution was cooled to room temperature, and the precipitate was collected *via* gravity filtration, yielding a red powder (147 mg, 0.313 mmol, 37%) of [Ni(L1)](NO_3). The following characterisation data were recorded: ES+: 407.0437 *m/z* (M^+), [calculated: 407.0443 *m/z*]. Elemental analysis: Calculated for $C_{22}H_{13}NiN_5O_4{\cdot}H_2O$: C, 54.14; H, 3.10; N, 14.35. (Found: C, 54.35; H, 3.49; N, 13.82).

The hexafluorophosphate salt was synthesised for X-ray crystallographic studies, using the following method. To a solution of [Ni(L1)](NO_3) (100 mg, 213 mmol) in methanol (50 mL) was added a saturated solution of potassium hexafluorophosphate(V) (10 mL) and the reaction mixture refluxed for two hours. The resulting solution was cooled to room temperature, and the precipitate was collected *via* gravity filtration and washed with water (2 × 10 mL), yielding a red precipitate (69 mg, 0.147 mmol, 70%). The following characterisation data were recorded: IR (powder, cm^{-1}): 1658 (s, ν(C=O)); 3650, 698 (s, ν(C-H)); 811 (s, ν(P-F_6)). UV (λ_{max}, ε, DMSO) [nm, M^{-1} cm^{-1}]: 262, 32473; 398, 6503.

2.5.4 Synthesis of N-(pyridin-2-ylmethyl)-1,10-phenanthroline-2-carboxamide nickel(II) nitrate(V)

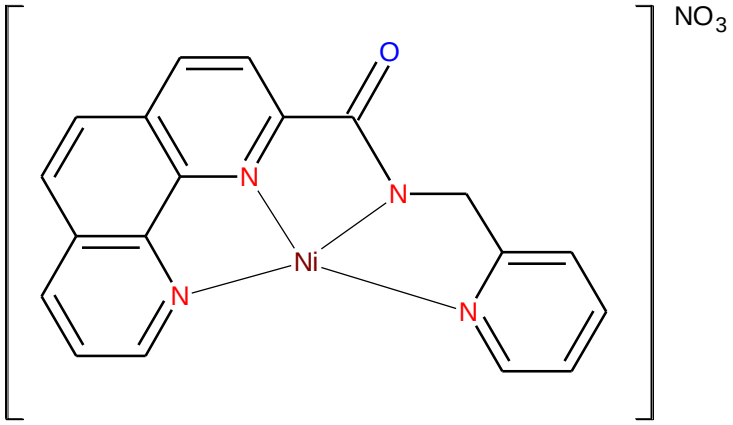

Figure 2.5.4: Structure of [Ni(L2)](NO_3).

To a solution of HL2 (300 mg, 0.954 mmol) dissolved in methanol (30 mL) was added a solution of $Ni(NO_3)_2{\cdot}6H_2O$ (278 mg, 0.958 mmol) dissolved in methanol (30 mL), with one molar equivalent of triethylamine (0.134 mL, 0.961 mmol) and the mixture refluxed for two hours. The solution was cooled to room temperature, and the precipitate collected *via* gravity filtration and washed with methanol (2 × 10 mL), yielding a yellow precipitate (78 mg, 0.180 mmol, 19%).

The following characterisation data were recorded: IR (powder, cm^{-1}): 3060 (broad s, ν(C-$H_{methylene}$)); 1637 (s, ν(C=O)); 711 (s, ν(C-$H_{aromatic}$)). UV (λ_{max}, ε, DMSO) [nm, M^{-1} cm^{-1}]: 277,

20966. ES+: 371.0452 *m/z* (M^+), [calculated: 371.0443 *m/z*]. Elemental analysis: Calculated for $C_{19}H_{13}N_5NiO_4 \cdot 3H_2O$: C, 46.76; H, 3.92; N, 14.35. (Found: C, 45.70; H, 3.93; N, 11.03).

2.5.5 Synthesis of N-(quinolin-8-yl)-1,10-phenanthroline-2-carboxamide palladium(II) chloride

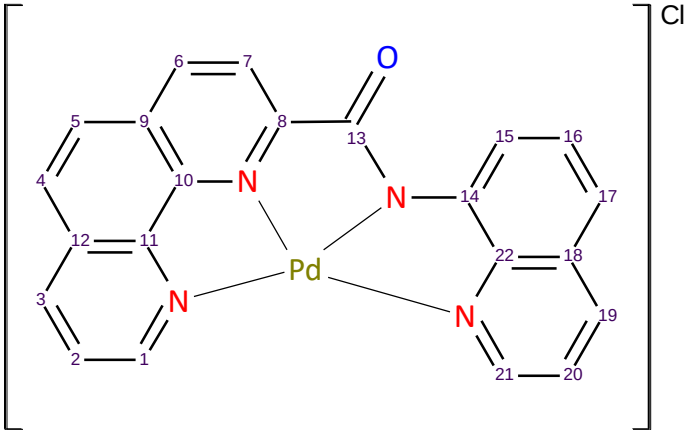

Figure 2.5.5: Structure and the atom numbering scheme of [Pd(L1)](Cl).

A solution of $K_2[PdCl_4]$ (300 mg, 0.919 mmol) in acetonitrile (30 mL) was refluxed for one hour. To the resulting solution was added HL1 (364 mg, 1.04 mmol) dissolved in acetonitrile (20 mL) and the mixture refluxed for four hours. The solution was cooled to room temperature, and the resulting precipitate collected by gravity filtration and washed with acetonitrile (2 × 10 mL), yielding a light brown precipitate (399 mg, 0.811 mmol, 88%).

The following characterisation data were recorded: ^{1}H NMR (400 MHz, DMSO-d_6, 303 K) [δ, ppm]: 9.34 (dd, 1H, J_1 = 4.4 Hz, J_2 = 1.7 Hz, 1); 9.12 (dd, 1H, J_1 = 3.9 Hz, J_2 = 1.5 Hz, 21); 8.92 (dd, 1H, J_1 = 7.3 Hz, J_2 = 0.6 Hz, 15); 8.84 (d, 1H, 6); 8.76 (dd, 1H, J_1 = 8.5 Hz, J_2 = 1.5, 7); 8.61 (d, 1H, 6); 8.50 (dd, 1H, J_1 = 8.4 Hz, J_2 = 1.7 Hz, 19); 8.20 (m, 2H, 4, 5); 7.97 (dd, 1H, J_1 = 7.9 Hz, J_2 = 4.6 Hz, 2); 7.76 (11 peaks, 3H, 16, 17, 21). ^{13}C NMR (100 MHz, DMSO-d_6, 303 K) [δ, ppm]: 167.7 (C-13); 152.9 (C-12); 149.2 (C-21); 144.8 (C-11); 144.5 (C-10); 139.0 (C-6); 137.1 (C-19); 130.6 (C-3); 129.9 (C-22); 129.7 (C-14); 128.8 (C-4); 127.8 (C-12); 127.1 (C-9); 125.2 (C-18); 123.8 (C-16); 123.4 (C-5); 123.3 (C-2); 123.0 (C-20); 122.5 (C-17); 122.4 (C-7); 121.3 (C-15). IR (powder, cm^{-1}): 3463 (broad s, ν(C-H)); 1649 (s, ν(C=O)). UV (λ_{max}, ε, DMSO) [nm, M^{-1} cm^{-1}]: 279, 27616; 390, 6409. ES+: 455.0141 *m/z* (M^+), [calculated: 455.0124 *m/z*].

2.5.6 Synthesis of N-(pyridin-2-ylmethyl)-1,10-phenanthroline-2-carboxamide palladium(II) chloride

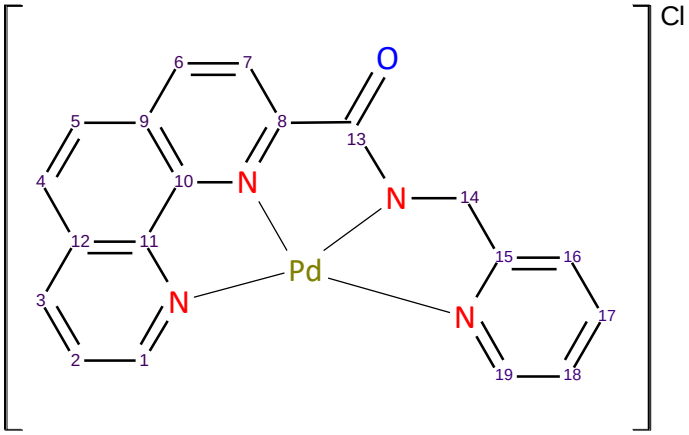

Figure 2.5.6: Structure of [Pd(L2)](Cl) showing the atom numbering scheme.

A solution of $K_2[PdCl_4]$ (300 mg, 0.919 mmol) in acetonitrile (30 mL) was refluxed for one hour. To the resulting solution was added HL2 (327 mg, 1.04 mmol) dissolved in acetonitrile (20 mL) and the mixture refluxed for four hours. The resulting solution was cooled to room temperature, the precipitate was collected by gravity filtration and washed with acetonitrile (2 × 10 mL), yielding a light brown precipitate (251 mg, 0.550 mmol, 60%).

The following characterisation data were recorded: ^{1}H NMR (400 MHz, DMSO-d_6, 303 K) [δ, ppm]: 9.40 (d, 1H, 6); 9.21 (d, 1H, 7); 8.89 (d, 1H, 1); 8.61 (d, 1H, 19); 8.56 (d, 1H, 2); 8.37 (m, 2H, 4, 5); 8.33 (d, 1H, 3); 7.86 (dd, 1H, J_1 = 7.9 Hz, J_2 = 1.7 Hz, 17); 7.61 (d, 1H, 16); 7.42 (d, 1H, 18); 4.85 (d, 2H, 14). ^{13}C NMR (100 MHz, DMSO-d_6, 303 K) [δ, ppm]: 172.4 (C-13); 166.6 (C-8); 153.1 (C-10); 150.0 (C-11); 148.6 (C-19); 147.0 (C-6); 144.4 (C-7); 140.0 (C-1); 137.7 (C-17); 130.9 (C-15); 130.0 (C-9); 129.5 (C-12); 127.5 (C-4); 127.1 (C-5); 124.4 (C-3); 123.9 (C-18); 123.7 (C-2); 122.9 (C-16); 52.1 (C-14). IR (powder, cm^{-1}): 3227 (s, ν(C-$H_{methylene}$)); 1674 (s, ν(C=O)); 760 (s, ν(C-$H_{aromatic}$)). UV (λ_{max}, ε, DMSO) [nm, M^{-1} cm^{-1}]: 270, 19356. ES+: 419.0142 *m/z* (M^+), [calculated: 419.0124 *m/z*].

2.6 Synthesis of Imine-based Metal Complexes

The copper(II) chelates with imine-based liagnds were synthesised using the general method below:

To a solution of 1,10-phenanthrolin-2-ylmethanaminium chloride (100 mg, 0.407 mmol) dissolved in methanol (30 mL) was added an aqueous solution of KOH (22 mg, 0.407 mmol) (10 mL). The corresponding 2-hydroxybenzaldehyde derivative (0.407 mmol) was then added to the solution, which was heated to reflux for two hours. This was followed by a solution of $Cu(NO_3)_2{\cdot}3H_20$ (70 mg, 0.407 mmol) dissolved in methanol (10 mL) and water (40 mL) and the mixture refluxed for a further two hours. The reaction mixture was cooled to room temperature, methanol (*ca.* 250 mL) was added and the solvent was then removed under reduced pressure. The precipitate was collected and recrystalised from methanol, yielding green powders for each chelate.

2.6.1 Synthesis of 2-{[(1,10-phenanthrolin-2-ylmethyl)imino]methyl}phenol copper(II) nitrate

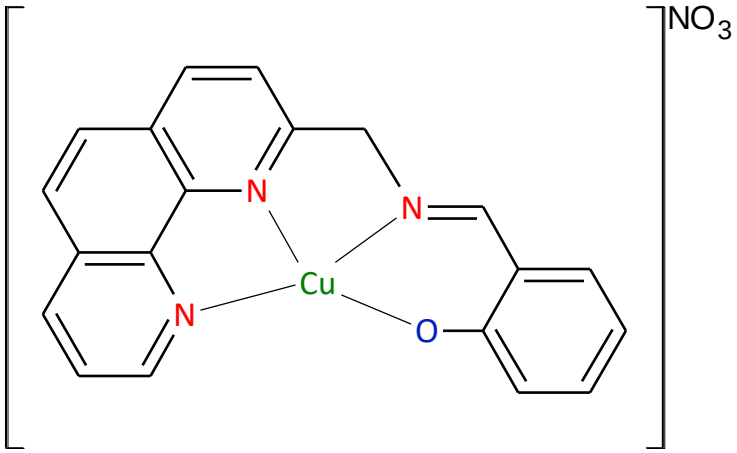

Figure 2.6.1: Structure of [Cu(L3)](NO$_3$).

Yield (150 mg, 0.343 mmol, 89.8%). The following characterisation data were recorded: IR (powder, cm^{-1}): 3056 (s, ν(C-H$_{methylene}$)); 1589 (s, ν(C=N)); 1503 (s, ν(O=N)); 1291 (s, ν(C-O)). UV (λ_{max}, ε, H_2O) [nm, M^{-1} cm^{-1}]: 205, 36981; 230, 19178; 273, 15089. ES+: 407 *m/z* (M^+ + Methanol).

2.6.2 Synthesis of 4-Chloro-2-{[(1,10-phenanthrolin-2-ylmethyl)imino]methyl}phenol copper(II) nitrate

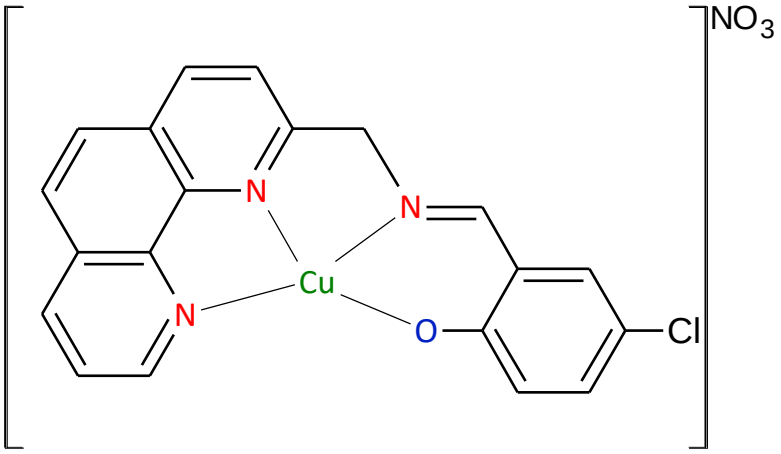

Figure 2.6.2: Structure of [Cu(L4)](NO$_3$).

Yield (152 mg, 0.321 mmol, 78.9%). The following characterisation data were recorded: IR (powder, cm^{-1}): 3056 (s, ν(C-H$_{methylene}$)); 1590 (s, ν(O=N)); 1503 (s, ν(C=N)); 1290 (s, ν(C-O)); 852(s, ν(C-Cl)). UV (λ_{max}, ε, H_2O) [nm, M^{-1} cm^{-1}]: 205, 74545; 230, 39344; 273, 32920; 294, 12830. ES+: 408.9948 *m/z* (M^+), [calculated: 409.0043 *m/z*]. Single crystal X-ray diffraction studies of [Cu(L4)](NO$_3$) confirmed the identity of this sample. The powder X-ray diffraction spectrum of [Cu(L4)](NO$_3$) was used to confirm that the phase of the bulk material matches that of the single crystal data (refer to Chapter 5).

2.6.3 Synthesis of 4-Bromo-2-{[(1,10-phenanthrolin-2-ylmethyl)imino]methyl}phenol copper(II) nitrate

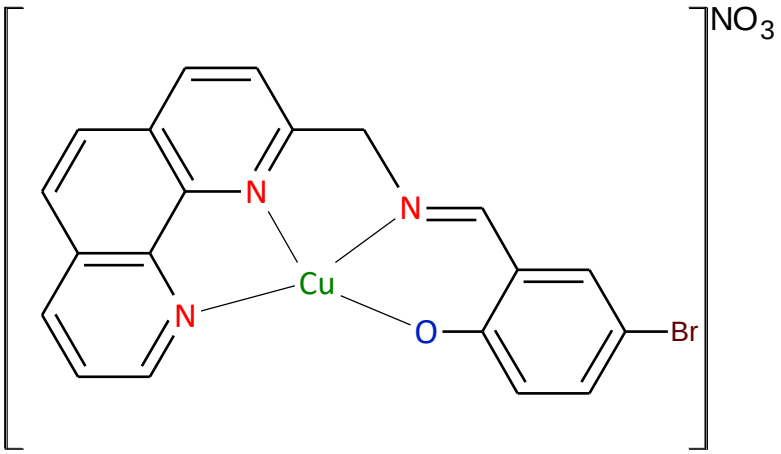

Figure 2.6.3: Structure of [Cu(L5)](NO$_3$).

Yield (173 mg, 0.335mmol, 82.3%). The following characterisation data were recorded: IR (powder, cm^{-1}): 3057 (s, ν(C-H$_{methylene}$)); 1588 (s, ν(C=N)); 1502 (s, ν(O=N)); 1289 (s, ν(C-O)). UV

(λ_{max}, ε, H_2O) [nm, M^{-1} cm^{-1}]: 205, 74303; 230, 20716; 273, 16691; 294, 6809. ES+: 454.9530 *m/z* (M^+), [calculated: 454.9520 *m/z*].

2.6.4 Synthesis of 4-Methyl-2-{[(1,10-phenanthrolin-2-ylmethyl)imino]methyl}phenol copper(II) nitrate

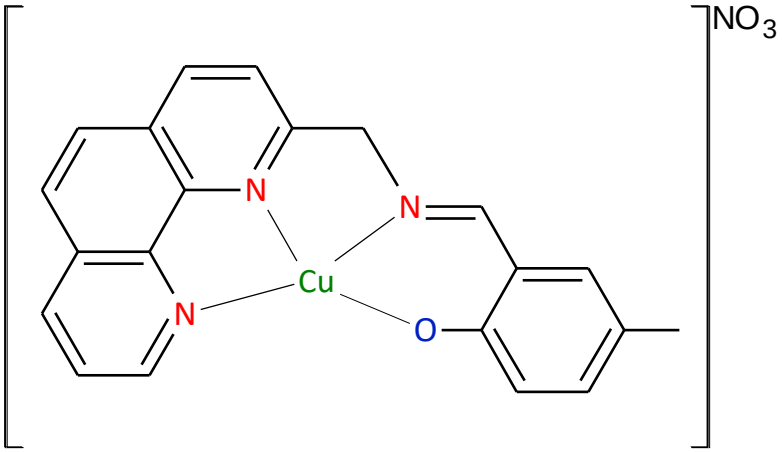

Figure 2.6.4: Structure of [Cu(L6)](NO_3).

Yield (101 mg, 0.223 mmol, 54.8%). The following characterisation data were recorded: IR (powder, cm^{-1}): 3050 (s, ν(C-$H_{methylene}$)); 1589 (s, ν(C=N)); 1502 (s, ν(O=N)); 1293 (s, ν(C-O)). UV (λ_{max}, ε, H_2O) [nm, M^{-1} cm^{-1}]: 205, 57291; 230, 31718; 273, 27218; 294, 10383. ES+: 389 *m/z* (M^+).

2.6.5 Synthesis of 4-Methoxy-2-{[(1,10-phenanthrolin-2-ylmethyl)imino]methyl}phenol copper(II) nitrate

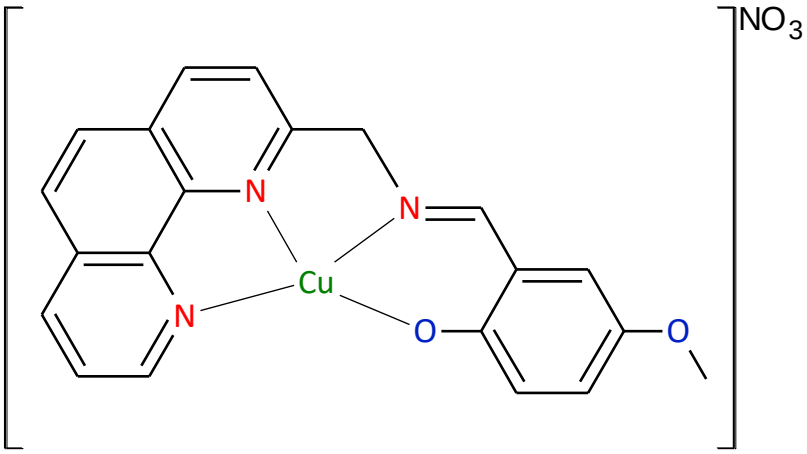

Figure 2.6.5: Structure of [Cu(L7)](NO_3).

Yield (157 mg, 0.336 mmol, 82.6%). The following characterisation data were recorded: IR (powder, cm^{-1}): 3056 (s, ν(C-$H_{methylene}$)); 1577 (s, ν(C=N)); 1502 (s, ν(O=N)); 1290 (s, ν(C-O)).

UV (λ_{max}, ε, H_2O) [nm, M^{-1} cm^{-1}]: 205, 36350; 230, 21014; 273, 13320; 280, 13139. ES+: 405.0554 *m/z* (M^+), [calculated: 405.0539 *m/z*]. Single crystal X-ray diffraction studies of [Cu(L7)](NO_3) confirmed the identity of this sample. The powder X-ray diffraction spectrum of [Cu(L7)](NO_3) was used to confirm that the phase of the bulk material matches that of the single crystal data (refer to Chapter 5).

2.6.6 Synthesis of 1-{[(1,10-phenanthrolin-2-ylmethyl)imino]methyl}naphthalen-2-ol copper(II) nitrate

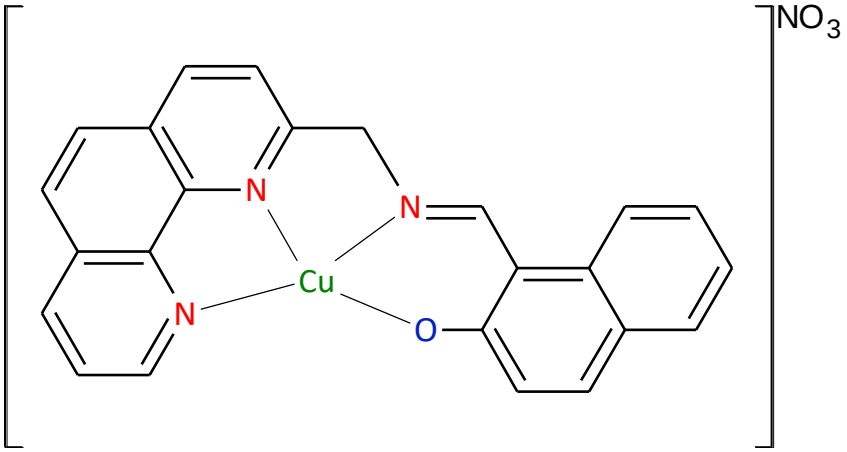

Figure 2.6.6: Structure of [Cu(L8)](NO_3).

Yield (186 mg, 0.381 mmol, 93.6%). The following characterisation data were recorded: IR (powder, cm^{-1}): 3056 (s, ν(C-$H_{methylene}$)); 1587 (s, ν(C=N)); 1505 (s, ν(O=N)); 1287 (s, ν(C-O)). UV (λ_{max}, ε, H_2O) [nm, M^{-1} cm^{-1}]: 205, 55519; 220, 53326; 273, 22483; 280, 21691. ES+: 425.0593 *m/z* (M^+), [calculated: 425.0589 *m/z*].

2.6.7 Synthesis of 4-tert-Butyl-2-{[(1,10-phenanthrolin-2-ylmethyl)imino]methyl}phenol copper(II) nitrate

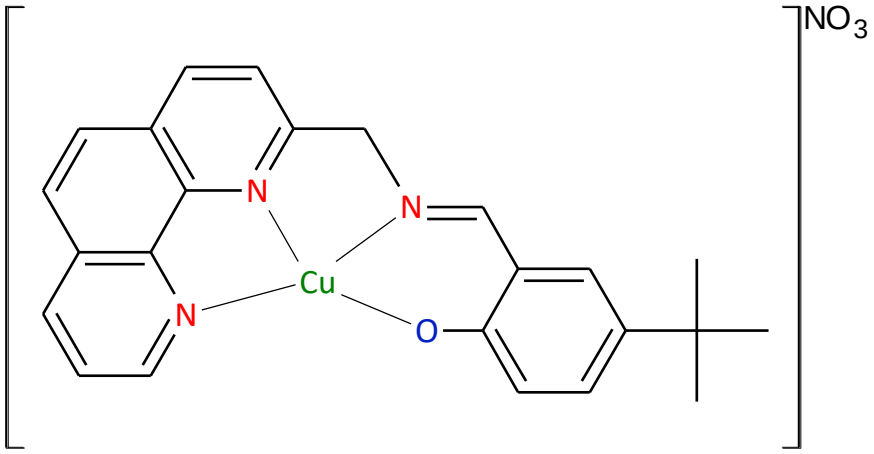

Figure 2.6.7: Structure of [Cu(L9)](NO_3).

Yield (67 mg, 0.136 mmol, 33.4%). The following characterisation data were recorded: IR (powder, cm^{-1}): 3051 (s, ν(C-$H_{methylene}$)); 1589 (s, ν(C=N)); 1501 (s, ν(O=N)); 1293 (s, ν(C-O)). UV (λ_{max}, ε, H_2O) [nm, M^{-1} cm^{-1}]: 205, 51606; 230, 29953; 273, 25480; 294, 9954. ES+: 431 *m/z* (M^+).

2.6.8 Synthesis of 4-Nitro-2-{[(1,10-phenanthrolin-2-ylmethyl)imino]methyl}phenol copper(II) nitrate

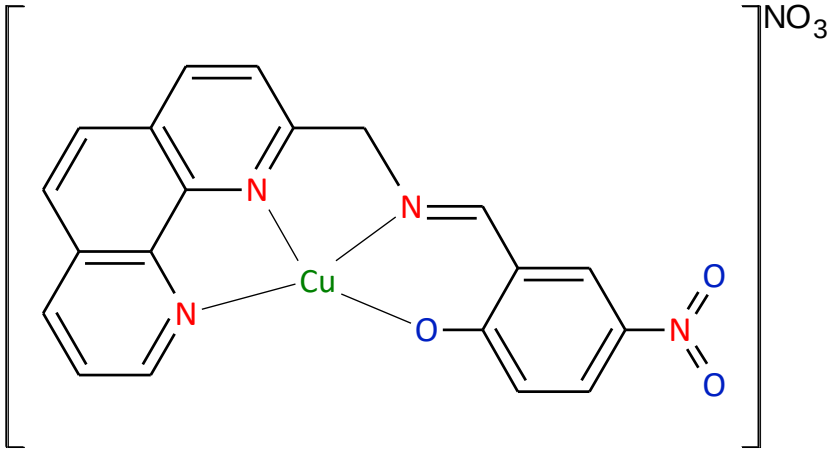

Figure 2.6.8: Structure of [Cu(L10)](NO_3).

Yield (172 mg, 0.356 mmol, 87.5%). The following characterisation data were recorded: IR (powder, cm^{-1}): 3055 (s, ν(C-$H_{methylene}$)); 1594 (s, ν(C=N)); 1493 (s, ν(N-O)); 1304 (s, ν(C-O)). UV (λ_{max}, ε, H_2O) [nm, M^{-1} cm^{-1}]: 205, 29265; 230, 16675; 273, 10277; 280, 10385. ES+: 420.0289 *m/z* (M^+), [calculated: 420.0284 *m/z*].

2.7 References

1. Corey, E. J.; Borror, A. L.; Foglia, T., *J Org. Chem.* **1965,** *30*, 288-290.
2. Sun, W. H.; Jie, S.; Zhang, S.; Zhang, W.; Song, Y.; Ma, H., *Organomet.* **2006,** *25*, 666-677.
3. Mazik, M.; Hartmann, A., *J. Org. Chem.* **2008,** *73*, 7444-7450.

Chapter 3: Analysis of Synthetic Procedures

3.1 Overview

Two classes of tetradentate ligands were synthesised in this work, using 1,10-phenanthroline as the starting material in a multi-step process. The ligands differ in the structure of the linker. The first class of compounds comprises 1,10-phenanthroline linked to either 8-aminoquinline or 2-picolylamine through an amide bond. The second class has an imine bond linking 1,10-phenanthroline to various derivatives of 2-hydroxybenzaldehyde. Two amide-based ligands were synthesised and characterised before chelating them to copper(II), nickel(II), and palladium(II). Eight imine-based ligands were synthesised, but not isolated for characterisation, chelating them directly to copper(II) in a one-pot process. The syntheses of both classes of ligands have some similarities, with the imine-based ligands diverging at the 1,10-phenanthroline-2-carbonitrile step. The following reaction scheme (Figure 3.1.1) shows the simplified synthetic routes to the two groups of compounds.

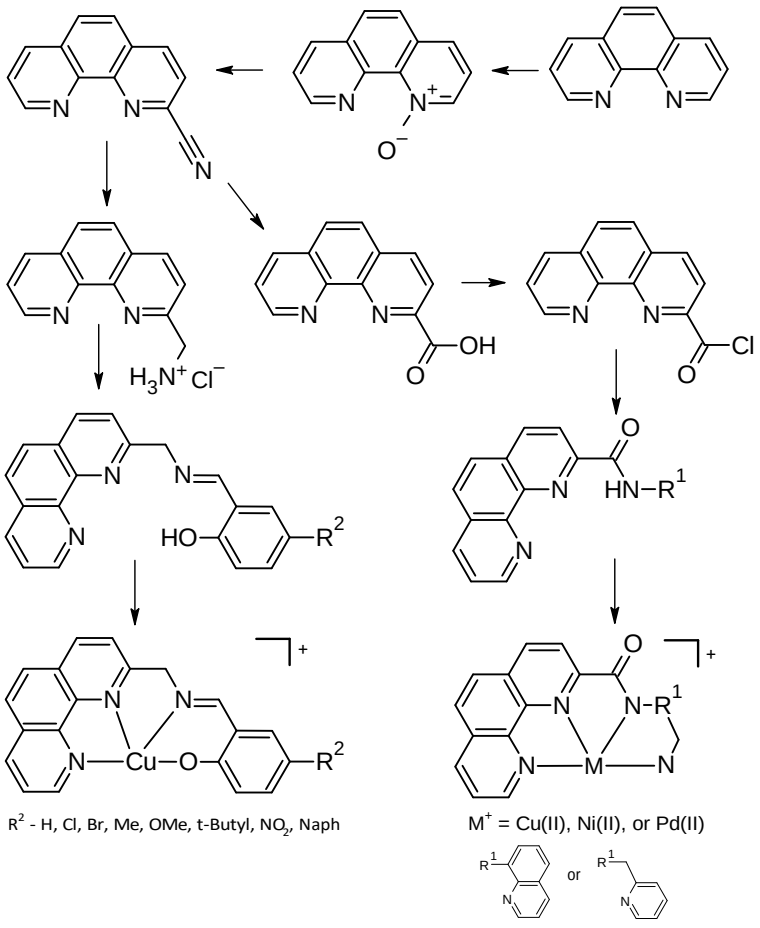

Figure 3.1.1: Simplified reaction route for complex synthesis.

The following sections discuss each reaction step in detail, with proposed mechanisms and an explanation for the reagent choices.

3.2 Synthesis of Ligand Precursors

The first step was the synthesis of 1,10-phenanthroline-1-oxide by reacting 1,10-phenanthroline and hydrogen peroxide in an acidic solution. The N1 atom of the 1,10-phenanthroline is oxidised by hydrogen peroxide. The oxidation is limited to N1 by employing a 1:1 ratio of 1,10-phenanthroline and hydrogen peroxide. It has been proposed that in acidic media the 1,10-phenanthroline-1-oxide is protonated, leading to a stable six-membered hydrogen-bonded ring (Figure 3.2.1). The ring will be resistant to undergoing a second oxidation step.[1] Figure 3.2.1 illustrates the protonated form of the N-oxide.

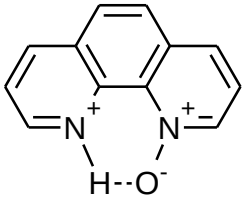

Figure 3.2.1: Structure of the protonated N-oxide species showing the intramolecular hydrogen bond, which stabilises the molecule, and prevents a second oxidation step.[1]

A study done by Rozen and Dayan[2] illustrated that the formation of 1,10-phenanthroline-*N,N'*-dioxide required the use of special reagents under unique conditions.[2] Rozen and Dayan[2] suggest that it is only possible to synthesise the desired mono-oxidised product using hydrogen peroxide.[2] The formation of 1,10-phenanthroline-*N,N'*-dioxide requires an extra step, after the synthesis of 1,10-phenanthroline-1-oxide. This requires HOF·CH_3CN, a potent oxidising agent, which is synthesised by bubbling fluorine gas through acetonitrile and water. The HOF·CH_3CN is used as an oxygen-transfer agent to insert the additional oxygen atom on the N2 nitrogen.[2] Figure 3.2.2 shows the X-ray structure and numbering scheme of 1,10-phenanthroline-*N,N'*-dioxide synthesied by Rozen and Dayan[2], which crystalised in the space group $P2_1/c$ (Z = 8) with two independent molecules in the asymmetric unit.[2]

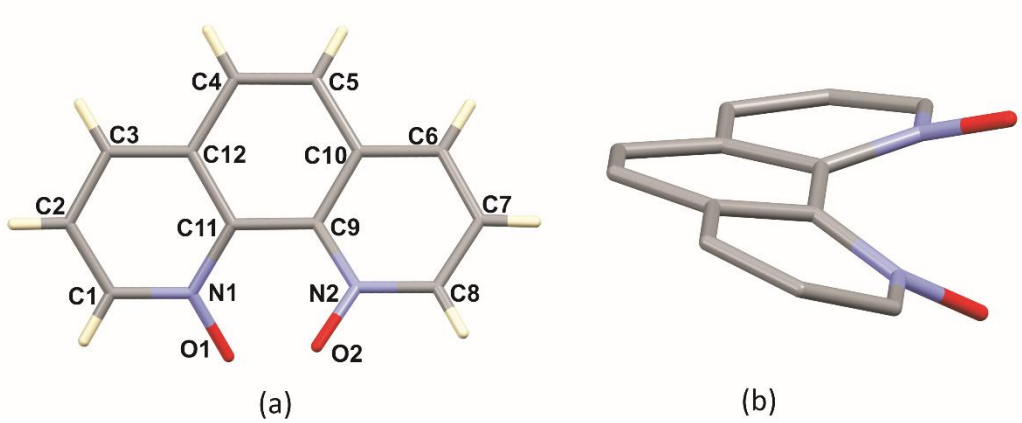

Figure 3.2.2: (a) X-ray structure of 1,10-phenanthroline-*N,N'*-dioxide showing the atom numbering scheme; (b) "side-view" showing the derivation from planarity of 1,10-phenanthroline-*N,N'*-dioxide. This twist is necessary to reduce the non-bonded repulsion between the two oxygen atoms.

The X-ray structure shows the torsion angle of O1-N1-C11-C9 measures -13.4(2)°, while the O2-N2-C9-C11 torsion angle measures -15.9(6)°. The N2-C9-C11-N1 torsion angle measures -31.4(2)°, the distortion from planarity of the dioxide is illustrated in Figure 3.2.2 (b) and is necessary to minimise the non-bonded repulsion between the two oxygen atoms. The X-ray structure suggests why the formation of the dioxide product is unfavourable. The limited space leads to a considerable steric strain between the two oxygen atoms. This strain forces the fused aromatic rings of the 1,10-phenanthroline to adopt a non-planar configuration, likely a high energy state.[2]

By mono-oxidising 1,10-phenanthroline, the C-2 position becomes more electrophilic, making it susceptible to nucleophilic attack. 1,10-Phenanthroline-1-oxide is reacted with potassium cyanide in this study to form 1,10-phenanthroline-2-carbonitrile. The cyanide group, a nucleophile, attacks the partial electrophile at C-2. The following diagram, Figure 3.2.3, shows the proposed mechanism.

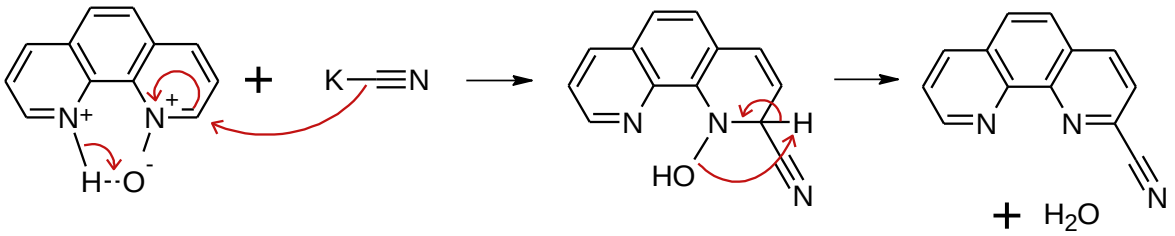

Figure 3.2.3: Proposed mechanism for the synthesis of 1,10-phenanthroline-2-carbonitrile.

1,10-phenanthroline-2-carbonitrile is converted to 1,10-phenanthroline-2-carboxylic acid, which will be used to synthesise the amide ligand. In an acidic environment, the cyano group is susceptible to attack from a nucleophile - OH^-, which forms a carbonyl substituent; producing the carboxylic acid moiety. The following scheme (Figure 3.2.4) shows the proposed mechanism for the formation of the carboxylic acid.

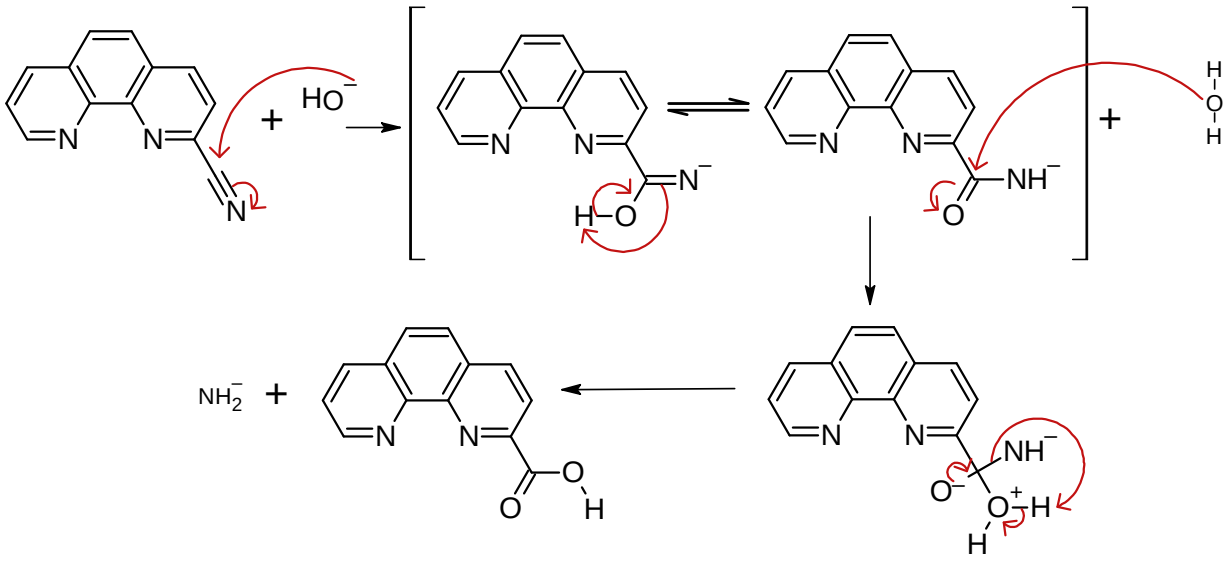

Figure 3.2.4: Proposed mechanism for the synthesis of 1,10-phenanthroline-2-carboxylic acid.

The proposed mechanism shows the hydroxide anion attacking the carbon of the cyanide group, reducing the triple bond to a double bond, with the electrons moving to the nitrogen, producing a negative charge. The intermediates are in equilibrium between an imidic acid form and an amide form. The carbonyl in the amide intermediate is attacked by water, which ejects an azanide anion, yielding 1,10-phenanthroline-2-carboxylic acid.[3]

The precursor for the imine complexes is synthesised from 1,10-phenanthroline-2-carbonitrile, the cyano group is converted to an ethylene amine chloride salt. The 1-(1,10-phenanthrolin-2-yl)methanamine chloride salt is part of a "one-pot" synthetic method to form each of the imine-based copper(II) complexes.

The formation of the 1-(1,10-phenanthrolin-2-yl)methanamine chloride salt involves the hydrogenation of the cyano moiety with the use of hydrogen gas and a palladium catalyst on carbon, following a modified method by McMillan, *et al.*.[4] Mild conditions were used for this reaction, these include H_2 gas in a balloon, in the presence of an acid, and the reaction temperature maintained at 30°C for 24 hours.[4] Acetic acid was initially used, but the resultant amine reacted with the acetic acid to form an amide compound. Figure 3.2.5 shows the proposed structure of this aceto-amide form.

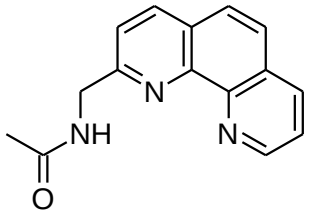

Figure 3.2.5: Structure of proposed by-product, *N*-[(1,10-phenanthrolin-2-yl)methyl]acetamide.

Hydrochloric acid was subsequently used instead of acetic acid to avoid the formation of the amide by-product. The excess hydrochloric acid must be neutralised before extracting the desired amine. The reaction scheme below (Figure 3.2.6) shows the proposed mechanism for the formation of 1-(1,10-phenanthrolin-2-yl)methanamine.

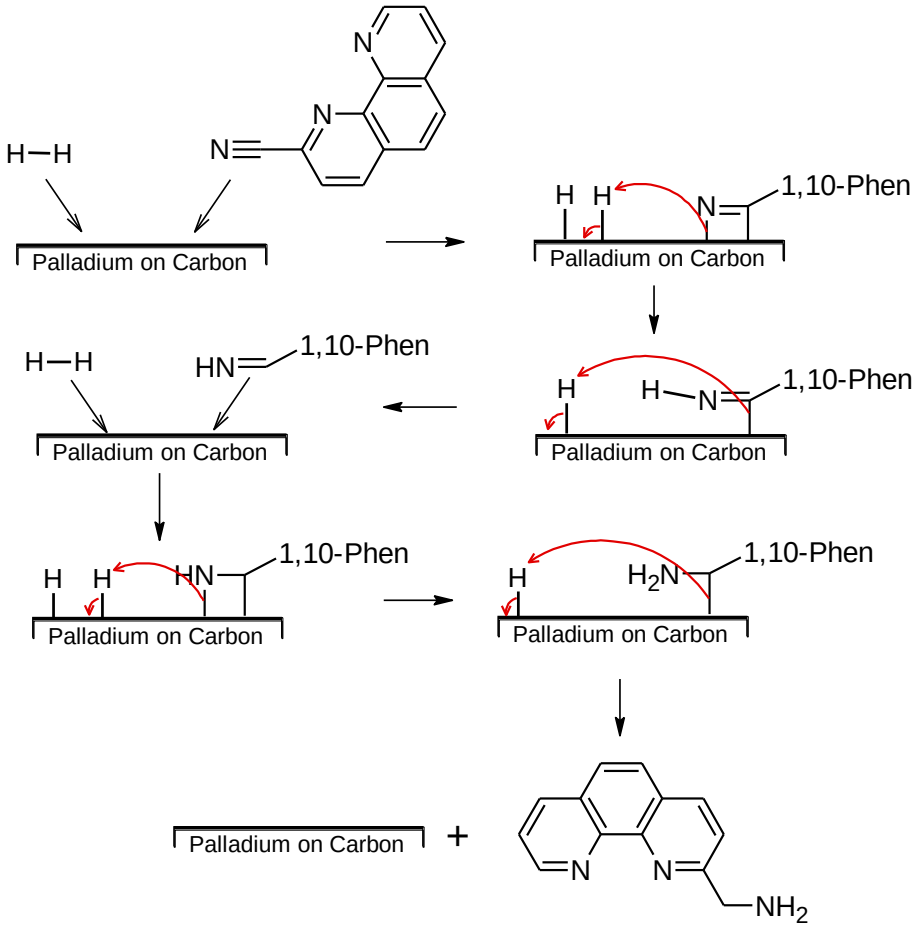

Figure 3.2.6: Proposed mechahism for the formation of 1-(1,10-phenanthrolin-2-yl)methanamine.

Hydrochloric acid was added to the solution to isolate the acid chloride salt form of 1-(1,10-phenanthrolin-2-yl)methanamine as a solid, shown in Figure 3.2.7, below.

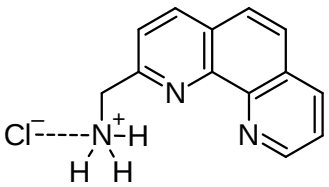

Figure 3.2.7: Structure of 1-(1,10-phenanthrolin-2-yl)methanamine chloride. The hydrochloride salt is easier to separate from the reaction mixture as a high-purity powder.

Attempts to optimise the hydrogenation reaction to reduce the reaction time, by increasing the pressure of the hydrogen gas and increasing the reaction temperature resulted in several unwanted by-products forming. The low pressure, low temperature balloon method proved to be optimal for this type of reaction.

3.3 Amide Ligand Synthesis

The first group of ligands synthesised in this work comprise a 1,10-phenanthroline moiety linked to either 8-aminoquinoline (HL1) or picolylamine (HL2) via an amide bond. To do this, the 1,10-phenanthroline-2-carboxylic acid is converted to the acid chloride form since the carbonyl is then more reactive and therefore more susceptible to nucleophilic attack by the amine.[5] The reaction scheme (Figure 3.3.1) shows the conversion of 1,10-phenanthroline-2-carboxylic acid to the acid chloride form.

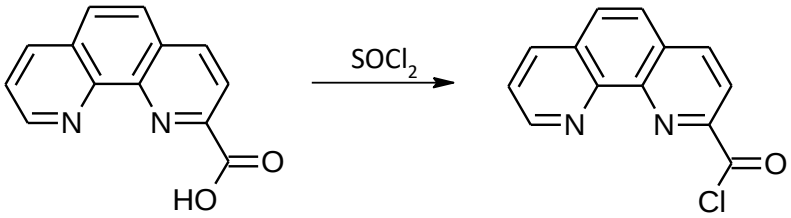

Figure 3.3.1: Reaction scheme for the synthesis of the acid chloride to enhance reactivity towards the incoming amine.[5]

This reaction was carried out in thionyl chloride, which acted as both the solvent and reagent. This approach was to ensure complete conversion of the 1,10-phenanthroline-2-carboxylic acid to the acid chloride form. The acid chloride form was not characterised as it is highly reactive, rendering isolation and storage challenging. The reaction between the acid chloride and either of the primary amines could be performed at room temperature with only continuous stirring due to the high reactivity of the acid chloride.[3,6,7] The mechanism (Figure 3.3.2) illustrates the reaction between the amines and the acid chloride.

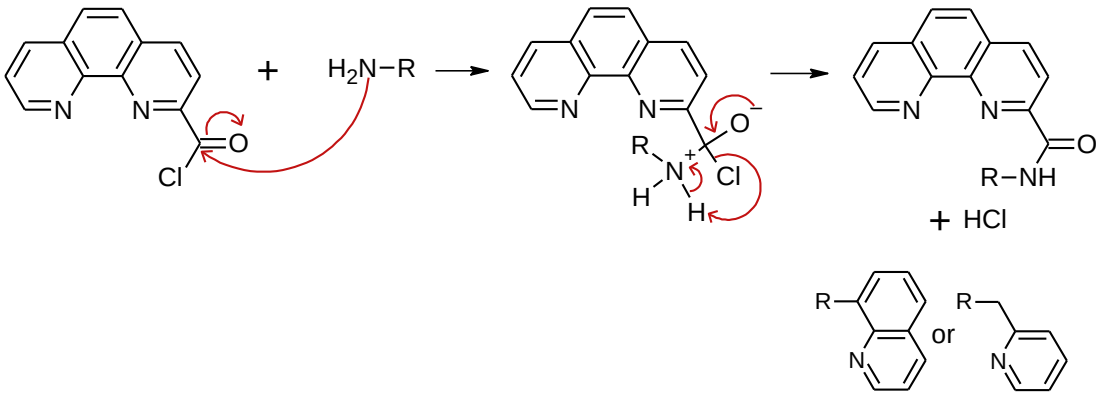

Figure 3.3.2: Mechanism for synthesis of the amide-based ligands HL1 and HL2.

The proposed mechanism shows the nitrogen of the amine attacking the carbonyl, forming a bond with the carbon. The chloride substituent is ejected from the compound as hydrogen chloride.[3,8]

A second method was used to synthesise HL1 and HL2, but was found to produce a lower yield compared to the thionyl chloride method. The second method used triphenylphosphite as a coupling reagent. Figure 3.3.3 illustrates the proposed mechanism for the coupling reaction.

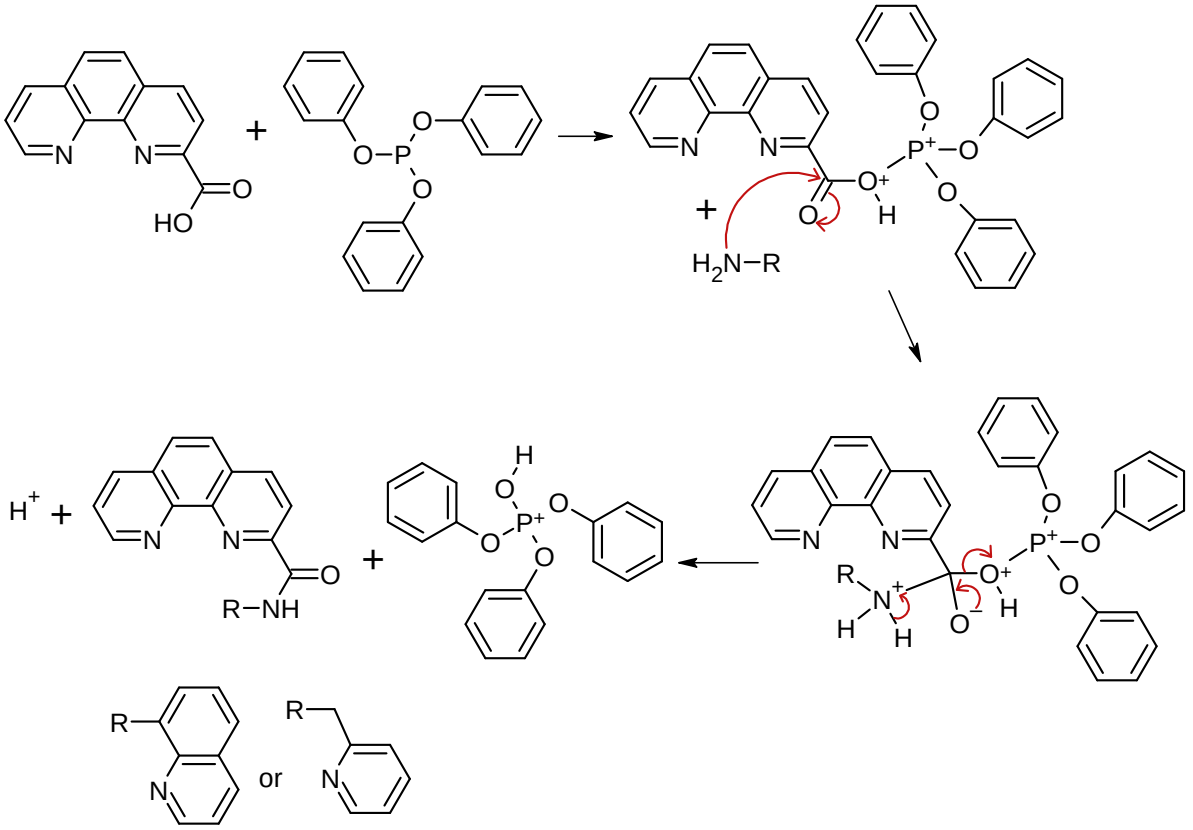

Figure 3.3.3: Proposed mechanism to synthesise HL1 and HL2 using triphenylphosphite as a coupling reagent.[6]

3.4 Synthesis of the Amide-based Metal Chelates

The tetradentate amide-based ligands synthesised in this work were chelated to Cu(II), Ni(II) and Pd(II). Metal chelation occurred with concomitant deprotonation of the amide group, yielding a monocationic metal chelate. The metallation procedure simply involved heating the ligand and appropriate metal salt in a 1:1 mole ratio in a suitable solvent, usually methanol. The addition of a base to deprotonate the amide group was unnecessary. The following schemes (Figure 3.4.1) show the reactions between the metal salts and either HL1 or HL2.

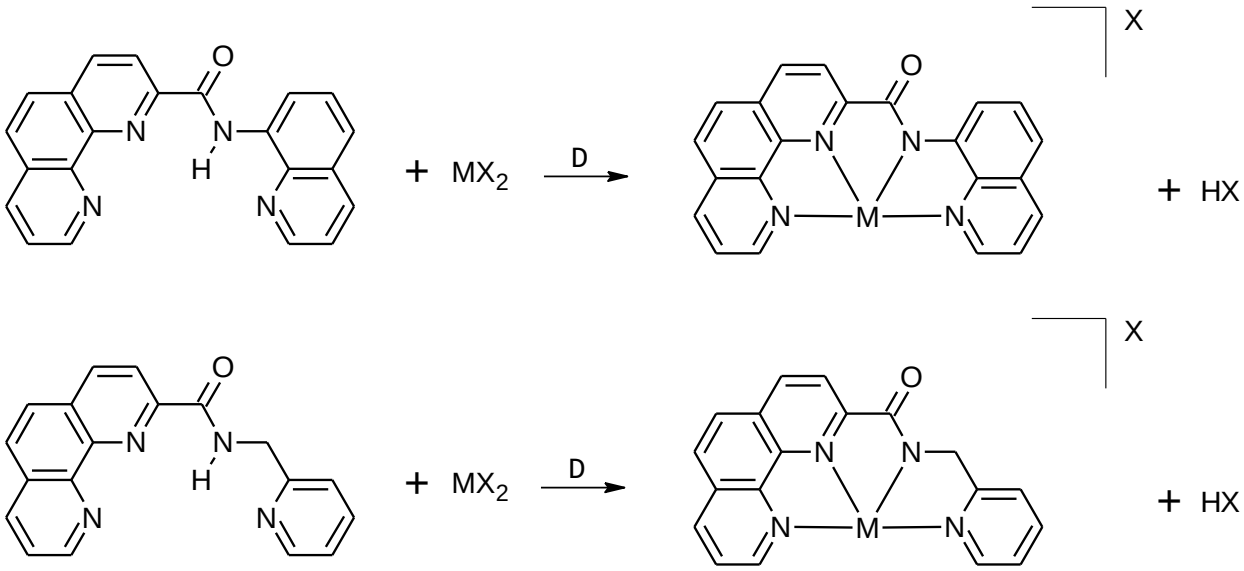

M = Cu; X = NO_3

M = Ni; X = NO_3

M = Pd; X = Cl

Figure 3.4.1: Reaction scheme for metal chelation of the amide-based ligands.

The copper(II) and nickel(II) reactions used methanol as a solvent because both HL1 and HL2 are soluble in methanol. The copper(II) and nickel(II) chelates are sparingly soluble in methanol, resulting in the complexes precipitating out of solution; this simplified the isolation procedure. The counter ion was changed from PF_6^- to NO_3^- for the copper(II) complexes [Cu(L1)](NO_3) and [Cu(L2)](NO_3) and the nickel(II) chelate [Ni(L1)](NO_3). This was done for two reasons. Firstly, to increase the aqueous solubility of the metal chelates as nitrate salts are typically more soluble in aqueous media than the corresponding hexafluorophosphate(V) salts. Secondly, changing the counter ion can aid crystallisation. The palladium(II) reactions used acetonitrile as the solvent because it is a better coordinating solvent than methanol. The palladium(II) reactions were first carried out in methanol, but no metal ion chelation was detected. Using acetonitrile, the palladium(II) chelates were successfully isolated. All the

metal chelates were recrystallised from methanol to remove any excess ligand which may have precipitated out with the metal chelates.

3.5 Synthesis of the Imine-based Metal Chelates

The synthesis of the imine-based copper(II) complexes was achieved *via* a "telescope" or "one-pot" reaction of 1-(1,10-phenanthrolin-2-yl)methanamine hydrochloride, analogues of 2-hydroxybenzaldehyde, and copper(II) nitrate trihydrate.[9] The choice of the one-pot reaction for these complexes is due to the difficulty in isolating the 2-[(E)-{[(1,10-phenanthrolin-2-yl)methyl]imino}methyl]phenol derivatised ligands. Most chromatography techniques that were used in an attempt to isolate these ligands either decomposed the Schiff base, or separation was insufficient to be useful. The formation of the chelates was confirmed with mass spectrometry; these spectra are available in appendix.

The proposed reaction scheme has the copper(II) nitrate playing two roles in the reaction, first as a catalyst to promote the formation of the Schiff base, thereafter chelating the ligand *in situ* and acting as a stabilising template.[10] A study by Zhang, *et al.*[10] showed the efficiency of a copper(II) complex in catalysing a homo-coupling reaction using a one-pot method without isolating the intermediates. The reaction yield was enhanced when compared to the multi-step synthetic route. The proposed reaction scheme, Figure 3.5.1, is based on the mechanism put forward by Ma and Cai.[11]

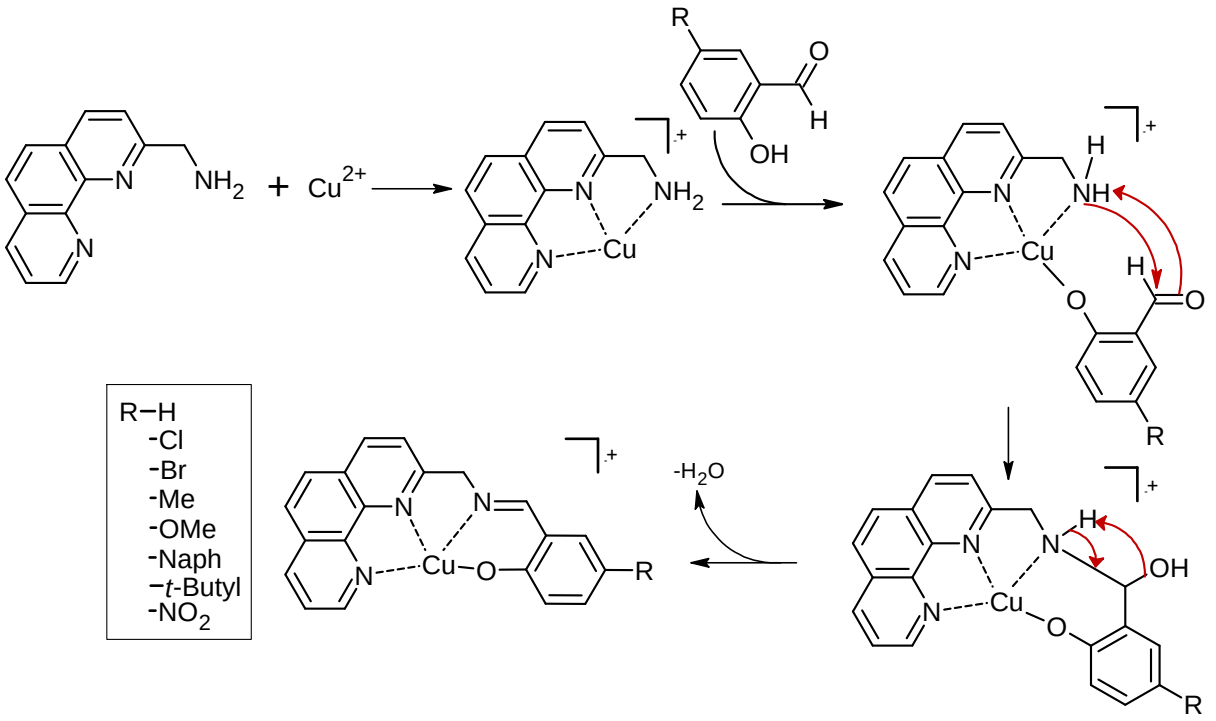

Figure 3.5.1: Proposed mechanism for the one-pot synthesis of the imine-based metal chelates.

A study by Naeimi, *et al.*[12] showed an improvement in reaction time and yield for the synthesis of double Schiff-base metal(II) chelates using a templating reaction. The reaction times were under 2 hours, with the yields over 90%. The templating reactions were performed on nickel(II), cobalt(II), copper(II), and uranyl(VI) (UO_2^{2+}), all of which were successful. Based on this study, Sebastian, *et al.*[13] showed the templating condensation reaction to be effective with other metal(II) centres, ie. manganese(II), iron(II), and zinc(II), with reaction times being three hours and yields over 55%.

3.6 Summary of Synthetic Procedures

The muilti-step reactions that produce the metal(II) chelates in this work start with activiating the 2-position of 1,10-phenanthroline. This functionalisation enables the formation of two classes of ligands from the cyano functional group at the 2-position. The amide-based ligands have been synthesised by conversion of the cyano moiety to an acid chloride and then reacted with either 8-aminoquinoline or 2-picolylamine to form an amide bridge with 1,10-phenanthroline at the 2-position. The coordination of the two amide-based ligands to copper(II), nickel(II), and paladium(II) produced six novel chelates.

The second classes of chelates (imine-based) were synthesised from hydrogenation of the cyano group to form the methanamine functional group. The imine-based chelates have copper(II) as the metal centre, and were synthesised using a templating condensation reaction of salicylaldehyde, and derivatives thereof, with 1-(1,10-phenanthrolin-2-yl)methanamine, forming a Schiff-base bridge between the salicylaldehyde moieties and the phenanthroline moiety. This templating reaction eliminates the ligand isolation step, making for an efficient synthetic procedure.

3.7 References

1. Corey, E. J.; Borror, A. L.; Foglia, T., *J Org. Chem.* **1965,** *30*, 288-290.
2. Rozen, S.; Dayan, S., *Angewandte Chemie International Edition* **1999,** *38* (23), 3471-3473.
3. Thomas, G., A Mechanistic Approuch to Organic Chemistry. 1st ed.; Edward Arnold Publishers: London, 1967.
4. McMillan, L.; Gilpin, L. F.; Baker, J.; Brennan, C.; Hall, A.; Lundie, D. T.; Lennon, D., *Journal of Molecular Catalysis A: Chemical* **2016,** *411*, 239-246.
5. Sun, W.-H.; Jie, S.; Zhang, S.; Zhang, W.; Song, Y.; Ma, H., *Organometalics* **2006,** *25*, 666-677.
6. March, J., *March's advanced organic chemistry: reactions, mechanisms, and structure*. 6th ed.; Wiley: New York, 2007.
7. March, J., *March's advanced organic chemistry: reactions, mechanisms, and structures*. 5th ed.; John Wiley & Sons: New York, 2001.
8. Carey, F. A., *Advanced Organic Chemistry*. 5th ed.; Springer: New York, 2007.
9. Chapter 21 A method for determining suitable order of introducing reagents in “one-pot” procedures. In *Data Handling in Science and Technology*, Carlson, R.; Carlson, J. E., Eds. Elsevier: 2005; Vol. 24, pp 509-515.
10. Zhang, J.-Q.; Huang, G.-B.; Weng, J.; Lu, G.; Chan, A. S. C., *Organic & Biomolecular Chemistry* **2015,** *13* (7), 2055-2063.
11. Ma, D.; Cai, Q., *Accounts of Chemical Research* **2008,** *41* (11), 1450-1460.
12. Naeimi, H.; Rabiei, K.; Salimi, F., *Journal of Coordination Chemistry* **2009,** *62* (7), 1199-1205.
13. Sebastian, M.; Arun, V.; Robinson, P. P.; Leeju, P.; Varsha, G.; Varghese, D.; Yusuff, K. K. M., *Journal of Coordination Chemistry* **2011,** *64* (3), 525-533.

Chapter 4: Analysis of Spectroscopic Data

4.1 Introduction

Electromagnetic radiation is used in many different fields of characterisation. This is because different wavelengths of light interact differently with a molecule, it therefore, generates a wide range of information.

Figure 4.1.1 shows a portion of the electromagnetic spectrum and the different ways it can be used for characterisation of a sample:

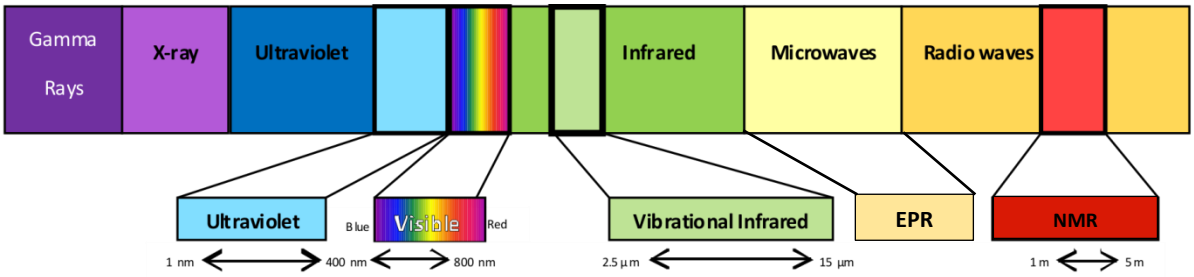

Figure 4.1.1: Electromagnetic spectrum with corresponding wavelengths, showing how they are used in chemical analysis.[1]

The spectrum shows the wavelength ranges of the different types of electromagnetic radiation. Ultraviolet and visible light radiation interact with the electrons of a compound; vibrational infrared interacts with the vibrations of atoms and bonds present in a compound. Radio waves interact with the atomic nuclei in a compound. These types of electromagnetic radiation have been used to characterise the ligand precursors, the ligands (HL1 and HL2), as well as the metal chelates.

4.2 Infrared Spectroscopy

4.2.1 Introduction

The majority of compounds, both organic and inorganic, have covalent bonds. These bonds absorb a variety of frequencies of electromagnetic radiation in the infrared region of the electromagnetic spectrum.[1] The infrared region of the electromagnetic spectrum sits between the visible and microwave regions with a range of 800 nm – 1 mm.[1] The electromagnetic radiation which is responsible for vibrational frequencies lies in the range of 2500 nm – 25000 nm (4000 cm^{-1} – 400 cm^{-1}).[1] Compounds only absorb specific frequencies of infrared radiation because the absorption of the radiation is a quantised process.[1]

The internal molecular energy of a compound is separated into three additive components: rotation of the compound, vibrations of the atoms in a compound and the electron movement within a compound.[1] The vibrational transitions occur at frequencies within the IR range, and therefore only the vibrational transitions are observed in the IR spectrum.[2] An infrared spectrum is produced when IR radiation is absorbed by the compound, causing transitions between the vibrational energy levels in the ground state.

The amide bond in both HL1 and HL2 has characteristic absorption bands. The N-H bond of the amide, ν(NH), is present in the ligands and upon metal ion chelation, disappears. The carbonyl of the amide in the ligands' ν(C=O) absorption band is expected to shift to a lower wavenumber when chelated to a metal ion. This is because the metal ion is electron deficient and withdraws electron density from the ligand. The result of this is a lowering of the bond order of the bonds near the metal centre. This lower order leads to a lower energy vibration. The region for a ν(N-H) stretch is typically in the range 3475 – 3150 cm^{-1} with one band, as it is a secondary amide, and the ν(C=O) stretch of the amide is observed in the range of 1680 – 1630 cm^{-1}, typical of a carbonyl.[1]

The imine-based chelates have a C=N bond in the ligand, which forms from the condensation of a primary amine and an aldehyde. A stretching frequency in the region of 1680 cm^{-1} will be one of the key features of these IR spectra, confirming synthesis of the ligand.[1]

4.2.2 Results and Discussion

The N-H bond in the amide-based ligands will absorb in two regions of the IR spectrum, one for the N-H stretching frequency and another for the N-H bending frequency. The N-H stretching frequency is typically observed in the range 3475 – 3150 cm^{-1} and the N-H bending

frequency in the range 1640 – 1550 cm^{-1}.[1] Table 4.2.1 summarises the amide N-H stretching and bending frequencies for HL1 and HL2.

Table 4.2.1: Frequencies of the N-H stretching and bending vibrations in the amide-based ligands.

Ligand	N-H stretching (cm^{-1})	N-H Bending (cm^{-1})
HL1	3339	1557
HL2	3401	1615

The N-H bending wavenumbers for the two amide-based ligands are quite different due to the varying aromaticity of each ligand. The HL1 amide group has the N-H bond adjacent to an aromatic quinoline ring, which is electron-withdrawing. An electron-withdrawing group would weaken the N-H bond and it therefore absorbs lower energy IR radiation. The HL2 amide group is adjacent to an electron-donating methylene group which strengthens the N-H bond, resulting in comparatively higher energy IR radiation being absorbed. These N-H bands are absent in the metal chelate IR spectra as metal chelation requires deprotonation of the amide N-H.

The carbonyl of an amide group has a distinct, sharp peak usually in the range of 1680 – 1630 cm^{-1} which is present in both the ligands and the metal chelates. Table 4.2.2 summarises the carbonyl stretching frequencies for both the free ligands and metal chelates.

Table 4.2.2: Wavenumbers of the carbonyl stretching frequency for the free amide-based ligands and the metal chelates.

Ligands	Free Ligand (cm^{-1})	Metal Chelate	Metal chelate (cm^{-1})
HL1	1671	[Cu(L1)]	1620
		[Ni(L1)]	1658
		[Pd(L1)]	1649
HL2	1669	[Cu(L2)]	1633
		[Ni(L2)]	1637
		[Pd(L2)]	1605

Table 4.2.2 illustrates that the C=O of free ligands absorb higher energy radiation compared to their metal chelate analogues. This is typical for metal chelation through a deprotonated amide nitrogen atom. The shift to lower energy radiation is attributed to the amide moiety changing from a secondary to a tertiary amide once chelated.[3]

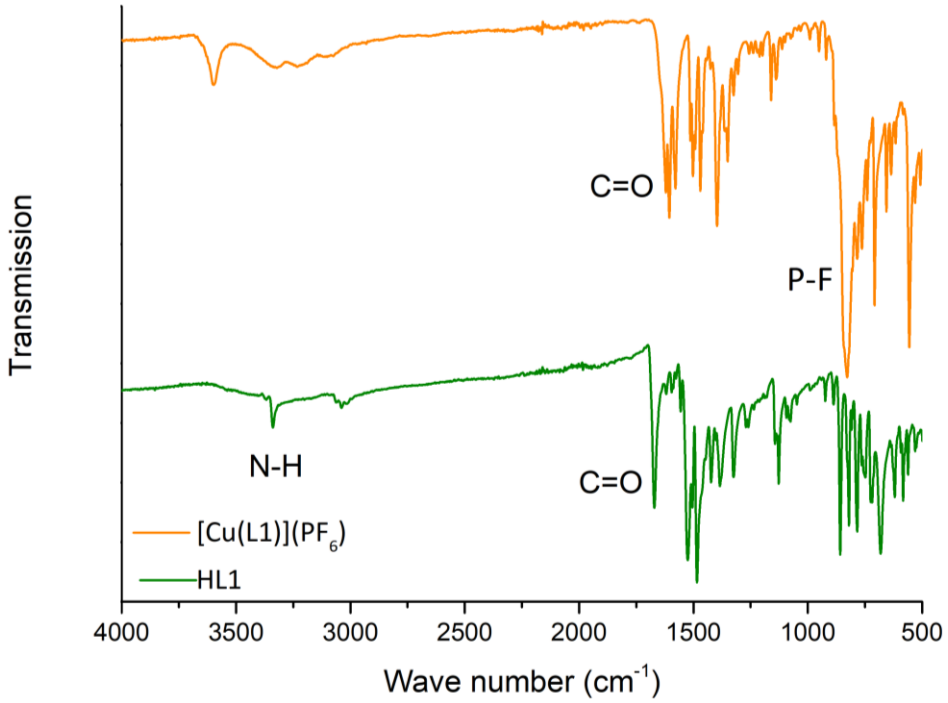

Figure 4.2.1: Comparison of IR spectra of HL1 and [Cu(L1)](PF_6) illustrating the differences in the spectra upon metal ion chelation.

Figure 4.2.1 shows a typical example of the changes in the IR spectra upon chelation of HL1 to a metal ion; in this instance, copper(II). The amide N-H peak evident in the HL1 spectrum has disappeared in the [Cu(L1)](PF_6) spectrum. The carbonyl peak shifted to a lower wavenumber when comparing HL1 to [Cu(L1)](PF_6), both indicating that the chelation of HL1 to copper(II) was successful. Additionally, in the spectrum of [Cu(L1)](PF_6) there is a new peak at approximately 800 cm^{-1} which corresponds to the P-F stretch of the hexafluorophosphate(V) anion of the chelate. [Cu(L1)](PF_6) was used as an example, but similar observations were noted for the bulk of the metal chelates.

The ligand precursor, 1,10-phenanthrolin-2-ylmethanaminium chloride, has a ν(N-H) band in the same range as the amide N-H of HL1. This band disappears upon ligand synthesis and chelation. This is shown in Figure 4.2.2 below.

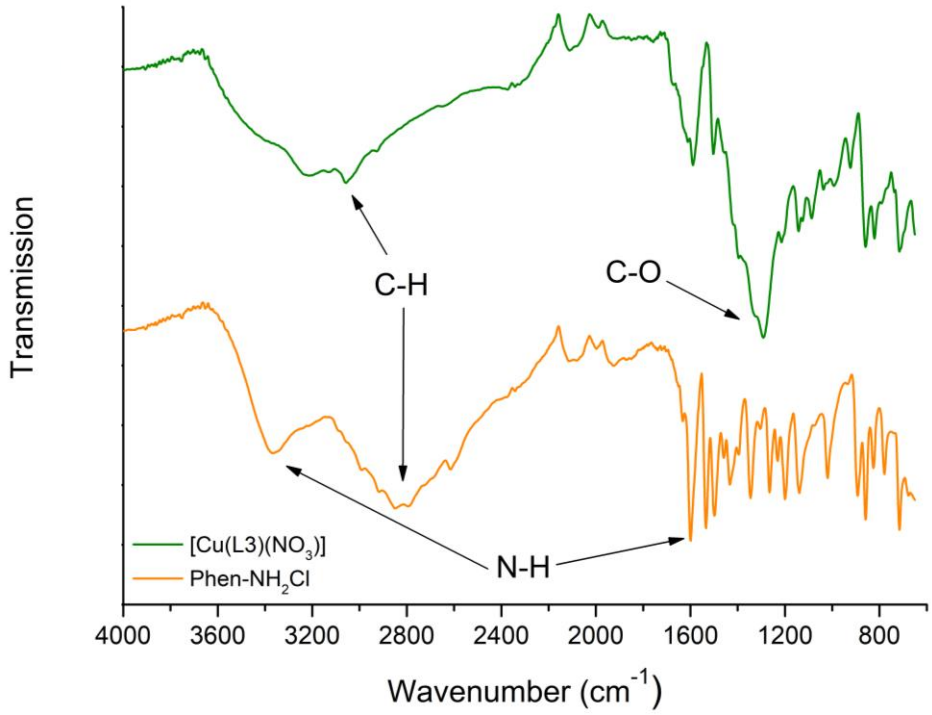

Figure 4.2.2: Comparison of IR spectra of 1,10-phenanthrolin-2-ylmethanaminium chloride and [Cu(L3)(NO_3)] illustrating the differences in the spectra upon metal ion chelation.

The imine-based chelates have a common C=N bond, with a stretching frequency range of 1594 – 1577 cm^{-1}, Table 4.2.3 below shows the stretching frequencies of the imine bond for the chelates [Cu(L3)](NO_3) - [Cu(L10)](NO_3).

Table 4.2.3: Wavenumbers corresponding to the imine vibration for the imine-based chelates [Cu(L3)](NO_3) - [Cu(L10)](NO_3).

Imine Chelates	Wavenumber (cm^{-1})	Imine Chelates	Wavenumber (cm^{-1})
[Cu(L3)(NO_3)]	1589	[Cu(L7)](NO_3)	1577
[Cu(L4)(NO_3)]	1590	[Cu(L8)](NO_3)	1587
[Cu(L5)(NO_3)]	1588	[Cu(L9)(NO_3)]	1589
[Cu(L6)(NO_3)]	1589	[Cu(L10)](NO_3)	1594

The ν(C=N) band in this class of chelates is a weak, but sharp peak, which differs from the expected intensity and shape of a strong sharp peak. This can be attributed to the ν(C=C) band partially masking the ν(C=N) band.[1] The effect of the copper(II) ion bonding to the phenolic oxygen moiety is evident with the ν(C-O) band shifting from a range of 1200 – 1000 cm^{-1} to 1287 – 1304 cm^{-1}. Chelates [Cu(L4)(NO_3)] and [Cu(L7)](NO_3) have different coordination geometries in the X-ray crystal structures, which will be discussed in Chapter 5. The IR spectra for these chelates are similar with the exception of the ν(C-Cl) band for [Cu(L4)(NO_3)] and the intensity of the ν(N-O) band, with [Cu(L4)(NO_3)] having a relatively higher intensity compared to [Cu(L7)](NO_3). The X-ray crystal structure of [Cu(L4)(NO_3)] has the nitrate ion in the inner

coordination sphere and [Cu(L7)](NO_3) has the nitrate ion in the outer sphere, which could be the reason for the differences in ν(N-O) band intensities. Figure 4.2.3 illustrates the comparison of the spectra of these two chelates.

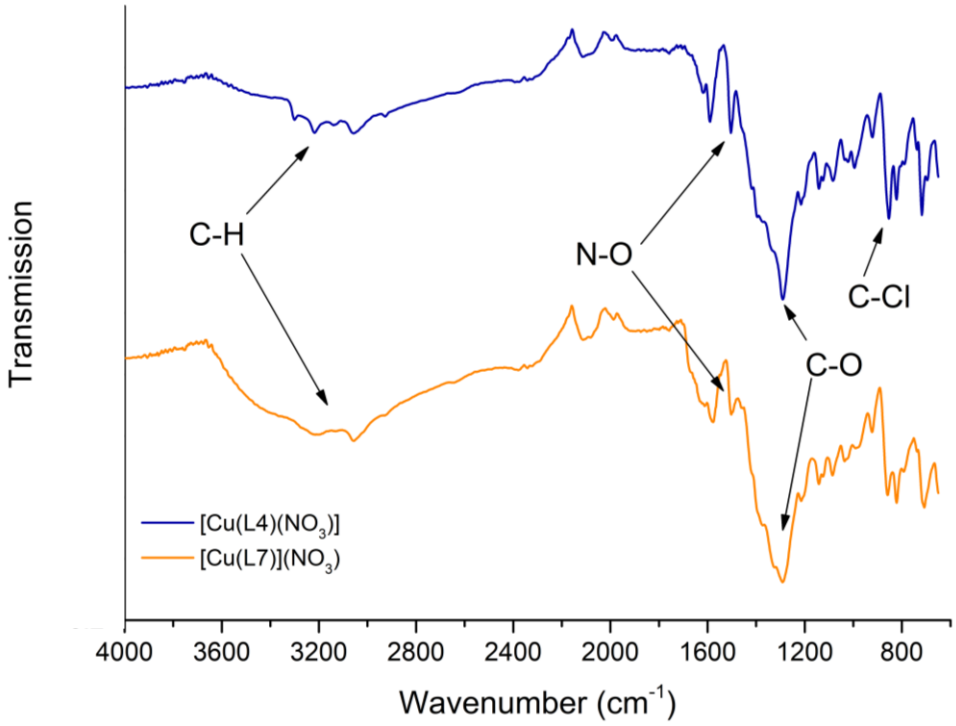

Figure 4.2.3: Comparison of the IR spectra of [Cu(L4)(NO_3)] and [Cu(L7)](NO_3), illustrating the differences in the spectra as a consequence of differing coordination geometries.

4.3 NMR Spectroscopy

4.3.1 Introduction

Nuclear Magnetic Resonance (NMR) spectroscopy was used for the characterisation of the synthetic ligand intermediates as well as for the palladium complexes. NMR spectroscopy uses the interaction of electromagnetic radio waves and the spin state of the nuclei in a compound to probe its structure.[4] The interaction is controlled with an applied magnetic field and the data obtained is due to the flipping of spin states of the nuclei, giving rise to a signal.[1] The electronic configuration of a compound plays an important role in NMR spectra with diamagnetic compounds giving rise to sharp distinct signal peaks and paramagnetic compounds exhibiting broader resonance across a much wider spectral window.[1] In paramagnetic samples, the paramagnetic centres cause large fluctuations in local magnetic fields which then becomes variable for each individual molecule. This means the ensemble of spins, which are ideally in-phase, will have different Larmor frequencies, depending on their local environment and orientation. Magnetic interactions between nuclei and the unpaired electron provide an additional (very efficient) relaxation pathway. This dramatically reduces the relaxation times, this shortens T2 which leads to extreme line broadening, loss of resolution and signal intensity, sometimes with no signal odserved.

The copper(II) chelates are paramagnetic due to the d^9 electronic configuration of the copper(II) centre with its associated unpaired electron. The palladium(II) chelates (low spin d^8) are diamagnetic. The nickel(II) chelates are expected to be diamagnetic in a square planar geometry but change to paramagnetic in a coordinating solvent (such as DMSO). This is due to the change in geometry of the chelates from square planar (diamagnetic) to octahedral (paramagnetic) in coordinating solvents. Coordination of axial solvent molecules changes the metal centre from low-spin to high-spin d^8 which is paramagnetic. The nickel(II) chelates synthesised in this work are soluble only in polar solvents, all of which are coordinating, and so NMR of the nickel(II) chelates was not possible in this instance.

4.3.2 Results and Discussion

The main area of interest for HL1 and HL2 is the N-H bond present in the amide region of both ligands. The reported chemical shift for the N-H of an amide is 5.0 ppm – 9.0 ppm,[1] but the chemical shifts observed for HL1 and HL2 are 12.63 ppm and 11.26 ppm, respectfully. The chemical shift of N-H (and indeed O-H) groups is known to be highly variable, being dependent on several factors such as concentration and hydrogen bonding in solution.[5]

The downfield shift of the N-H signal of HL1 relative to HL2 is due to the deshielding effect of the aromatic phenanthroline and quinoline moieties of HL1 compared to the reduced

aromaticity of HL2. The N-H group is also likely to be involved in hydrogen bonding which can significantly influence the chemical shift.

Metal chelation occurs with concomitant deprotonation of the amide NH group; thus metal chelation can be confirmed by the disappearance of the amide NH signal. The increased electron density of the complexes increases the deshielding, causing the peaks to shift downfield.[1] A study by Makedonas[6] showed that a metal centre, in this case palladium(II), can cause deshielding of the hydrogen atoms in a phenanthroline system. The deshielding is largely attributed to the lopsided charge distribution of the valence orbitals of the metal.[6]

Figure 4.3.1 shows the assigned ^{1}H NMR spectra of [Pd(L1)]Cl and HL1. A similar plot for the ^{13}C NMR spectra is shown in Figure 4.3.2.

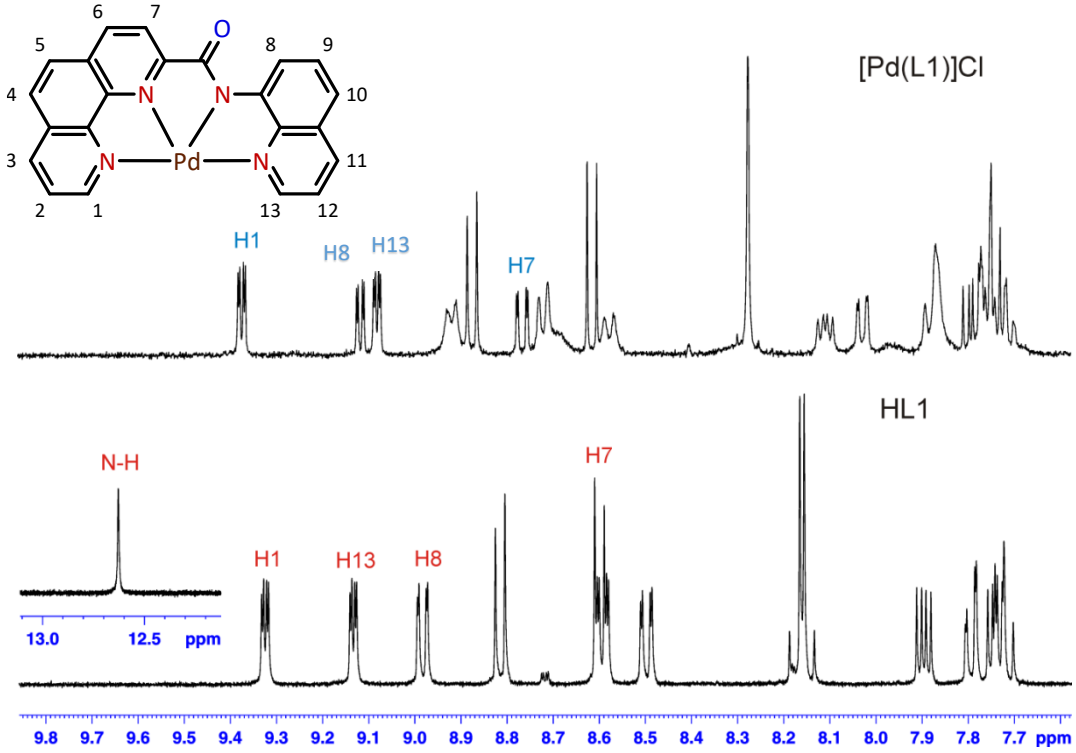

Figure 4.3.1: Conparison of the ^{1}H NMR (400 MHz, DMSO-d_6) spectra of HL1 (below) and [Pd(L1)]Cl (above), with insert of the structure of [Pd(L1)]Cl with atom numbering numbering scheme.

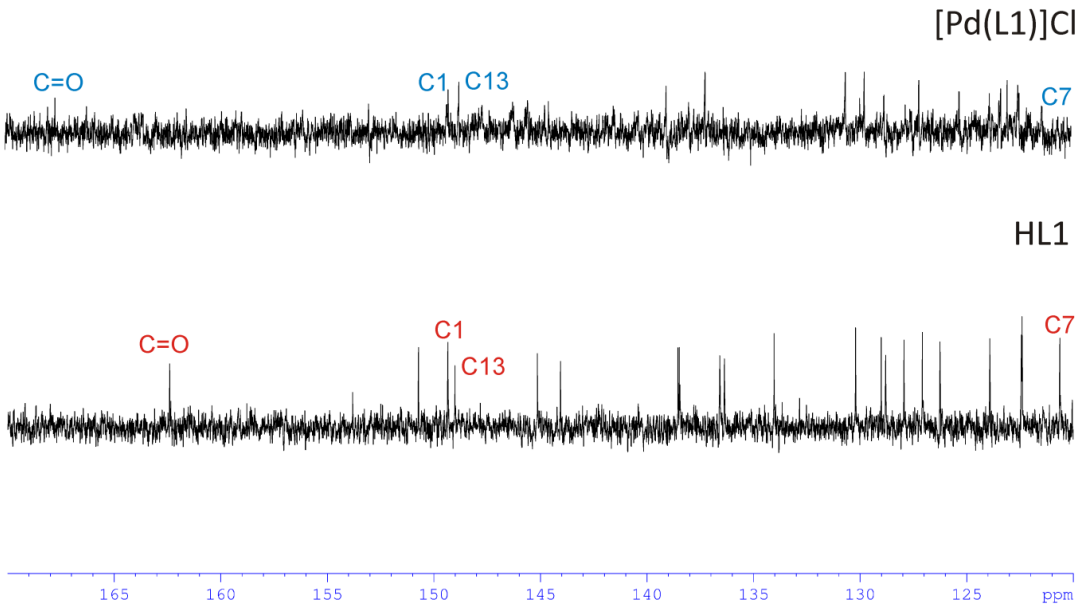

Figure 4.3.2: Comparison of the ^{13}C NMR (100 MHz, DMSO-d_6) spectra of HL1 (below) and [Pd(L1)]Cl (above).

The ^{1}H NMR chemical shifts of [Pd(L1)]Cl, have moved downfield, relative to HL1, due to the deshielding effect of the palladium(II) ion. With the exception of H13. The ^{13}C NMR chemical shifts exhibit similar downfield shifts to that observed in the ^{1}H NMR spectra. Table 4.3.1 and Table 4.3.2 summarise the changes in selected hydrogen and carbon atom chemical shifts in the ^{1}H and ^{13}C NMR spectra of the free ligand HL1 and Pd(II) chelate [Pd(L1)]Cl.

Table 4.3.1: Summary of the ^{1}H NMR chemical shifts for HL1 and [Pd(L1)]Cl.

Proton	HL1 (ppm)	[Pd(L1)]Cl (ppm)
H1	9.32	9.33
H8	8.97	9.11
H7	8.58	8.76
H13	9.13	9.06

Table 4.3.2: Summary of the ^{13}C NMR chemical shifts for HL1 and [Pd(L1)]Cl.

Carbon	HL1 (ppm)	[Pd(L1)]Cl (ppm)
C1	149.8	149.2
C8	116.7	121.3
C7	121.1	122.4
C13	149.5	148.7
C=O	162.9	167.7

The change in chemical shifts in the ^{13}C NMR spectrum of HL1 upon coordination to palladium(II), Table 4.3.2, is not as significant as that of the ^{1}H NMR spectra. This is commonly reported in similar studies. This phenomenon is attributed to the deshielding effects of the metal centre not being as strongly felt by the carbon atoms in comparison to the hydrogen atoms in the system, with the exception of the carbonyl carbon which is effected more by the deshielding effects upon chelation due to the break in resonance of the amide moiety.[7]

4.4 EPR Spectroscopy

4.4.1 Introduction

Electron Paramagnetic Resonance (EPR) spectroscopy was used to characterise the copper(II) chelates. EPR is similar to NMR in some respects. EPR involves the same interaction between electrons and radio waves under an applied magnetic field, the difference being that the unpaired electron gives rise to a much stronger signal compared to an NMR signal.[8] NMR signals require an applied magnetic field of ± 10 tesla whereas EPR signals only require ± 0.5 tesla, indicating the magnetic moment of an unpaired electron (EPR) is 20-fold greater than a paired electron's (NMR) magnetic moment.[8]

The key result obtained from an EPR experiment is the *g*-value; this represents the nature of the orbital in which the unpaired electron resides.[9] An electron (free) in a vacuum has a *g*-value of $g = 2.0023$,[9] the *g*-value of a compound can be less than this value, but the majority are greater than 2.0023.[9] More than one g-value can be obtained from an EPR spectrum with the *g*-values representing environments with differing angular momenta.[9] The *g*-values are represented on a Cartesian coordinate system with symmetry along the diagonal. The two axial spectra of the tetragonal system are: the *z*-axis, where $g_x = g_y > g_z$ and the *g*-value is represented as g_z; and *xy*-axis, where $g_x = g_y < g_z$ and the *g*-value is represented as g_{xy}. A tetragonal system (symmetrical) has two sets of *g*-values, g_z and g_{xy}, representing the field either perpendicular (g_{xy}) to the angular momentum or parallel (g_z) to the angular momentum of the compound.[9,10] A rhombic system (asymmetrical) has three *g*-values, $g_x \neq g_y \neq g_z$, representing the axes of the system.[9] Copper(II) has a d^9 configuration which follows a Jahn-Teller distortion, this distortion can lead to copper(II) compounds being square planar, as is the case in this work.[9]

Signals in an EPR spectrum can be coupled to the donor atoms of the ligand when it is coordinated to a paramagnetic metal centre, similar to the coupling observed in NMR. This coupling, known as hyperfine coupling, is observed in the $g_{\|}$ region of the EPR spectrum.[9] Hyperfine coupling occurs when the unpaired electron is influenced by various other sets of equivalent nuclei, that is, the environment of the system.[9] The splitting of the peak is of the order $2nI + 1$, where *n* is the number of equivalent nuclei, and *I* is the spin of the nucleus.[9]

The following calculation shows how the expected number of lines is determined for copper(II), which has a spin of $I = 3/2$:

$$\text{Number of lines} = 2nI + 1$$
$$= (2 \times 3/2) + 1$$
$$= 4 \text{ lines expected in the copper(II) EPR spectrum}$$

The hyperfine coupling constant, denoted *A*, is the result of the coupling of an electron to any magnetic nuclei present. The hyperfine coupling constant gives information about the donor atoms of the ligand. If the donor atoms are all equivalent, then the hyperfine coupling signals will all be of the same magnitude and evenly spaced.

The spectra in this work were recorded both in the solid-state and in solution. The EPR spectra of solid-state samples are broadened due to spin-lattice relaxation. It is, therefore, not possible to measure the hyperfine coupling constant in the solid-state, and thus, solution-state spectra were also recorded. Since water has a high dielectric constant, it absorbs the microwave radiation used for the data collection; this can lead to heating of the sample and consequently low-resolution spectra. To overcome this problem, a flat cell was used to minimise the volume of solvent-exposed to the microwave radiation.

The EPR spectra in this work were collected on a Bruker EMX-Plus spectrometer at 298 K, with all the spectra acquired for the X band at ~9 GHz.

4.4.2 Results and Discussion

The d^9 configuration of the copper(II) chelates have typical *g*-value ranges for g_z and g_{xy}, with $2.02 < g_{xy} < 2.07$ and $2.1 < g_z < 2.35$.[9] Table 4.4.1 shows the *g*-values obtained for [Cu(L1)](PF_6) and [Cu(L2)](NO_3):

Table 4.4.1: Table of *g*-values and hyperfine coupling constants for the amide-based copper(II) chelates.

Copper(II) Chelate	g_{xy}	g_z	A ($\times 10^{-4}$ cm^{-1})	g_z/A (cm^{-1})
[Cu(L1)](PF_6)	2.077	2.182	188.6	115.7
[Cu(L2)](NO_3)	2.094	2.166	132.4	163.6

The spectra for the copper(II) chelates were recorded in an aqueous solution to obtain the hyperfine coupling constants. These could not be measured in the solid-state due to the line broadening effect of the spin-lattice relaxation in the powder form.[9] The reasoning for the difference in hyperfine coupling constant could be due to the difference in the structure of L1 and L2 when coordinated to the copper(II) ion. The difference being due to the electron density around the nitrogen in the amide region.

Square planar, tetradentate *N*-donor copper(II) chromophores, such as [Cu(L1)](PF_6) and [Cu(L2)](NO_3), normally have g_z values of 2.200 and *A* values in the region $180 - 200 \times 10^{-4}$ cm^{-1}.[11] The g_z values for both the copper(II) chelates are slightly below the region classified for square planar. The [Cu(L1)](PF_6) g_z value is closer to 2.200 compared to the [Cu(L2)](NO_3) g_z value. Conversely, the *A* value for [Cu(L1)](PF_6) is in the square planar,

while the data for [Cu(L2)](NO$_3$), however, suggests that the geometry is potentially different. The g_z/A value is calculated to determine whether or not a complex has tetrahedral distortion in the structure.[11] The g_z/A range for a complex to be square planar with no tetrahedral distortion is approximately 110 – 140 cm. If the square-planar complex contains tetrahedral distortion, however, the g_z/A value is expected to be greater than 150 cm.[11] The complex [Cu(L1)](PF$_6$) has a g_z/A value of 115.7 cm confirming that the structure is square planar, but [Cu(L2)](NO$_3$) has a g_z/A value of 163.6 cm suggesting that the complex has square pyramidal distortion. The distortion is likely due to the picolyl moiety of the L2 complexes forming moderately flexible square planar structures because of the methylene group. This is in contrast to the L1 complexes which form rigid square planar complexes. The nitrate anion is also more strongly coordinating than hexafluorophosphate and it is possible that the nitrate ion is coordinated to the metal centre in [Cu(L2)](NO$_3$). Nitrate ion coordination to the copper(II) centre is noted in the X-ray structures of some of the chelates (see Chapter 5).

The amide nitrogen is deprotonated during metal chelation, making it a sigma-donor ligand, thus, decreasing the positive charge on the copper ion. This property of the amide nitrogen can, therefore, induce hyperfine coupling of the copper(II) EPR spectrum. L1 has the amide nitrogen adjacent to the quinoline moiety, leading to the aromaticity extending through the entire ligand. L2 has the amide nitrogen adjacent to the picolyl moiety with the aromaticity stopping at the carbonyl, making it less aromatic ligand and, therefore, the hyperfine coupling is not as well defined as that of [Cu(L1)]$^+$.

Figure 4.4.1 is an illustration of the EPR spectra obtained for [Cu(L1)](PF$_6$), both in powder form and in solution.

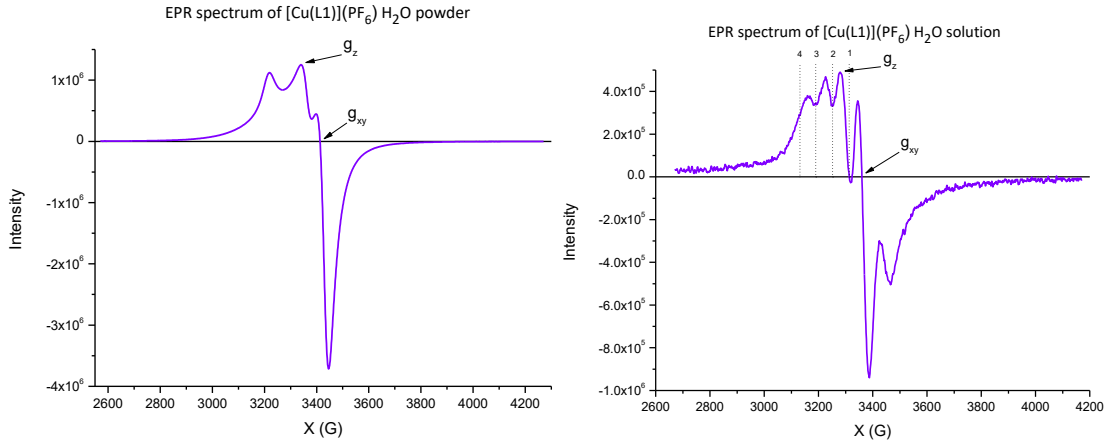

Figure 4.4.1: EPR spectra of [Cu(L1)](PF$_6$) in both the solid state and as an aqueous solution, showing g-values.

Figure 4.4.1 shows the EPR spectra obtained for the powder and H_2O solution of [Cu(L1)](PF$_6$), the aqueous solution spectrum shows the hyperfine coupling of the chelate.

The imine-based chelates, [Cu(L3)](NO$_3$) - [Cu(L10)](NO$_3$), have similar EPR spectra to [Cu(L2)](NO$_3$). The A-values for the imine-based chelates are much lower than expected for

square planar copper(II), which suggests these chelates have similar geometry to [Cu(L2)](NO_3). The g_z/A values for the imine-based chelates are much higher than 150 cm, indicating a non-square planar geometry and more of a tetragonally distorted geometry. This unusual geometry could be partially attributed to the phenol moiety of the imine-based ligands having a more flexible donor atom configuration compared to [Cu(L1)](PF_6), because of the bridging methylene group. Table 4.4.2 below summarises the g-values and A-values for these chelates:

Table 4.4.2: Table of g-values and hyperfine coupling constants for the imine-based copper(II) chelates, [Cu(L3)](NO_3) - [Cu(L10)](NO_3).

Copper(II) Chelate	g_{xy}	g_z	A ($\times 10^{-4}$ cm^{-1})	g_z/A (cm)
[Cu(L3)](NO_3)	2.112	2.197	104.03	205.87
[Cu(L4)](NO_3)	2.085	2.195	100.51	213.10
[Cu(L5)](NO_3)	2.078	2.194	102.32	209.42
[Cu(L6)](NO_3)	2.091	2.204	103.99	205.87
[Cu(L7)](NO_3)	2.105	2.199	81.13	264.05
[Cu(L8)](NO_3)	2.109	2.163	93.31	229.18
[Cu(L9)](NO_3)	2.082	2.202	103.98	205.87
[Cu(L10)](NO_3)	2.071	2.211	77.64	276.06

Figure 4.4.2 shows the structural similarities of [Cu(L2)](NO_3) and [Cu(L3)](NO_3) and the similar corresponding powder and liquid EPR spectra.

As mentioned in Section 4.2, chelates [Cu(L4)(NO_3)] and [Cu(L7)](NO_3) have different coordination geometries in the solid state. In the case of [Cu(L4)(NO_3)], the nitrate ion is part of the inner coordination sphere. While [Cu(L7)](NO_3) has the nitrate ion in the outer sphere. The A-values of these two chelates are different with [Cu(L7)](NO_3) having a lower value. Chelates[Cu(L8)](NO_3) and [Cu(L10)](NO_3) also have a lower A-value which could indicate similar coordination geometries to [Cu(L7)](NO_3), with the rest of the imine-based chelates having similar coordination geometries to [Cu(L4)(NO_3)].

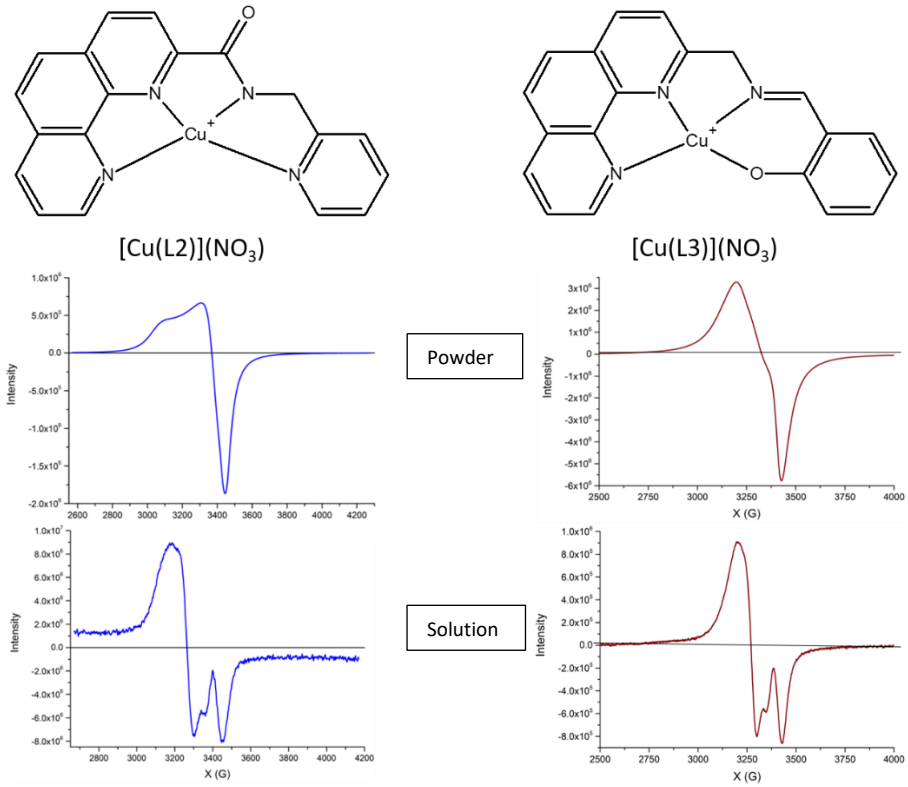

Figure 4.4.2: Structures and EPR spectra (powder [top], and solution [bottom]) of [Cu(L2)](NO_3) and [Cu(L3)](NO_3), highlighting their similarity. This similarity suggests that the complexes have the same coordination geomtry.

4.5 UV/Visible Spectroscopy

4.5.1 Introduction

Ultraviolet/visible (UV/vis) electromagnetic radiation is used to probe the electronic configuration of compounds. UV/vis radiation has a wavelength range of 1 nm – 800 nm, the energy of this radiation is in the same range as the energy between the ground and excited electronic states of compounds.[1] The process is quantised, that is, UV/vis radiation is absorbed by compounds only if the energy is equal to the energy difference between the ground state and excited states of a compound.[1]

The transition between the ground state and an excited state is the movement of an electron between energy levels of the compound. The electron moves from an occupied molecular orbital to an unoccupied molecular orbital.[1]

Compounds can absorb UV/vis radiation differently at various wavelengths.[1] The strength of the absorbance is measured as the molar extinction coefficient (ε).[1] The greater the ε value, the greater the compounds ability to absorb energy at that specific wavelength.[1]

UV/vis spectroscopy has been used in this work to characterise the ligands and metal complexes and probe their electronic configurations. It was additionally used to determine the ability of the copper(II) chelates to catalyse the production of hydroxyl radicals. Finally, it was used to determine the DNA binding affinity of the metal chelates.

4.5.2 Results and Discussion

Absorption spectra were recorded for both the ligands and metal chelates. The spectra of HL1 and [Cu(L1)](PF_6) are given as representative examples of the amide-based complexes in Figure 4.5.1. The balance of the spectra are available in **Appendix A.**

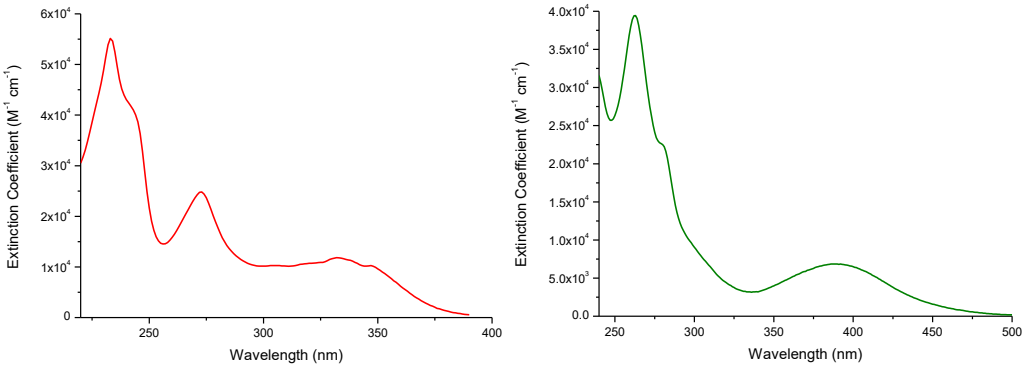

Figure 4.5.1: Absorption spectra of HL1, red, and [Cu(L1)](PF_6), green. Both aborption spectra were recorded in DMSO.

Both HL1 and HL2 exhibit a high-intensity π→π* transition which manifests as a peak in the region 270 – 280 nm.[12] The smaller, less intense absorption peaks of the L1 metal chelates, in the region of 390 nm are due to metal-to-ligand charge transfer (MLCT) transitions, typically metal ion → n(π*) transitions.[12] The free ligand also shows a high energy π–π* transition at *ca.* 225 nm. This peak is obscured in the metal chelate because of absorption by the solvent, DMSO. Table 4.5.1 shows the extinction coefficients and corresponding wavelengths for the absorption bands of the ligands and metal chelates.

Table 4.5.1: Summary of the extinction coefficients and corresponding wavelengths for the ligands and metal chelates.

Compound	λ (nm)	ε (M^{-1} cm^{-1})	λ (nm)	ε (M^{-1} cm^{-1})
HL1	273	24 704	332	12 959
[Cu(L1)](PF_6)	263	39 156	390	6 872
[Ni(L1)](PF_6)	262	32 473	398	6 503
[Pd(L1)]Cl	279	27 616	390	6 409
HL2	274	18 916	328	1 829
[Cu(L2)](PF_6)	276	26 742	-	-
[Ni(L2)](NO_3)	277	20 966	-	-
[Pd(L2)]Cl	270	19 356	-	-

The similarity in the wavelengths of the π-π* transitions in the free ligands HL1 and HL2 as well as their metal chelates, suggests that this transition originates in the phenanthroline portion of the ligand. Indeed, the imine-based chelates have this same peak, again, suggesting that it is linked to the phenanthroline moiety which is common to all ligands. The L2 metal chelates do not have a peak in the region of 390 – 400 nm indicating the chelates have a different electronic configuration compared to the L1 metal chelates. In general, the influence of an alkyl group on absorption spectra is minimal, but in this case, it breaks the aromaticity of the ligand. By reducing the aromaticity of HL2 in comparison to HL1, the spectrum shows fewer absorption bands. The data in Table 4.5.1 show that the extinction coefficients of HL2 and its metal chelates are considerably lower than those of HL1 and its metal chelates. This is again attributed to the reduced aromaticity of HL2 relative to HL1.

The imine-based chelates have a peak at 273 nm, with a similar extinction coefficient range as the L2 complexes; this can be attributed to their similarity in the phenanthroline region of the molecules. Figure 4.5.2 shows the extinction coefficients of the eight imine-based chelates.

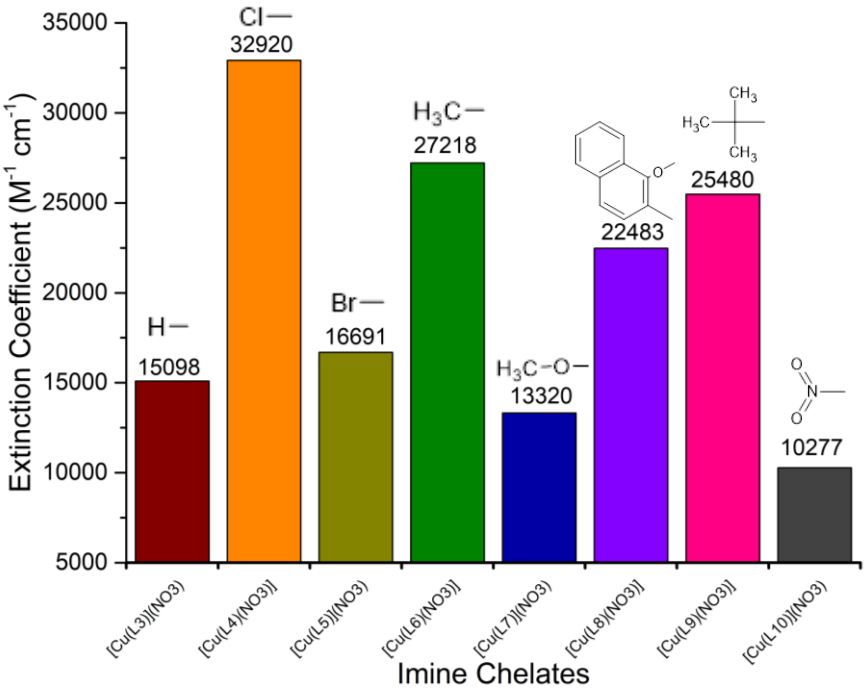

Figure 4.5.2: Extinction coefficients of the imine-based chelates.

There is no clear trend between the extinction coefficients and substituents on the salicylic moiety for the 273 nm peak in the imine-based chelates; however, a trend is observed with the spectra of the imine-based chelates. Figure 4.5.3 shows the two groups of chelates with similarly shaped spectra.

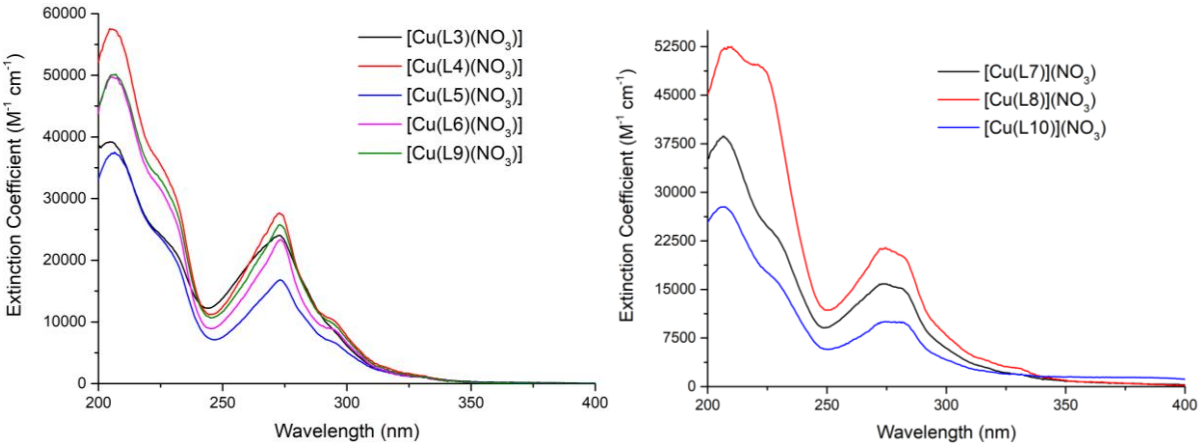

Figure 4.5.3: Absorption spectra of (left) [Cu(L3)(NO$_3$)], [Cu(L4)(NO$_3$)], [Cu(L5)(NO$_3$)], [Cu(L6)(NO$_3$)], and [Cu(L9)(NO$_3$)]; and (right) [Cu(L7)](NO$_3$), [Cu(L8)](NO$_3$), and [Cu(L10)](NO$_3$). All absorption spectra were recorded in water. These superposition plots highlight the similarities of some of the electronic spectra of the metal chelates.

The peak at 273 nm for [Cu(L4)(NO$_3$)] is sharper than that of [Cu(L7)](NO$_3$), which indicates the two chelates have different coordination geometries. Based on this, it is possible that the chelates [Cu(L8)](NO$_3$), and [Cu(L10)](NO$_3$) may have the same square planar geometry as [Cu(L7)](NO$_3$) with the nitrate ion in the outer coordination sphere. [Cu(L3)(NO$_3$)],

[Cu(L5)(NO_3)], [Cu(L6)(NO_3)], and [Cu(L9)(NO_3)] may be similar to the square pyramidal geometry of [Cu(L4)(NO_3)] with the nitrate ion in the inner coordination sphere.

4.6 DNA Binding Studies

4.6.1 Introduction

Both classes of metal chelates in this work have been designed to act as chemotherapeutic agents, exerting their cytotoxicity through DNA intercalation and, in the case of the copper(II) chelates, hydroxyl radical catalysis and the associated DNA cleavage. DNA binding constants for the metal chelates were determined *via* fluorescence competitive binding titrations. The competitive binding titrations make use of a known DNA intercalator, ethidium bromide (EB), intercalated between the base pairs of calf thymus DNA (ctDNA). The intercalated EB-ctDNA complex has an emission spectrum with an intense peak at approximately 614 nm after excitation at 500 nm. The addition of a second DNA binding agent to the EB-ctDNA complex can displace the EB from the ctDNA forming a new ctDNA complex.[13] The addition of the second DNA binding agent therefore quenches the emission from the EB-ctDNA conjugate since EB is only emmisive while intercalated in the DNA helix.

For this study, the respective metal chelates were added to the EB-ctDNA solution, in a concentration range of 0 - 200 µM. By monitoring the quenching of the emission as a function of metal chelate concentration, the apparent binding constant of the metal chelate can be calculated.

Since the metal chelates will displace the ethidium bromide from the DNA during the titration, the DNA binding affinity of the EB must be measured under the same conditions to calculate the apparent binding constant of the metal chelate. The binding constant of the EB was determined *via* direct DNA titrations. The direct method involved monitoring the absorption spectrum of EB, as aliquots of ctDNA were added to the solution. The absorption band of the EB in the range 650 – 350 nm decreases in intensity upon the addition of ctDNA. The EB in solution intercalates the ctDNA, effectively reducing the concentration of free EB in solution, resulting in a lowered absorption by the sample. By monitoring this change in absorption as a function of DNA concentration, the binding constant of ethidium bromide can be calculated. This direct method could not be used for the metal chelates as the intensity of the MLCT band in the absorption spectrum was too low to effectively monitor during the titrations at a suitable concentration. The π-π^* bands at *ca.* 270 nm are of a suitable intensity to monitor in a direct titration, but the ct-DNA absorption (λ_{max} of 260 nm) obscures this band.

Compounds with apparent binding constants, K_{app}, higher than that of EB would be considered effective DNA binding agents. Several studies have shown that a higher DNA binding affinity manifests as a larger K_{app} value.[13-16] A benchmark range of K_{app} values for a strong DNA binders, such as copper(II) phenanthroline complexes, is 1.5 - 7.0 × 10^6 M^{-1}.[13-16]

4.6.2 Experimental

The ctDNA stock solution used for both the direct and competitive DNA titrations was prepared with ctDNA, purchased from Sigma Aldrich, in 25 mM Tris-HCl buffer, prepared with ultrapure water (resistivity = 18 MΩ) and adjusted to pH 7.0 with 1 M HCl. The concentration of the ctDNA stock solution was determined by using the Beer-Lambert law, measuring the absorption intensity of the ctDNA at 260 nm and using the extinction coefficient of 13 200 M^{-1} cm^{-1} per DNA base pair to calculate the concentration.

The concentration of the EB stock solution used in the DNA titration was 9.856 × 10^{-5} M in a 10% DMSO-Tris-HCl buffer (pH 7.0) solution at 37 °C in a 1.0 cm path length quartz cuvette. The ctDNA stock solution, with a concentration of 2.411 × 10^{-3} M, was added to the EB solution in small aliquots (5 – 50 µL) with 10 minutes incubation period after each addition. The absorption spectra were recorded in the range of 800 – 200 nm. The absorbance values at 492 nm were fitted with the non-linear equation below.[17-18]

$$\frac{\varepsilon_a - \varepsilon_f}{\varepsilon_b - \varepsilon_f} = \frac{b - \sqrt{b^2 - \frac{2\,K_b^2\,Ct\,[DNA]}{s}}}{2\,K_b\,Ct}$$

Equation 1

Where $b = 1 + K_b\,Ct + \frac{K_b\,[DNA]}{2\,s}$

Where ε_a is the extinction coefficient of the monitored absorption band at a given [DNA], ε_f is the extinction coefficient of the EB before the addition of ctDNA, ε_b is the extinction coefficient of EB fully intercalated with ctDNA, *s* is the binding site size (the number of nucleotides per ethidium bromide), *Ct* is the concentration of EB, [DNA] is the concentration of ctDNA base pairs, and K_b is the equilibrium binding constant of EB.[17,18]

The concentration range of the metal chelate stock solutions (dissolved in DMSO), for the competitive DNA titrations was 1.85 – 1.62 mM, of which aliquots (2 – 10 µL) were added to a solution containing 15 µM ctDNA base pairs and 15 µM EB in 10% DMSO/25 mM Tris-HCl buffer (pH 7.0) and the resulting solution's emission spectra were recorded.

The concentration of the metal chelate, C_{50} or [complex], that resulted in 50% quenching of the initial EB fluorescence was determined from the emission spectrum and used in the following equation to determine the apparent binding constant for each metal chelate:[13-19]

$$K_{app} = \frac{K_b\,[EB]}{[complex]}$$

Equation 2

Where [EB] is the concentration of EB, K_{app} is the apparent binding constant and K_b is the binding constant of EB (as determined in the direct DNA titration).[13-19]

The quenching of fluorescence of the EB-ctDNA conjugate can be confirmed with the use of a plot, fitted with the linear Stern-Volmer equation:[13-20]

$$I_0/I = 1 + kr$$

Equation 3

Where I_o is the emission intensity of EB-ctDNA complex without the presence of a second intercalator, I is the emission intensity of the quenched EB-ctDNA complex, *r* is the ratio of the total concentration of the second intercalator to the DNA concentration, and *k* is the Stern-Volmer constant.[13-20]

4.6.3 Results and Discussion

The results of the direct EB titration with ct-DNA is shown in Figure 4.6.1:

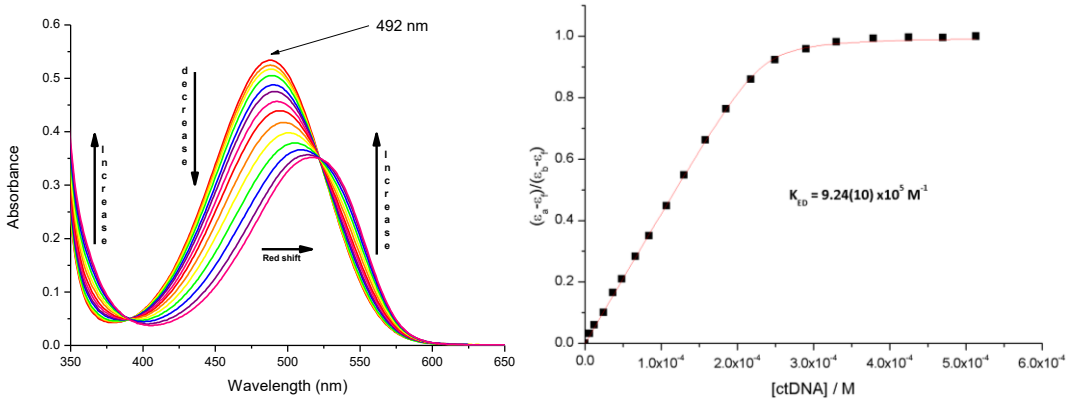

Figure 4.6.1: [Left] Absorption spectra of ethidium bromide with increasing concentrations of ctDNA, with arrows indicating spectral changes. [Right] Non-linear fit, Equation 1, of EB titration with ctDNA at 492 nm.

The spectra in Figure 4.6.1 show the hypochromism and the bathochromic shift, which is characteristic of the DNA intercalation process. The binding constant was found to be 9.24(10) × 10^5 M^{-1} (bp) for the EB, K_b, under these experimental conditions.

Figure 4.6.2 shows the emission spectra obtained from the competitive DNA titration with increasing concentrations of [Cu(L1)](PF_6). The least-squares fit of the change in ethidium bromide emission at 614 nm with increasing concentration of the metal chelate to determine the concentration of the complex at 50% reduction in emission is also shown.

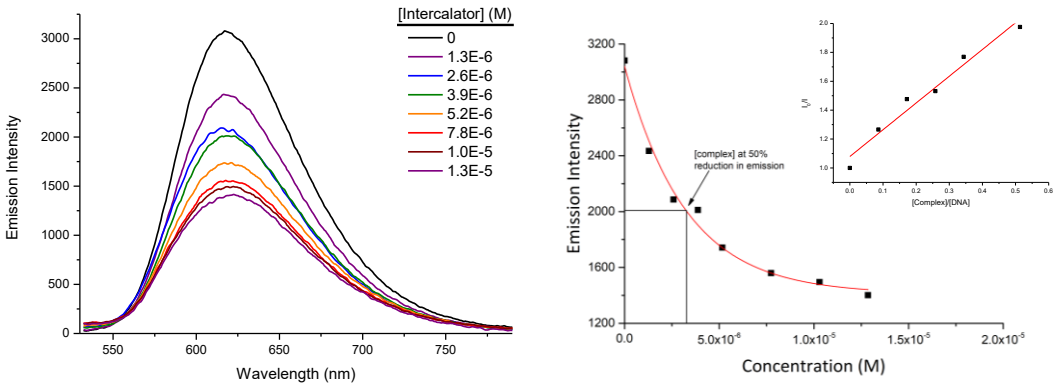

a b

Figure 4.6.2: (a) Emission spectra of ctDNA-intercalated ethidium bromide with increasing concentrations of [Cu(L1)](PF_6). (b) Least-squares fit of emission intensity at 614 nm with increasing metal chelate concentration. The inset is a Stern-Volmer plot, Equation 3, for [Cu(L1)](PF_6).

Figure 4.6.1 summarises the apparent binding constants for each of the metal chelates.

Table 4.6.1: Apparent binding constants of the metal chelates.

Metal Chelate	K_{app} ($\times 10^6$ M^{-1})	Metal Chelate	K_{app} ($\times 10^6$ M^{-1})
[Cu(L1)](PF_6)	5.91	[Cu(L2)](PF_6)	4.18
[Ni(L1)](PF_6)	2.32	[Ni(L2)](NO_3)	N/A
[Pd(L1)]Cl	5.25	[Pd(L2)]Cl	2.43
[Cu(L3)](NO_3)	0.412	[Cu(L7)](NO_3)	0.242
[Cu(L4)](NO_3)	0.213	[Cu(L8)](NO_3)	0.441
[Cu(L5)](NO_3)	0.280	[Cu(L9)](NO_3)	0.388
[Cu(L6)](NO_3)	0.432	[Cu(L10)](NO_3)	0.112

Table 4.6.1 shows that there is a moderate variation in the DNA binding affinity of the metal chelates, which is dependent on the ligand structure and the identity of the central metal ion. The structure of each of the metal chelates plays an important role in the magnitude of the apparent binding constant. These data show that the L1 metal chelates have higher K_{app} values, which is due to the extended aromaticity of the ligand L1 in comparison to L2. In general, the greater the extent of the aromaticity, the more effectively a complex can intercalate DNA.[21] The L1 chelates are planar throughout the complexes whereas the L2 chelates are only planar over the aromatic rings and not over the -N-CH_2- region. In addition to the planarity of an aromatic complex aiding intercalation, aromaticity also leads to favourable π···π interactions between the chelates and the aromatic DNA bases. These attractive forces increase the stability of the DNA/drug conjugate, which results in a higher DNA binding constant.[21]

The imine-based chelates have lower DNA binding constants when compared to the amide-based chelates, with the imine-based complexes having a range of 1.12 – 4.41 × 10^5 M^{-1}. This is an order of magnitude lower than that of the amide chelates. The largest K_{app} in this group is [Cu(L8)](NO_3), which has a naphthalene moiety that extends aromaticity which, as stated

above, enhances intercalation. The lower binding constants for the imine-based chelates could be attributed to the geometry of the structures being square pyramidal, reducing the intercalation ability of these chelates; there is evidence of this geometry in the EPR spectra. In addition, the amide-based complexes have a carbonyl group on the ligand. This group could be involved in hydrogen bonding interactions with the DNA base pairs. Intermolecular interactions can have a significant stabilising effect on the DNA/drug conjugate which manifests as a larger K_{app}. Charge is another factor that can influence DNA binding affinity. In this case, both classes of compounds are monocationic, so this should not be relevant. An additional factor that could cause a lower K_{app} values for the imine-based complexes is that these chelates could have multiple modes of binding. The imine-based chelates could have DNA intercalating and groove binding properties, which could lower the K_{app} values.[22]

The copper(II) and palladium(II) amide-based chelates have higher K_{app} values due to the square planar geometry in solution. The nickel(II) chelates which are suspected to be octahedral in the presence of coordinating solvents, such as water. The octahedral shape, caused by the axial water molecules coordinating to the nickel(II) centre, results in a geometry less suitable for DNA intercalation, this manifests as reduced K_{app} values. In the case of [Ni(L2)](NO_3), no DNA binding was detected. This could be due to the lack of planarity of both the ligand system and the metal centre. Figure 4.6.3 illustrates reported K_{app} values for a range of copper(II) chelates and how they compare to those of [Cu(L1)](PF_6).

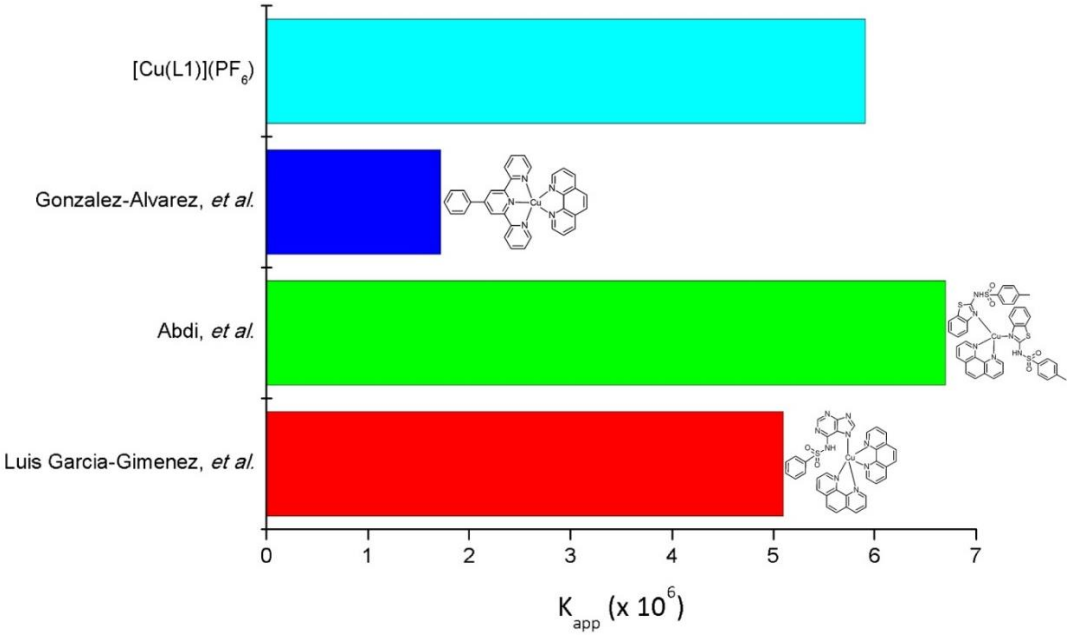

Figure 4.6.3: Bar graph of the K_{app} values of various copper(II) chelates compared with [Cu(L1)](PF_6).[13,15,16]

The bar graph shows that the DNA affinity of [Cu(L1)](PF_6) compares favourably with previous studies of similar copper(II) chelates. This confirms the chelate is a sufficiently strong DNA binder to be considered a potential chemotherapeutic agent. The previous work also shows a

clear relationship between the extent of aromaticity and the DNA binding constant. A future avenue of this project will therefore be to extend the aromaticity of the ligands.

4.7 Hydroxyl Radical Assay

4.7.1 Introduction

One of the key factor which enhance the cytotoxicity of copper(II) chelates is their ability to catalyse the synthesis of hydroxyl radicals and other reactive oxygen species *in vivo*. These radicals are electron-deficient and will attack aromatic DNA base pairs, inducing single and double-stranded DNA cleavage. The latter is particularly difficult for tumour cells to repair. The hydroxyl radical assays illustrate the production of radicals in solution in the presence of H_2O_2. The presence of hydrogen peroxide in cells is due to either the breaking down of some amino acids or proteins that specialise in producing hydrogen peroxide for the cell. Hydrogen peroxide can cause DNA damage, if in excess in cells. Homeostasis is maintained by other proteins in the cell, such as oxidoreductase enzymes.[23]

When copper(II) chelates are introduced to a cell, in the presence of natural thiols and hydrogen peroxide, the copper(II) centres produce hydroxyl radicals. These then degrade the aromatic base pairs of DNA in the cell. This DNA cleavage induces cell apoptosis (refer to section 1.4 in Chapter 1).[13,24] Figure 4.7.1 illustrates the above-mentioned reaction, which takes place in human cells.

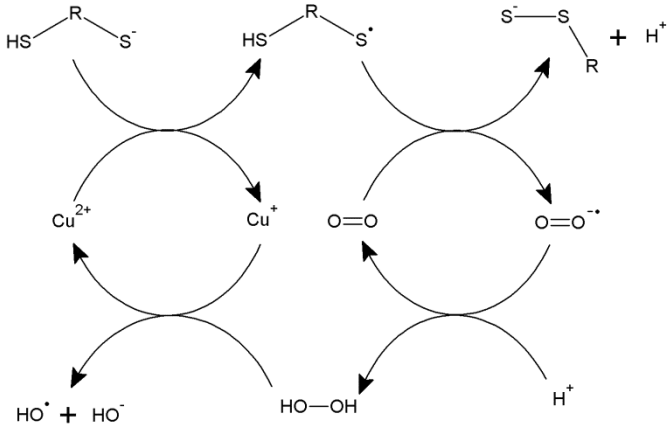

Figure 4.7.1: Hydroxyl radical production cycle with a copper(II) catalyst.[13,24]

The copper(II) ion oxidises a natural thiol anion to form a thiyl radical. This thiyl radical reduces the molecular oxygen in the cells to form the highly reactive superoxide anion. The superoxide anion undergoes a disproportionation reaction in the presence of H^+, forming hydrogen

peroxide. The copper(I) ion, produced by the thiol oxidation to the thiyl radical, then reduces the hydrogen peroxide, forming the hydroxide anion, hydroxyl radical, and copper(II) ion.

The hydroxyl radical assay is performed by running a kinetic scan at a specific wavelength after the addition of the metal chelate to a dye solution. The hydroxyl radical assays are performed using the Ni(II) and Pd(II) analogues as a control to determine whether the copper(II) chelates are the only complexes that are redox-active. The dye used is Rhodamine B, which is highly conjugated, and as the electron-deficient radicals are produced, they attack the electron-rich π-system of the dye and degrade it. The loss of extended conjugation in the dye leads to a decrease in the absorption intensity. The electron-rich dye acts as an analogue of the electron-rich DNA base pairs which are equally susceptible to attack by the electron-deficient hydroxyl radicals. Monitoring the decay of the absorption peak of the Rhodamine B will therefore be a measure of the hydroxyl radicals being produced. Figure 4.7.2 shows the structure of Rhodamine B.

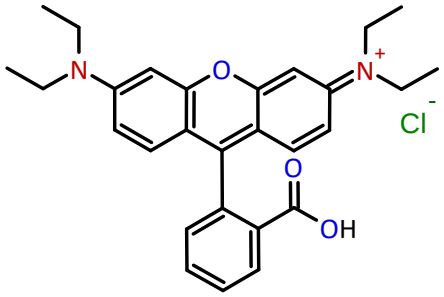

Figure 4.7.2: Structure of Rhodamine B, highlighting the aromatic nature of the dye, which makes it susceptible to degradation by hydroxyl radicals.

4.7.2 Experimental

The use of sodium ascorbate in the hydroxyl radical assays is to simulate the thiols present in the mammalian cellular environment.
Table 4.4.1 shows the stock reagents, and the associated concentrations, required for each hydroxyl radical assay.

Table 4.7.1: Table of the concentrations of the required solutions for the hydroxyl radical assay.

Stock solution	Rhodamine B	Metal chelate	Hydrogen peroxide	Sodium ascorbate
Concentration (M)	3.60×10^{-5}	1.0×10^{-2}	2.70×10^{-2}	2.60×10^{-3}

A 1 mL 1:1 (v/v) solution of the Rhodamine B stock solution and the respective metal chelate stock solution (solution A) was added to a 1 cm quartz UV cell. 1 mL of a 1:1 (v/v) solution of the sodium ascorbate and hydrogen peroxide (solution B) was added to the cell. Immediately

upon addition of solution B to solution A, the decay of the Rhodamine B absorption was monitored at 553 nm as a function of time. The total time taken for each run was 20 minutes.[25]

4.7.3 Results and Discussion

Figure 4.7.3 illustrates the kinetic traces of the L1 metal chelates and water during the hydroxyl radical assay.

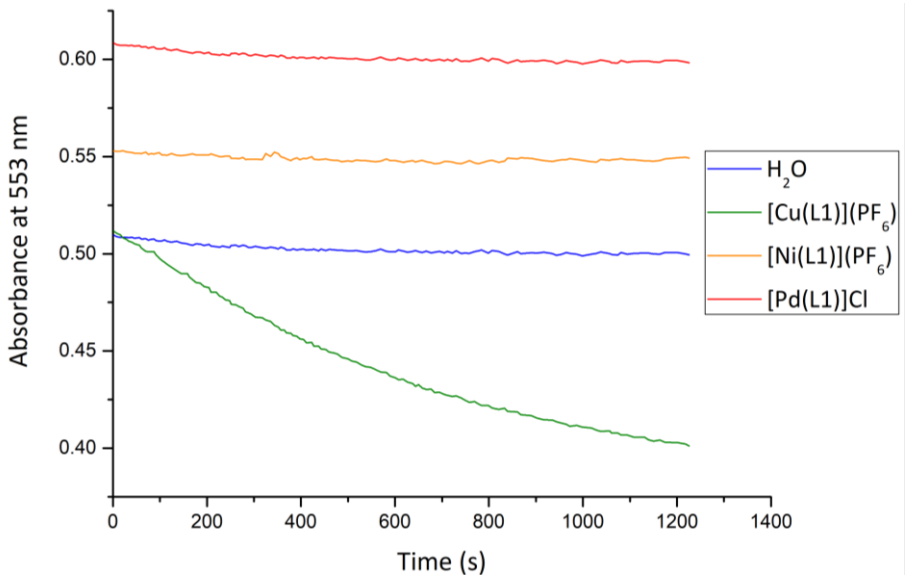

Figure 4.7.3: Kinetic traces of hydroxyl radical assays for the L1 metal chelates and water (control).

The kinetic run for water was used as a control to ensure that the reagents do not produce the hydroxyl radicals without the metal centre to act as a catalyst. The nickel(II) and palladium(II) chelates, being redox inactive, show a similar, flat curve to that of water, proving that the nickel(II) and palladium(II) chelates do not produce the hydroxyl radicals. The curve of the copper(II) chelate illustrates that the presence of the chelate catalyses the production of hydroxyl radicals which in turn decomposes the dye. The assay results for the L2 metal chelates are the same as the L1 chelates, proving the copper(II) metal centre is essential for the catalytic production of hydroxyl radicals. The imine-based chelates have the same decay profile as the amide-based copper(II) chelates. The decay profiles of [Cu(L2)](NO_3), [Cu(L3)(NO_3)], [Cu(L4)(NO_3)] [Cu(L7)](NO_3) chelates are shown in Figure 4.7.4.

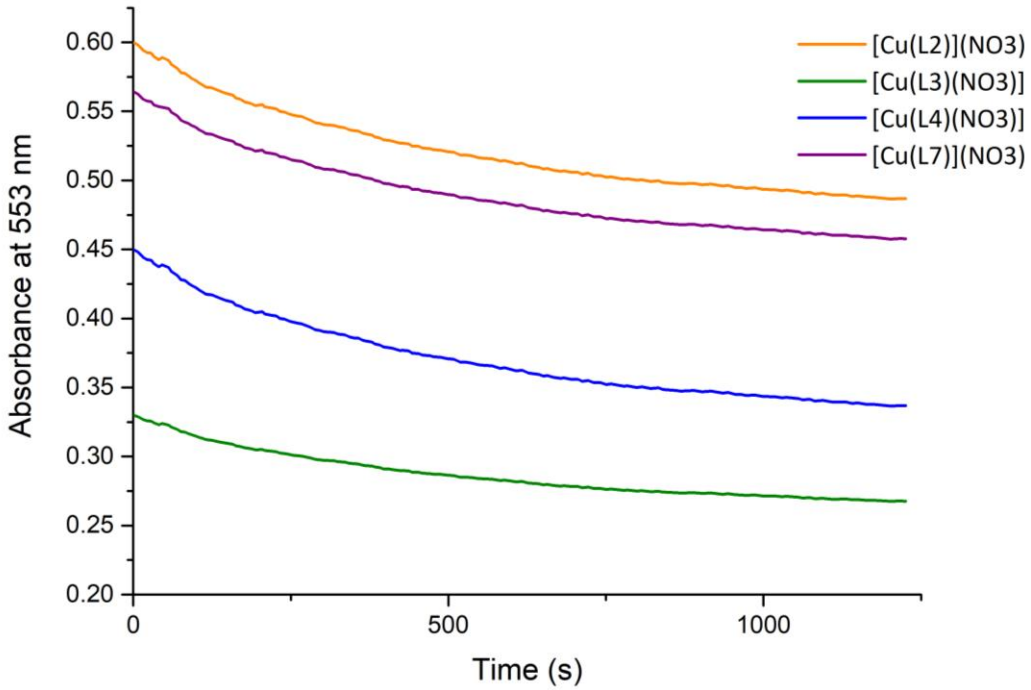

Figure 4.7.4: Kinetic traces of hydroxyl radical assays for the [Cu(L2)](NO_3), [Cu(L3)(NO_3)], [Cu(L4)(NO_3)] [Cu(L7)](NO_3) chelates.

4.8 Summary of Spectroscopic Data

The various spectroscopic techniques that were used to characterize the ligands and metal chelates in this work were analysed in this chapter. Further spectroscopic techniques were also used to determine the physiochemical properties of the complexes.

The IR data confirmed the structural characteristics of the two amide ligands and the corresponding amide-based chelates. The spectra of the amide-based chelates verify that the ligands had been chelated to the metal ions, forming the amide-based complexes, showing a decrease in wavenumber of the carbonyl vibration after chelation. The imine-based ligands were not isolated and so their spectra could not be compared to the metal complexes. However, the presence of the imine bond stretching frequency confirmed for all eight imine-based chelates had been synthesised.

NMR spectra were obtained for the amide ligands and the palladium(II) chelates. The shift in ^{1}H and ^{13}C NMR signals and the disappearance of the amide N-H peak in the palladium(II) chelate NMR spectra confirmed coordination.

EPR spectra of the copper(II) chelates were able to show the coordination geometries of the copper(II) ion in the complexes. The shape of the spectrum of [Cu(L2)](NO_3) was similar to that of the imine-based chelates, suggesting a similarity in their structures. The spectrum of [Cu(L1)](PF_6) showed the hyperfine coupling of the chelate which is attributed to the higher aromaticity when compared to the other copper(II) chelates.

Electronic absorption spectra of the metal chelates were also used to confirm the coordination geometry of the chelates. Similar to the EPR spectra, the imine-based chelates had comparable absorption spectra to [Cu(L2)](NO_3). The imine-based chelates have two groups of spectra that differ in profile. The difference could be attributed to the coordination spheres of the chelates, with [Cu(L4)(NO_3)] having the nitrate ion in the inner sphere (as shown by X-ray diffraction) and [Cu(L7)](NO_3) having the nitrate ion in the outer sphere. Chelates [Cu(L3)(NO_3)], [Cu(L5)(NO_3)], [Cu(L6)(NO_3)], and [Cu(L9)(NO_3)] have similar spectra to [Cu(L4)(NO_3)] and chelates [Cu(L8)](NO_3) and [Cu(L10)](NO_3) have spectra similar to [Cu(L7)](NO_3).

The DNA binding constants of the metal chelates were measured through a competitive fluorescence study and showed that [Cu(L1)](PF_6) has the highest affinity for DNA with a K_{app} of 5.91×10^{-6} M^{-1}. The imine-based chelates all had a significantly lower binding constants, ranging from 1.12×10^{-7} M^{-1} to 4.41×10^{-7} M^{-1}. These lower binding constants could be due to different binding modes, intercalation vs groove binding.

The copper(II) chelates have an ideal redox potential to catalyse the formation of hydroxyl radicals *in vivo*. This was confirmed by a time dependent assay, measuring the decay in absorption of Rhodamine B, in the presence of the copper(II) chelates. Conversely, the nickel(II) and palldium(II) chelates showed no decrease in absorption and a similar profile to that of water, showing that they do not catalyse the production of hydroxyl radicals under these conditions.

4.9 References

1. Pavia, D. L., *Introduction to spectroscopy: a guide for students of organic chemistry*. 3rd ed.; Harcourt College Publishers: Fort Worth, 2001.
2. Silverstein, R. M., *Spectrometric identification of organic compounds*. 7th ed.; John Wiley & sons: Hoboken, NJ, 2005.
3. Kemp, W., *Organic spectroscopy*. 3rd ed.; Macmillan Education: 1991; p 1.
4. Bruice, P. Y., *Organic Chemistry*. 5th ed.; Pearson Prestice Hall: Upper Saddle River, NJ, 2007.
5. Barry, K.-L.; Grimmer, C. D.; Munro, O. Q.; Akerman, M. P., *RSC Advances* **2020,** *10* (13), 7867-7878.
6. Makedonas, C.; Mitsopoulou, C. A., *Eur. J. Inorg. Chem.* **2006,** *2006* (12), 2460-2468.
7. Romeo, R.; Carnabuci, S.; Plutino, M. R.; Romeo, A.; Rizzato, S.; Albinati, A., *J. Inorg. Chem.* **2005,** *44* (5), 1248-1262.
8. Clayden, J.; Greeves, N.; Warren, S.; Wothers, P., *Organic Chemistry*. Oxford University Press: Oxford, 2001.
9. Parish, R. V., *NMR, NQR, EPR, and Mössbauer spectroscopy in inorganic chemistry* 1st ed.; E. Horwood: New York, 1990.
10. Garribba, E.; Micera, G., *Journal of Chemical Education* **2006,** *83* (8), 1229.
11. Palaniandavar, M.; Somasundaram, I.; Lakshminarayanan, M.; Manohar, H., *J. Chem. Soc., Dalton Trans.* **1996,** (7), 1333-1340.
12. Selvakumar, B.; Rajendiran, V.; Uma Maheswari, P.; Stoeckli-Evans, H.; Palaniandavar, M., *J. Inorg. Biochem.* **2006,** *100* (3), 316-330.
13. Luis García-Giménez, J.; González-Álvarez, M.; Liu-González, M.; Macías, B.; Borrás, J.; Alzuet, G., *J. Inorg. Biochem.* **2009,** *103* (6), 923-934.
14. Nagaraj, K.; Sakthinathan, S.; Arunachalam, S., *J. Fluoresc.* **2014,** *24* (2), 589-598.

15. Abdi, K.; Hadadzadeh, H.; Weil, M.; Rudbari, H. A., *Inorg. Chim. Acta* **2014,** *416* (0), 109-121.
16. González-Álvarez, M.; Alzuet, G.; del Castillo, L.; Borrás, J.; Liu-González, M., *Eur. J. Inorg. Chem.* **2006,** *2006* (19), 3823-3834.
17. Carter, M. T.; Rodriguez, M.; Bard, A. J., *J. Am. Chem. Soc.* **1989,** *111* (24), 8901-8911.
18. Barton, J. K.; Goldberg, J. M.; Kumar, C. V.; Turro, N. J., *J. Am. Chem. Soc.* **1986,** *108* (8), 2081-2088.
19. Sheng, X.; Guo, X.; Lu, X.-M.; Lu, G.-Y.; Shao, Y.; Liu, F.; Xu, Q., *Bioconjug. Chem.* **2008,** *19* (2), 490-498.
20. Eftink, M. R.; Ghiron, C. A., *Anal. Biochem.* **1981,** *114* (2), 199-227.
21. Almaqwashi, A. A.; Zhou, W.; Naufer, M. N.; Riddell, I. A.; Yilmaz Ö, H.; Lippard, S. J.; Williams, M. C., *J Am Chem Soc* **2019,** *141* (4), 1537-1545.
22. Molphy, Z.; Prisecaru, A.; Slator, C.; Barron, N.; McCann, M.; Colleran, J.; Chandran, D.; Gathergood, N.; Kellett, A., *Inorganic Chemistry* **2014,** *53* (10), 5392-5404.
23. Few, J. E.; Jones, P., *Analytical Letters* **1985,** *18* (13), 1579-1592.
24. Halliwell, B.; Gutteridge, J. M., *Biochem. J.* **1984,** *219* (1), 1-14.
25. Pamatong, F. V.; Detmer, C. A.; Bocarsly, J. R., *J. Am. Chem. Soc.* **1996,** *118* (23), 5339-5345.

Chapter 5: X-ray Diffraction

5.1 Introduction

X-ray crystallography is the study of molecular structures of crystalline compounds by way of diffraction of X-rays by electrons in compounds with regularly repeating lattices. The data obtained from X-ray crystallographic experiments give the crystal unit cell size and packing, as well as atomic coordinates, from which bond lengths and bond of a sample can be determined.[1] The wavelength range of X-rays is 0.1 – 100 Å which makes them ideal for X-ray diffraction because of the size range of atom radii being 0.3 – 3 Å. The X-ray crystal structure is obtained by measuring the diffraction pattern of the compound at various angles to gain a 3-dimensional diffraction pattern of the compound. The diffraction pattern and the internal symmetry of the unit cell then determines the atom coordinates and therefore the three-dimensional molecular structure of the compound of interest.

The Cambridge Structural Database (CSD)[2] was used to survey previously reported X-ray structures related to both the free ligands and metal chelates, presented in this work. The ligands synthesised in this work are novel structures, but a search of the CSD showed that several closely related structures had been previously studied both as free ligands and metal chelates. The previously reported X-ray structures have the phenanthroline bound to other moieties *via* an amide or imine bond similar to the ligands herein. The reported free ligand X-ray crystal structures are summarised in Table 5.1.1 below.

Table 5.1.1: Reported X-ray crystal structures of relevant derivatised phenanthroline compounds as free ligands.

CSD[2] Ref. Code	Compound Name	Lit. Reference
ZIFSIU	4,7-dichloro-N^2,N^9-bis(4-cyclohexylphenyl)-N^2,N^9-diethyl-1,10-phenanthroline-2,9-dicarboxamide	3
KEKBIP	N^2,N^9-dimethyl-N^2,N^9-diphenyl-1,10-phenanthroline-2,9-dicarboxamide	4
BESSUO	*N*,*N*′-bis(2-amino-6-pyridyl)-1,10-phenanthroline-2,9-dicarboxamide	5
DUHFOB	1,10-Phenanthroline-2,9-dicarbaldehyde dioxime	6

Table 5.1.2 contains the X-ray data for the structures listed in Table 5.1.1.

Table 5.1.2: Summary of X-ray data for the relevant structures reported in CSD.[2]

Crystal Data	ZIFSIU	KEKBIP	BESSUO	DUHFOB
Formula	C_{42} H_{44} Cl_2 N_4 O_2	C_{28} H_{22} N_4 O_2	$C_{24}H_{18}N_8O_2$	C_{28} H_{26} N_8 O_7
Cell	Triclinic	Monoclinic	Monoclinic	Monoclinic
Space Group	*P-1*	$P2_1/c$	$P2_1/c$	$P2_1/c$
a / Å	10.966(2)	11.1276(9)	9.1763(11)	7.5156(6)
b / Å	14.744(3)	10.8556(9)	14.2033(7)	20.0795(15)
c / Å	14.944(3)	19.0605(15)	16.3085(12)	18.2339(14)
α / °	67.571(4)	90	90	90
β / °	74.834(4)	92.435(4)	102.525(8)	90.708(9)
γ / °	84.560(4)	90	90	90
T / K	120(2)	295(2)	293(2)	180(2)
Z	2	4	4	4
V / Å^3	2155.59	2300.37	2125.5	2751.46
R-Factor / %	5.63	4.53	3.93	5.81

The fused aromatic rings of the phenanthroline moiety are planar in all the free ligands listed in Table 5.1.1. The appendages of the ligands deviate from this plane for these samples, with the exception of DUHFOB which is fully planar. Figure 5.1.1 shows the structures of the reported free ligands.

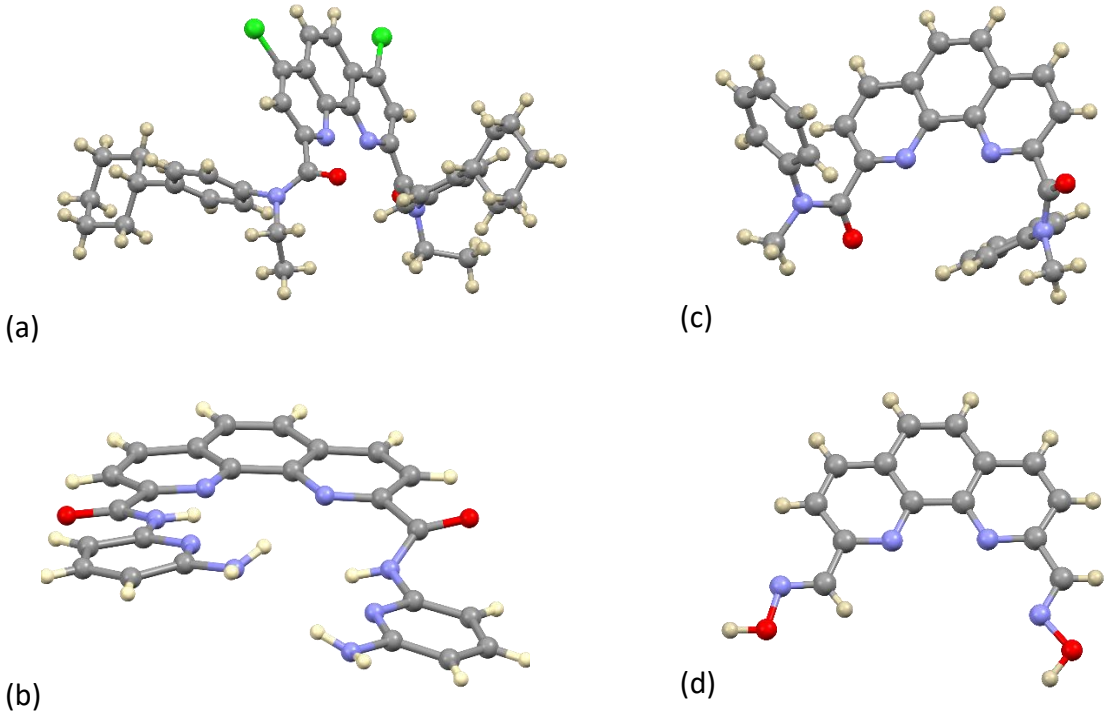

Figure 5.1.1: X-ray crystal structures of (a) ZIFSIU[3], (b) KEKBIP[3], (c) BESSUO[5], and (d) DUHFOB[6]. The crystal structures of these reported compounds have similarities to the free ligands in this work.

Compounds ZIFSIU, KEKBIP, and BESSUO have an amide group bridging the phenanthroline moiety and various substituents on the free ligands, and DUHFOB having an imine bridging

group. It is notable that these amide groups have different bond angles between the phenanthroline moiety and the other half of the free ligands, with KEKBIP having a pseudo-planar structure, whereas ZIFSIU and BESSUO are in a nearly perpendicular orientation. This difference is due to the KEKBIP having a secondary amide while ZIFSIU and BESSUO are tertiary amides. DUHFOB is a comparatively small compound with a C=N-OH group on the 2 and 9 positions of phenanthroline.

The reported X-ray data for compounds closely related to the copper(II) chelates in this work are summarised in Table 5.1.3.

Table 5.1.3: Reported X-ray crystal structures of relevant derivatised phenanthroline copper(II) chelates.

CSD[2] Ref. Code	Compound Name	Lit. Reference
OCUCOE	Dichloro-(2-(dimethylamino(hydroxy)methyl)-9-methyl-1,10-phenanthroline)-copper(II)	[7]
DUHHET	Dichloro-(1,10-phenanthroline-2,9-dicarbaldehyde dioxime-*N,N′,N″*)-copper(II)	[6]
QADPAP	bis(m2-2,9-bis(((2-(Quinolin-8-ylamino)phenyl)imino)methyl)-1,10-phenanthroline)-di-copper bis(tetrafluoroborate) helicate	[8]

The crystal data for these previously reported derivatised phenanthroline copper(II) chelates are summarised in Table 5.1.4 below

Table 5.1.4: Summary of X-ray data for relevant previously reported derivatised phenanthroline copper(II) chelate structures reported in CSD.[2]

Crystal Data	OCUCOE	DUHHET	QADPAP
Formula	$C_{16}H_{17}Cl_2CuN_3O$	$C_{36}H_{44}Cl_4Cu_2N_8O_8S_4$	$C_{28}H_{22}N_4O_2$
Cell	Monoclinic	Triclinic	Monoclinic
Space Group	*P 2₁/c*	*P-1*	*P 2₁/c*
a / Å	9.03(1)	9.100(2)	11.1276(9)
b / Å	16.47(2)	16.396(3)	10.8556(9)
c / Å	11.333(9)	16.890(3)	19.0605(15)
α / °	90	67.11(3)	90
β / °	100.31(8)	88.56(3)	92.435(4)
γ / °	90	80.77(3)	90
T / K	296	160	293
Z	4	2	4
V / Å^3	1658.28	2289.62	2300.37
R-Factor / %	3.53	3.95	4.53

The structures of these reported copper(II) chelates are shown in Figure 5.1.2 below.

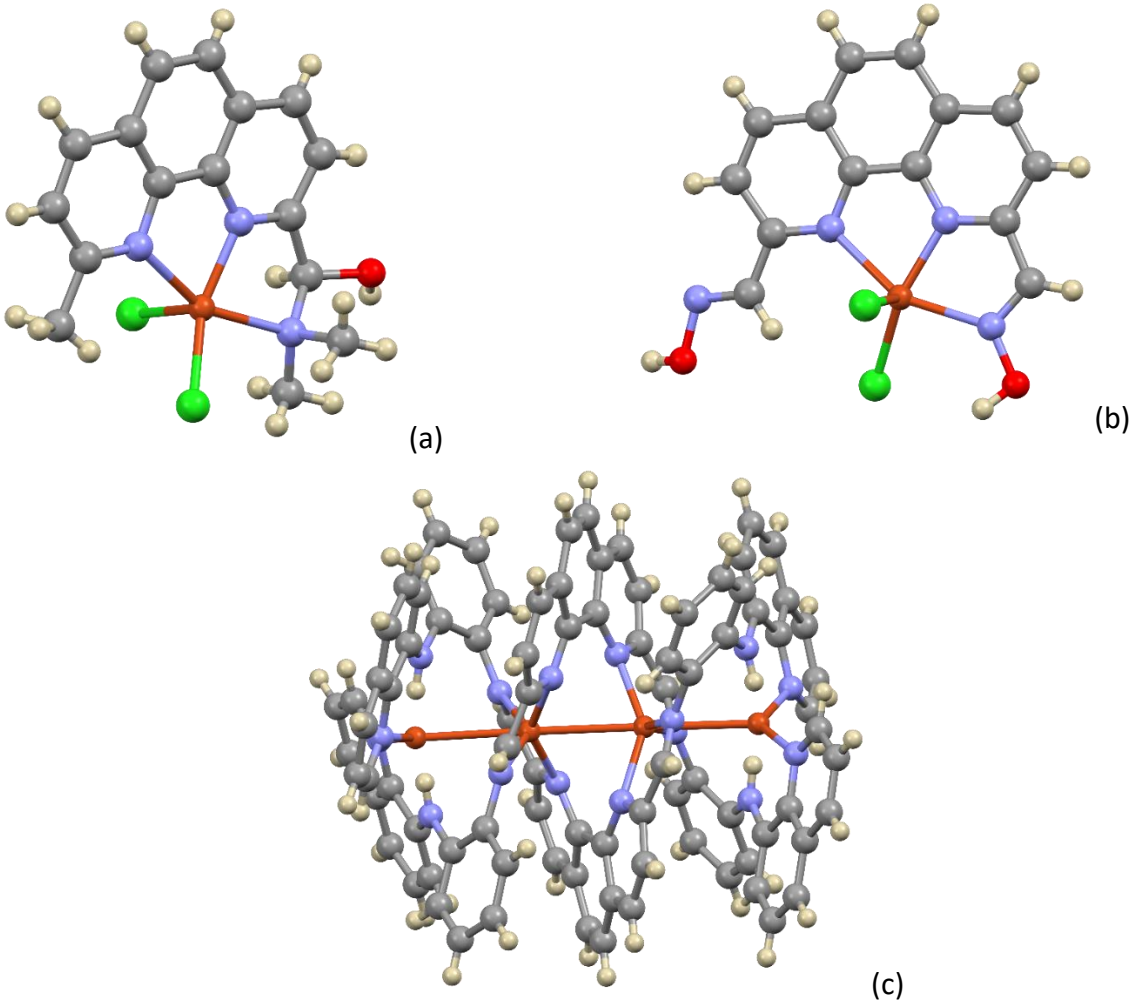

Figure 5.1.2: X-ray crystal structures of (a) OCUCOE[7], (b) DUHHET[6], and (c) QADPAP[8]. These compounds all have ligands derived from 1,10-phenanthroline coordinated to copper(II).

OCUCOE has an amino-alcohol moitey on the 2-postion of the phenanthroline moiety, which is coordinated to copper(II) chloride with the copper(II) ion adopting a distorted square pyramidal geometry. The phenanthroline-derived ligand is neutral and forms the "base" of the square pyramid with a chlorido group in the axial position. This geometry is similar to DUHHET, which has a hydroxylamine group. The free ligand of DUHHET is DUHFOB and apon chelatation, the C-N bond length of the imine group increases slightly from 1.272(5) Å to 1.280(4) Å, likely indicating a decrease in bond order following metal ion chelation. The structure of QADPAP has the phenanthroline moiety bent out-of-plane due to the helical coordination of the ligand to multiple copper(II) centres. The two inner copper(II) ions in this structure have a distorted octahedral geometry, with the outer two copper(II) ions having a trigonal planar geometry. The structure also indicates a M-M bond, with copper(II) ions bonded to each other with a bond length range of 2.808(2) – 2.828(3) Å.

5.2 Experimental

Two crystal growing methods were used for the compounds presented in this chapter, liquid-liquid diffusion, and slow evaporation. The crystals for HL1 were grown using liquid-liquid diffusion, with HL1 dissolved in ethanol and layered with hexanes. The crystals for $[Cu(L4)(NO_3)]$ and $[Cu(L7)](NO_3)\cdot(H_2O)_2$ were grown using slow-evaporation with each of the complexes dissolved in methanol, which reduces in volume due to the slow evaporation, promoting crystal grow. Crystals for chelates $[Cu(L1)](PF_6)$ and $[Ni(L1)](PF_6)$ were grown using liquid-liquid diffusion with each of the chelates dissolved in ethanol and layered with hexanes. X-ray diffraction data were recorded on a Bruker Apex Duo diffractometer equipped with an Oxford Instruments Cryojet operating at 100(2) K and an Incoatec microsource operating at 30 W power. The data were collected with Mo Kα (λ = 0.71073 Å) radiation at a crystal-to-detector distance of 50 mm using omega and phi scans with exposures taken at 30 W X-ray power and 0.50° frame widths using APEX2.[9]

The data were reduced with the programme SAINT[9] using outlier rejection, scan speed scaling, and standard Lorentz and polarisation correction factors. A SADABS semi-empirical multi-scan absorption correction[9] was applied to the data. Unless otherwise stated, direct methods SHELXS-2014[10] and WinGX32[11] were used to solve the structures. All non-hydrogen atoms in each of the structures were located in the difference density map and refined anisotropically with SHELXL-2014[10]. All hydrogen atoms in each of the structures were included as idealised contributors in the least-squares process with standard SHELXL-2014[10] parameters. The amide hydrogen atom was located in the difference density map and allowed to refine isotropically. All diagrams were rendered using Mercury 2020.2.0.

The final ligand structure was validated using an IUCR checkcif: the report is available in **Appendix B**. The reason for the Alert level B in the IUCR checkcif of HL1 is due to the structure having a positional disorder in the lattice. The structure was solved, taking into account only the major component of the disorder. There is a second minor component (< 5%) which has the phenanthroline ring on the opposite side.

5.3 X-ray Structure of HL1

The structure of HL1 was determined using single-crystal X-ray diffraction; the structure is shown in Figure 5.3.1. The crystallographic data are summarised in

Table 5.3.1.

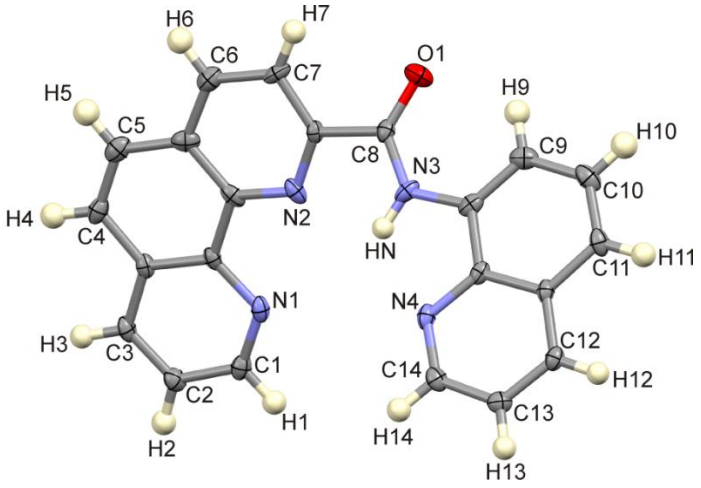

Figure 5.3.1: Thermal ellipsoid plot (50% probability surfaces) showing the structure and atom numbering scheme of HL1. Hydrogen atoms have been rendered as spheres of orbitrary radius.

Table 5.3.1: Summary of X-ray data for HL1.

Crystal Data	**HL1**
Formula	$C_{22}H_{14}N_4O$
M_r	350.37
Crystal system, space group	Monoclinic, *Cc*
a, *b*, *c* / Å	10.316(5), 12.123(5), 13.272(4)
β / °	109.298
T / K	100
Z	4
V / Å^3	1566.55
R-Factor / %	7.08
Radiation type	Mo *Kα*
μ / mm^{-1}	0.10
Crystal size / mm	0.40 × 0.25 × 0.10

Table 5.3.1: Continued.

Data Collection	**HL1**
Diffractometer	Bruker *APEX*-II CCD
Absorption correction	Multi-scan *SADABS*, Bruker 2010
T_{min}, T_{max}	0.963, 0.991
No. of measured, independent and observed [$I > 2\sigma(I)$] reflections	9945, 5621, 5053
R_{int}	0.018
Refinement	
$R[F^2 > 2\sigma(F^2)]$, $wR(F^2)$, S	0.071, 0.209, 1.03
No. of reflections	5621
No. of parameters	248
No. of restraints	3
H-atom treatment	H atoms treated by a mixture of independent and constrained refinement
$\Delta\rho_{max}$, $\Delta\rho_{min}$ / e Å^{-3}	0.80, −0.32
Absolute structure	Flack H D (1983), Acta Cryst. A39, 876-881
Flack parameter	0.3 (15)

The carbonyl oxygen in the solid-state structure of HL1 is involved in intermolecular interactions. Table 5.3.2 summarisies the bond lengths and bond angles of the intra- and intermolecular hydrogen bonds associated with this moiety.

Table 5.3.2: Geometric parameters describing the hydrogen bonding of HL1.

	Bond	**Bond Length (Å)**	**Bond Angle**
Intermolecular[i]	O1 ··· H6	2.482(2)	169.5(1)°
	O1 ··· C6	3.420(3)	
	C6 – H6	0.950(2)	
Intramolecular	O1 ··· H9	2.184(2)	123.0(1)°
	O1 ··· C9	2.816(3)	
	C9 – H9	0.950(2)	

i – Symmetry code: x, -y, $-^1/_2$ + z

The intermolecular C-H···O interaction between a phen C-H group and the amide oxygen atom links the molecules into an infinite, one-dimensional chain co-linear with the *c*-axis. C-H···O interactions are usually considered to be weak intermolecular interactions. Length does not necessarily correlate linearly to the strength of an interaction, due to packing constraints in the lattice. The interaction distance and the associated angle must be evaluated simultaneously to estimate the significance of an interaction. These interaction lengths are significantly shorter than the sum of the van der Waals radii of the interacting atoms, by -0.238 Å. This, coupled with the fact that the interaction angle does not deviate significantly

from ideality (180°), suggests that the interaction is likely to be moderately strong. Figure 5.3.2 shows the one-dimensional chain of HL1. The diagram shows the bifurcated nature of the amide oxygen atom.

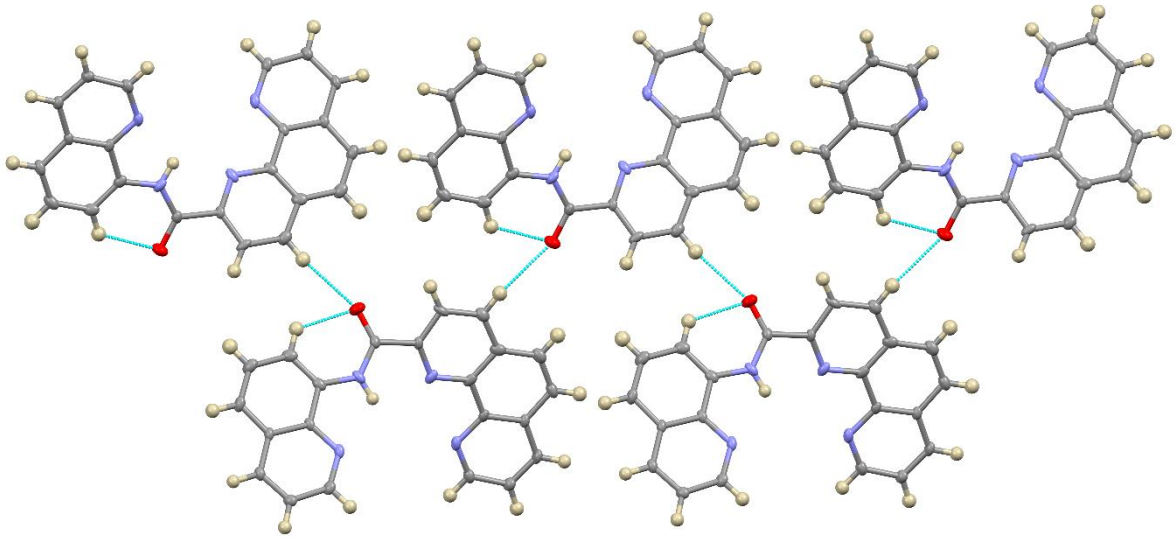

Figure 5.3.2: Hydrogen-bonded, one-dimensional chain of HL1, which is co-linear with the *c*-axis, supported by C-H···O interactions between C6-H6 and the amide oxygen atom of an adjacent molecule.

Although the phenanthroline and quinoline moieties are in themselves planar, as a consequence of their aromaticity, the ligand is not planar. The phenanthroline moiety of HL1 is in a different plane to the quinoline moiety, affording a C1-C7-C9-C14 torsion angel of 35.0(1)°. This deviation from the planarity is illustrated in Figure 5.3.3.

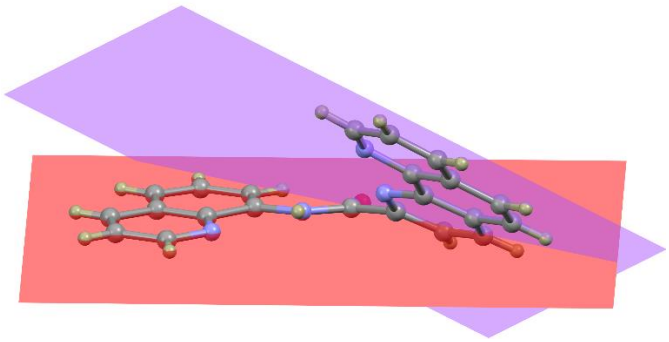

Figure 5.3.3: Illustration of the out-of-plane rotation of the quinoline ring relative to the phenanthroline moiety. The 10-atom mean plane of the phenanthroline is shown in purple. The two planes subtend an angle *ca.* 38°.

The C–N bond of the amide group of HL1 has a bond length of 1.341(3) Å. This bond length is in the range for typical amide C–N bonds (1.325 – 1.346 Å)[12,13], indicating that the bond is Csp^2-Nsp^2 with a trigonal planar geometry. The C–N bond is usually longer than 1.4 Å, but due to the nature of the amide group, the bond is shorter; this difference is attributed to the resonance between the -N-C=O bond. The C=O bond of the same amide group has a bond length of 1.265(3) Å and is also within the typical range (1.231 – 1.293 Å)[12,13] for such bond, and highlighting the double bond character.

5.4 Low-Resolution Structures of [Cu(L1)](PF$_6$) and [Ni(L1)](PF$_6$)

The [Cu(L1)](PF$_6$) and [Ni(L1)](PF$_6$) chelates were characterised using single-crystal X-ray diffraction. The correct space group of the complexes was not evident despite having good crystal data, therefore, a high-resolution structure of the complexes could not be determined. The difficulty in determining the space group of the L1 metal chelates could be due to the pseudo-two-fold symmetry of the complexes. The 1,10-phenanthroline moiety is symmetrical with the quinoline moiety of the L1 metal chelates except for one atom. The following figure shows the pseudo symmetry of the L1 metal chelates:

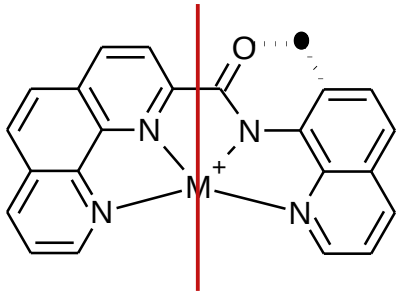

Figure 5.4.1: Structure showing pseudo two-fold symmetry of the [M(L1)](PF$_6$) chelates.

The black dot in Figure 5.4.1 illustrates how the L1 metal chelate forms pseudo symmetry, a possible explanation for the difficulty in assigning a space group for the L1 metal chelates.

Low-resolution structures of [Cu(L1)](PF$_6$) and [Ni(L1)](PF$_6$) were determined by solving the data in the space group *P*-1, the bond lengths and bond angles are not reported as they could not be measured with a reasonable standard uncertainty. The following diagram (Figure 5.4.2) shows the low-resolution structures of the complexes of [Cu(L1)](PF$_6$) and [Ni(L1)](PF$_6$):

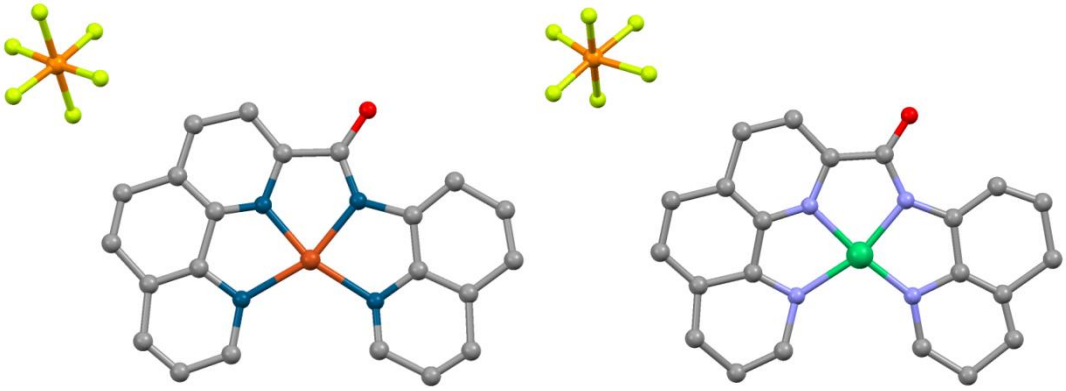

Figure 5.4.2: Low-resolution structure of the [Cu(L1)](PF$_6$) (left) and [Ni(L1)](PF$_6$) (right), with hexafluorophosphate(V) counter ions.

The low-resolution structures confirm the chelates to be nominally square planar with a hexafluorophosphate(V) anion. Additionally, the data illustrates the planarity of the chelates, suggesting that they are suitable for DNA intercalation.

5.5 X-ray Structures of $[Cu(L4)(NO_3)]$ and $[Cu(L7)](NO_3)$

Two imine-based copper(II) complexes have been analysed by single-crystal diffraction: $[Cu(L4)(NO_3)]$ (Figure 5.5.1-above) and $[Cu(L7)](NO_3)(H_2O)_2$ (Figure 5.5.1-below). The crystallographic data are reported in Table 5.5.1.

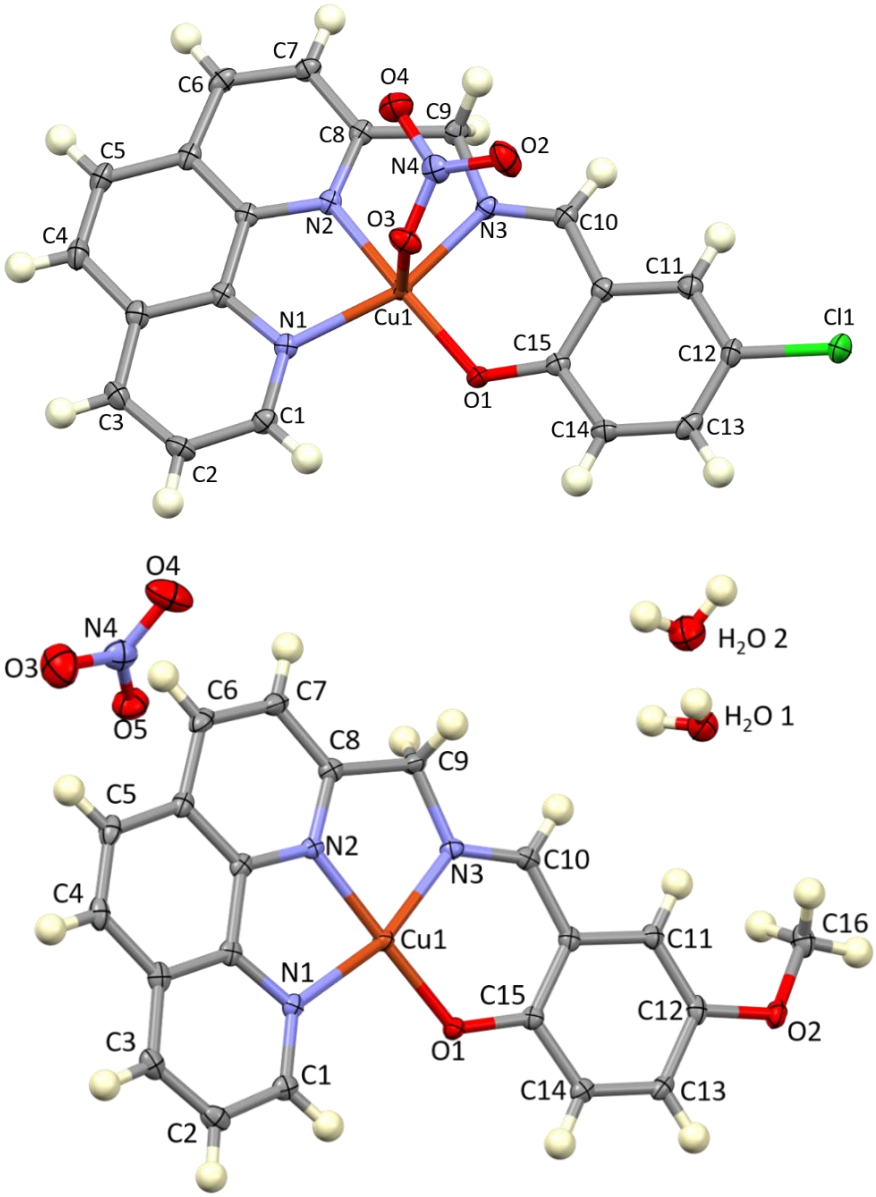

Figure 5.5.1: Thermal ellipsoid plot (showing 50% probability surfaces) showing the asymmetric unit and atom numbering scheme of $[Cu(L4)(NO_3)]$ (above) and $[Cu(L7)](NO_3)\cdot(H_2O)_2$ (below). Hydrogen atoms have been rendered as spheres of arbitrary radius.

Table 5.5.1: Summary of X-ray data for [Cu(L4)(NO_3)] and [Cu(L7)](NO_3)·(H_2O)$_2$.

Crystal Data	**[Cu(L4)(NO_3)]**	**[Cu(L7)](NO_3)·(H_2O)$_2$**
Formula	$C_{20}H_{13}N_4O_4CuCl$	$C_{21}H_{20}N_4O_7Cu$
M_r	472.33	503.95
Crystal system, space group	Monoclinic, $P2_1/n$	Monoclinic, $P2_1/n$
a, b, c / Å	9.7744(14), 17.072(3), 10.893(4)	12.7034(8), 7.5344(5), 21.2995(14)
β / °	90.378	99.202
T / K	100	100
Z	4	4
V / Å^3	1817.7(5)	2012.4(2)
R-Factor / %	4.45	4.13
Radiation type	Mo $K\alpha$	Mo $K\alpha$
μ / mm^{-1}	1.39	1.14
Crystal size / mm	0.26 × 0.20 × 0.16	0.36 × 0.14 × 0.12
Data Collection		
Diffractometer	Bruker *APEX*-II CCD	Bruker *APEX*-II CCD
Absorption correction	Multi-scan *SADABS*, Bruker 2010	Multi-scan *SADABS*, Bruker 2010
T_{min}, T_{max}	0.513, 0.746	0.651, 0.758
No. of measured, independent and observed [$I > 2\sigma(I)$] reflections	17064, 4450, 3757	35939, 5359, 4719
R_{int}	0.070	0.028
Refinement		
$R[F^2 > 2\sigma(F^2)]$, $wR(F^2)$, S	0.045, 0.122, 1.04	0.041, 0.109, 1.12
No. of reflections	4450	5359
No. of parameters	271	313
No. of restraints	0	5
H-atom treatment	H atoms treated by constrained refinement	H atoms treated by constrained refinement
$\Delta\rho_{max}$, $\Delta\rho_{min}$ / e Å^{-3}	1.16, −0.63	0.71, −0.47

The key difference between the solid-state structures of the two imine-based chelates reported herein is the coordination geometry of the copper(II) ion. [Cu(L4)(NO_3)] has the nitrate counter-ion bonded to the copper(II) centre giving a square pyramidal coordination geometry whereas in the dihydrate [Cu(L7)](NO_3)·(H_2O)$_2$ the nitrate anion is outside the cooridination sphere. The compound [Cu(L7)](NO_3) crystallises as the dihydrate. This compound is present as a dimer in the solid state. Each copper(II) ion of the dimer is coordinated to a single ligand, this tetradentate ligand occupies the four equatorial coordination sites. Two of these monomers bond through an additional Cu-O bond to the deprotonated phenol of an adjacent molecule. This phenol oxygen atom is in the axial

position, each of the copper(II) ions in the dimer therefore has a square pyramidal coordination geometry. The two structures are shown in Figure 5.5.2 below.

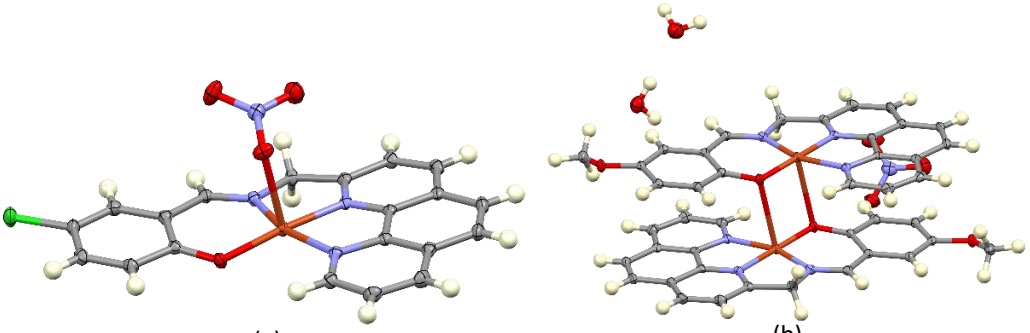

(a) (b)

Figure 5.5.2: Structural differences of the X-ray structures of (a) [Cu(L4)(NO_3)], and (b) [Cu(L7)]$_2$(NO_3)·(H_2O)$_2$. [Cu(L4)(NO_3)] is a discrete molecule in the asymmetric unit with the nitrate ion occupying the fifth coordination site. [Cu(L7)] crystallises as a dimer, the symmetry-completed dimer is shown.

Key geometric parameters of these two complexes are summarised in Table 5.5.2 below.

Table 5.5.2: Selected geometric parameters for [Cu(L4)(NO_3)] and [Cu(L7)](NO_3)(H_2O)$_2$.

Structural Data	[Cu(L4)(NO_3)]	[Cu(L7)](NO_3)(H_2O)$_2$
Bond lengths (Å)		
N1 – Cu1	2.096(2)	2.070(2)
N3 – Cu1	1.974(2)	1.955(2)
O1 – Cu1	1.910(2)	1.858(2)
Cu1 – O_{axial}	2.422(2)	2.767(2)
Bond Angles (°)		
C15 – O1 – Cu1	123.1(2)	123.7(1)
O1 – Cu1 – N1	102.61(8)	100.56(7)
O1 – Cu1 - O_{axial}	91.18(7)	92.78(6)
Torsion Angle (°)		
N1 – N2 – N3 – O1	3.55(9)	4.84(9)

Where the O_{axial} is either the nitrile ion for [Cu(L4)(NO_3)] or phenol moiety oxygen for [Cu(L7)](NO_3)(H_2O)$_2$.

The two chelates have generally similar geometric parameters, except for the Cu1 – O_{axial} bond length and the N1 – N2 – N3 – O1 torsion angle. The Cu1 – $O_{opposite}$ bond lengths differ by approximately 0.34 Å, which could be attributed to the different charge distributions of the two chelates. Chelate [Cu(L4)(NO_3)] has an electron-withdrawing substituent, -Cl, and [Cu(L7)](NO_3) has an electron-donating substituent, -OCH_3. The electron-donating group of [Cu(L7)](NO_3) pushes electron density onto the metal centre which results in the metal centre having a slightly less positive dipole moment when compared to [Cu(L4)(NO_3)]; this results in [Cu(L4)(NO_3)] having the nitrile counter-ion coordinated to the metal centre, while

$[Cu(L7)](NO_3)(H_2O)_2$ forms a dimer. DFT simulations (see Chapter 6) confirm the differences in dipole moments.

H-bonding is present in both the chelates' crystal structure, with $[Cu(L4)(NO_3)]$ having intra- and intermolecular H-bonds forming a dimer. $[Cu(L7)](NO_3)(H_2O)_2$ only has intermolecular H-bonds forming a polymer-like chain. This is illustrated in Figure 5.5.3, with the solvent and counter-ion omitted for $[Cu(L7)](NO_3)(H_2O)_2$ for clarity.

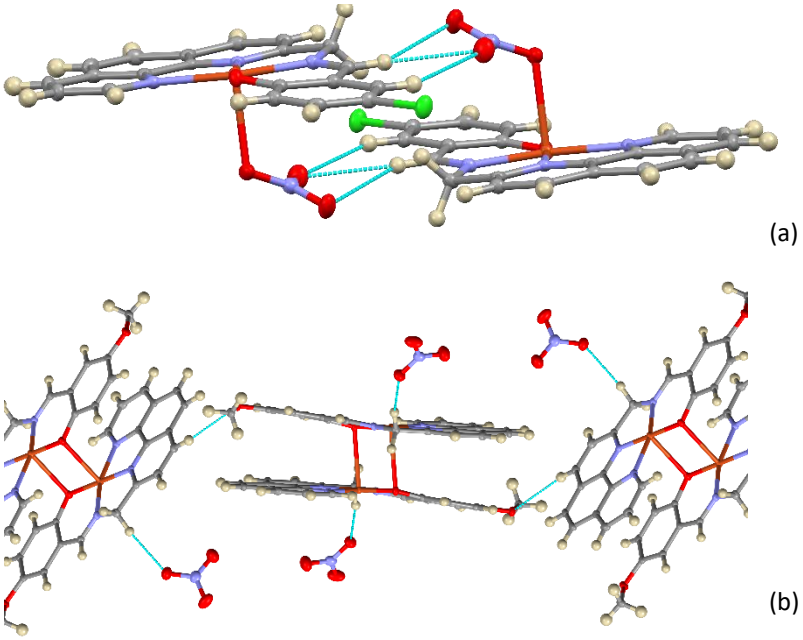

Figure 5.5.3: Structures of (a) $[Cu(L4)(NO_3)]$, and (b) $[Cu(L7)]$; showing the H-bonding in the crystal structure.

Both these characteristics, electron density and H-bonding, play a role in the packing of the chelates in the unit cell. The copper(II) chelates have a Z value of 4 and the unit cells is shown in Figure 5.5.4.

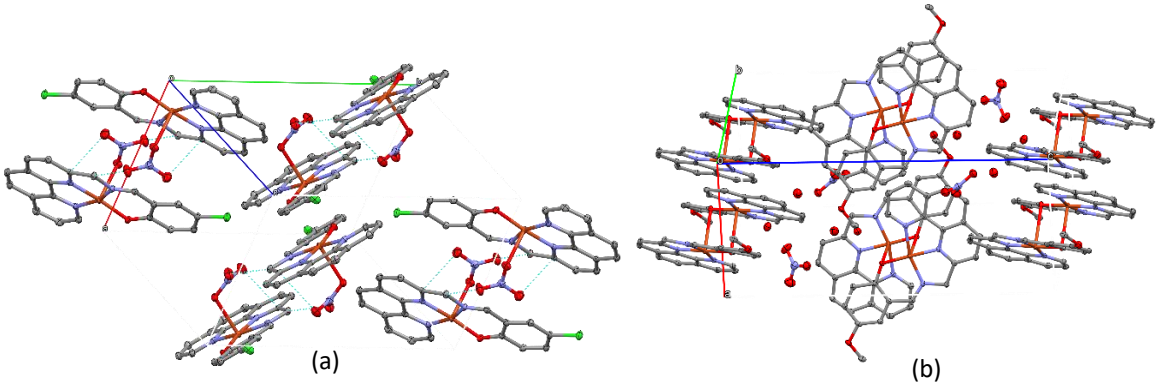

Figure 5.5.4: Crystal structures of (a) $[Cu(L4)(NO_3)]$, and (b) $[Cu(L7)](NO_3)(H_2O)_2$; showing chelate packing in the unit cell, with hydrogens omitted for clarity.

In both cases, the tetradenatate ligand, which is equatorially-coordinated, deviates from planarity. The angle subtended by the phenanthroline moiety plane and the phenol moiety

plane, of 8.20° for [Cu(L4)(NO_3)] and 8.14° for [Cu(L7)](NO_3)(H_2O)$_2$. Figure 5.5.5 shows the structures of the two chelates with the planes.

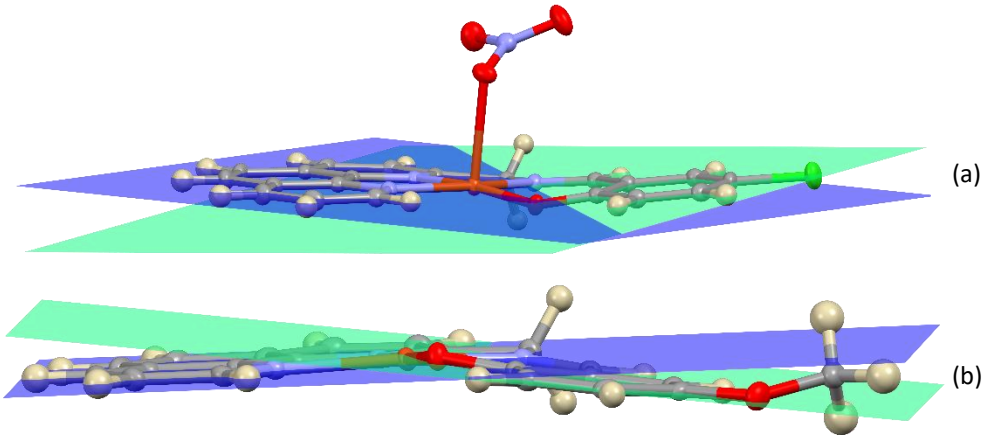

Figure 5.5.5: Crystal structures showing internal planes of the (green) phenol moiety and (blue) phenanthroline of (a) [Cu(L4)(NO_3)], and (b) [Cu(L7)].

The intraplanar angles present in both structures have one difference. The orientation of the phenol moitey is bent below the plane of the phenanthroline moitey for [Cu(L7)] whereas for [Cu(L4)(NO_3)] the phenol moiety is bent above the phenanthroline moitey.

Chelates [Cu(L4)(NO_3)] and [Cu(L7)](NO_3) have bond lengths for the C=N of 1.293 Å and 1.282 Å, respectively, and are in the bond length range (1.279 – 1.316 Å) for typical C=N bond, indictaing this bond is sp^2 hybridised. The C-O bond of the phenol moiety for these two complexes is 1.312 Å for [Cu(L4)(NO_3)] and 1.326 Å for [Cu(L7)](NO_3), which is shorter than the typical C-O bond for phenol, 1.362 Å, and could be due to the nature of the ligand affecting the bond length.[12,13] An interesting note with regards to the C-O bond of the two complexes is that the bond length is shorter for [Cu(L4)(NO_3)] and could be from the chloride electron-withdrawing group present, compared to the methoxy electron-donating group of [Cu(L7)](NO_3).

A challenge with single crystal X-ray diffraction is determining whether the single crystal X-ray data is representative of the bulk sample. To confirm that the bulk material was of the same phase as that of the single crystal X-ray diffraction data, the powder X-ray diffraction (PXRD) pattern of the sample was recorded. The PXRD pattern of [Cu(L4)](NO_3) is depicted in Figure 5.5.6 below, the same data for [Cu(L7)](NO_3) is available in **Appendix B**. The pattern was collected at room temperature and ambient pressure. The bulk material was analysed without any further purification. The trace obtained for compound [Cu(L4)](NO_3) (shown in black) is consistent with the calculated pattern (shown in red) from the single-crystal data. The agreement between the experimental data and the calculated pattern (from the single crystal structure) strongly implies the phase purity of the bulk material, i.e., the structure determined in the single crystal X-ray diffraction study is representative of the bulk material.

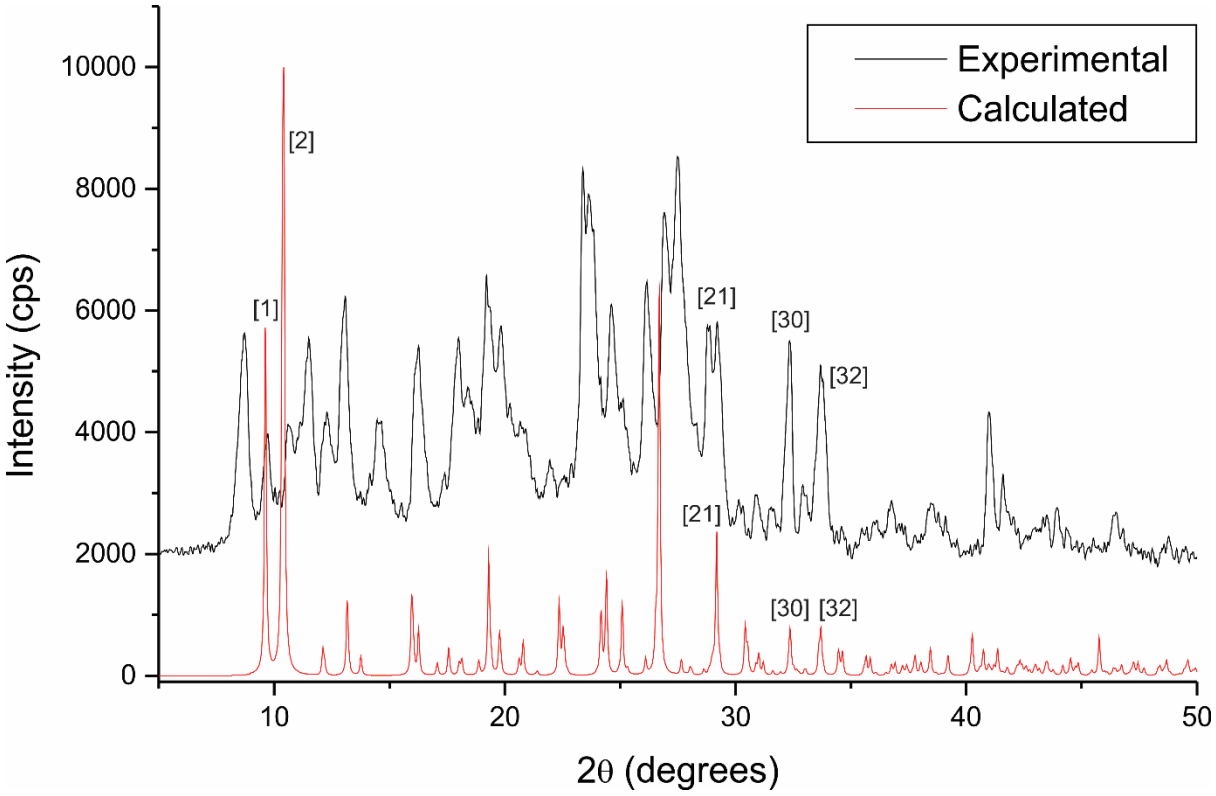

Figure 5.5.6: Comparison of the experimental powder X-ray diffraction pattern of [Cu(L4)](NO$_3$) (black) and the spectrum calculated from single-crystal data (red) show that the bulk material is the same phase as the single crystal data.

5.6 Summary of X-ray Diffraction

The solid-state structure of HL1 was elucidated by single crystal X-ray diffraction. The data showed that (despite the extended aromaticity) the ligand was not planar, with the phenanthroline and quinoline moieties subtending an angle of *ca.* 35°. The carbonyl of the ligand is involved in two intermolecular interactions (a bifurcated interaction) with quinoline and phenanthroline C–H groups of adjacent molecules. These interactions lead to a one-dimensional supramolecular structure. Low resolution structures of [Cu(L1)](PF$_6$) and [Ni(L1)](PF$_6$) showed that the structures exhibit the expected square planar geometry: ideal for DNA intercalation. The structure of the imine based chelate [Cu(L4)(NO$_3$)] showed that the nitrate ion is coordinated to the metal centre in the solid state, giving a square pyramidal coordination geometry. In [Cu(L7)](NO$_3$)·2H$_2$O, the nitrate is outer-sphere. The metal complex [Cu(L7)](NO$_3$)·2H$_2$O forms a dimer in the solid state with complementary bonds between the metal ion and phenol oxygen, i.e. the oxygen atom bridges two copper(II) ions. The metal chelates were shown to have properties that would make them suitable as DNA binding agents, i.e., planar with aromatic ligands. The PXRD data correlates with the powder X-ray pattern calculated from the single crystal data. This suggests that that phase of the bulk sample matches that of the single crystal.

5.7 References

1. Smyth, M. S.; Martin, J. H., *Mol Pathol* **2000,** *53* (1), 8-14.
2. Allen, F. H., *Acta Crystallogr. Sect. B* **2002,** *58* (3 Part 1), 380-388.
3. Petrov, V. S.; Avagyan, N. A.; Lamport, P. S.; Matveev, P. I.; Evsiunina, M. V.; Roznyatovsky, V. A.; Tarasevich, B. N.; Isakovskaya, K. L.; Ustynyuk, Y. A.; Nenajdenko, V. G., *Russian Chemical Bulletin* **2023,** *72* (3), 697-705.
4. Yang, X.-F.; Li, F.-F.; Ren, P.; Yuan, L.-Y.; Liu, K.; Geng, J.-S.; Tang, H.-B.; Chai, Z.-F.; Shi, W.-Q., *Separation and Purification Technology* **2021,** *277*, 119521.
5. Rais, D.; Gould, Ian R.; Vilar, R.; White, Andrew J. P.; Williams, David J., *Eur. J. Inorg. Chem.* **2004,** *2004* (9), 1865-1872.
6. Angeloff, A.; Daran, J.-C.; Bernadou, J.; Meunier, B., *European Journal of Inorganic Chemistry* **2000,** *2000* (9), 1985-1996.
7. Kenichi, O.; Masayoshi, U.; Hong, L.; Eishun, T., *Bulletin of the Chemical Society of Japan* **2001,** *74* (5), 869-870.
8. Begum, A.; Seewald, O.; Seshadri, T.; Flörke, U.; Henkel, G., *European Journal of Inorganic Chemistry* **2016,** *2016* (8), 1157-1160.
9. Inc., B. A., *Bruker APEX2, SAINT and SADABS*. Madison: Wisconsin, USA, 2012.
10. Sheldrick, G. M., *Acta. Cryst.* **2015,** *C71* (29), 3-8.
11. Farrugia, L. J., *J. Appl. Cryst.* **2012,** *45*, 849-854.
12. Allen, F. H.; Kennard, O.; Watson, D. G.; Brammer, L.; Orpen, A. G.; Taylor, R., *Journal of the Chemical Society, Perkin Transactions 2* **1987,** (12), S1-S19.
13. Haynes, W. M., *CRC Handbook of Chemistry and Physics, 94th Edition*. CRC Press: 2016.

Chapter 6: Computational Chemistry

6.1 Introduction

6.1.1 General

The computational studies presented here have been used to gain a deeper understanding of the experimental data obtained. In general, simulation data is obtained by generating the wavefunction of a compound; the wavefunction is then used to predict the electronic structure of a compound.[1] The exact position of an electron cannot be calculated; thus, the wavefunction gives the probability of finding an electron in certain locations in a compound.[1] Calculating the wavefunctions of molecules is a difficult task; therefore, an indirect method is used; in this case, Density Functional Theory (DFT). DFT uses the electron distribution of a molecule to determine the ground-state electronic configuration which is then used to determine the wavefunction.[2,3] The physical characteristics, such as NMR, IR and UV-Vis spectra, of a molecule in conjunction with the newly determined wavefunction can be calculated. The size of the basis sets and density functional used with DFT methods largely determine the accuracy of the simulated data.[4]

The density functional used in this work is Becke 3-parameter-Lee–Yang–Parr (B3LYP), which makes use of both the electron spin densities and electron spin gradients and is, therefore, classified as a gradient-corrected functional.[1]

Basis sets are a group of functions that describe the type and number of atomic orbitals used in a simulation of a specific atom.[2,3] It is essentially the region of space to which each electron is restricted.[2,3] The number of restrictions on the electron positions is inversely proportional to the accuracy of the simulations. However, with fewer restrictions imposed on the electrons, there is a significant increase in computational time taken. The basis sets used in this work are either 6-311G, used for the metal-free ligands, nickel(II) and copper(II) chelates, or LanL2DZ (Los Alamos National Laboratory 2-Double-Zeta), used for the palladium(II) chelates.

The 6-311G basis set is limited to atoms in the range of H-Kr and produces more precise results than the smaller 3-21G. The increased accuracy of results with the 6-311G basis set is a direct result of the limited restrictions imposed by this basis set, but results in a longer computational time for the simulations. The 6-311G basis set is an appropriate basis set for the metal-free ligands as well as the nickel(II) and copper(II) chelates.

The LanL2DZ[5-7] basis set is used for the palladium(II) chelates because the atom range for the basis set is H, Li-Ba, La-Bi. The size of the atoms (number of electrons) in the second row of the Periodic Table and beyond is overwhelming for the 6-311G basis set, and thus effective

core potentials (ECP) are applied in the LanL2DZ basis set. The electrons in the core of an atom, which are only slightly affected by the environment of the atom and mainly act to shield the nuclei and provide an effective field for the electrons, can thus effectively be replaced by a single equivalent potential.[1] This greatly reduces the computational time taken as a large number of core electrons are not explicitly included in the simulations, but accuracy is, to a large extent, maintained.

6.1.2 Previous Computational Studies

A literature review of the computational studies performed on copper(II) chelates related to those in this work showed examples of phenanthroline coordinated to copper(II) ions and other transition metal ions. The previously simulated parameters for the phenanthroline chelates include electronic, thermal, and structural properties. The calculations were performed using DFT with the B3LYP hybrid functional and a wide range of basis sets including LanL2DZ, 6-31G and 6-311G.[8-11]

A DFT study by Panina, *et al.*[12] on bi-1,10-phenanthroline ligands showed good agreement with the experimental data. Figure 6.1.1 illustrates the structure of the bi-1,10-phenanthroline structure studied by DFT at the B3LYP/6-31G level of theory.

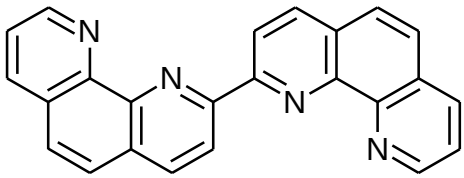

Figure 6.1.1: Structure of bi-1,10-phenanthroline, which has been studied with DFT methods.

The geometry optimisation of bi-1,10-phenanthroline found the interatomic distances of the pyridine and benzene rings were in good agreement with the experimental distances.[12] The vibrational frequencies were also found to agree with experimental data; such frequencies included the out-of-plane C-H bend, the C=C stretch of the aromatic rings, and the C=N stretching frequency.[12] The dipole moments were calculated from the electron density distributions and found the nitrogen atoms of the phenanthroline carried partial negative charges making them favourable for metal chelation.[12] The donor properties of the phenanthroline were confirmed by the energy calculations, demonstrating the low energy required for electron removal from the highest occupied molecular orbital (HOMO).[12]

A study of a copper(II) phenanthroline complex by Caglar *et al.*[10] showed that the DFT- calculated bond parameters describing the coordination sphere of the Cu(II) ion were in good agreement with the experimental X-ray structure. These parameters are summarised in Table 6.1.1.[10] The DFT calculations (at the B3LYP/LanL2DZ level of theory) for both the vibrational frequencies and the orbital energies were consistent with the experimental data.[10]

Table 6.1.1: Summary of the results obtained by Caglar *et al.*[10] for the X-ray and simulated structures.

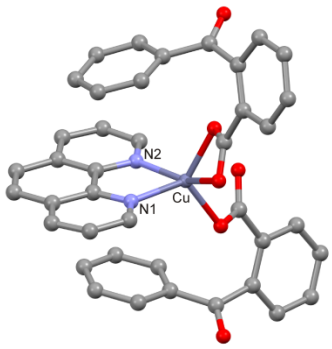

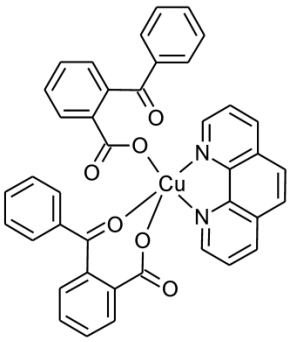

Bond lengths (Å)		
Bond	**Exp.**	**Calc.**
Cu-N1	2.01(2)	2.059
Cu-N2	1.99(2)	2.056
Bond angle (°)		
Bond	**Exp.**	**Calc.**
N2-Cu-N1	82.01(8)	81.65

6.1.3 Objectives

Geometry optimisations, vibrational frequencies, NMR spectra and electronic transitions will be simulated for the compounds synthesised in this study. The objective of these simulations is to compare and contrast the results with the experimental data and to use the data to gain a deeper understanding of the experimental work. The simulations were used to expand our comprehension of the chemistry involving the free and metal-coordinated ligands. The vibrational frequency data were used to better understand the IR spectra of the compounds. Additionaly, these data were used to determine whether the true global minimum on the potential energy surface was attained from the geometry optimisations.

6.2 Experimental

The DFT simulations were performed using Gaussian 09W,[13] with no symmetry constraints imposed on any of the calculations. The input structures used coordinates generated by GaussView 5.0.[14]

The full geometry optimisations were run at the B3LYP/6-311G or B3LYP/LanL2DZ level of theory. The basis set 6-311G was used for the simulations of the free ligands and for the copper(II) and nickel(II) chelates. The palladium(II) chelates used the LanL2DZ basis set.

The outputs from the calculations were analysed using GaussView version 5.0.[14] None of the vibrational eigenvalues found were imaginary, showing the geometry optimisations were true minima on the global potential energy surface. The energy calculations were performed using time-dependent (TD) DFT solving for 30 N states.

The NMR simulations were performed using the GIAO method at the same level of theory used for the geometry optimisations. The ^{1}H and ^{13}C NMR chemical shifts were calculated by comparisons with NMR isotropic shifts computed for TMS. All the Gaussian job and output files are available in **Appendix D**.

6.3 Results and Discussion

6.3.1 DFT Results of the Free Ligands

6.3.1.1 Geometry Optimisation Results

The geometry optimisation of HL1 was performed at the level of theory described in the experimental section. A comparison of the calculated and experimental structures for selected bond lengths, bond angles and torsion angles is shown in Table 6.3.1.

Table 6.3.1: Summary of the DFT-calculated and experimental X-ray data for HL1.

Structural Features	Calculated	Experimental	Difference* (%)
Bond Lengths (Å)			
N1-N2	2.827	2.740(3)	-3.2
C13-N3	1.396	1.341(3)	-4.1
C14-N3	1.425	1.395(3)	-2.2
C13-O1	1.221	1.265(3)	3.5
N3-N4	2.792	2.707(3)	-3.1
Bond Angles (°)			
C13-O1-N3	30.20	28.1(1)	-7.5
N2-C13-C12	28.30	29.88(9)	5.3
O1-C8-C13	26.48	27.3(1)	3.0
Torsion Angles (°)			
N1-N2-N3-N4	0.17	30.3(1)	99.4
C1-C8-C13-C22	0.28	37.1(1)	99.2

*Percentage difference = $\frac{(Exp-Calc)}{Exp} \times 100\ \%$

The differences between the calculated and experimental bond distances and bond angles are minimal. This indicates that the calculated structure is a good representation of the X-ray structure of HL1. The larger errors in the torsion angles, however, show the calculated structure (gas phase) does not reflect the solid-state geometry of HL1. Figure 6.3.1 shows a least-squares fit of the calculated and experimental structures, illustrating the differences in geometry.

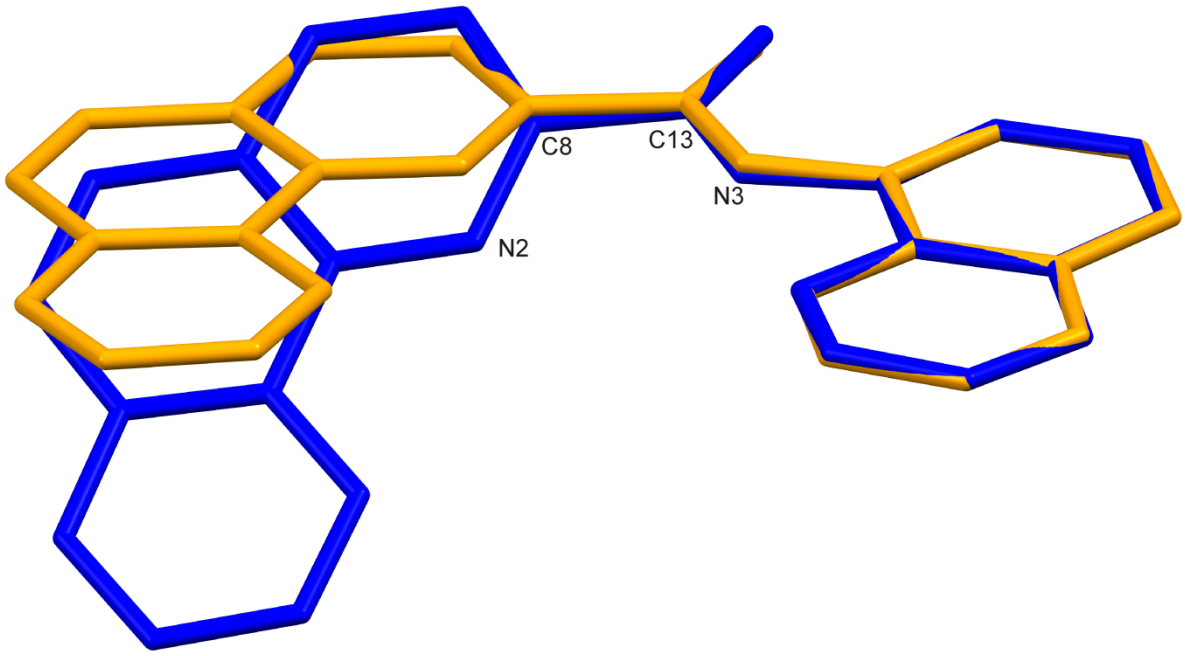

Figure 6.3.1: Partially labelled least-squares-fit of the DFT-calculated (orange) and experimental (blue) structures of HL1. The fit shows that there is a significant difference in the planarity of the molecule in the gas phase versus the solid-state.

The overlay of the amide bond and quinoline moiety of the calculated and experimental structures gives a root-mean-square deviation, RMSD, of 0.0679 Å. This small RMSD shows the amide and quinoline region of the calculated structure has been accurately simulated when compared to the experimental structure. The most notable difference between the two is the torsion angle of the phenanthroline moiety relative to the amide bond and quinoline group. In the absence of packing constraints *in vacuo*, the ligands can adopt the lowest energy conformation. In the solid state, the geometry has to deviate from this true low energy conformation to allow for optimal packing in the lattice and to enable the formation of stabilising intermolecular interactions.

An energy scan calculation was performed on HL1 to determine whether the simulated geometry-optimised structure represents the lowest energy conformation. Additionally, these data were used to determine the energy difference between the X-ray structure and the lowest energy structure *in vacuo*. Figure 6.3.2 shows the energy of the system as a function of the N2-C8-C13-N3 torsion angle rotating by 15° per step, with a total of 24 steps.

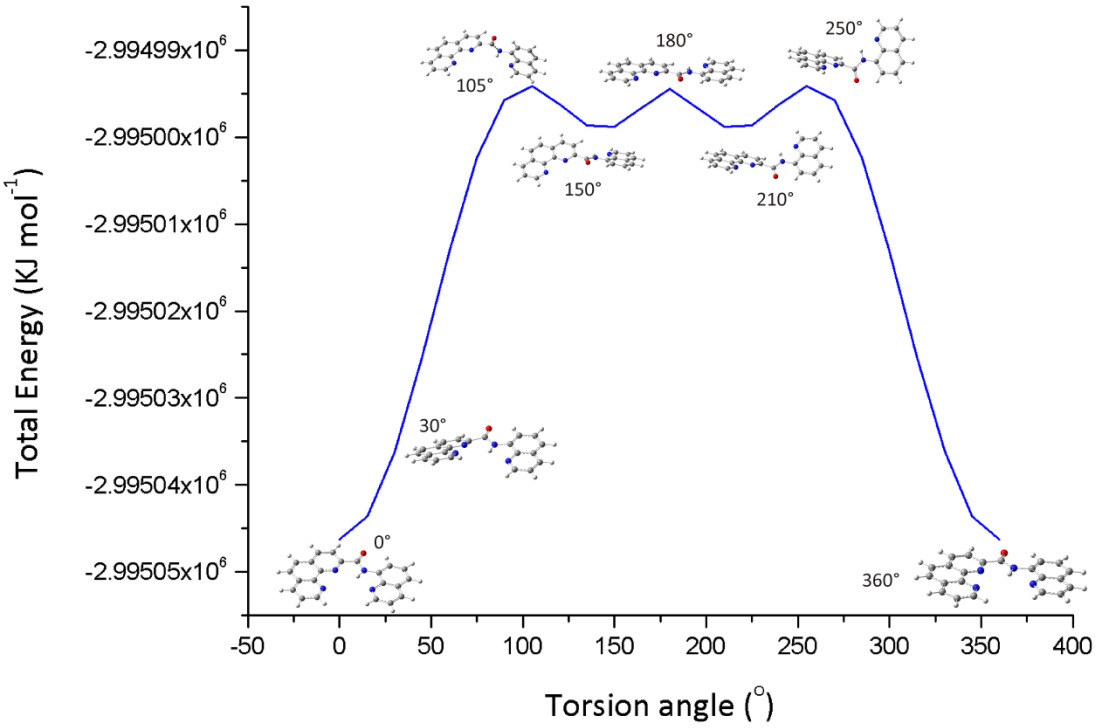

Figure 6.3.2: Total energy of HL1 versus torsion angle of N2-C8-C13-N3.

The calculated structure at 30° is an approximate representation of the X-ray structure of HL1, for which the equivalent torsion angle measures 29.7(3)°. The planar molecule is 10.12 kJ mol^{-1} lower in energy than that with a 30° torsion angle. It would seem that the energy gained by the more favourable packing of the non-planar molecule in the lattice is sufficient to offset the energy required for the out-of-plane rotation.

Ligand HL2 was not studied by X-ray diffraction. The simulated geometry-optimised structure of HL2, therefore, cannot be compared to any experimental data. The input structure of HL2 for the geometry optimisation was produced using GaussView 5.0.[14] The geometry-optimised structure (Figure 6.3.3) shows HL2 is not planar, exhibiting an out-of-plane rotation of the phenanthroline group relative to the picolylamine moiety. The torsion angle between the two planes is larger than the equivalent torsion angle in HL1.

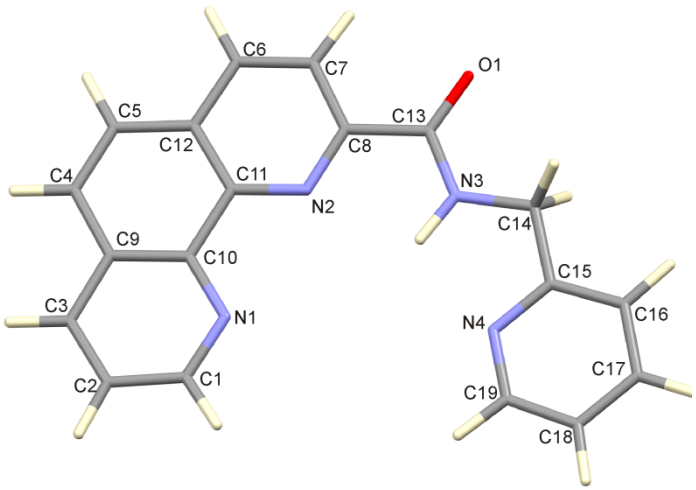

Figure 6.3.3: Fully labelled geometry-optimised structure of HL2 (B3LYP/6-311G level of theory).

Selected bond parameters of the geometry-optimised structures of HL1 and HL2 are summarised in Table 6.3.2.

Table 6.3.2: Comparison of the mean bond lengths and bond angles of the geometry-optimised structures of HL1 and HL2.

Structural Feature	Bond Length (Å)		Bond Angle (°)		Torsion Angle (°)
	C13-N3	C14-N3	C8-O1-C13	C13-C14-N3	C1-C8-C14-C19
HL1	1.396	1.425	33.65	27.21	0.24
HL2	1.347	1.443	32.12	28.35	2.54

A comparison of the bond lengths, bond angles and torsion angles of HL1 and HL2 show the structures are similar. The most notable difference is the torsion angle of HL2, which is larger than that of HL1. This is attributed to the less aromatic structure of HL2 being more susceptible to an out-of-plane rotation. The N3 and N4 nitrogen atoms are again in a *cis*-conformation. This allows for a stabilising intramolecular H-bond.

6.3.1.2 Vibrational Frequency Results

The vibrational frequency calculations were primarily performed to determine whether the geometry optimisation results represented the true minimum on the global potential energy surface. However, these data also assisted with the interpretation of the experimental IR spectra. Figure 6.3.4 shows an overlay of the experimental and calculated frequency spectra of HL1.

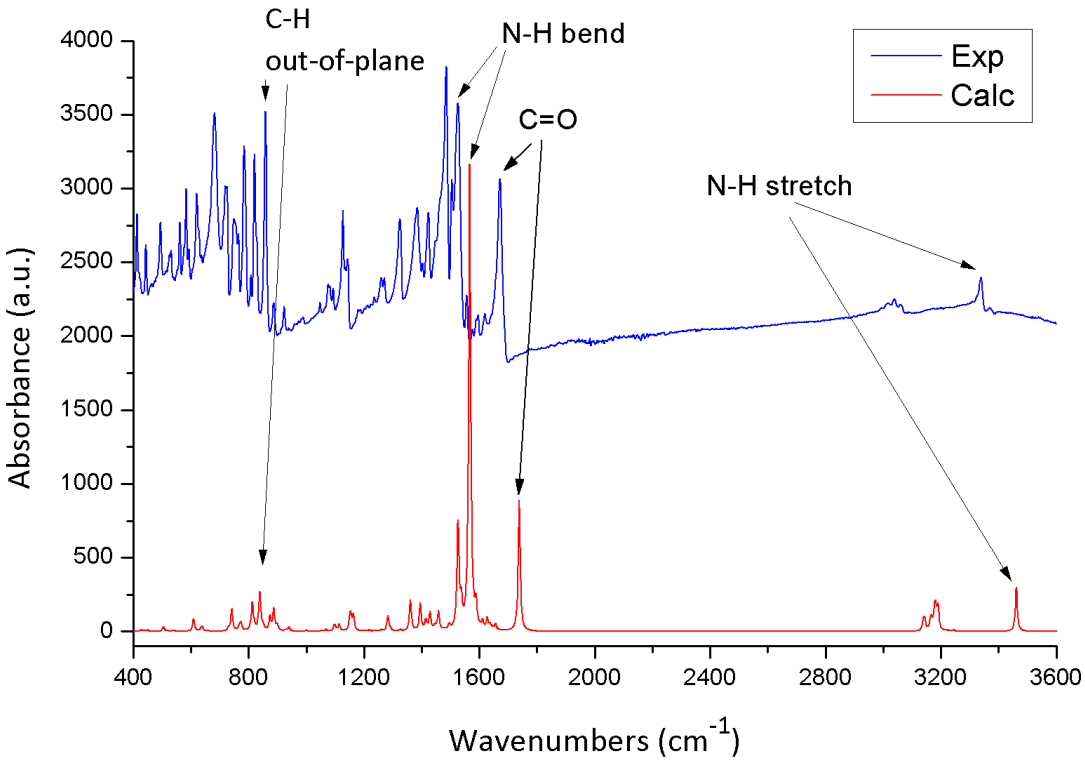

Figure 6.3.4: Overlay of DFT-calculated and experimental IR frequency data for HL1 with key peaks labeled.

The plot in Figure 6.3.4 shows that the simulated frequencies are consistently at higher energies than the experimental data. To determine whether the error in the simulated data was random or systematic, the frequencies of the experimental spectra were plotted against the calculated data, the plot is illustrated in Figure 6.3.5. The linear relationship between the data suggests that the error in the simulated data is systematic, and therefore a correction factor could be applied. The gradient of the slope gives a scaling factor which can be used to correct for the systematic errors in the simulated frequency data.

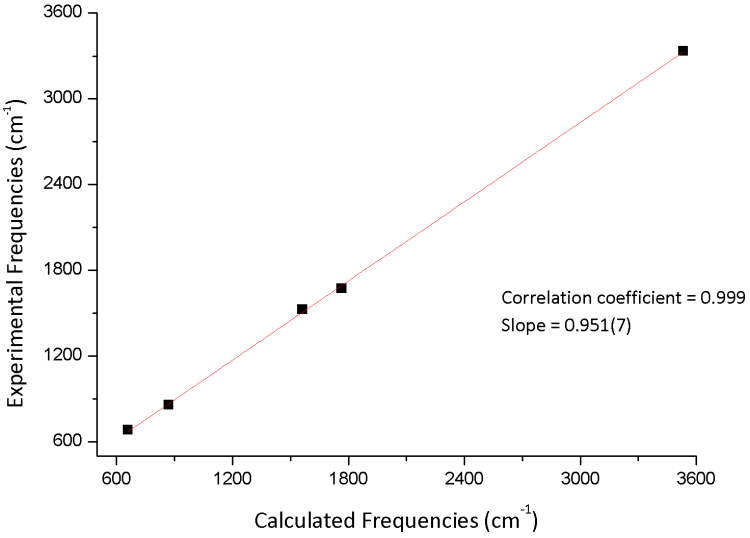

Figure 6.3.5: Plot of experimental versus calculated frequencies for HL1. The slope gives a scaling factor of 0.951(7).

Since the plot in Figure 6.3.5 passes through the origin and is linear, the scaling factor can be determined directly from the slope of the line. The scaling factor illustrates that, on average, the experimental IR frequencies are lower than the calculated IR frequencies by a factor of 0.951(7). The overlay of experimental and calculated frequency data and the plot of experimental versus calculated frequencies of HL2 are available in **Appendix C**. A comparison of select calculated and experimental frequencies for HL1 and HL2 are summarised in Table 6.3.3.

Table 6.3.3: Summary of the experimental and calculated vibrational frequencies of HL1 and HL2.

Vibrational Mode	N-H stretch (amide)	C=O	N-H bend (amide)	Phen* C-H wagging	Quino** C-H wagging
HL1					
Calculated (cm^{-1})	3461	1738	1566	887	661
Experimental (cm^{-1})	3334	1671	1525	858	681
Difference (%)	-3.8	-4.0	-2.7	-3.4	2.9
HL2					
Calculated (cm^{-1})	3537	1735	1546	888	767
Experimental (cm^{-1})	3401	1736	1519	873	772
Difference (%)	-4.0	0.1	-1.8	-1.7	0.6

* **Phenanthroline moiety,** ** **Quinoline moiety**

The percentage differences between the calculated and experimental frequencies are low, indicating the simulated data are relatively accurate. The data in Table 6.3.3 show that in general, the vibrational frequencies of the ligand HL2 were more accurately simulated than those of HL1.

6.3.1.3 NMR Data

The ^{1}H and ^{13}C NMR spectra of HL1 and HL2 were simulated using the GIAO method with the B3LYP density functional and 6-311G basis set. The reference used was TMS calculated at the same level of theory. A DMSO solvent model was used in the HL1, HL2 and TMS simulations. The solvent continuum model takes the solvent effects into account. This is done by placing the molecule of interest in a pocket with a dielectric constant equivalent to that of the selected solvent. This approach reduces computational time as it does not explicitly include solvent molecules in the simulations. The experimental and simulated ^{1}H NMR spectra of HL1 and HL2 were compared; these data are summarised in Table 6.3.4.

Table 6.3.4: Summary of selected experimental and calculated ^{1}H NMR chemical shifts for HL1 and HL2.

Proton	Exp. (ppm)	Cal. (ppm)	Difference (%)*	Proton	Exp. (ppm)	Cal. (ppm)	Difference (%)*
HL1				*HL2*			
N-H	12.63	10.49	16.9	N-H	11.26	7.88	30.0
C1-H	9.32	9.56	-2.6	C7-H	9.23	8.31	10.0
C21-H	9.13	9.22	-1.0	C19-H	8.62	8.89	-3.1
C4,5-H	8.16	8.42	-3.2	C1-H	8.92	9.53	-6.8
C7-H	8.58	8.47	1.3	C4,5-H	8.43	8.35	0.9
C15-H	8.98	9.51	-5.9	C16-H	7.53	7.76	-3.1
				C14-H	4.97	4.89	1.6
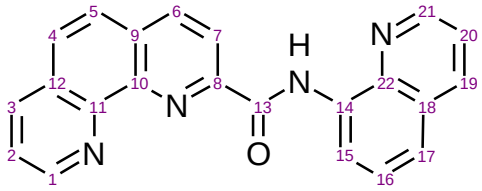				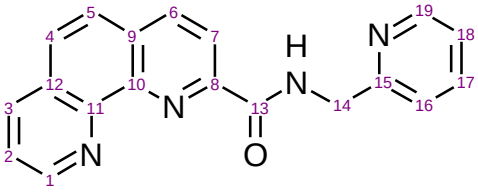			

* **Percentage difference =** $\frac{(Exp-Calc)}{Exp} \times 100\ \%$

The calculated ^{1}H NMR chemical shifts are in good agreement with the experimental chemical shifts, with the exception of the amide proton. This is most likely due to the fact that the simulations do not take into account intermolecular interactions, such as hydrogen bonding, with neighbouring ligand molecules which are likely in a solution-state NMR experiment. These intermolecular interactions can have a significant impact on chemical shifts.

The differences between the spectra are inconsistent with the simulated chemical shifts being both upfield and downfield of the experimental data. The correlation between the calculated and experimental chemical shifts of HL1 differs from those of HL2. The most notable difference is with the amide N-H chemical shift, for which there is a 30% error, indicating that the experimental data is heavily influenced by intermolecular interactions. This trend is also noted in the ^{13}C NMR chemical shifts of both HL1 and HL2, but the errors in the calculated ^{13}C NMR chemical shifts (of HL1) are more consistent than those of the ^{1}H NMR chemical shift. The simulated ^{13}C NMR chemical shifts are further upfield than the experimental data in all cases. The calculated and experimental ^{13}C NMR chemical shifts are summarised in Table 6.3.5.

Table 6.3.5: Summary of calculated and experimental ^{13}C NMR chemical shifts of HL1 and HL2.

Carbon	Exp. (ppm)	Cal. (ppm)	Difference (%)*	Carbon	Exp. (ppm)	Cal. (ppm)	Difference (%)*
HL1				*HL2*			
21	149.5	152.5	-2.0	13	170.66	165.14	3.2
14	134.5	140.8	-4.7	15	158.87	136.49	14.1
13	162.9	168.3	-3.3	8	158.29	163.64	-3.4
8	151.2	157.6	-4.2	1	154.21	139.07	9.8
1	149.8	154.4	-3.1	19	152.73	148.61	2.7
5	126.8	131.1	-3.4	10	150.35	153.07	-1.8
10	144.6	150.7	-4.2	14	46.32	41.72	9.9

* **Percentage difference =** $\frac{(Exp-Calc)}{Exp} \times 100\ \%$

The errors in the simulated ^{13}C NMR spectrum of HL2 are more random than those of HL1 with the isotropic shielding tensors being both over and underestimated. The chemical shift of C13, for example, has been under-estimated for HL2 while the chemical shift for the equivalent carbon in HL1 was over-estimated with a similar percentage error.

The 6-311G basis set used for both HL1, and HL2 has simulated the NMR chemical shifts with reasonable accuracy, particularly for those atoms which are not involved in intermolecular interactions.

6.3.2 DFT Results of the Amide-based Metal Chelates

6.3.2.1. Geometry Optimisation Results

High resolution experimental (X-ray) structures of $[Cu(L1)]^+$ and $[Ni(L1)]^+$ could not be elucidated (refer to Section 5.4). The bulk of the metal chelates: $[Pd(L1)]^+$, $[Cu(L2)]^+$, $[Ni(L2)]^+$ and $[Pd(L2)]^+$, did not produce crystals suitable for X-ray diffraction experiments. The geometry-optimised structures of the metal chelates, therefore, cannot be compared to any experimental structures. The atomic coordinates of the metal chelates for the geometry optimisation calculations were prepared using GaussView 5.0.[14] The geometry-optimised structures of all the metal chelates are shown in Figure 6.3.6 and show that the chelates are planar: ideal for DNA intercalation, and the same geometry noted in the low-resolution structures.

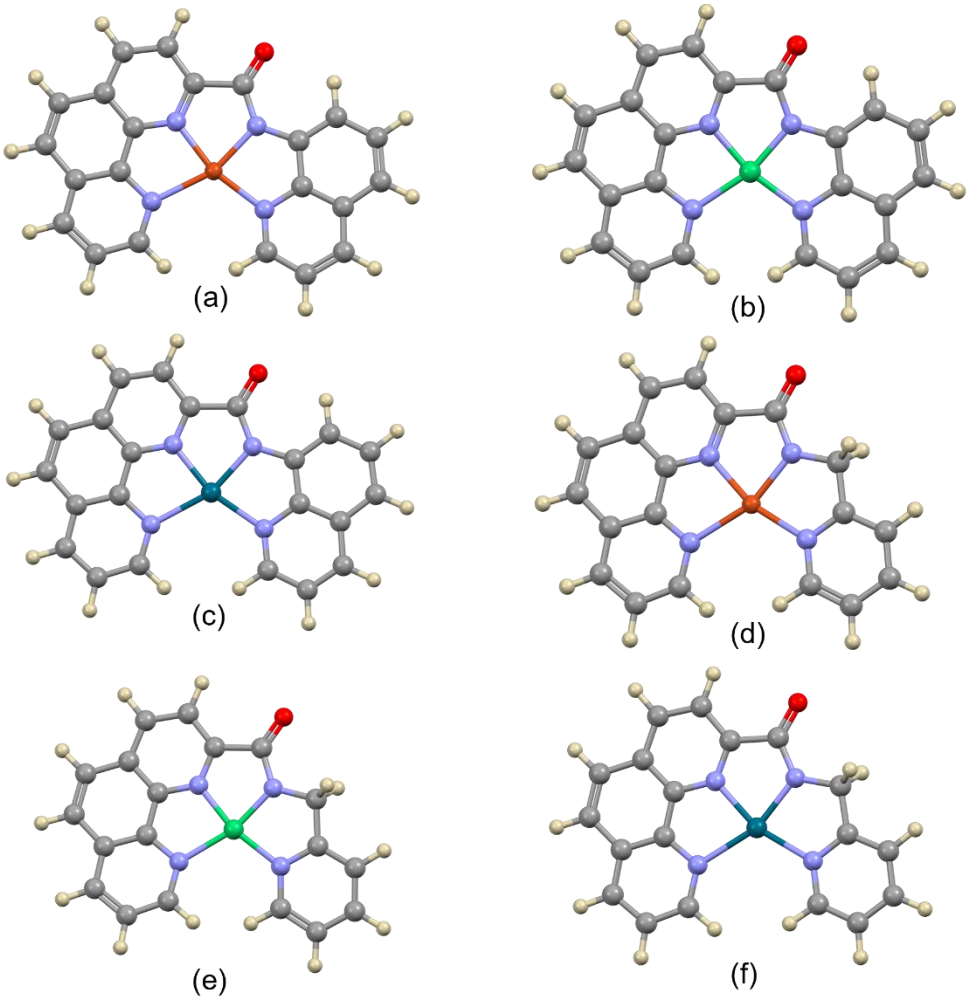

Figure 6.3.6: Geometry-optimised structures of (a) $[Cu(L1)]^+$, (b) $[Ni(L1)]^+$, (c) $[Pd(L1)]^+$, (d) $[Cu(L2)]^+$, (e) $[Ni(L2)]^+$ and (f) $[Pd(L2)]^+$.

The bond parameters describing the coordination sphere of the divalent metal ions in the geometry-optimised structures of the six metal chelates are summarised in Table 6.3.6.

Table 6.3.6: Summary of bond lengths and bond angles of the geometry-optimised structures of the amide-based metal chelates.

Structural Feature	M^{2+}	$[Cu(L1)]^+$	$[Ni(L1)]^+$	$[Pd(L1)]^+$	$[Cu(L2)]^+$	$[Ni(L2)]^+$	$[Pd(L2)]^+$
Bond Length (Å)	N1 - M^{2+}	2.148	2.036	2.19	2.154	2.035	2.201
	N2 - M^{2+}	1.934	1.841	1.969	1.936	1.84	1.973
	N3 - M^{2+}	1.948	1.858	1.985	1.922	1.833	1.966
	N4 - M^{2+}	1.977	1.927	2.069	1.988	1.923	2.075
Bond Angle (°)	N1 - M^{2+} - N2	79.74	82.6	79.52	79.57	82.63	79.28
	N3 - M^{2+} - N4	84.11	85.27	82.64	83.46	84.68	82.12
	N1 - M^{2+} - N4	116.06	110.37	117.26	116.75	111.02	118.16
	N2 - M^{2+} - N3	80.09	81.77	80.57	80.21	81.83	80.44

The bond angles for both $[Cu(L1)]^+$ and $[Cu(L2)]^+$ are within the range reported for N-Cu-N bond angles of ± 80°, with the exception of the N1-Cu1-N4 bond angle.[10] This suggests that the geometry-optimised structures are good representations of the structures of the copper(II) chelates. The N1-M-N4 bond angle is significantly more obtuse than the other bond angles defining the coordination sphere. This is attributed to the relatively short, two-carbon bridge between N2 and N3. This leads to a scissoring effect, forcing the N1 and N4 atoms further apart, resulting in an increase in the N1-M-N4 bond angle, and decrease in the N2-M-N3 bond angle. This is a consequence of the ligand geometry and is independent of the identity of the metal ion. The bond angles are therefore similar, irrespective of the metal ion present. The N1-M bond lengths are longer than the N3-M bond lengths due to N3 carrying a formal negative charge resulting in a stronger dative covalent bond and, therefore, shorter bond length. The bond lengths for both $[Ni(L1)]^+$ and $[Ni(L2)]^+$ are consistently shorter than the copper(II) analogues, as the nickel(II) ion is larger than the copper(II) ion. The bond angles of the nickel(II) chelates are greater than the copper(II) chelates, with the exception of the N1-M-N4 bond angle. The N2-M-N3 bond angle is similar in all six metal chelates due to the fixed bite angle of L1 and L2.

The bond lengths for the palladium(II) chelates are longer than both the copper(II) and nickel(II) chelates, due to the size of the palladium(II) ion.[15] This variation in bond length is consistent with comparable bond lengths in previously reported X-ray structures of copper(II), nickel(II) and palladium(II) when they are chelated to the same ligand. A bis(pyrrolide-imine) ligand bonded to these three metal ions is used to illustrate this trend. The data is summarised in Table 6.3.7.

Table 6.3.7: Average bond lengths (Å) of metal to pyrrole and imine nitrogen atoms.

Metal Chelate	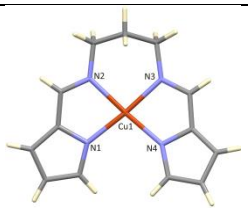 16	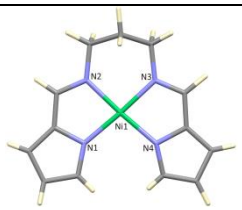 17	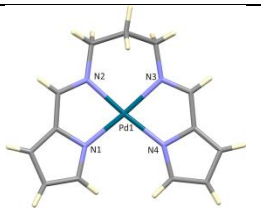 18
M – N (pyrrole)	1.948 Å	1.878 Å	2.007 Å
M – N (imine)	1.980 Å	1.890 Å	2.013 Å

The data in Table 6.3.7 shows the nickel(II) chelate has the shortest bond lengths and the palladium(II) chelate has the longest bond lengths of the three structures. This is consistent with the trend observed in this work, again suggesting that the results of the simulations are reliable.

6.3.2.2 Vibrational Frequency Results

As with the ligands, the vibrational frequencies were simulated primarily to determine whether the geometry-optimised structures represent the global minimum on the potential energy surface. The calculated frequencies were also compared to the experimental data using a superposition plot, as illustrated in Figure 6.3.7 for $[Ni(L1)]^+$. The superposition of the calculated and experimental data shows that there is a moderate correlation between the data, although the simulated data are consistently predicted to be of higher energy than the experimental data. To determine whether the error in the simulated data is systematic, the experimental versus calculated data were plotted. If the plot yields a straight line, the gradient of the slope will give a scaling factor which can be used to correct for the systematic errors in the simulated frequencies. Figure 6.3.8 shows the linear relationship between the experimental and calculated data of $[Ni(L1)]^+$, similar plots for the bulk of the metal chelates are available in **Appendix C**.

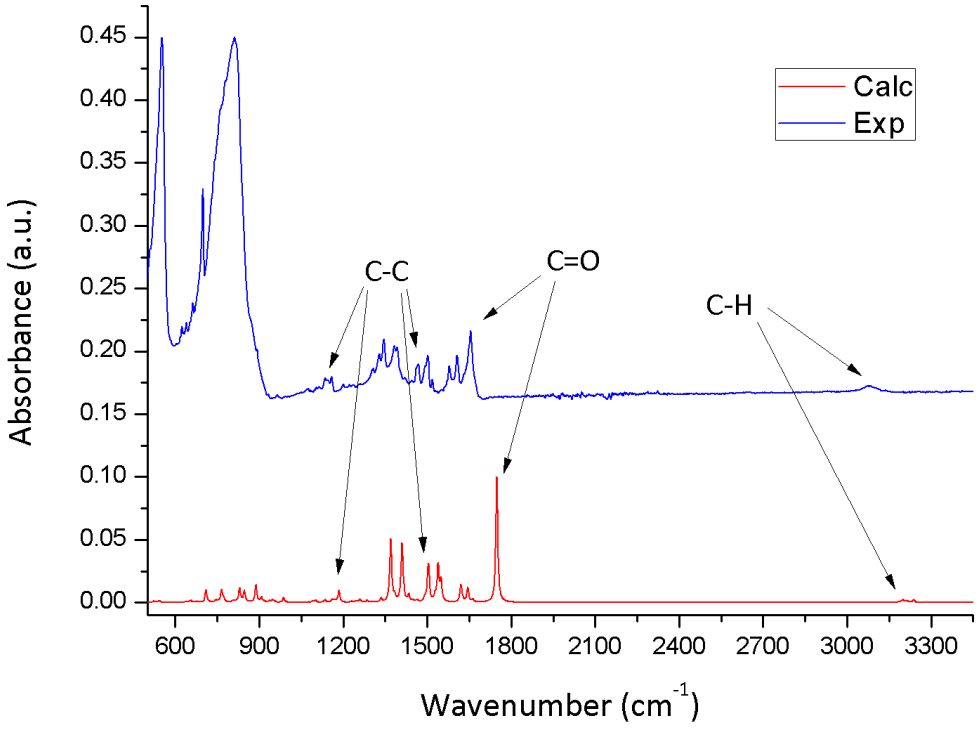

Figure 6.3.7: Overlay of the calculated and experimental vibrational frequencies of $[Ni(L1)]^+$.

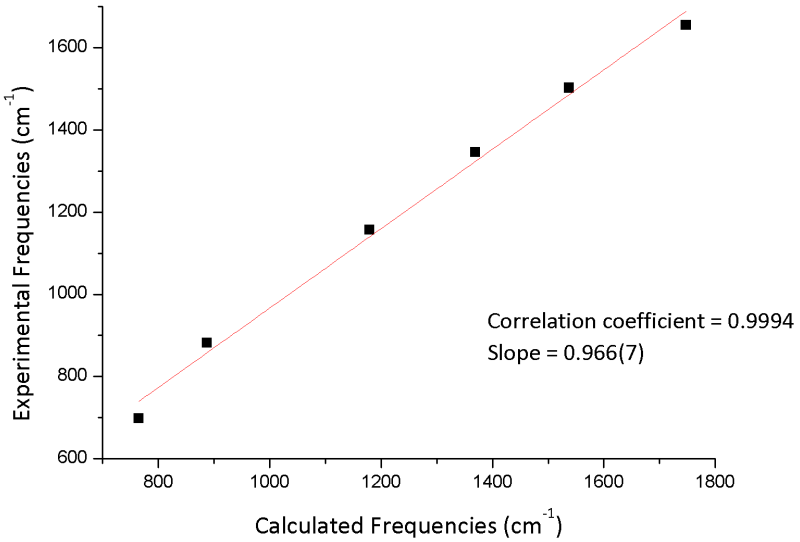

Figure 6.3.8: Plot of experimental versus calculated frequencies for $[Ni(L1)]^+$. The slope gives a scaling factor of 0.966(7).

Figure 6.3.7 shows a large peak present in the experimental spectrum of $[Ni(L1)]^+$ which is due to the P-F stretch of the hexafluorophosphate(V) counter ion. The simulations excluded the anions which is why peak is absent in the simulated spectrum.

The scaling factor for $[Ni(L1)]^+$ is 0.966(7), equal to the slope of the line since it passes through the origin, indicating the experimental vibrational frequencies are lower in energy, on average, than the calculated vibrational frequencies by a factor of 0.966(7).

The scaling factor for $[Ni(L2)]^+$ was found to be 0.954(5) indicating the experimental vibrational frequencies are smaller than the calculated frequencies, similar to $[Ni(L1)]^+$. Figure 6.3.9 shows the experimental and calculated IR spectra of $[Ni(L2)]^+$.

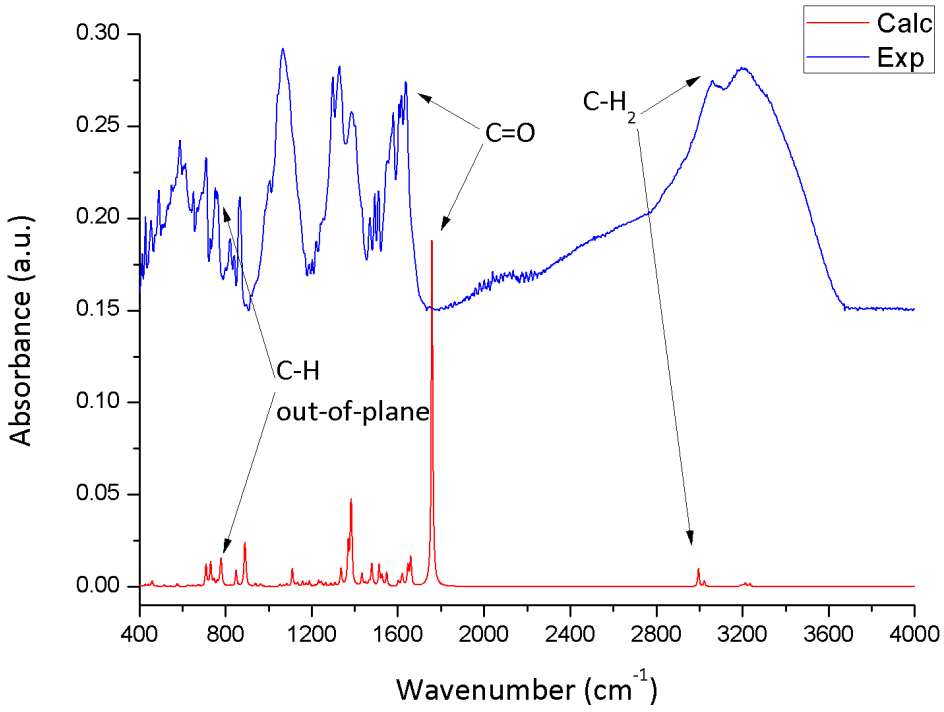

Figure 6.3.9: Overlay of the calculated and experimental vibrational frequencies of $[Ni(L2)]^+$.

A summary of selected calculated and experimental vibrational frequencies for all six metal chelates is available in Table 6.3.8.

Table 6.3.8: Summary of calculated and experimental vibrational frequencies for all the amide-based metal chelates.

Vibrational Mode	Cal. (cm^{-1})	Exp. (cm^{-1})	Diff. (%)	Vibrational Mode	Cal. (cm^{-1})	Exp. (cm^{-1})	Diff. (%)
$[Cu(L1)]^+$				**$[Cu(L2)]^+$**			
C-H	3197	3339	4.3	C-H	3214	3367	4.5
C=O	1733	1671	-3.7	$C-H_2$	2988	3045	1.9
C-C (Quino**)	1498	1484	-0.9	C=O	1747	1633	-7.0
C-C (Phen*)	1183	1127	-5.0	Phen* C-H wagging	895	881	-1.5
Phen* C-H wagging	854	856	0.3	Pyridyl*** C-H wagging	734	728	-0.9
Quino** C-H wagging	777	763	-1.9				
$[Ni(L1)]^+$				**$[Ni(L2)]^+$**			
C-H	3236	3650	11.4	C-H	3213	3196	-0.5
C=O	1748	1655	-5.6	$C-H_2$	2995	3060	2.1
C-C (Quino**)	1538	1502	-2.4	C=O	1759	1637	-7.4
C-C (Phen*)	1159	1157	-0.1	Phen* C-H wagging	889	867	-2.6
Phen* C-H wagging	888	811	-9.5	Pyridyl *** C-H wagging	731	711	-2.8
Quino** C-H wagging	765	698	-9.7				
$[Pd(L1)]^+$				**$[Pd(L2)]^+$**			
C-H	3235	3404	5.0	C-H	3234	3419	5.4
C=O	1622	1649	1.6	$C-H_2$	3025	3227	6.3
C-C (Quino**)	1502	1509	0.4	C=O	1633	1674	2.5
C-C (Phen*)	1137	1142	0.4	Phen* C-H wagging	920	935	1.6
Phen* C-H wagging	920	939	2.0	Pyridyl *** C-H wagging	800	808	1.0
Quino** C-H wagging	807	826	2.3				

* = Phenanthroline moiety, ** = Quinoline moiety, *** = Pyridyl moiety.

The simulated stretching and bending frequencies for the copper(II) and nickel(II) chelates are mostly higher in energy than the experimental data. In contrast, the simulated frequencies for the palladium(II) chelates are consistently lower in energy than the experimental data. Despite these differences, the accuracy (as determined by the percentage errors) of the calculations using both the 6-311G and LanL2DZ basis sets was satisfactory.

6.3.2.3 NMR Data

The ^1H and ^{13}C NMR spectra of $[Pd(L1)]^+$ and $[Pd(L2)]^+$ were calculated using the GIAO method with the B3LYP density functional and the LanL2DZ basis set. The reference used was TMS calculated at the same level of theory. A DMSO solvent model was included in the simulations.

The experimental and calculated ^{1}H NMR data were compared, a summary is shown in Table 6.3.9 for $[Pd(L1)]^{+}$ and $[Pd(L2)]^{+}$.

Table 6.3.9: Summary of the experimental and calculated chemical shifts for the ^{1}H NMR spectra of $[Pd(L1)]^{+}$ and $[Pd(L2)]^{+}$.

Proton	Exp. (ppm)	Cal. (ppm)	Difference (%)*	Proton	Exp. (ppm)	Cal. (ppm)	Difference (%)*
$[Pd(L1)]^{+}$				$[Pd(L2)]^{+}$			
C1-H	9.34	9.71	-4.0	C6-H	9.40	8.40	10.6
C21-H	9.12	9.41	-3.2	C7-H	9.21	7.84	14.9
C15-H	8.92	9.49	-6.4	C1-H	8.89	8.72	1.9
C6-H	8.84	9.30	-5.2	C19-H	8.61	8.33	3.3
C7-H	8.76	8.89	-1.5	C2-H	8.56	8.19	4.3
C4,5-H	8.20	8.96	-9.3	C14-H	4.85	4.60	5.2

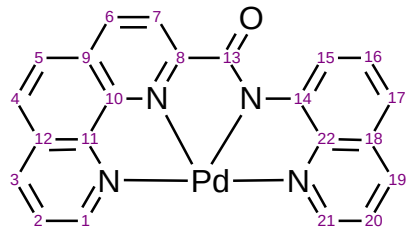

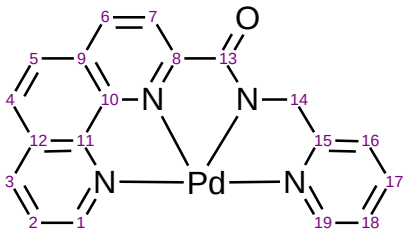

* Percentage difference = $\frac{(Exp-Calc)}{Exp} \times 100\ \%$

There is a moderate agreement between the calculated and experimental chemical shifts for the palladium(II) chelates. This is despite the LanL2DZ basis set using effective core potentials. By using ECPs the shielding effect of the palladium(II) ion is not always accurately predicted, potentially reducing the accuracy of the results. The calculated chemical shifts are all deshielded relative to the experimental data for $[Pd(L1)]^{+}$. An unusual result is that although the chemical shifts for $[Pd(L1)]^{+}$ have all been predicted at a deshielded chemical shift, the calculated ^{1}H chemical shifts of $[Pd(L2)]^{+}$ are all shielded relative to the experimental data. The low percentage error again shows the data were accurately predicted.

The simulated ^{13}C NMR chemical shifts were marginally less accurately predicted than the ^{1}H chemical shifts for both palladium(II) chelates. The calculated ^{13}C NMR chemical shifts are deshielded relative to the experimental data, similar to the ^{1}H chemical shifts. The data suggest that the LanL2DZ basis set is underestimating the shielding tensor of the carbon atoms, resulting in a downfield shift relative to the experimental data. A summary of selected chemical shifts is shown in Table 6.3.10.

Table 6.3.10: Summary of calculated and experimental ^{13}C NMR chemical shifts of $[Pd(L1)]^+$ and $[Pd(L2)]^+$.

Carbon	Exp. (ppm)	Cal. (ppm)	Difference (%)*	Carbon	Exp. (ppm)	Cal. (ppm)	Difference (%)*
$[Pd(L1)]^+$				$[Pd(L2)]^+$			
C13	167.7	179.47	-7.0	C13	172.4	180.44	-4.7
C8	152.9	158.35	-3.6	C8	166.6	157.32	5.6
C1	149.2	157.61	-5.6	C1	140.0	157.11	-12.2
C21	148.7	155.29	-4.4	C19	148.6	155.76	-4.8
C14	129.7	149.20	-15.0	C10	153.1	148.88	2.8
C10	144.5	148.85	-3.0	C14	52.1	63.37	-21.6

* Percentage difference = $\frac{(Exp-Calc)}{Exp} \times 100\ \%$

Similar to HL1 and HL2, the errors in the simulated ^{13}C NMR spectrum of $[Pd(L2)]^+$ are more random than those of $[Pd(L1)]^+$ with the isotropic shielding tensors being both over and underestimated. The LanL2DZ basis set used for both palladium(II) chelates has simulated the NMR chemical shifts with less accuracy compared to the 6-311G basis set. This is likely a consequence of the use of ECPs.

6.3.2.4 Electronic Spectra Results

The electronic spectra of the metal chelates, as with the ligands, were simulated to obtain a deeper understanding of the molecular orbitals involved in the experimental transitions. The data were simulated using the TD-DFT method, solving for 30 excited states, at the same level of theory used for the previous simulations. A DMSO solvent model was included in the simulations to take into account solvent effects.

The calculated absorption spectra matched the profiles of the experimental spectra for the nickel(II) and palladium(II) chelates. The electronic absorption spectra of the paramagnetic copper(II) chelates were less accurately predicted. Figure 6.3.10 shows overlays of the calculated and experimental spectra for the L1 metal chelates.

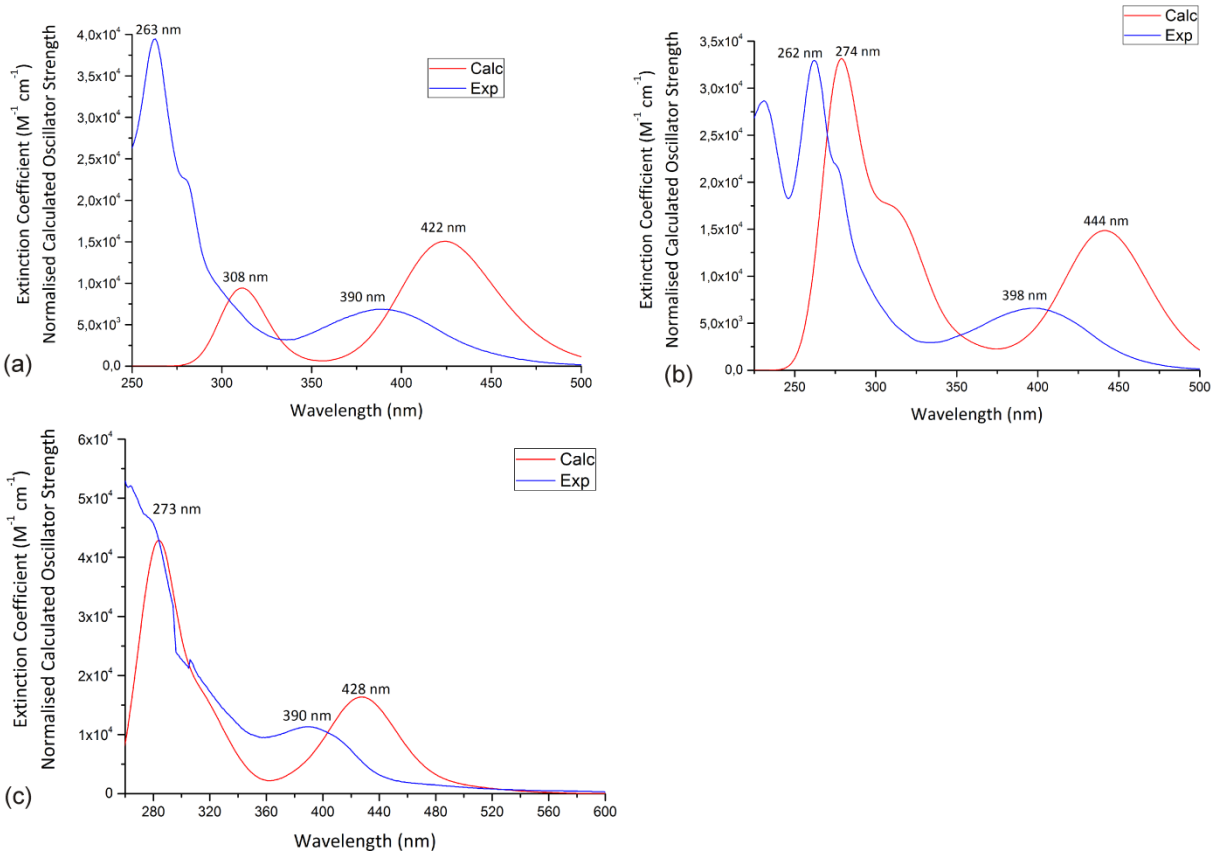

Figure 6.3.10: Overlay of the calculated and experimental absorption spectra of (a) $[Cu(L1)]^+$, (b) $[Ni(L1)]^+$ and (c) $[Pd(L1)]^+$. The superposition plots show that the simulated data is red-shift relative to the experimental data. The calculated spectra have been normalised.

The $[Cu(L1)]^+$ overlay shows that the profile of the experimental spectrum is similar in some respects to the calculated spectrum. The oscillator strengths of the peaks in the UV region have, however, been underestimated and the extinction coefficient of the peaks in the visible region have been overestimated. The $[Ni(L1)]^+$ and $[Pd(L1)]^+$ spectra are in better agreement; both spectra were simulated with reasonable accuracy. The fine details of the experimental spectra, such as the shoulder of the peak at 262 nm for the nickel(II) chelate, have been predicted. Though in both cases the simulated spectra are red-shifted relative to the experimental data. This similarity suggests that the data regarding the orbital transitions are likely to be reliable. The same trends are noted with the L2 metal chelates, and is likely due to the copper(II) chelates being paramagnetic, which seemingly complicates prediction of the electronic transitions.

The calculated spectra generally show a bathochromic shift relative to the experimental data, with the exception of $[Ni(L2)]^+$ for which the calculated spectrum shows a hypsochrmic shift. Table 6.3.11 presents a summary of the main calculated transitions for the metal chelates, and Figure 6.3.11 shows the molecular orbitals of $[Cu(L1)]^+$ that are involved in the electronic transitions.

Table 6.3.11: Selected experimental and calculated electronic transitions for the metal chelates.

Wavelength/nm		Oscillator strength, *f*	Molecular Orbitals	Assignment
Exp	**Calc**			
[Cu(L1)]				
263	308	0.0659	105 → 109	π(quino) → π*(phen, quino)
			103 → 107	π(phen) → π*(phen, quino)
			101 → 106	π(phen) → π*(phen, quino)
390	422	0.1699	105 → 107	π(quino) → π*(phen, quino)
[Ni(L1)]				
262	274	0.2112	97 → 106	Ni[dxz]L π→ π*(phen, quino)
			101 → 109	π(phen, quino) → π*(phen, quino)
398	444	0.1440	104 → 106	π(quino) → π*(phen, quino)
			95 → 108	Ni[dx^2-y^2]→ Ni[dxy]Lσ*
[Pd(L1)]				
279	273	0.1241	93 → 101	π(phen, quino) → π*(phen, quino)
			96 → 102	π(phen, quino) → π*(phen, quino)
390	428	0.2178	99 → 101	π(quino) → π*(phen, quino)
[Cu(L2)]				
276	298	0.0284	95 → 99	π(phen, pico) → π*(phen, pico)
[Ni(L2)]				
277	274	0.2417	90 → 97	π(phen, pico) → π*(phen)
			93 → 99	π(phen, pico) → Ni[dxy]Lσ*
[Pd(L2)]				
270	267	0.1602	85 → 92	π(phen, pico) → π*(phen)
			84 → 92	π(phen, pico) → π*(phen)

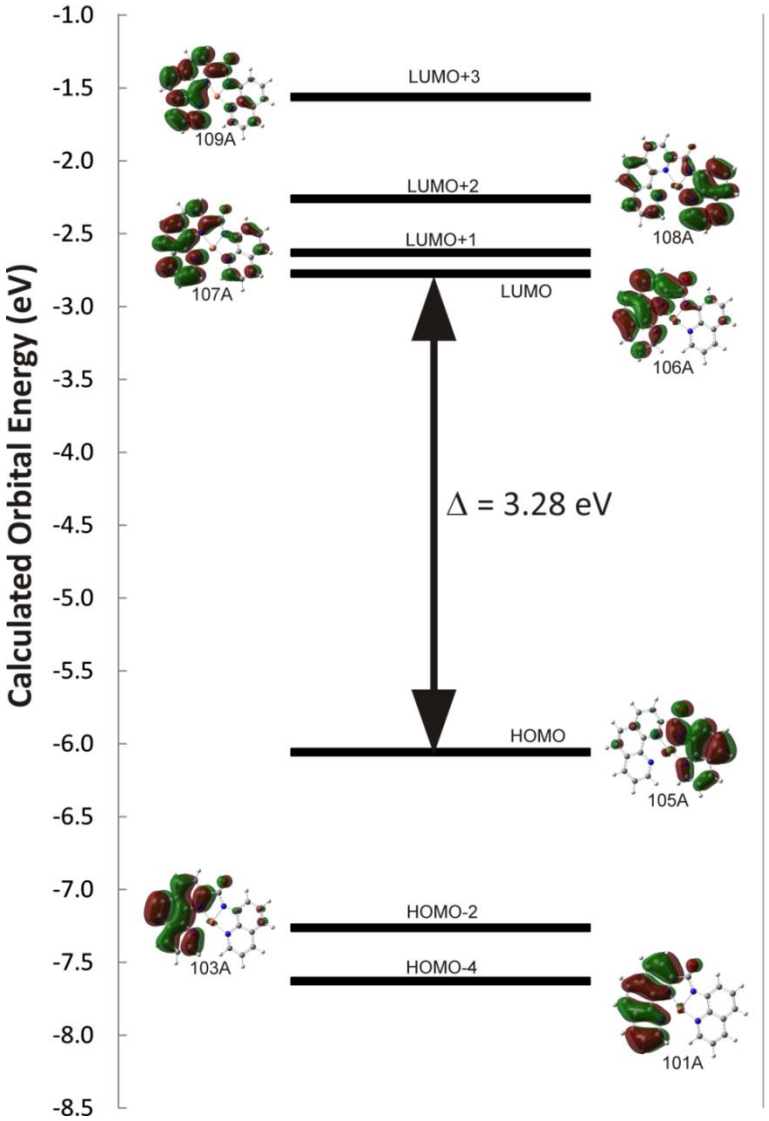

Figure 6.3.11: Molecular orbital diagram of $[Cu(L1)]^+$ showing the relative energies of the orbitals. The energy gap between the HOMO and the LUMO is 3.28 eV.

Figure 6.3.12 shows an energy plot of the six metal chelates with the energy gap between the HOMO and LUMOs of each of the metal chelates.

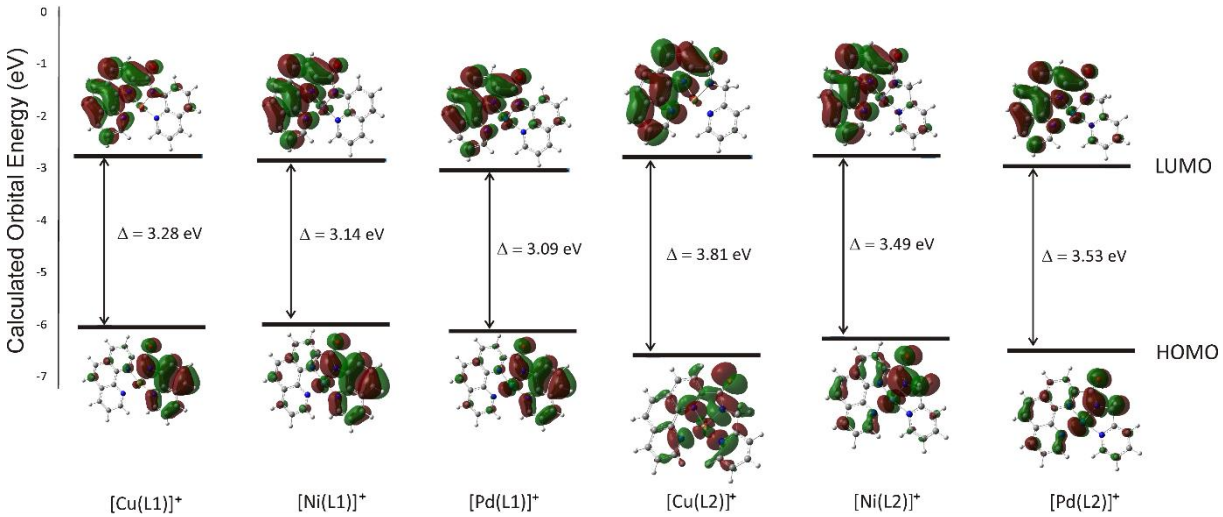

Figure 6.3.12: Energy gaps between the HOMOs and LUMOs of the amide-based metal chelates.

Figure 6.3.12 shows the L1 metal chelates have smaller HOMO-LUMO energy gaps compared to the L2 metal chelates. This is due to the L1 structure having an extended aromatic region over the quinoline moiety. The energy gap of both the copper(II) chelates is larger than that of both the nickel(II) and palladium(II) chelates.

6.3.3 DFT Results for the Imine-based Chelates

6.3.3.1 Geometry Optimisation Results

The X-ray coordinates for [Cu(L4)(NO_3)] and [Cu(L7)](NO_3) were used as the input structures for the geometry optimisation calculations. Outer-sphere anions and solvent molecules were removed before the geometries were optimised. The resulting geometric parameters from these calculations were compared with the experimental results, i.e. the crystal structures. The differences between the geometric parameters are summarisied below in Table 6.3.12.

Table 6.3.12: Summary of the DFT-calculated and experimental geometric parameters for [Cu(L4)(NO$_3$)] and [Cu(L7)]$^+$.

	[Cu(L4)(NO$_3$)]			[Cu(L7)]$^+$		
Structural Features	**Calculated**	**Experimental**	**Difference* (%)**	**Calculated**	**Experimental**	**Difference* (%)**
Bond Lengths (Å)						
N1-Cu1	2.116	2.096(2)	-0.95	2.093	2.070(2)	-1.11
N3-Cu1	1.972	1.974(2)	0.10	1.946	1.955(2)	0.46
O1-Cu1	1.882	1.910(2)	1.47	1.850	1.858(2)	0.43
N3-C10	1.288	1.293(3)	0.39	1.303	1.282(3)	-1.64
Bond Angles (°)						
C15-O1-Cu1	125.68	123.1(2)	-2.10	125.28	123.7(1)	-1.28
O1-Cu1-N1	101.79	102.61(8)	0.80	100.70	100.56(7)	-0.14
O1-Cu1-N3	96.04	95.78(8)	-0.27	97.40	96.98(8)	-0.43
Moiety Plane Angles (°)						
Phen-Phenol	6.59	6.89	4.35	0.05	7.85	99.36

*Percentage difference = $\frac{(Exp-Calc)}{Exp} \times 100\ \%$

The geometric parameters in Table 6.3.12 highlight the similarity of the experimental and simulated structures. This similarity suggests that the level of theory used was appropriate, and that the bulk of the simulations are, therefore, likely to be reliable. The biggest percentage difference between the two structures is -2.10% for the C15-O1-Cu1 bond angle of [Cu(L4)(NO$_3$)]. The key difference between the simulated and experimental structures is the planarity. The lowest energy geometry-optimised structure is planar *in vacuo*, as shown by the angle subtended by the six and 14-atom mean planes of the phenol and phenanthroline moieties. These angles measure 6.59° and 0.05° in [Cu(L4)(NO$_3$)] and [Cu(L7)]$^+$, respectively, compared to 6.89° and 7.85° in the experimental structures. Figure 6.3.13 shows the crystal structures overlaid with the calculated structures for [Cu(L4)(NO$_3$)] and [Cu(L7)]$^+$.

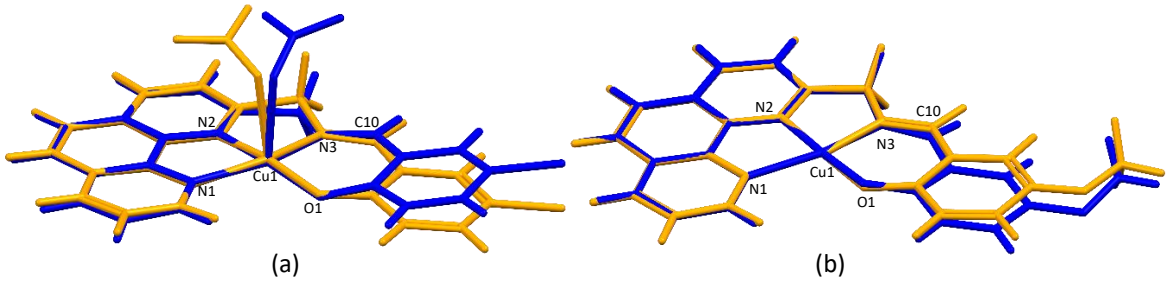

Figure 6.3.13: Partially labelled least-squares-fit of the DFT-calculated (orange) and experimental (blue) structures of (a) [Cu(L4)(NO$_3$)] and (b) [Cu(L7)]$^+$.

The overlays show the phenol moiety of each crystal structure is out-of-plane with respect to the phenanthroline moiety. The root-mean-square deviation (RMSD) of 0.0558 Å for [Cu(L4)(NO$_3$)] and 0.0220 Å for [Cu(L7)]$^+$ highlights the similarity of the geometry-optimised and experimental structures. The energy differences between the simulated and experimental

structures are 22.89 kJ mol^{-1} and 10.57 kJ mol^{-1}, respectively. This deviation from the lowest energy conformation is likely to allow for more efficient packing in the solid state. Favourable interactions in the lattice would be sufficient to offset this modest energy difference

X-ray data was only available for $[Cu(L4)(NO_3)]$ and $[Cu(L7)]^+$. The geometry-optimised structures for the remaining chelates were calculated at the same level of theory as that used above. Given the similarity of the experimental and simulated structures, as highlighted above, it is likely that the geometry optimisation results are realistic depictions of these molecules in the solid state. The geometric parameters of these chelates are summarised in Table 6.3.13.

Table 6.3.13: Summary of selected bond lengths and bond angles of the geometry-optimised structures of the metal chelates $[Cu(L3)]^+$ to $[Cu(L10)]^+$.

Structural Feature	$[Cu(L3)]^+$	$[Cu(L4)(NO_3)]$	$[Cu(L5)]^+$	$[Cu(L6)]^+$
Bond Length (Å)				
N1-Cu1	2.090	2.116	2.089	2.093
N3-Cu1	1.949	1.972	1.951	1.948
O1-Cu1	1.851	1.882	1.853	1.851
N3-C10	1.300	1.288	1.299	1.302
Bond Angle (°)				
C15-O1-Cu1	125.57	125.68	125.54	125.31
O1-Cu1-N1	100.63	101.79	100.69	100.6
O1-Cu1-N3	97.47	96.04	97.32	97.53
	$[Cu(L7)]^+$	**$[Cu(L8)]^+$**	**$[Cu(L9)]^+$**	**$[Cu(L10)]^+$**
Bond Length (Å)				
N1-Cu1	2.093	2.097	2.094	2.083
N3-Cu1	1.946	1.934	1.947	1.955
O1-Cu1	1.850	1.852	1.850	1.859
N3-C10	1.303	1.308	1.302	1.296
Bond Angle (°)				
C15-O1-Cu1	125.28	126.73	125.19	125.94
O1-Cu1-N1	100.70	101.78	100.57	100.77
O1-Cu1-N3	97.40	95.91	97.57	97.07

The bond lengths and bond angles summarised in Table 6.3.13 are comparable to the experimental data of $[Cu(L4)(NO_3)]$ and $[Cu(L7)]^+$, suggesting that the calculated structures for the remaining imine-based chelates are reliable representations of the molecules. This is expected since the metal ion is square planar and the ligands have relatively few degrees of freedom. The geometry-optimised structures for remaining imine-based copper(II) chelates are shown in Figure 6.3.14.

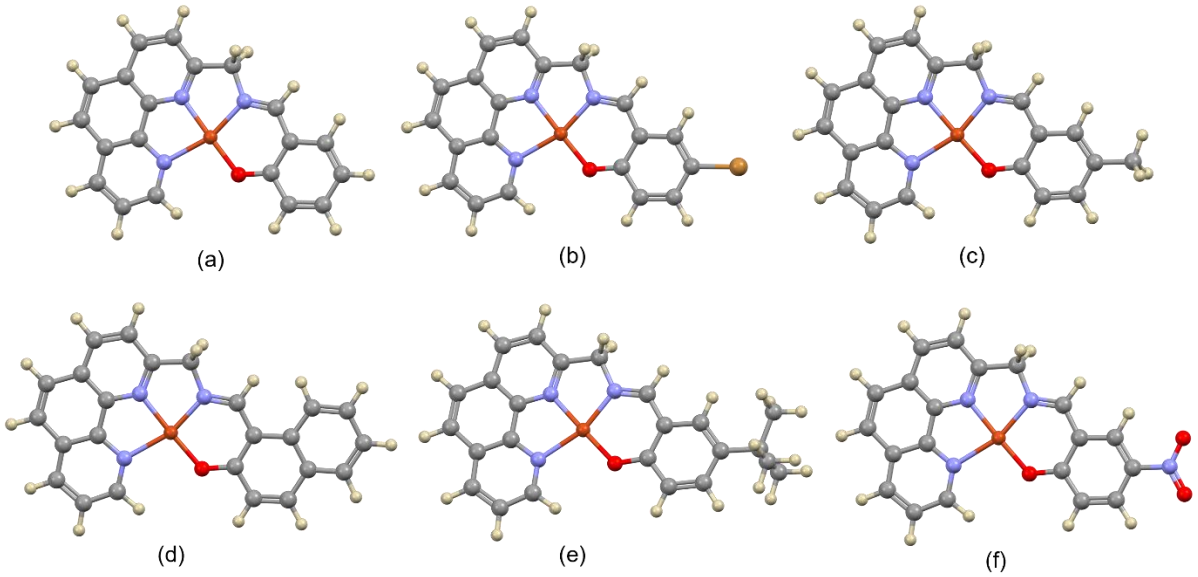

Figure 6.3.14: Geometry-optimised structures of (a) $[Cu(L3)]^+$, (b) $[Cu(L5)]^+$, (c) $[Cu(L6)]^+$, (d) $[Cu(L8)]^+$, (e) $[Cu(L9)]^+$, and (f) $[Cu(L10)]^+$.

6.3.3.2 Vibrational Frequency Results

As with the previous class of compounds, the vibrational frequencies were simulated primarily to determine if the geometry-optimised structures represent the true minimum on the global potential energy surface. As a secondary point of interest, the frequency results can be used to better interpret the experimental IR data. The vibrational frequency of the N=C bond of the calculated spectra was compared with the experimental frequency of each metal chelate. The comparison is summarised in Table 6.3.14.

Table 6.3.14: Summary of the experimental and calculated vibrational frequencies for the N=C bond of the imine-based copper(II) chelates.

	Experimental	Calculated	Difference*
$[Cu(L3)]^+$	1589	1646	-3.59
$[Cu(L4)(NO_3)]$	1590	1683	-5.85
$[Cu(L5)]^+$	1588	1654	-4.16
$[Cu(L6)]^+$	1589	1644	-3.46
$[Cu(L7)]^+$	1577	1642	-4.12
$[Cu(L8)]^+$	1587	1644	-3.59
$[Cu(L9)]^+$	1589	1642	-3.34
$[Cu(L10)]^+$	1594	1658	-4.02

*Percentage difference = $\frac{(Exp-Calc)}{Exp} \times 100\ \%$

The difference between the calculated and experimental values of the C=N stretching frequency are acceptable. This low percentage difference suggests that the geometry-optimised structures, from which the vibrational data are calculated, are accurate representations of the experimental molecules. Similar to the IR data in Chapter 4, the substituents on the phenol ring have minimal impact on the stretching frequencies of the imine bond.

6.3.3.3 Electronic Spectra Results

The electronic spectra of the imine-based metal chelates were calculated to better understand the molecular orbitals involved in the experimental transitions. The data were simulated using the TD-DFT method, solving for 30 excited states, at the same level of theory used for the previous simulations. A water solvent model was included in the simulations to account for solvent effects.

The experimental absorption spectra of these chelates were compared to the calculated data. It was found that the profiles of the calculated spectra are similar to experimental data, but the simulated data is red-shifted by *ca.* 90 nm. This relatively poor correlation between the energies of the transitions may be due to the paramagnetic nature of copper(II) complexes. In the case of the amide-based ligands, the simulated spectra for the copper(II) chelates were also less accurately predicted than those of either the palladium(II) or nickel(II) compounds. This is illustrated in Figure 6.3.17 with $[Cu(L3)]^+$.

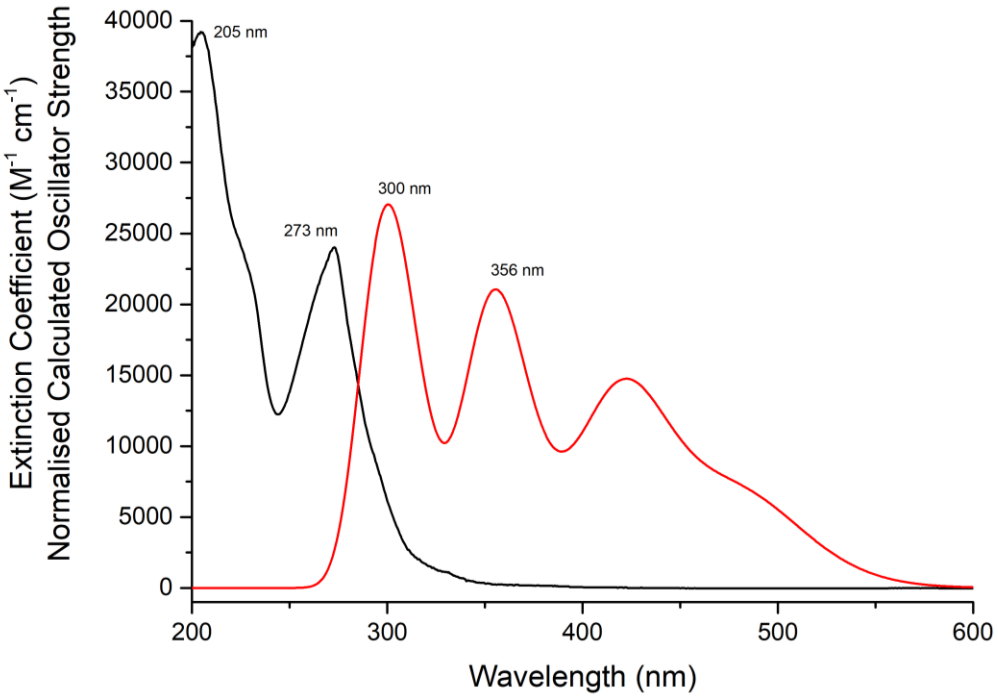

Figure 6.3.15: Overlay of the calculated (black) and experimental (red) absorption spectra of $[Cu(L3)]^+$.

The electronic transitions were calculated for both the cationic structures, i.e. [Cu(L)]+, and the neutral compounds with the nitrate anion coordinated, i.e. $[Cu(L)(NO_3)]$. The correlation between the former and the experimental data was significantly better than the correlation with the latter. This possibly suggests that in solution the nitrate ion is not coordinated to the metal centre.

The HOMO and LUMO orbitals for the imine-based metal chelates were simulated and are shown in Figure 6.3.16 with their corresponding band gaps.

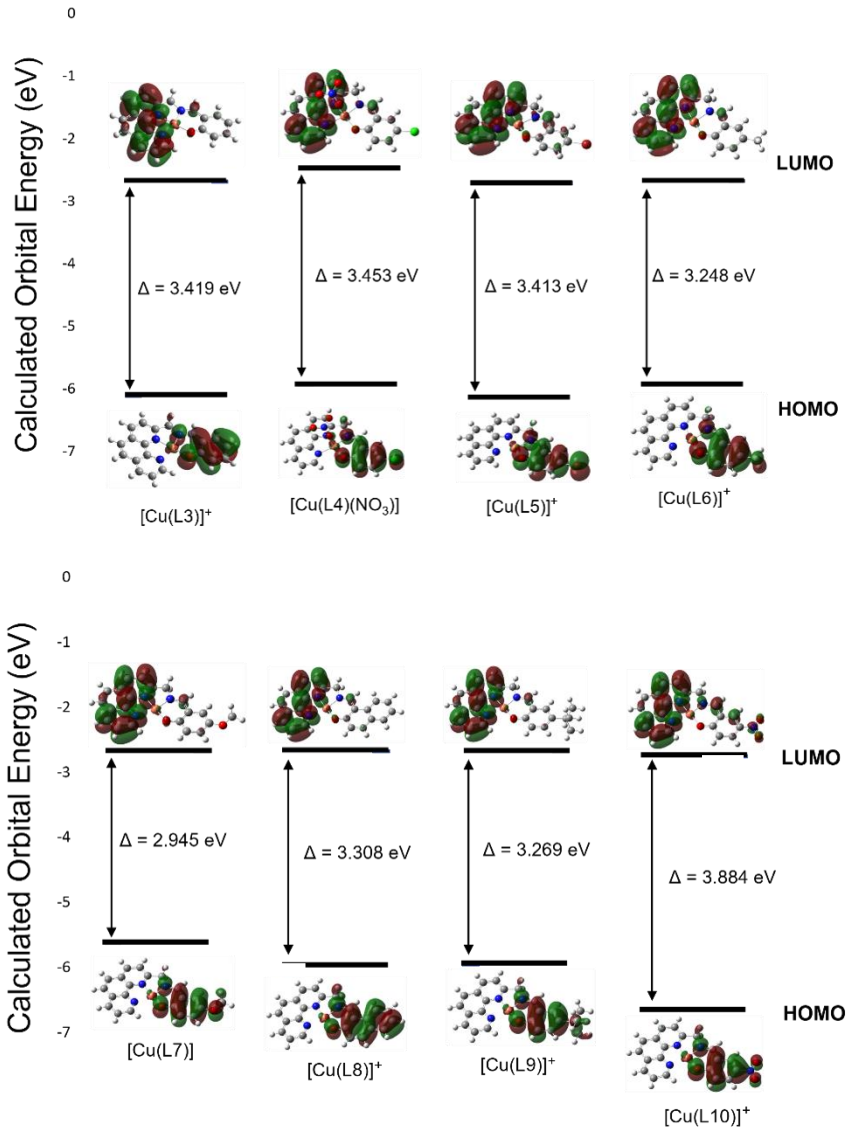

Figure 6.3.16: Energy gaps between the HOMOs and LUMOs of the imine-based metal chelates.

The energy gaps between the HOMO and LUMO orbitals show that the complexes with electron-withdrawing groups, $[Cu(L4)(NO_3)]$, $[Cu(L5)]^+$, and $[Cu(L10)]^+$, are larger when compared to $[Cu(L3)]^+$. Whereas, those with the electron-donating groups, $[Cu(L6)]^+$, $[Cu(L7)]^+$, $[Cu(L8)]^+$, and $[Cu(L9)]^+$, are lower in energy. This is most pronounced when comparing the HOMO-LUMO energy gaps of $[Cu(L10)]^+$ and $[Cu(L7)]^+$; with the electron-withdrawing group, $-NO_2$, leading to a large value of 3.884 eV and the electron-donating group, $-OCH_3$, reducing the band gap to 2.945 eV.

An interesting observation regarding the HOMO and LUMO orbitals for these chelates is that the HOMO orbitals are of π-symmetry and are located only over the phenol moiety, including the substituent. The LUMO orbitals are also of π-symmetry, but are located only over the phenanthroline moiety. This can explain how the substituents at the 4-position influence the energy gap for these chelates.

Table 6.3.15 contains a summary of the main calculated transitions for the metal chelates, and Figure 6.3.17 shows the molecular orbitals of $[Cu(L3)]^+$ which are involved in the electronic transitions.

Table 6.3.15: Selected experimental and calculated electronic transitions for the metal chelates.

Wavelength/nm		Oscillator strength, *f*	Molecular Orbitals	Assignment
Exp	**Calc**			
[Cu(L3)]				
205	298	0.0331	92A → 97A	π(phen) → π*(phen)
			93A → 98A	π(phen,phenol) → π*(phen)
273	307	0.0244	94A → 97A	π(phenol) → π*(phen)
-	355	0.0561	96A → 99A	π(phenol) → π*(phenol)
-	420	0.0127	96A → 97A	π(phenol) → π*(phen)
[Cu(L4)]				
205	287	0.0346	101A → 105A	π(phenol) → π*(phen)
273	297	0.0251	100A → 105A	π(phen) → π*(phen)
			102A → 106A	π(phen) → π*(phen)
-	354	0.0596	103A → 107A	Cu[dx2-y2]Lσ → π*(phenol)
			104A → 107A	Cu[dx2-y2]Lσ → π*(phenol)
-	425	0.0242	103A → 105A	Cu[dx2-y2]Lσ → π*(phen)
			103A → 107A	Cu[dx2-y2]Lσ → π*(phenol)
[Cu(L5)]				
206	290	0.0688	110A → 114A	π(phen,phenol) → π*(phen)
			111A → 115A	π(phen) → π*(phen)
			109A → 114A	π(phen,phenol) → π*(phen)
273	366	0.0558	113A → 116A	π(phenol) → π*(phenol)
-	421	0.031	113A → 114A	π(phenol) → π*(phen)
[Cu(L6)]				
205	297	0.0536	96A → 101A	π(phen) → π*(phen)
			98A → 102A	π(phen,phenol) → π*(phen)
273	356	0.0565	99A → 103A	Cu[dx2-y2]Lσ → π*(phenol)
			100A → 103A	π(phenol) → π*(phenol)
205	297	0.0536	96A → 101A	π(phen) → π*(phen)
[Cu(L7)]				
206	296	0.0351	101A → 105A	π(phenol) → π*(phen)
			102A → 106A	π(phen) → π*(phen)
			100A → 105A	π(phen) → π*(phen)
273	371	0.0308	104A → 107A	π(phenol) → π*(phenol)
-	388	0.0273	104A → 107A	π(phenol) → π*(phenol)

Wavelength/nm		Oscillator strength, *f*	Molecular Orbitals	Assignment
Exp	**Calc**			
[Cu(L8)]				
	313	0.0961	107A → 112A	π(naph) → π*(phenol)
			106A → 110A	π(phen) → π*(phen)
	316	0.1903	107A → 112A	π(naph) → π*(phenol)
			106A → 110A	π(phen) → π*(phen)
	356	0.1068	107A → 110A	π(naph) → π*(phen)
			108A → 112A	Cu[dx2-y2]Lπ → π*(phenol)
			109A → 112A	Cu[dx2-y2]Lπ → π*(phenol)
[Cu(L9)]				
208	297	0.0228	109A → 114A	π(phen) → π*(phen)
			108A → 113A	π(phen) → π*(phen)
-	315	0.0273	109A → 113A	π(phen) → π*(phen)
275	356	0.0536	112A → 115A	π(phenol) → π*(phenol)
-	388	0.0215	112A → 114A	π(phenol) → π*(phen)
[Cu(L10)]				
205	318	0.1613	106A → 110A	π(phenol) → π*(NO2,phen)
			106A → 111A	π(phenol) → π*()
273	330	0.0741	106A → 110A	π(phenol) → π*(NO2,phen)
-	342	0.0823	106A → 109A	π(phenol) → π*(phen,NO2)

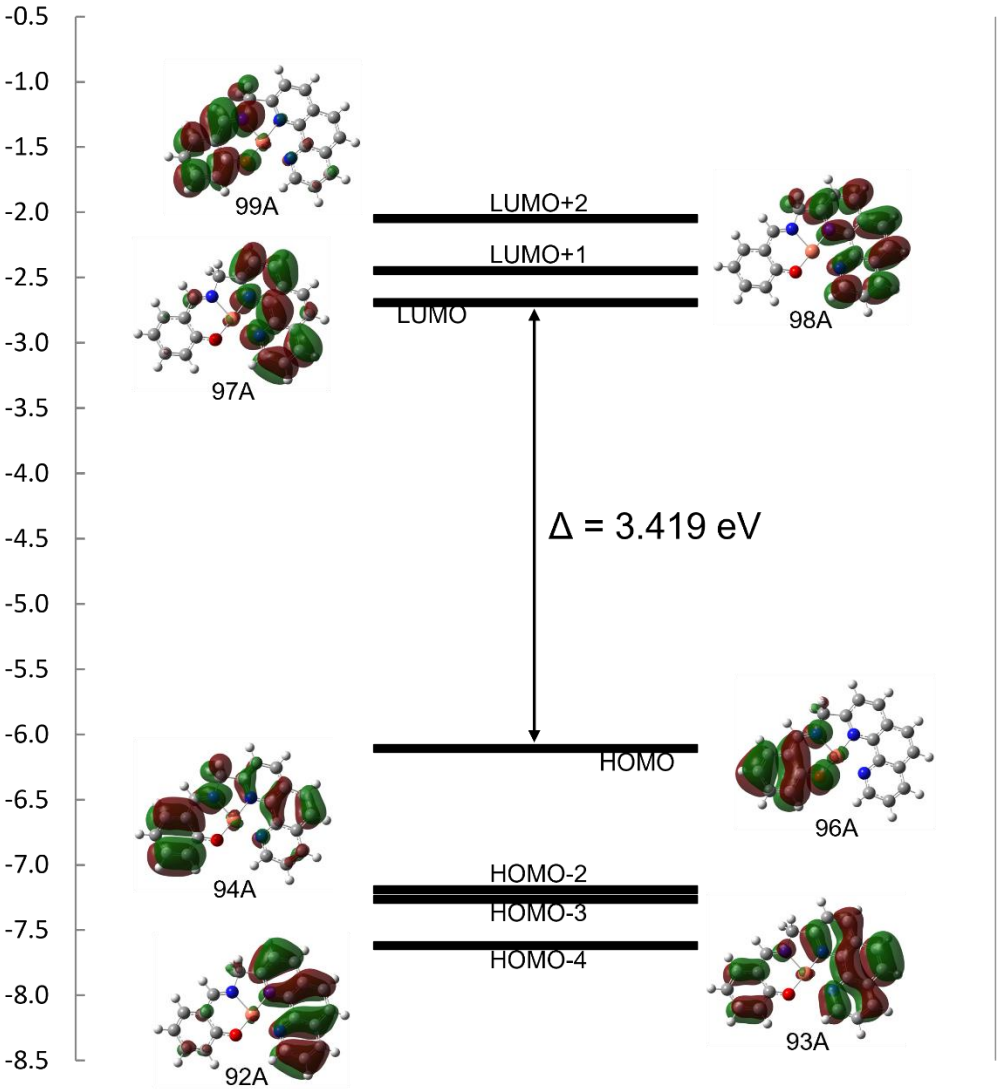

Figure 6.3.17: Molecular orbital diagram of $[Cu(L3)]^+$ showing the relative energies of the orbitals. The energy gap between the HOMO and the LUMO for this complex is 3.419 eV.

6.4 Summary of Computational Chemistry

The geometry-optimised structure of HL1 showed moderate agreement with the experimental X-ray structure. The most notable difference is that *in vacuo* the lowest energy structure is planar. An energy plot of the torsion angle between the phenanthroline and quinoline moieties of HL1 showed the planar geometry is 10.12 kJ mol^{-1} lower in energy than the solid-state structure. The bond lengths and bond angles of the DFT-calculated structures for HL2, copper(II) and nickel(II) amide-based chelates were in agreement with literature values. This illustrates the accuracy of the basis set used. The two imine-based chelates for which there were solid-state structures showed a good correlation with the geometry-optimised structures with regards to the bond lengths and angles. The geometry-optimisied structures of $[Cu(L4)(NO_3]$ and $[Cu(L7)]^+$ are lower in energy by 22.89 kJ mol^{-1} and 10.57 kJ mol^{-1}, respectivefully, with $[Cu(L4)(NO_3)]$ having a square pyramidal geometry and $[Cu(L7)]^+$ with a square planar geometry. The B3LYP/LanL2DZ level of theory used for the palladium(II) amide-based chelates similarly produced accurate geometry-optimised structures. The geometry-optimised structures of the amide-based metal chelates were congruent, all exhibiting square planar coordination geometry.

In general, the correlation between the calculated and experimental vibrational frequencies for the amide-based ligands was moderate, but the calculated values were predicted to be higher in energy. This trend of over estimating the frequencies was also observed with the copper(II) and nickel(II) amide-based chelates, but not with the palladium(II) amide-based chelates, which used a different basis set. The imine-based chelates showed a good correlation between the calculated and experimental C=N stretching frequency, with the highest difference being -5.85% for $[Cu(L4)(NO_3)]$. The absence of negative vibrational eigenvalues for the ligands and metal chelates indicate that the geometry-optimised structures are true minima on the global potential energy surface.

Electronic transition data calculated using the TD-DFT method gave an understanding of the transitions responsible for the absorption peaks in the experimental spectra. The L1 metal chelates have a smaller energy gap between the HOMO and LUMOs of each chelate compared to the L2 metal chelates. The imine-based chelates have smaller band gaps when compared to the L1 and L2 chelates. The electronic transition data for the imine-based chelates showed the HOMO orbitals preside over the phenol moiety and the LUMO orbitals over the phenanthroline moiety. This trend of the imine-based chelates could explain the influence of the substituents on the energy gap.

Overall, the 6-311G basis set was shown to yield more accurate simulated data compared to the LanL2DZ basis set, as the 6-311G basis set is larger than the LanL2DZ basis set.

6.5 References

1. Hinchliffe, A., *Modelling molecular structures*. 2nd ed.; Wiley: Chichester, Sussex, 2000.
2. Jensen, F., *Introduction to computational chemistry*. 2nd ed.; John Wiley & Sons: Chichester, England ; Hoboken, NJ, 2007.
3. Young, D. C., *Computational chemistry : a practical guide for applying techniques to real world problems*. 1st ed.; Wiley: New York, 2001.
4. Martin, J. M. L.; Bauschlicher, C. W.; Ricca, A., *Computer Physics Communications* **2001,** *133* (2), 189-201.
5. Hay, P. J.; Wadt, W. R., *J. Chem. Phys.* **1985,** *82* (1), 270 - 283.
6. Hay, P. J.; Wadt, W. R., *J. Chem. Phys.* **1985,** *82* (1), 299 - 310.
7. Hay, P. J.; Wadt, W. R., *J. Chem. Phys.* **1985,** *82* (1), 284 - 298.
8. Erras-Hanauer, H.; Mao, Z.-W.; Liehr, G.; Clark, T.; van Eldik, R., *Eur. J. Inorg. Chem.* **2003,** *2003* (8), 1562-1569.
9. Spodine, E.; Venegas-Yazigi, D.; Ushak, S.; Le Fur, E.; Pivan, J.-Y., *Physica B* **2006,** *384* (1–2), 120-122.
10. Caglar, S.; Demir, S.; Heren, Z.; Büyükgüngör, O., *Polyhedron* **2011,** *30* (8), 1389-1395.
11. Zhao, F.; Wang, J.-x.; Wang, Y.-b., *J. Theor. Comput. Chem.* **2011,** *973* (1–3), 40-46.
12. Panina, N. S.; Demidov, V. N.; Simanova, S. A., *Russ. J. Gen. Chem.* **2008,** *78* (5), 913-918.
13. Frisch, M. J.; Trucks, G. W.; Schlegel, H. B.; Scuseria, G. E.; Rob, M. A.; Cheeseman, J. R.; J. A. Montgomery, J.; Vreven, T.; Kudin, K. N.; Burant, J. C.; Millam, J. M.; Iyengar, S. S.; Tomasi, J.; Barone, V.; Mennucci, B.; Cossi, M.; Scalmani, G.; Rega, N.; Petersson, G. A.; Nakatsuji, H.; Hada, M.; Ehara, M.; Toyota, K.; Fukuda, R.; Hasegawa, J.; Ishida, M.; Nakajima, T.; Honda, Y.; Kitao, O.; Nakai, H.; Klene, M.; Li, X.; Knox, J. E.; Hratchian, H. P.; J. B. Cross, V. B.; Adamo, C.; Jaramillo, J.; Gomperts, R.; Stratmann, R. E.; Yazyev, O.; Austin, A. J.; Cammi, R.; Pomelli, C.; Ochterski, J. W.; Ayala, P. Y.; Morokuma, K.; Voth, G. A.; Salvador, P.; Dannenberg, J. J.; Zakrzewski, V. G.; Dapprich, S.; Daniels, A. D.; Strain, M. C.; Farkas, O.; Malick, D. K.; Rabuck, A. D.; Raghavachari, K.; Foresman, J. B.; Ortiz, J. V.; Cui, Q.; Baboul, A. G.; Clifford, S.; Cioslowski, J.; Stefanov, B. B.; Liu, G.; Liashenko, A.; Piskorz, P.; Komaromi, I.; Martin, R. L.; Fox, D. J.; Keith, T.; Al-Laham, M. A.; Peng, C. Y.;

Nanayakkara, A.; Challacombe, M.; Gill, P. M. W.; Johnson, B.; Chen, W.; Wong, M. W.; Gonzalez, C.; Pople, J. A. *Gaussian 09, Revision A.1*, Gaussian, Inc.: Wallingford CT, 2004.

14. Dennington, R.; Keith, T.; Millam, J.; Eppinnet, W. L. *GaussView*, Version 5.0; Semichem, Inc.: Shawnee Mission, KS, USA, 2008.
15. O'Keefe, M.; Brese, N. E., *Journal of the American Chemical Society* **1991,** *113* (9), 3226-3229.
16. Yang, L.; Chen, Q.; Li, Y.; Xiong, S.; Li, G.; Ma, Jin S., *Euro. J. Inorg. Chem.* **2004,** *2004* (7), 1478-1487.
17. Sakon, J.; Reiter, A.; Mertes, K. B.; Takusagawa, F., *Acta Cryst.* **1989,** *C45*, 1311 - 1314.
18. Bacchi, A.; Carcelli, M.; Gabba, L.; Ianelli, S.; Pelagatti, P.; Pelizzi, G.; Rogolino, D., *Inorg. Chim. Acta.* **2003,** *342*, 229-235.

Chapter 7: Biological Studies

7.1 Cytotoxicity of the Metal Chelates

7.1.1 Introduction

The last step in assessing the metal chelates as potential chemotherapeutic agents is screening the chelates against a panel of human cancer cell lines *in vitro* to determine the cytotoxicity of each metal chelate. The cytotoxicity studies will show how effectively the metal chelates control the proliferation of tumour cells. It will additionally show any preference the chelates may have towards particular cell lines. With this data, the most promising drug candidates can be identified and tested further. The further testing includes *in vivo* biodistribution studies with the radiolabelled equivalent of the compound. These xenograft experiments will also give an indication of the potential of these compounds as theranostic agents, i.e. the same compound being used for both diagnosis and therapy.

The four cancerous human cell lines used for testing against the amide-based chelates in this study are non-small cell lung carcinoma, A549; human renal adenocarcinoma, TK-10; central nervous system cancer, U251; and human colon adenocarcinoma, HT29. These cell lines are a select few from the many different types of known human cancer cells, but represent some of the deadliest types of cancer.

The cell lines used for testing against the imine-based metal chelates are healthy human embryonic kidney, HEK293; triple-negative breast cancer, MDA-MB231; human cervix epithelioid carcinoma, HeLa; and neuroblastoma, SH SY5Y. The inclusion of the healthy cell line in the testing allows for the selectivity index of the compounds to be determined. This is an important aspect of understanding whether a compound has any application *in vivo*. A compound which is highly cytotoxic, but has a poor selectivity ratio is of limited interest.

Cytotoxicity can be represented by several growth inhibition parameters. There are three measures of cytotoxicity commonly used, each of which are the concentrations required to terminate a specific proportion of the tumour cells. Figure 7.1.1 shows a dose-response curve, illustrating the three different cytotoxicity parameters in relation to the growth inhibition curve of daunorubicin:

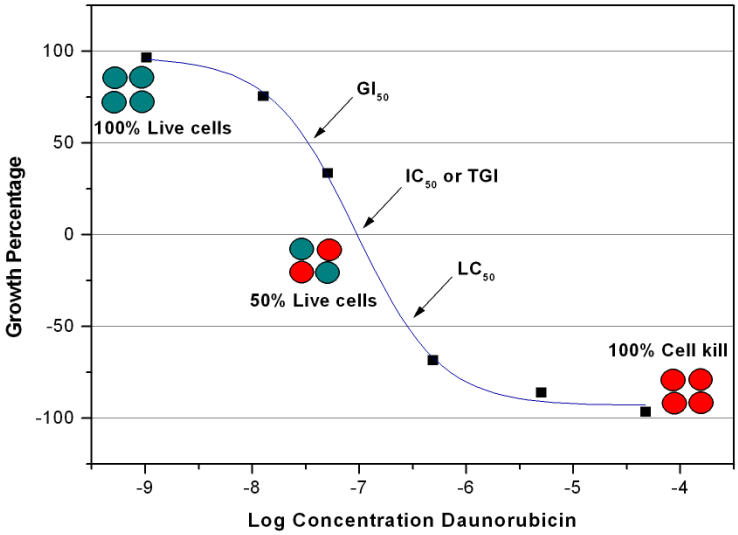

Figure 7.1.1: Growth inhibition curve of daunorubicin, highlighting the relationship between cell kill rates and growth percentage.

The first parameter is the median growth inhibition concentration (GI_{50}). This is the concentration of the compound which causes the growth rate of the cells to be reduced by 50%, achieved by the termination of 25% of the cell population. The second parameter is the lethal inhibition concentration (LC_{50}) which results in a negative growth rate, with 75% of the cell population terminated by the compound. The most widely used parameter is the total growth inhibition concentration (IC_{50}) which is the concentration of the compound that terminates 50% of the cell population, resulting in an overall growth rate of zero.
The cytotoxicity parameter used in this work is the IC_{50} value of the metal chelates. Since cancer is the uncontrolled growth of cells, by reducing the growth rate, the cancer will be controlled.

7.1.2 Experimental

7.1.2.1 Amide-based Chelates

The cell screening experiments were performed at Mintek (South Africa). The assay endpoint was determined *via* the CellTiter Aqueous Non-Radioactive Assay.[1-3] A 96-well microtiter plate was seeded with cells at a low passage number, at a concentration of 2×10^5 cells mL^{-1} in a total volume of 100 µL complete medium (TK-10, A549, U251 and HT-29). The media contained 10% foetal bovine serum (FBS, Highveld Biological, RSA) and necessary antibiotics. After an incubation period of 24 hours, at 37 °C and 5% CO_2, the test compounds were added in two-fold serial dilutions for a total of 7 concentrations (50 – 0.78 µM). After an incubation period of 96 hours, 10 µL of the CellTiter solution was added to each well; the contents gently mixed and the plates incubated under the previously described conditions. The plates were read at time intervals of 2 and 4 hours at an absorbance wavelength of 490 nm on a multi-

plate reader (xMarkTM, Bio-Rad). Total growth inhibition concentrations, IC_{50}, values were determined as the concentration of the test substance required to reduce cell viability by 50% using OriginPro® version 8.0 software (OriginLab Corporation, Northampton, MA 01060 USA).

7.1.2.2 Imine-based Chelates

The cytotoxicity assay was conducted as per a previously described, standard method.[4] Briefly, 96-well microtiter plates were seeded with the cell line (HEK293, MDA-MB231, HeLa, SH SY5Y) at a concentration of 2×10^5 cells/mL and allowed to stabilise for 4 hours at 37°C and 5% CO_2. Thereafter, the chelate solutions were added to the plate through two-fold serial dilution to allow for eight final concentrations of the metal complex ranging from 100 to 0.781 µM in a total volume of 200 µL / well. The plate was then incubated for 96 hours at 37°C and 5% CO_2. To each well, 20 µL CellTiter 96 Aqueous One Solution (Promega, Madison, WI, USA) was added, and the plates were incubated for 4 hours as previously described. Absorbance was read at 490 nm on a multi-plate reader (Molecular Devices, San Jose, CA, USA). EC_{50} values were determined as the concentration of each compound required to reduce cell viability by 50% and were calculated using OriginPro 8.0 software.[5] The values recorded are averages of at least three separate experiments.

7.1.3 Results and Discussion

7.1.3.1 Amide-based Chelates

The IC_{50} values for five of the six synthesised amide-based metal chelates against a panel of four human tumour cell lines were determined. In general, the lower the IC_{50} value, the more effectively a compound controls the proliferation of tumour cells. The IC_{50} value will be represented as the $-\log IC_{50}$, in some instances, in order to get a better understanding of the data. A lower concentration of the chelate will have a higher $-\log IC_{50}$ value, indicating the chelate has higher cytotoxicity, this approach makes understanding the data in a bar chart more intuitive. Figure 7.1.2 is a bar graph which shows the $-\log IC_{50}$ values of the amide-based metal chelates.

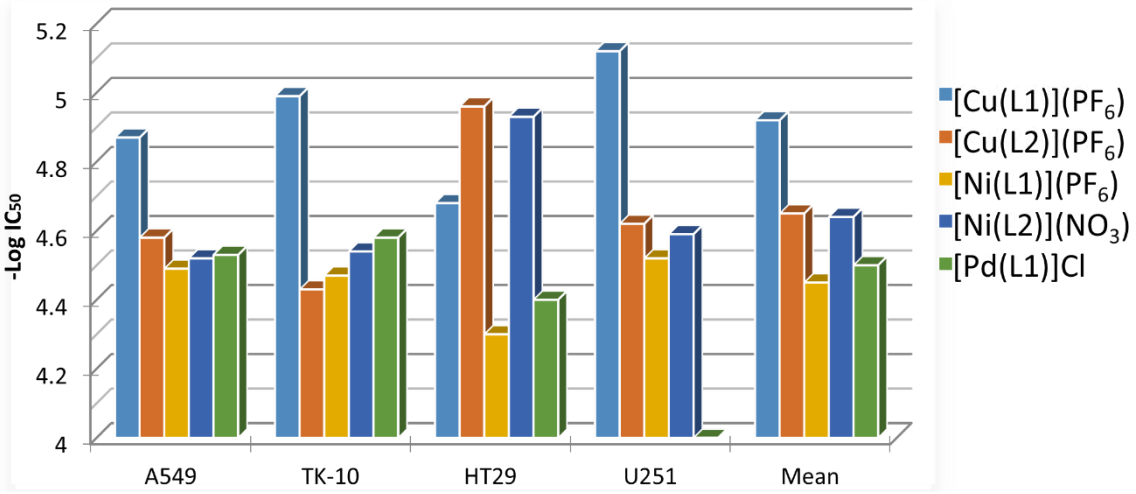

Figure 7.1.2: Bar graph of -log IC_{50} values of the amide-based metal chelates against four tumour cell lines.

Table 7.1.1 reports the IC_{50} values for the five amide-based metal chelates as well as cisplatin, carboplatin and bleomycin (data obtained from the NCI DTP database).[6]

Table 7.1.1: Summary of IC_{50} values (μM) for the amide-based metal chelates and select commercially available chemotherapeutics.

Metal Chelate	A549	TK-10	HT29	U251	Mean
[Cu(L1)](PF_6)	13.490	10.233	20.893	7.586	12.023
[Ni(L1)](PF_6)	32.359	33.884	50.119	30.200	35.481
[Pd(L1)]Cl	29.512	26.303	39.811	>100	31.623
[Cu(L2)](PF_6)	26.303	37.154	10.965	24.547	22.387
[Ni(L2)](NO_3)	30.200	28.840	11.749	25.704	22.909
Cisplatin	4.677	12.303	10.965	2.399	6.166
Carboplatin	112.202	251.189	251.189	67.608	147.911
Bleomycin	0.724	13.183	14.454	0.759	3.236

The data in Figure 7.1.2 and Table 7.1.1 show that the cytotoxicity of the metal chelates varies significantly. Additionally, the cytotoxicity of each chelate varies against each cell line. This is an encouraging result as it shows that the metal chelates drugs with a well-defined mechanism of action. The mean cytotoxicity against the four cancer cell lines for [Cu(L1)](PF_6) is higher than the mean for [Cu(L2)](PF_6) by almost 2-fold, which is likely due to the different ligand geometry of each copper(II) chelate. The main difference between the copper(II) chelates is the extent of aromaticity in the ligands. [Cu(L1)](PF_6) has a more rigid and planar aromatic structure than [Cu(L2)](PF_6) due to the aminoquinoline moiety of L1 having an extra fused ring, compared to the picolylamine moiety of L2, which has a methylene bridge. The DNA binding constants reflect these differences in structure. This trend is not observed with the nickel(II) chelates, which is likely due to [Ni(L1)](PF_6) forming an octahedral complex *in situ*. The octahedral configuration disrupts the intercalating ability of the nickel(II) chelate by making it more sterically hindered and, therefore, reduces the cytotoxicity.

The copper(II) chelates are more cytotoxic than either the palladium(II) or nickel(II) compounds, this suggests that the catalysis of hydroxyl radicals *in vitro* may be part of the mechanism of action. The trend observed in the cytotoxicity values mirrors that of the DNA binding constants, with the exception of [Ni(L2)](NO_3). This trend is illustrated in Table 7.1.2.

Table 7.1.2: Effectiveness of the metal chelates in the binding studies and cytotoxicity studies.

Most Effective					**Least Effective**
DNA Binding Affinities					
[Cu(L1)](PF_6)	[Pd(L1)]Cl	[Cu(L2)](PF_6)	[Pd(L2)]Cl	[Ni(L1)](PF_6)	[Ni(L2)](NO_3)
Cytotoxicity Studies*					
[Cu(L1)](PF_6)	[Cu(L2)](PF_6)	[Ni(L2)](PF_6)	[Pd(L1)]Cl	[Ni(L1)](NO_3)	

* The cytotoxicity is represented by the mean IC_{50} against the four tumour cell lines.

The correlation between the mean IC_{50} values and the binding constants for the metal chelates are noteworthy. The exception of [Ni(L2)](NO_3), suggests, though, that the intercalation ability plays a role in the cytotoxicity of the chelates, but is not the only factor. It is also interesting to note that the copper and nickel analogues of L2 have comparable activity to cisplatin towards HT29. In this case, it seems that the structure of the ligand is what results in the cytotoxicity as opposed to the identity of the metal ion. A comparison of the data for [Cu(L1)]PF_6 and [Pd(L1)]Cl is particularly interesting, highlighting the significance of the redox activity of the copper(II) ion. These two metal chelates have similar DNA binding constants; if that was the only factor in predicting their cytotoxicity, then the two chelates would have similar cytotoxicity. The fact that their cytotoxicities are significantly different shows that the additional function of the copper(II) centre catalysing the production of hydroxyl radicals is a key factor in the cytotoxicity. This is further supported by the fact that the complex [Cu(L2)](PF_6), which is not a particularly strong DNA binder, shows significant cytotoxicity.

Cisplatin, carboplatin and bleomycin are used in the chart in Figure 7.1.3 to show how the most cytotoxic metal chelate, [Cu(L1)](PF_6), compares with well-known commercially available anti-cancer drugs. The graph shows that [Cu(L1)](PF_6) has similar cytotoxicity to the widely used cisplatin and in the case of TK-10 is more cytotoxic than cisplatin, carboplatin and bleomycin. The mean values in the bar graph show the copper(II) chelate has lower cytotoxicity compared to cisplatin and bleomycin but has significantly higher cytotoxicity than carboplatin. This trend shows the metal chelate is effective towards cancer cells and is sufficiently cytotoxic to warrant further testing.

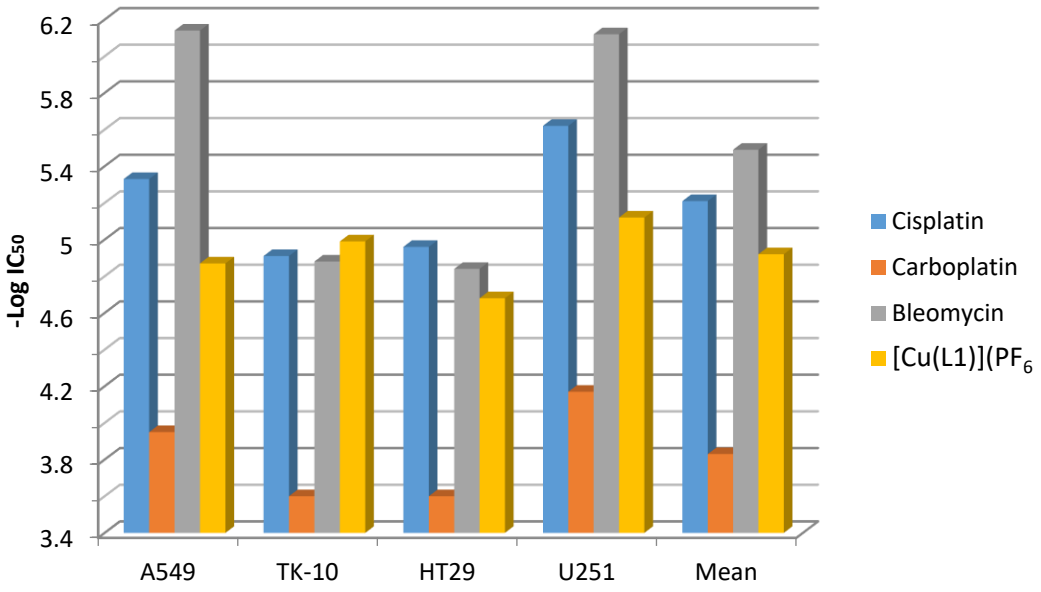

Figure 7.1.3: Bar graph of -log IC_{50} values of [Cu(L1)](PF_6), cisplatin, carboplatin and bleomycin against four tumour cell lines.

This preliminary cell screening data shows that the design features that were included in the metal chelates are important for their efficacy. In particular, the extent of aromaticity and the ability to catalyse the production of hydroxyl radicals *in vitro*.

Table 7.1.3 compares the cytotoxicity of [Cu(L1)](PF_6) with that of other copper(II) chelates reported in literature against the cell lines A549 and HT29.

Table 7.1.3: IC_{50} values (µM) of [Cu(L1)](PF_6) and selected copper(II) chelates, with X-ray structures.

Compound	[Cu(L1)](PF_6)	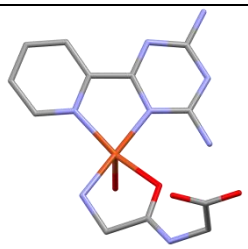 7	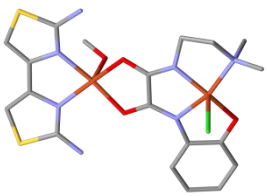 8	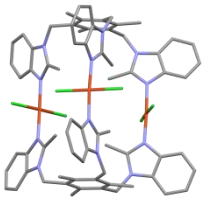 9
A549	13.490	41.687	4.266	N/A
HT29	20.893	N/A	N/A	7.586

N/A = Not available.

The data in Table 7.1.3 shows that [Cu(L1)](PF_6) has cytotoxicity that falls in the range of other copper(II) chelates reported in literature. This confirms [Cu(L1)](PF_6) is sufficiently cytotoxic to contend with other copper(II) chelates.

The X-ray structure obtained by Fu, *et al.*[7] (Table 7.1.3 - 7) showed that the complex interacted with the DNA structure *via* groove binding in adenine and thymine rich regions of the DNA.[7] The copper(II) ions produce hydroxyl radicals, $^{\cdot}OH$, as well as superoxide, $^{\cdot}O_2^-$, which further attack the DNA structure similar to [Cu(L1)](PF_6).[7] The compound is water-soluble, making uptake by the cells of the body more effective.[7]

A study by Zheng, *et al.*[8] presented a chemotherapeutic compound containing two copper(II) ions that produce hydroxyl radicals *in situ*, similar to all copper(II) chelates. The presence of two metal centres increases the rate of production of the hydroxyl radicals, and therefore, higher cytotoxicity is observed.[8] Unlike the study by Fu, *et al.*[7] and [Cu(L1)](PF_6), the dicopper(II) chelate binds to DNA *via* electrostatic bonds with the DNA structure.[8] The compound also has a high binding affinity towards bovine serum albumin, which is a protein used to determine the binding sites *in vitro*, due to the structure homology with human serum albumin.[8]

The tri-copper(II) chelate studied by Zhao, *et al.*[9] shows that an increase in the number of copper(II) ions again increases the cytotoxicity of a compound.[9] This illustrates the significance of the catalytic nature of the copper(II) ion in the cytotoxicity of the complexes.

7.1.3.2 Imine-based Chelates

The IC_{50} values for seven of the eight imine-based chelates have also been determined, but different cell lines were used, namely, HEK293, MDA-MB231, HeLa, and SH SY5Y. The use of HEK293 is to compare the cytotoxicity of a healthy cell line with those of neoplastic cell lines to determine the selectivity index. The -log IC_{50} values for these chelates are summarised in Table 7.1.4 and Figure 7.1.4 with cisplatin as the positive control.

Table 7.1.4: Summary of IC_{50} values and standard deviation (µM) for the imine-based metal chelates and cisplatin.

Metal Chelate	HEK293	MDA-MB231	HELA	SH SY5Y
[Cu(L3)]Cl	50.01 ± 6.55	13.51 ± 2,27	55.76 ± 4.67	25.17 ± 4.32
[Cu(L4)]Cl	70.72 ± 4.79	13.63 ± 1.15	51.76 ± 3.61	9.88 ± 2.16
[Cu(L5)]Cl	93.19 ± 2.31	27.16 ± 2.12	84.31 ± 3.20	32.72 ± 7.78
[Cu(L6)]Cl	70.71 ± 2.40	49.11 ± 2,19	55.85 ± 6.28	20.19 ± 3.68
[Cu(L7)]Cl	61.32 ± 3.71	8.36 ± 2.70	36.35 ± 4.81	9.33 ± 1.60
[Cu(L8)]Cl	11.54 ± 3.65	14.80 ± 5.09	64.40 ± 5.65	11.83 ± 0.34
[Cu(L9)]Cl	67.71 ± 3.19	6.19 ± 2.87	14.10 ± 1.13	8.95 ± 0.27
Cisplatin	14.2 ± 3.8	>50	22.68 ± 4.89	ND

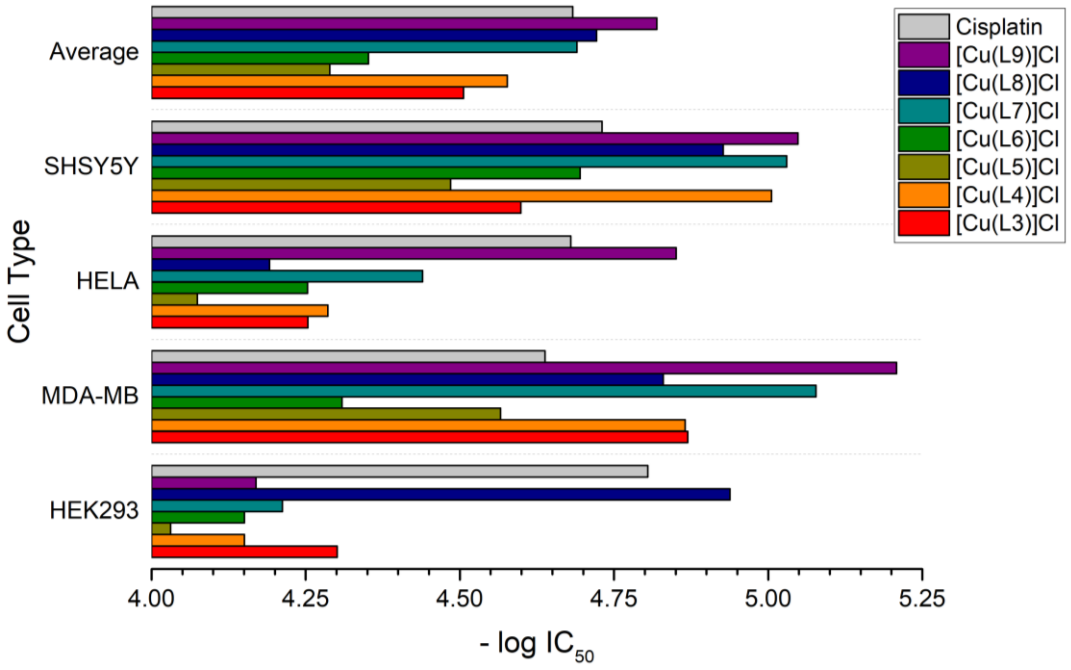

Figure 7.1.4: Bar graph of -log IC_{50} values of the imine-based chelates and cisplatin, showing their cytotoxicity against healthy, HEK293, and tumour cell lines: MDA-MB, HELA, and SHSY5Y.

Based on the cell screening data, the selectivity index was determined for the imine-based chelates and cisplatin using HEK293 as the reference healthy cell line. The data are shown in Table 7.1.5.

Table 7.1.5: Selectivity index for the imine-based chelates and cisplatin, with HEK293 as the reference healthy cell line.

Compound	Selectivity Index			
	HEK293	MDA-MB	HELA	SHSY5Y
Cisplatin	1.00	<0.28	0.63	ND
[Cu(L3)]Cl	1.00	3.70	0.90	1.99
[Cu(L4)]Cl	1.00	5.19	1.37	7.16
[Cu(L5)]Cl	1.00	3.43	1.11	2.85
[Cu(L6)]Cl	1.00	1.44	1.27	3.50
[Cu(L7)]Cl	1.00	7.33	1.69	6.57
[Cu(L8)]Cl	1.00	0.78	0.18	0.98
[Cu(L9)]Cl	1.00	10.94	4.80	7.57

The selectivity index for cisplatin is lower than the imine-based chelates, which indicates that cisplatin is not as selective towards cancer cells. The imine-based chelates have a higher

selectivity index towards the MDA-MB cell line, compared to the other two cell lines, showing that the imine-based chelates are more effective towards triple-negative breast cancer. One of the chelates, [Cu(L8)]Cl, also has a lower selectivity index, whereas, [Cu(L9)]Cl has the highest selectivity index across the three cancer cell lines.

The results of this cell screening are significant. The data clearly show that compound [Cu(L9)]Cl is the next lead compound from this library. The cytotoxicity of [Cu(L9)]Cl towards tumour cell lines is an order of magnitude higher than that of healthy cells. This implies that this compound is highly specific towards neoplastic tissue and will be the lead compound for the next round of *in vivo* studies where potential tumour uptake will be determined.

7.2 Gel Mobility Shift Assay

7.2.1 Introduction

Gel mobility shift assays are performed using gel electrophoresis, which is a technique used to separate out charged molecules, usually nucleotides and proteins, in a gel with an applied electric field.[10] The gel is analysed using light, normally UV light, and a fluorescing dye. Figure 7.2.1 illustrates the basic setup of a gel electrophoresis experiment:

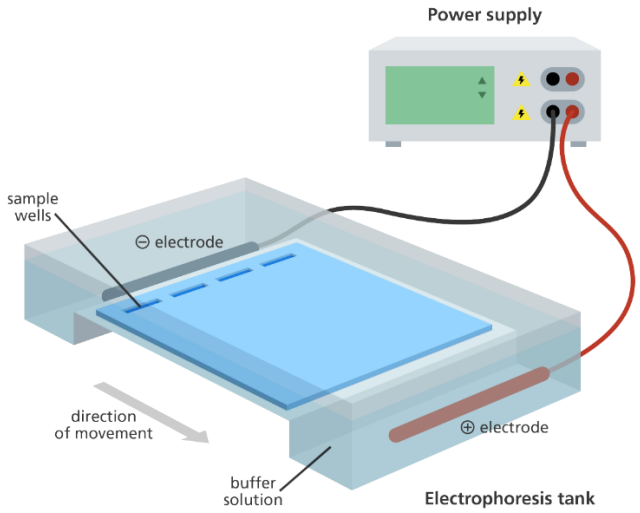

Figure 7.2.1: Schematic of a gel electrophoresis experiment.[11]

There are two types of gels most commonly used for gel electrophoresis: polyacrylamide and agarose. Polyacrylamide is generally used for protein analysis and DNA with small fragments. Agarose is used for DNA with large nucleotide fragments. Agarose is a polymeric network of molecules that forms pores, whose size is determined by the concentration of the agarose and buffer solution used.[10] The concentration of the gel, therefore, determines the separation efficiency for different size DNA fragments as well as the buffer used. The buffer solutions used all contain ethylenediaminetetraacetic acid (EDTA); the most commonly used buffer solution for double-strand DNA experiments is tris-acetate-EDTA (TAE).[10] The voltage and current used also play a role in the mobility of the DNA in the gel. Ultimately, it is the size of DNA fragments used in an experiment that will determine the type of analysis required.[10]
The DNA is visualised after the experiment *via* a dye or stain. The most commonly used stain is ethidium bromide (EtBr), which when added to the gel intercalates with the DNA base pairs and fluoresces when illuminated with UV light (This is the same property of EtBr that allowed for its application in the competitive DNA binding experiments in Chapter 4).[10] The image shown in Figure 7.2.2 is a schematic example of a gel electrophoreses experiment.

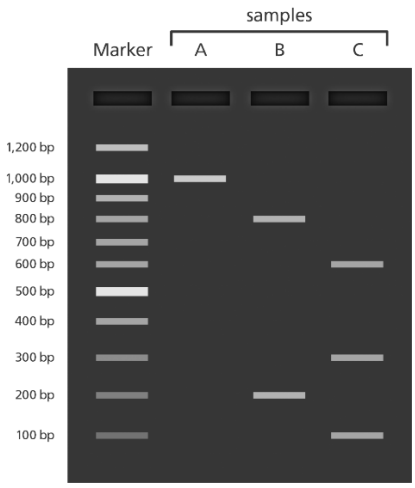

Figure 7.2.2: Typical gel electrophoreses experimental result, showing DNA bands separated on a gel. The length of the DNA fragments of the samples are compared to the marker which contains fragments of known length.[11]

In this study, gel electrophoresis is used to elucidate the interactions of the most promising metal chelate with DNA *via* a gel mobility shift assay. A gel mobility shift assay is a technique used to assess the DNA-drug interactions. This method determines the change in electrophoresis of the DNA interaction. If no interaction is observed, the DNA is said to have no interactions with the compound of interest, and if there is an interaction, the DNA's electrophoresis changes, which is shown in the gel mobility shift assay.

7.2.2 Experimental

The interaction with plasmid DNA, were determined *via* agarose gel electrophoreses for the most cytotoxic metal chelate and reference chelates. The experiments were carried out in 10X Tris-acetate-EDTA (TAE) buffer (400 mM Tris, 200 mM acetic acid, 10 mM EDTA, pH 8.0). The stock solution of [Cu(L1)](PF_6) was prepared in DMSO, while the stock solutions of [Cu(L3)](NO_3), [Cu(L4)(NO_3)], and [Cu(L7)](NO_3) were prepared in H_2O. pcDNA-APP Plasmid DNA (0.15 µg) was used for [Cu(L1)](PF_6), and pcDNA_DEST40 plasmid DNA (0.15 µg) was used for chelates [Cu(L3)](NO_3), [Cu(L4)(NO_3)], and [Cu(L7)](NO_3). The metal chelates were added to the plasmid DNA with a concentration range of 0.5 µM – 500 µM, with additives, and were brought to a final sample volume of 10 µL by adding UltraPure water. The mixtures were then incubated at 37 °C for 30 min. The reactions were quenched after incubation by the addition of 2 µL of gel loading dye (6X DNA loading dye (Thermo Fisher Scientific). Electrophoresis was then carried out at 80 V for 90 minutes at 500 mA on a 1% (w/v) agarose gel in 1X TAE buffer (40 mM Tris, 20 mM acetic acid, 1 mM EDTA, pH 8.0). The GeneRuler 1 kb DNA ladder (Thermo Fisher Scientific) was included as a molecular weight marker. The gel was stained with a 0.5 µg/mL ethidium bromide solution (10 mg/ml stock, MilliporeSigma) in UltraPure water for 30 minutes and then destained in UltraPure water for 20 minutes. The gel was visualised by UV

light and photographed for analysis using G:BOX Chemi XR5 (Syngene, India) in the GeneSys software (2012).

7.2.3 Results and Discussion

The gel mobility shift assay of [Cu(L1)](PF_6) is reported in Figure 7.2.3 and shows the interaction of this chelate with plasmid DNA.

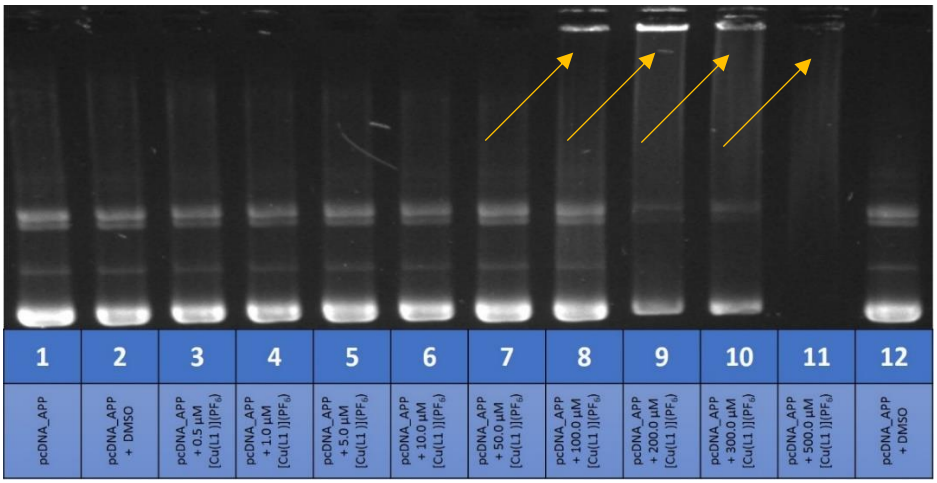

Figure 7.2.3: Gel mobility shift assay of [Cu(L1)](PF_6). Arrows showing the destruction of DNA by [Cu(L1)](PF_6) at concentrations 100 µM - 500 µM. Lane 1 – pcDNA_APP control; Lanes 2 and 12 – pcDNA_APP + DMSO; Lanes 3 – 11 – pcDNA_APP + [Cu(L1)](PF_6) (0.5 µM, 1.0 µM, 5.0 µM, 10.0 µM, 50.0 µM, 100.0 µM, 200.0 µM, 300.0 µM, 500.0 µM respectively)

Figure 7.2.3 shows a clear interaction between the plasmid DNA and [Cu(L1)](PF_6), especially at concentrations above 100 µM, lane 8 – 11. The increase in the concentration of the metal chelate from 100 µM to 500 µM shows an increase in the destruction of the DNA to a point where the DNA in lane 11 is no longer visible. This can be accredited to the strength of [Cu(L1)](PF_6)'s intercalating ability and generation of hydroxyl radicals during the experiment. A study by Manikandamathavan, *et al.*[12] showed the difference in interaction of two mixed ligand copper(II) complexes with plasmid DNA, whereby the 1,10-phenanthroline (phen) complex was more destructive towards the DNA than the 2,2'-bipyridine (bpy) complex. These data are shown in Figure 7.2.4.

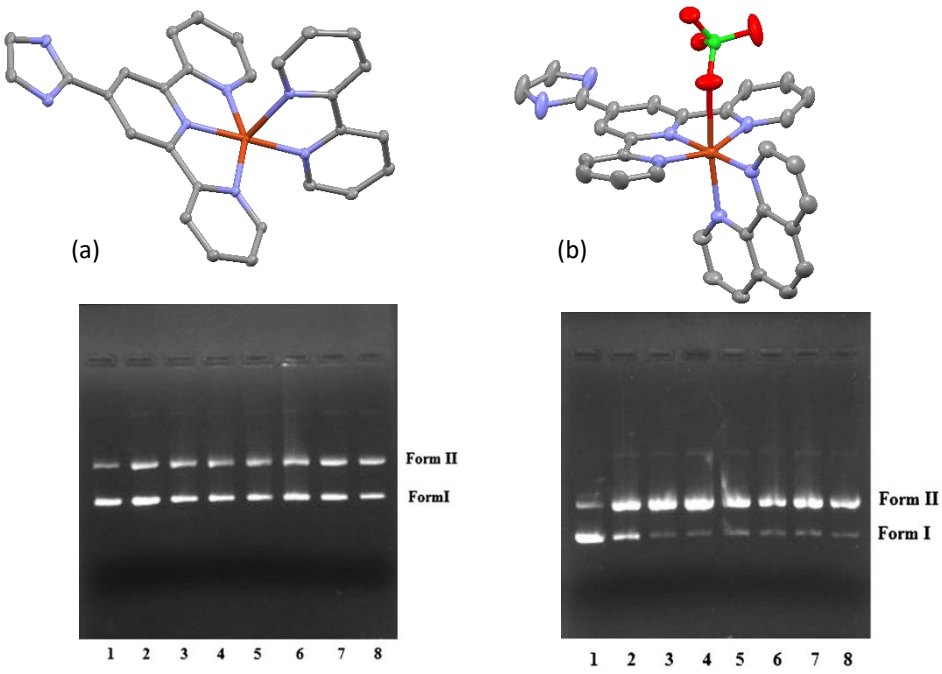

Figure 7.2.4: Crystal structures and corresponding agarose gel electrophoresis patterns of supercoiled pUC19 plasmid DNA of: (a) [Cu(4'-(1H-imidazole-2-yl)-2,2':6',2"-terpyridine)(bpy)]$(ClO_4)_2$·(H2O); Lane 1 - DNA control; lanes 2 – 8 - DNA and (a) at (100 mM, 200 mM, 300 mM, 400 mM, 500 mM, 600 mM, 700 mM respectively); and (b) [Cu(4'-(1H-imidazole-2-yl)-2,2':6',2"-terpyridine)(phen)(ClO_4)](ClO_4)·(H_2O); Lane 1 - DNA control; lanes 2 – 8 - DNA and (b) (40 mM, 60 mM, 80 mM, 100 mM, 120 mM, 140 mM, 160 mM respectively).[12]

The phen complex is shown to interact more strongly with the DNA, similar to [Cu(L1)](PF_6), as compared to the bpy complex, supporting the combination of a phenanthroline moiety with copper(II) as a potential antitumour agent.

The gel mobility shift assays of three of the imine-based chelates, [Cu(L3)](NO_3), [Cu(L4)(NO_3)], and [Cu(L7)](NO_3), shown in Figure 7.2.5 illustrate similar interactions with the plasmid DNA, however, not to the extent of [Cu(L1)](PF_6).

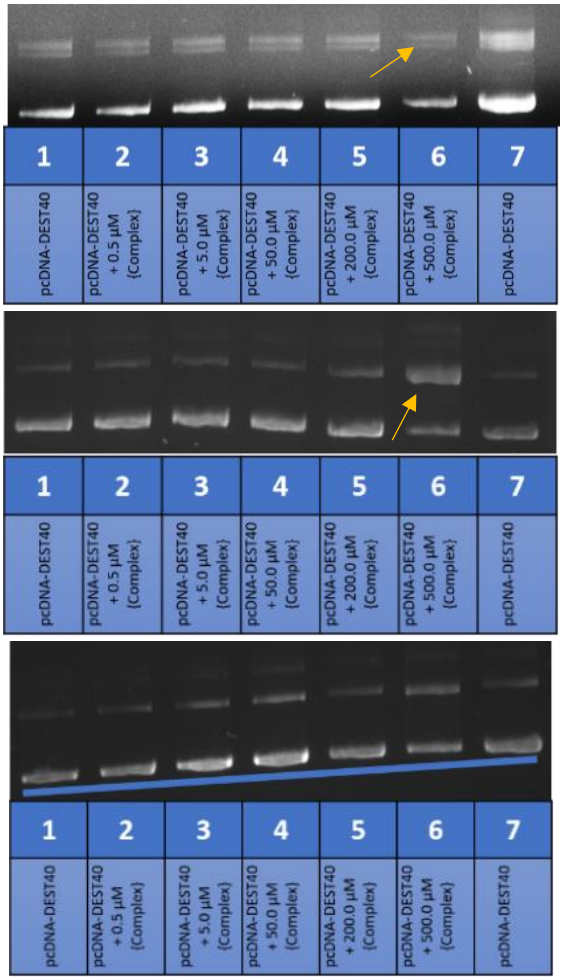

Figure 7.2.5: Gel mobility shift assays of (a) [Cu(L3)](NO_3), (b) [Cu(L4)(NO_3)], and (c) [Cu(L7)](NO_3), with pcDNA-DEST40. Arrows showing the points of interest. Lanes 1 and 7 – pcDNA-DEST40; lanes 2 - 6 – pcDNA-DEST40 + metal chelates (0.5 µM, 5.0 µM, 50.0 µM, 200.0 µM, 500.0 µM).

The gel mobility shift assays of these three imine-based chelates show that at a concentration of 500.0 µM, chelates [Cu(L3)](NO_3) and [Cu(L4)(NO_3)] cause destruction of the plasmid DNA while [Cu(L7)](NO_3) has no interaction. This trend, however, does not follow the DNA affinity studies (in Chapter 4) trend, where [Cu(L3)](NO_3) had a higher K_{app} value compared to [Cu(L4)(NO_3)] and [Cu(L7)](NO_3). This change in trend could be attributed to the differences in DNA between the two studies; the DNA affinity studies used calf thymus DNA and the gel mobility studies used plasmid DNA.

7.3 Octanol-Water Partition Coefficients

7.3.1 Introduction

The octanal-water partition coefficient is a physiochemical parameter of a molecule which indicates the lipophilicity (or hydrophilicity) of said molecule, and specifies the probable location of the molecule *in vivo*. Lipophilicity affects the behaviour of a compound *in vivo* by affecting the solubility and absorption of the compound. Compounds that are hydrophilic will be more likely to concentrate in the serum (blood) which allows for plasma protein binding and distribution of the compound throughout the blood system. Those that are lipophilic will more likely accumulate in the lipid-rich tissues, such as the liver which is involved in excretion of the compound and will also more easily cross the phospholipid bilayer of cells.[13] The coefficient is represented as a logarithmic value, Log $P_{o/w}$, where $P_{o/w}$ is equal to the ratio of the concentration of the molecule in water-saturated octanol and the concentration of the molecule in octanol-saturated water.[13,14] The value of the Log $P_{o/w}$ for a compound shows whether the compound is lipophilic, Log $P_{o/w} \geq 0$, or hydrophilic, Log $P_{o/w} \leq 0$.

7.3.2 Experimental

The octanol-water partition coefficients, Log $P_{o/w}$, were determined using the 'shake-flask' method for [Cu(L1)](PF_6) and [Cu(L2)](NO_3). The method uses water-saturated octanol and octanol-saturated water; this is important to prevent artificial carry over between the two phases.[13] The solvents were prepared by shaking analytical grade octanol with ultra-pure water (resistivity = 18 MΩ cm^{-1}). The two phases were allowed to equilibrate over 24 hours before centrifugation and separation of the two saturated phases. An aqueous solution of approximately 5×10^{-3} M concentration of the respective metal chelates was prepared. This solution was shaken with an equal volume of water-saturated octanol and allowed to separate for 2 hours before the solution was centrifuged to fully separate the two phases. The absorbance and, therefore, the concentrations of the chelate in each phase was determined by UV-visible spectroscopy. The spectroscopy was done using a Shimadzu UV-1800 (with a fixed slit width = 1 nm) double-beam spectrophotometer in a 1.0 cm path length quartz cuvette. The Log $P_{o/w}$ for the imine-based copper(II) complexes will be measured as part of the future work in this project.

7.3.3 Results and Discussion

The log $P_{o/w}$ values for [Cu(L1)](NO_3) and [Cu(L2)](NO_3) are -1.17(5) and -1.64(8), respectively. These relatively large and negative values show that the chelates are more hydrophilic, despite the extended aromatic nature of the ligands. This aqueous solubility is attributed to

the monocationic nature of the chelates. This is in contrast to the majority of organic and inorganic anti-cancer agents, for which the log $P_{o/w}$ values are positive, indicating poor aqueous solubility. Table 7.3.1 compares the log $P_{o/w}$ values of these copper(II) chelates with cisplatin (chemotherapeutic agent) and doxycycline (broad-spectrum antibiotic).

Table 7.3.1: Log $P_{o/w}$ values of [Cu(L1)](NO_3), [Cu(L2)](NO_3), cisplatin, and doxycycline.

Compound	Log $P_{o/w}$ value
[Cu(L1)](NO_3)	-1.17
[Cu(L2)](NO_3)	-1.64
Cisplatin[15]	-2.27
Doxycycline[15]	0.60

The copper(II) chelates have a similar log $P_{o/w}$ to cisplatin, with cisplatin being more hydrophilic, and could be attributed to these complexes having a positive charge. The copper(II) chelates are slightly less hydrophilic due to the size of the ligands compared to those of cisplatin. Doxycycline has a more lipophilic log $P_{o/w}$ compared to the complexes, which works in its favour as the compound needs to penetrate the cell membranes of bacteria.

Considering the Lipinski rule of five, these copper(II) chelates have the correct physicochemical properties for small molecules acting as chemotherapeutics.[16] That is, they have a molecular mass of less than 500 Da, they have fewer than five hydrogen bond donors, less than ten hydrogen bond acceptors, and an octanol–water partition coefficient of less than 5. Although the Lipinski rules are divisive amongst chemists, they do provide some useful boundaries during the drug development process.[16]

7.4 Human Serum Albumin Binding

7.4.1 Introduction

Human serum albumin is a protein found in relatively high concentrations in the blood, and is responsible for regulating intercellular fluxes. This extracellular protein has many binding sites for both organic and inorganic molecules, thus, making it a reliable regulator that plays a role in the behaviour of pharmaceutical drugs *in vivo*.[17] The structure of HSA in Figure 7.4.1 shows the different potential binding sites of the protein.

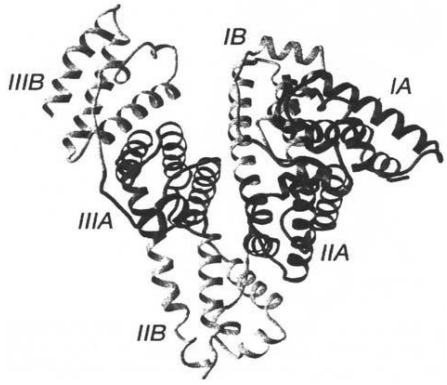

Figure 7.4.1: Structure of HSA, illustrating binding sites.[17]

Before the *in vivo* biodistribution and xenograft studies of [Cu(L1)](PF_6), the binding affinity of the complex for HSA must be determined. A higher affinity for HSA inversely correlates to a lower concentration of free chelate in the body, which may lead to lower efficiency of the chemotherapeutic agent *in vivo*.[17]

7.4.2 Experimental

The affinity of [Cu(L1)](PF_6) and [Cu(L2)](NO_3) for human serum albumin (HSA) was determined using UV-visible spectroscopic titrations. The absorbance was measured using a Shimadzu UV-1800, with a fixed slit width = 1 nm, double-beam spectrophotometer in a 1.0 cm path length quartz cuvette. The absorbance of HSA at 280 nm as a function of the concentration of the metal chelates over a concentration range of *ca.* 6 to 60 µM was measured.[17] The HSA solution was prepared by dissolving 200.4 mg of HSA in 5.0 mL of phosphate-buffered saline (pH 7.1, 0.1 M ionic strength). The concentration of HSA was 5.80 × 10^{-4} M, using 69000 Da as the mass of HSA. From Equation 1 below:

$$\frac{A_0}{A - A_0} = \frac{\varepsilon_{HSA}}{\varepsilon_B} + \frac{\varepsilon_{HSA}}{\varepsilon_B \times K} \times \frac{1}{C_{drug}}$$

Equation 1

The binding constant (K) can be determined from the linear double reciprocal plot of $1/(A - A_0)$ vs $1/C_{drug}$ (where C_{drug} is the concentration of the metal chelate) as the ratio of the intercept to the slope.

7.4.3 Results and Discussion

The interaction of $[Cu(L1)](NO_3)$ and $[Cu(L2)](NO_3)$ with human serum albumin (HSA) was determined through analysis of the absorption spectra of HSA in the presence of increasing concentrations of the metal chelates, as shown in Figure 7.4.2.

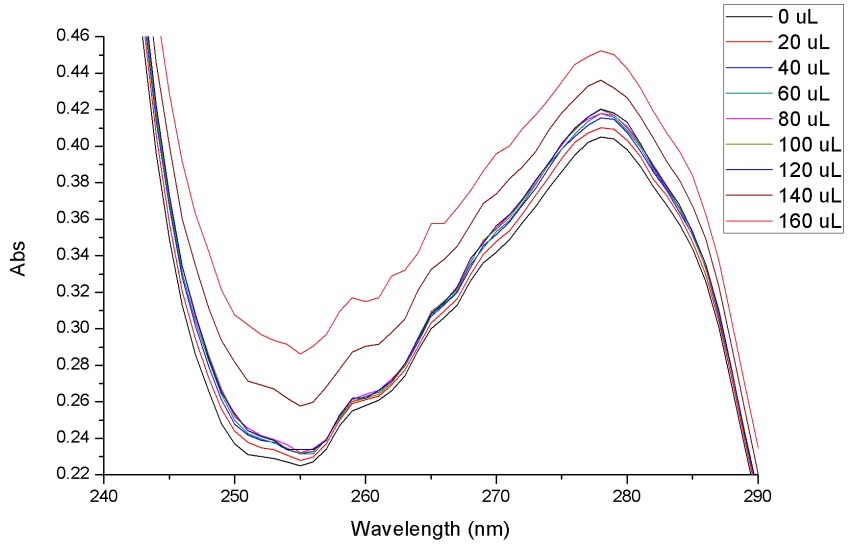

Figure 7.4.2: UV spectra of HSA in the presence of increasing concentrations of $[Cu(L1)](NO_3)$.

The double reciprocal plot of $1/(A - A_0)$ vs $1/C_{drug}$ for $[Cu(L1)](NO_3)$ is shown in Figure 7.4.3, and from this graph, the ratio of the intercept to the slope gives a binding affinity of 2.01×10^4 M^{-1} for $[Cu(L1)](NO_3)$.

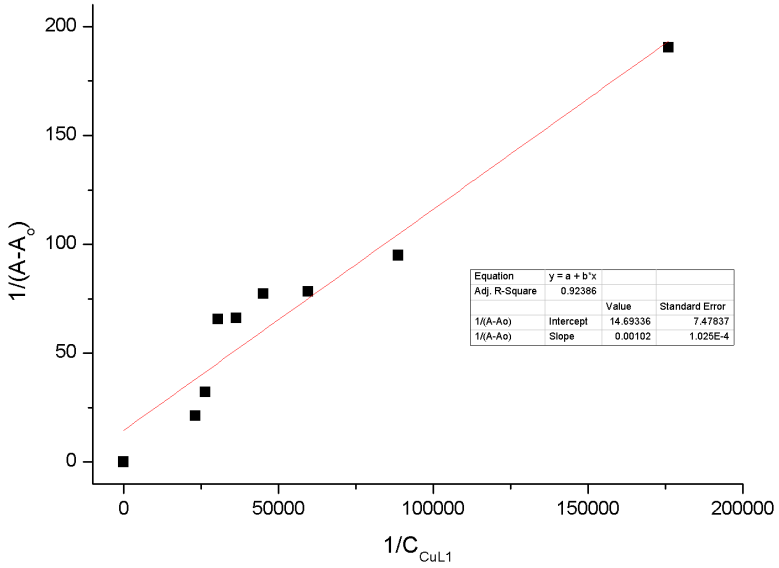

Figure 7.4.3: Double reciprocal plot of [Cu(L1)](NO$_3$) binding to HSA. From the data, the binding constant was determined to be 2.01 × 10^4 M^{-1}.

The binding constant for [Cu(L2)](NO$_3$) measures 2.7 × 10^4 M^{-1}. These data show that the compounds have an HSA affinity comparable to those of commercially available drugs. The copper(II) chelates exhibit an affinity for HSA higher than that of cisplatin (8.52 × 10^2 M^{-1}), but lower than that of free metal ions such as VO^{2+} (1.2 × 10^8 M). The lower HSA binding affinity (and higher effective concentration *in vivo*) of [Cu(L1)](NO$_3$) coupled with the increased cytotoxicity of [Cu(L1)](NO$_3$) versus [Cu(L2)](NO$_3$) suggests that [Cu(L1)](NO$_3$) is the more promising drug candidate. This is an important result, because of the various possible coordination geometries of copper(II), the square planar chelate is susceptible to off-target protein binding.

7.5 Biodistribution Studies of [Cu(L1)]Cl

7.5.1 Introduction

Understanding how a drug behaves *in vivo* is an essential aspect of the development of new pharmaceuticals. There are two main methods for determining biodistribution, with subgroups in each. The first category is non-invasive - using drugs linked with contrasting agents and viewing the subject under different optical sources, or imaging the radiolabeled drugs *via* CT or MRI scans. Alternatively, invasive techniques using radiolabeled drugs and harvesting the organs posthumously can be used in early stages of development with animal models.[18] The non-invasive techniques have the advantage of not sacrificing the subject to obtain the biodistribution data, however, these techniques have relatively low resolution and potentially expose the subject to harmful radiation.[18] Invasive techniques yield a highly resolved model of biodistribution, but by definition, they necessitate the test subject to be sacrificed.[18] The biodistribution of [Cu(L1)]Cl was initially determined *via* an invasive technique using the copper-64 radiolabelled equivalent. This data gave some positive indications for the further testing of the compound, and with new equipment that became available, further testing using a xenograft model was also possible. In both cases, the copper-64 isotope was used to synthesise an analogue of [^{nat}Cu(L1)]Cl.

The radioactive analogues were used in xenograft experiments, which indicates whether the complex exhibits favourable uptake in neoplastic versus healthy tissue.[19] The experiment involves the inocluation of a particular line of cancer cells into an animal with a growth medium. This injection site develops into a vasculated tumour over a few weeks, depending on the growth rate of the cells. The radiolabeled analogue of the chelate of interest can then be administered to the animal and the uptake in the tumour and other organs measured.[19] The radioactivity of the xenograft is measured, and therefore the selective uptake of the complex can be calculated as a percentage of the injected dose.

An additional use for the radioactive chelates is molecular imaging *via* positron emission tomography (PET) coupled with computerised tomography (CT), used as a diagnostic technique. This technique can be used to effectively determine the location and size of infected tissue, such as a tumour, in a patient.[20] PET-CT involves the injection of radioactive chelates into a specimen in order to obtain an image.[20] The non-invasive nature of PET-CT makes it an ideal diagnostic imaging tool as diseased tissue can be imaged and monitored without surgery.[20] Figure 7.5.1 shows a full-body PET-CT image of a tumour bearing mouse after being injected with a radiolabelled copper-64 chelate. ^{64}Cu-based chelates are effective as PET-CT imaging agents due to the unique radioactive characteristics of the isotope ($t_{1/2}$ = 12.7 h, β^+ 17.4 %, E_{max} = 0.656 MeV, β^- 39 %, E_{max} = 0.573 MeV) and it can be produced with a high specific activity.[21] The high specific activity means that a small mass of a compound can be used in the imaging experiments. The half-life of the ^{64}Cu isotope makes it ideal for delayed

imaging, so that background interference can be accounted for.[21] Another radioactive isotope used is ^{68}Ga with a mean E_{max} = 1.90 MeV and a half-life of 68 minutes.[22] The longer half-life of ^{64}Cu allows for delayed imaging, but the half-life is still short enough that the time for "total" decay is still relatively short, minimising the exposure of the patient to radiation.

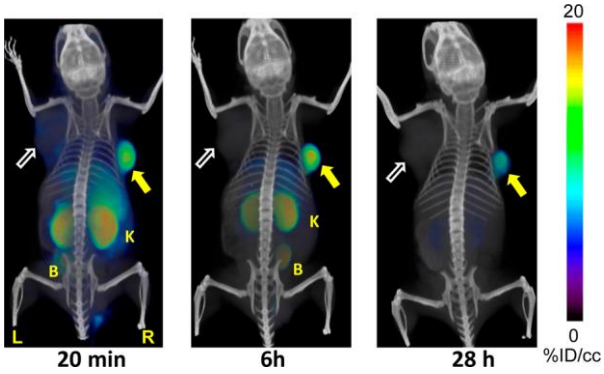

Figure 7.5.1: Whole-body PET-CT image of a tumour-bearing mouse with a ^{64}Cu labelled complex, at 20 minutes, 6 hours and 28 hours. K is the kidneys and B is the bladder.[21]

Not all radioactive isotopes can be used for PET imaging, Figure 7.5.2 illustrates the imaging process of PET and shows why it is only possible using isotopes that decay via positron emission. A positron is emitted from a nucleus and collides with an electron in the infected tissue, resulting in annihilation radiation which is detected by the PET scanner.[20] The annihilation radiation given off is two photons with energy of 511 keV, travelling 180° apart from each other.[20] It is the coincident nature of the photons emitted during the decay process that enables the imaging.

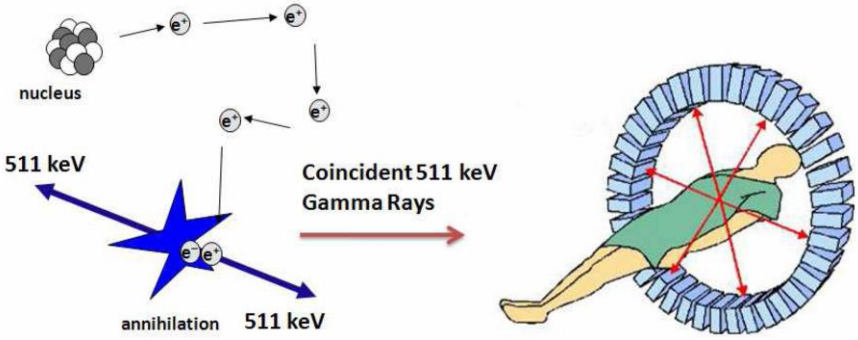

Figure 7.5.2: Schematic of PET imaging showing how the coincident photons are used to pinpoint the location of the accumulated complex. If the complex has some tumour specificity, then the technique will show the location of a tumour.[20]

A study by Boswell, *et al.*[23] showed an increase in stability *in vivo* of altered structures of already known analogues of radiolabelled ^{64}Cu complexes with 1,4,8,11-tetraazacyclotetradecane-1,4,8,11-tetraacetic (TETA), improving the biodistribution of the analogues.[23] The instability of these complexes was due to the *in vivo* interaction of the radioactive metal centre and proteins, reducing the availability of the complex, therefore, reducing the biodistribution of the complexes.[23] The biodistribution technique initially used for this study was an invasive one which involved injecting the radioactive complexes into

Sprague-Dawley rats. The rats were sacrificed - harvesting their organs to measure the radioactivity. The concentration of the complexes in each organ was used to obtain the biodistribution data.[23] In this study, the compounds have been shown moderate interaction with HSA, this will, hopefully, translate into good biodistribution.

A study by Philpott, *et al.*[24] used a non-invasive technique to observe the effectiveness of a well-known anti-colorectal carcinoma monoclonal antibody (MAb 1A3) coupled to ^{64}Cu as a diagnostic tool *via* PET-CT imaging.[24] Patients suspected of having colorectal carcinomas were administered ^{64}Cu-Mab 1A3. They were then monitored over a period of time to determine if there was any accumulation of the compound in a specific site. The outcome of the study showed that the radiolabelled antibody, used as a diagnostic agent, confirmed 89% to 96% of the predicted tumour site of the carcinoma. The compounds could aid in detecting tumours not seen by CT or MRI.[24] Figure 7.5.3 shows an example of one of the patients with tumours in their pelvis region, previously not detected with CT scans.

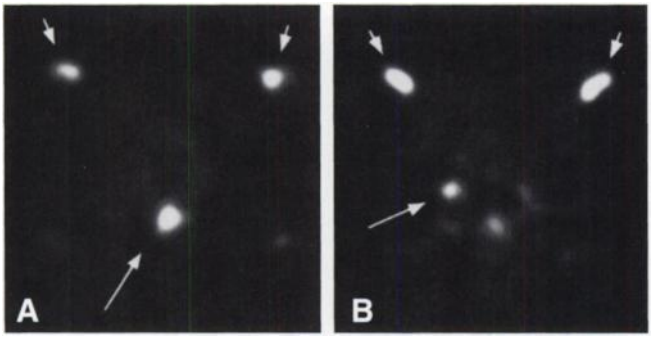

Figure 7.5.3: Trans axial PET images of the pelvis obtained after injection of ^{64}Cu-MAb 1A3(7 mg, 10 mCi) in a male with biopsy-proven recurrent rectal carcinoma.[24]

Through *in vitro* cell testing, it has been shown that [Cu(L1)](PF_6) can effectily control the proliferation of tumour cells. This is with the copper(II) metal centre in it's natural state. Through radiolabelling, it is possible to firstly determine the biodistribution of the compound. The biodistribution of a compound *in vivo* gives an indication of the serum stability of a compound and also shows any problematic organ accumulation which would prevent the further development of the drug candidate. If the biodistribution in healthy rats is satisfactory, then the compound can be further tested in a xenograft model to check if the compound exhibits any inherent selectivity towards neoplastic tissue. If there is elevated upatake in the xenograft, then the application of the compound can be diversified into diagnosis. The compound would then have applications in tumour treatment in the natural state state and for the diagnosis of disease as the radiolabelled analogue. The development of a single compound which has applications in therapy and diagnosis (a "theranostic" agent) is an exciting prospect in drug discovery.

7.5.2 Experimental

Initial Biodistribution Study

The biodistribution study was performed with the approval of the ethics committee of the University of the Free State (UFS) in accordance with the guidelines of the National Code for Animal Use in Research, Education, Diagnosis and Testing of Drugs and related substances in South Africa. Eight adult male Sprague Dawley rats were obtained from the Animal Experimentation unit of UFS with masses ranging from 348 to 414 g. The animals were anaesthetised in a vessel containing isoflurane. A 24 G jelco was inserted into the tail vein of the animals to administer the [^{64}Cu(L1)]Cl radiolabelled compound. The rats were each injected with 500 µL of a 10/90 ethanol/saline solution of [^{64}Cu(L1)]Cl. The activity of the dose ranged from 110 to 116 µCi for the rats used in the four hour study (n = 3) and 62.0 to 67.8 µCi for the 24 hour study (n = 4). The brain, heart, lung, liver, kidney, spleen, stomach, bladder, large and small intestine and tail as well as the femur and muscle tissue from the left hind leg were harvested. Approximately 5 mL of blood and all the urine in the bladder (where applicable) was also collected. All the organs were weighed and placed in a shielded 3 × 3 inch NaI(Tl) well crystal. The output from the well crystal was fed into a multichannel analyser card (ORTEC® MAESTRO®-32, Advanced Measurement Technology, Inc.). An energy window was set over the energy spectrum of ^{64}Cu and the radioactivity accumulated in each organ was recorded for a pre-set time of 60 seconds.

Xenograft Study

The xenograft study was performed in accordance with the ethical clearance granted by North West University, South Africa in accordance with the guidelines of the National Code for Animal Use in Research, Education, Diagnosis and Testing of Drugs and related substances in South Africa. A total of five female Rowett Nude (RNU) rats, which were inoculated with the human tumour cell line A549 (a non-small cell lung carcinoma) were obtained from the Pre-Clinical Drug Development platform at North West University. At two weeks, after the development of the tumour, the rats were injected with the radiolabelled analogue, [^{64}Cu(L1)]Cl. They were scanned using a Mediso nanoScan® PET/CT (microPET-CT) scanner at the South African Nuclear Energy Corporation (Necsa). Scans were taken at 1, 3, 6, and 24 hours intervals. Image acquisition was performed at 1, 3, 6 and 24 hours after injection of a *ca.* 200 MBq (100 µL of solution) of [^{64}Cu(L1)]Cl into the tail vein. The animal was placed in an induction box and anesthetised with 4% isoflurane. Once unconscious, the animal was placed in the imaging cell with its head contained in a mask directly connected to the anesthesia station in order to ensure a continuous flow of isoflurane at 1.5% during the acquisition. Conservation of body temperature during acquisition was maintained via a forced air circulation system through thin channels integrated into the bed of the imaging cell. A drop of ocrygel on the eyes of the rat was used to prevent the eyes drying out. After imaging, the

animals were sacrificed by anesthesia and cervical dislocation. Each relevant organ was collected, weighed and placed in a plastic tube that was then counted using a well gamma counter.

Radiosynthesis of [^{64}Cu(L1)]Cl

The ^{64}Cu sample was prepared by irradiation of natural copper(II) oxide for 10–12 min in the SAFARI-1 nuclear reactor (South African Nuclear Energy Corporation, Phelindaba South Africa), at a thermal flux of 8.0×10^{13} ncm^{-2} s^{-1}.

A solution of HL1 was prepared by dissolving a 1.5 mg sample in 150 µL of DMF and 350 µL of methanol to give a total volume of 500 µL. A sample of ^{64}CuO was received from the SAFARI-1 nuclear reactor at the Nuclear Energy Corporation of South Africa, the activity of the sample was 2110 MBq with a mass of 1.11 mg. The ^{64}CuO target was dissolved in 50 µL of 30% HCl solution and then diluted with 950 µL of water. A 100 µL aliquot of the sample contained 1.39 µmol of Cu^{2+} with an activity of 211 MBq. The $^{64}CuCl_2$ solution (100 µL) was added to 300 µL of 0.1 M NH_4OAc. The stock solution of HL1 (325 µL, a 2:1 mole ratio) was added to the $^{64}CuCl_2$ solution and the pH adjusted to 5.5. The mixture was heated to 90 °C for 30 min. The solvent was removed under Argon with heating and redissolved in phosphate-buffered saline (PBS, 900 µL). Some of the solid did not dissolve and the solution was passed through a 0.2 µm filter. An additional 300 µL of PBS solution was used to rinse the vial and passed through the filter. HPLC analysis of the final sample was done using gradient elution: water (0.1% TFA) 95% to 5% with acetonitrile (0.1% TFA) over 20min. The chromatogram is shown in Figure 7.5.4. Once the purity of the sample was confirmed through HPLC, the solution was injected into the animals (175 µL per animal, *ca.* 200 MBq).

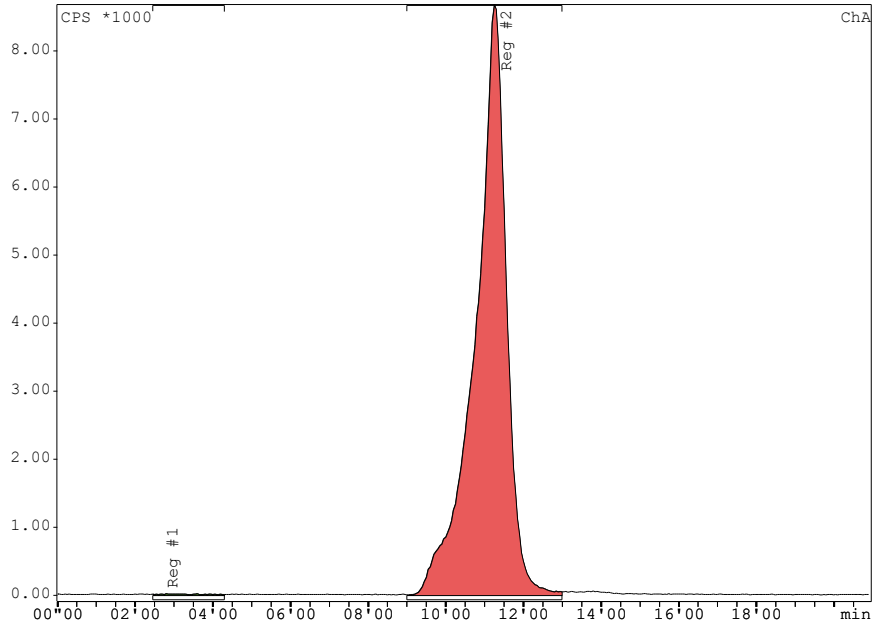

Figure 7.5.4: HPLC chromatogram of the final sample of [^{64}Cu(L1)]Cl, using a gradient elution, showing free $^{64}Cu^{2+}$ at a retention time of 2'54 and a peak area of 0.40%. The radiolabelled target compound, [^{64}Cu(L1)]Cl, eluted at 11'15 with a peak area of 99.60%. This shows that the compound is above the 95% purity requirement for animal testing.

7.5.3 Results and Discussion

Results and Discussion of the Radiosynthesis

An effective radiosynthetic method was developed using a high specific activity of ^{64}Cu. It was not possible to scale up the reaction, on a larger scale reaction, only around 40% of the radiolabeled product remains in solution after passing through the filter. This indicates very poor solubility of the product in water/PBS. If an ethanol/water solution was used to wash the filter, most of the product dissolves. However, the product in the first PBS solution is of high purity while the ethanol/water solution contains other impurities. Therefore, despite the loss in activity, the PBS solution was used for the *in vivo* studies.

Results and Discussion of the Biodistribution

The biodistribution studies of [^{64}Cu(L1)]Cl were done using two different methods, this was because during this project Necsa acquired a microPET-CT scanner. Based on the initial success of the biodistribution data, a second biodistribution study using xenografted rats with tumours derived from the A549 cell line was completed.

In the first experiment, the normal distribution of the lead drug candidate [Cu(L1)]Cl was used to assess the *in vivo* stability and biodistribution. This was done by synthesising the ^{64}Cu radiolabelled analogue i.e. [^{64}Cu(L1)]Cl which was administered to eight male Sprague Dawley rats. The rats were sacrificed after a specified period and the radioactivity (and hence effective concentration) of the chelate in the various organs of the rats was measured using a well-type counter. Static scans to monitor the biodistribution of the metal chelate in real-time were not possible with the equipment available at the time. The biodistribution at 4 hours (n = 3) and 24 hours (n = 4) post injection was measured. Figure 7.5.5 and Table 7.5.1 show the biodistribution of [^{64}Cu(L1)]Cl at 4 hours and 24 hours post-injection. The activity has all been corrected to the time of injection to account for radioactive decay.

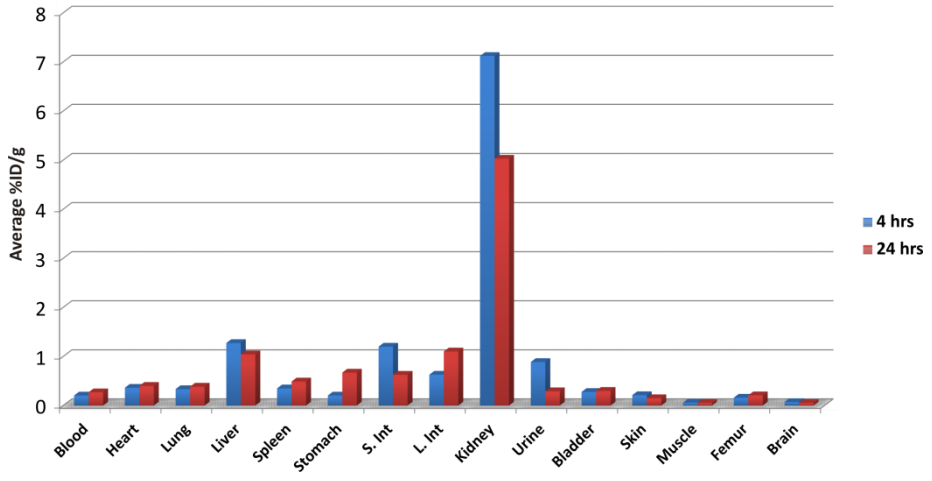

Figure 7.5.5: Biodistribution of [^{64}Cu(L1)]Cl in male Sprague Dawley rats after 4 and 24 h, as determined by β-particle emission, measured in %ID/g.

The biodistribution data highlight a few key factors that show [Cu(L1)]Cl has potential as a chemotherapeutic agent. Significantly, the data show that there is minimal accumulation of the compound in the liver and the liver accumulation is transient. This is very encouraging as liver accumulation, and its associated toxicity, can be problematic with copper-based chemotherapeutics.[25-27] The largest proportion of the injected dose at both 4 and 24 hours (7.1(3) and 5.0(5) %ID/g, respectively) resides in the kidneys. This would suggest that excretion of the compound is via the kidneys and urine, which also shows an elevated %ID/g at the 4 hour data point. The low liver accumulation and excretion via the kidneys are both indicative of good *in vivo* stability. The rate of excretion is, however, marginal with only 20(8)% of the compound excreted within 24 hours. This rate of excretion is lower than other metal-based chemotherapeutics such as square planar gold(III) chelates, which is 31% in the same time period.[28] The rate of excretion is, however, comparable to other copper(II) chelates which can show as little as 10% clearance over 24 hours.[29]

Table 7.5.1: Biodistribution of [^{64}Cu(L1)]Cl in rats expressed in %ID/g 4 hours post injection (n = 3) and 24 hours post injection (n = 4).

	4 Hours			24 Hours		
	Average %ID/g	**SD[a]**	**%SD[b]**	**Average %ID/g**	**SD**	**%SD**
Blood	0.20	0.14	69	0.27	0.05	18
Heart	0.36	0.06	16	0.40	0.06	16
Lung	0.33	0.03	9.3	0.38	0.03	8.1
Liver	1.27	0.14	11	1.04	0.14	13
Spleen	0.35	0.11	32	0.49	0.10	20
Stomach	0.20	0.06	31	0.67	0.51	76
S. Int	1.20	0.36	30	0.63	0.11	17
L. Int	0.63	0.17	27	1.10	0.07	6.3
Kidney	7.12	0.34	4.8	5.03	0.47	9.4
Urine	0.89	0.07	7.3	0.29	0.09	30
Bladder	0.28	0.04	13	0.30	0.03	9.8
Skin	0.21	0.05	23	0.15	0.01	7.9
Muscle	0.06	0.04	70	0.05	0.01	17
Femur	0.16	0.02	15	0.21	0.02	7.7
Brain	0.07	0.05	70	0.05	0.01	27
Excretion[c]	NA[d]	NA	NA	20	8	40

[a]The standard deviation (SD) for the measured %ID/g values.

[b]The SD as a fraction of the average %ID/g, shown as a percentage.

[c]Excretion was calculated indirectly by subtracting the activity accounted for in all the organs and carcass from the injected activity and is given in %ID.

[d]The excretion after four hours was too low to be reliably determined.

Strong interactions of metal-based drugs with serum proteins have been shown to lead to accumulation in the lungs.[28] The copper chelate shows very little accumulation in the lungs, suggesting that the interaction of the chelate with HSA does not negatively impact its potential as a chemotherapeutic. Unexpectedly, the proportion of the compound in the blood pool is low and relatively stable over time (0.2(1) and 0.27(5) %ID/g at 4 and 24 hours, respectively). Considering the hydrophilicity of the chelate, as indicated by a log $P_{o/w}$ of -1.17, coupled with the moderate HSA binding affinity, the concentration of the compound in the blood pool is expected to be elevated. Seemingly the kidneys are able to efficiently remove and excrete the chelate, preventing blood pool accumulation.

Subsequent to the biodistribution study described above, Necsa acquired a Mediso NanoSCAN PET-CT. This was an exciting development in the study as it allowed for the radiochemical studies to move beyond basic biodistribution in harvested organs to static scans at various time points. This enables the compound to be monitored over a period of time and not only at pre-selected time intervals where the animals were sacrificed. In this second study, xenograft models of the A549 non-small cell lung carcinoma were used. This enabled any tumour-specific uptake to be determined.

Figure 7.5.6 shows one of the rats with the xenograft on the right thigh, the tumour (post-experiment), as well as the microPET-CT scanner used for the study.

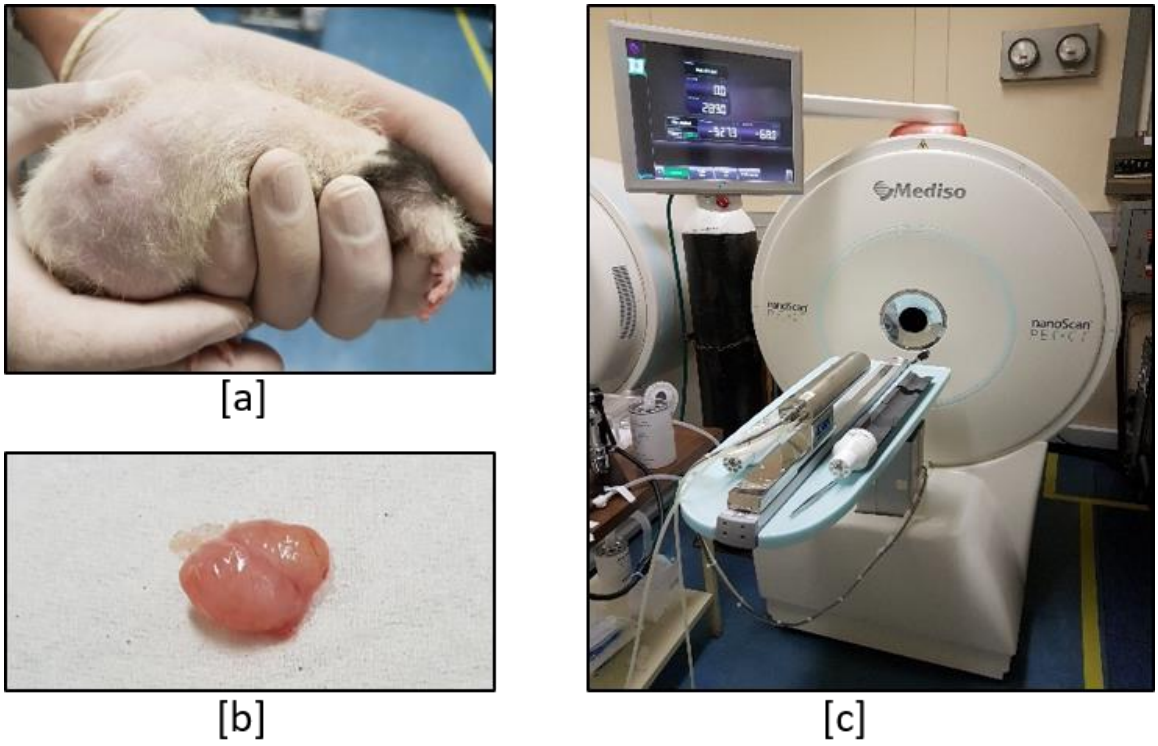

Figure 7.5.6: [a] Rat with a xenograph pre-experiment; [b] the tumour that was removed in the post-scan organ harvesting; and [c] the microPET-CT scanner used for biodistribution experiments.

The scans at 1, 3, 6 and 24 hours post-injection are shown in Figure 7.5.7. The scans show some really interesting results. Initially, the compound is noted to accumulate in the small intestines, with general circulation around the other organs and some accumulation in the tumour. By the six-hour time point, the compound has largely moved out of the small intestines and there is increased concentration in the liver, kidneys and the tumour. There is also some accumulation in the thyroid. The reason for the accumulatioin in the thyroid gland is not clear, but it is a highly vasculated organ and the accumulation may be attributable to the hydrophilic nature of the complex. By 24 hours, there is a high concentratioin in the kidneys. This is an interesting result, it suggests that the compound is being excreted through the kidneys. Once again, the retention of the compound by the tumour is highlighted at the 24-hour time point. The accumulation in the thyroid has also been reduced. This is significant as it shows that the compound is clearing from these organs. As noted above, retention in organs, particularly the liver, is problematic in drug development. There is no concerning liver accumulation in the present study.

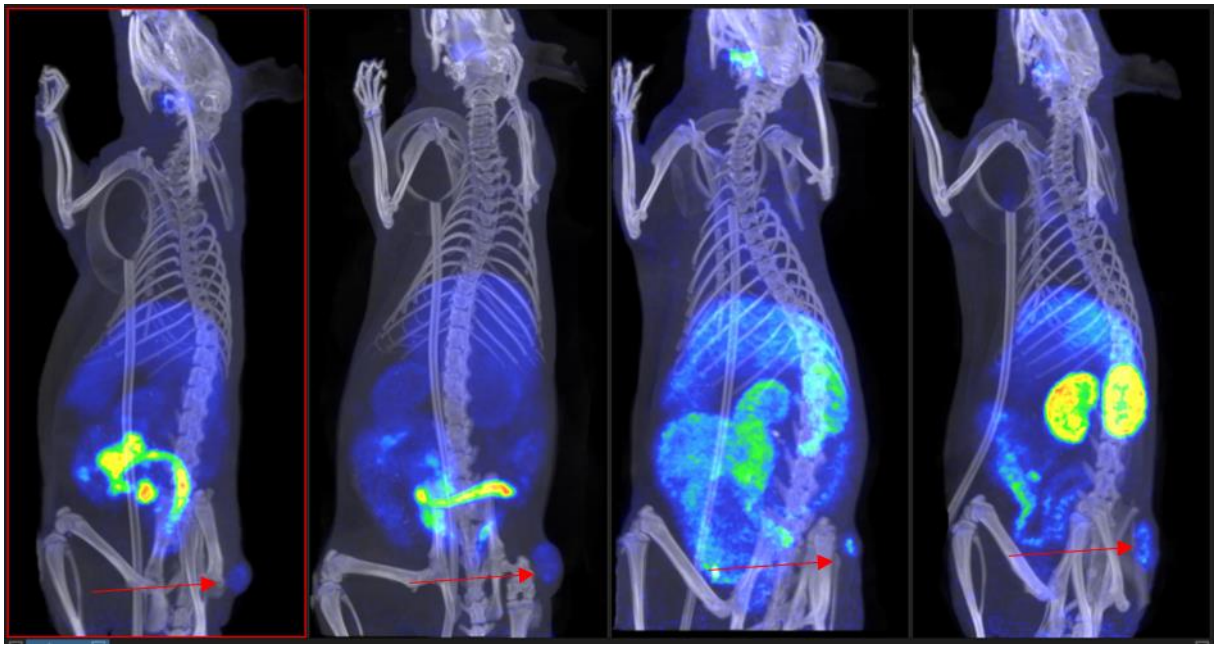

Figure 7.5.7: MicroPET-CT scans at 1, 3, 6 and 24 hours post injection. The images show how the biodistribution of the compound changes as a function of time. By the 24-hour time point, the compound is found in high concentrations in the kidneys and the tumour. The tumour is indicated with a red arrow.

A time activity curve showing the time-dependent nature of the compound in various organs is shown in Figure 7.5.8. The time activity curves are a numerical means of describing the biodistribution that is evident in Figure 7.5.7.

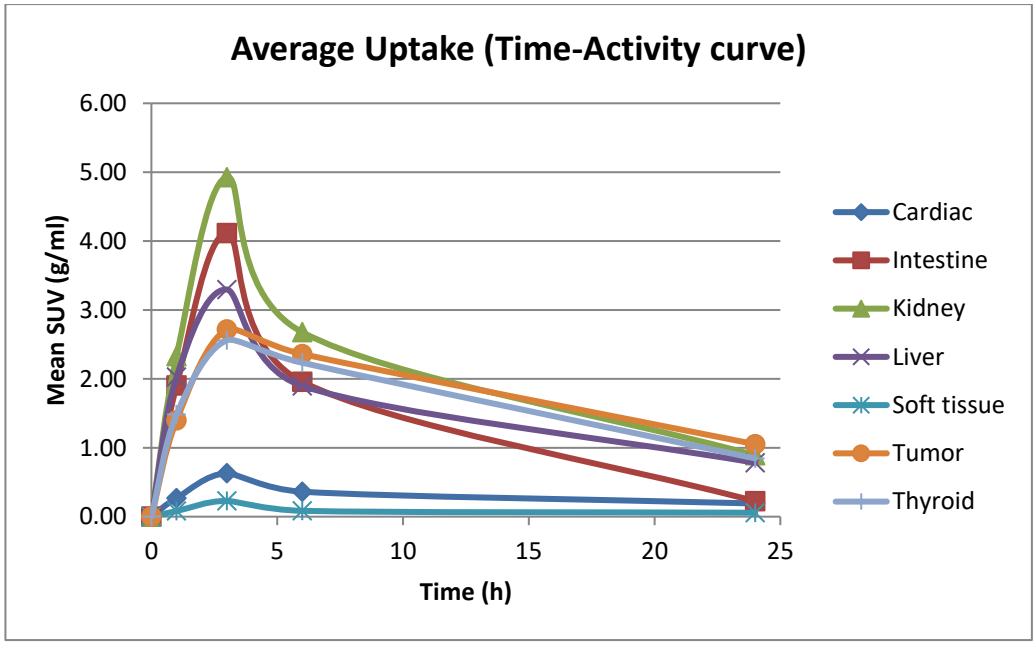

Figure 7.5.8: Time-activity curve of [^{64}Cu(L1)]Cl for different organs and the tumour. This represents a mean of the five animals that were scanned.

The time-activity curve shows that the concentration of the complex is initially high in the kidneys, liver, thyroid and intestine, reaching a peak at approximately three hours post-injection. The concentration in the tumour also reaches a peak at approximately three hours post-injection. It is noteworthy that the concentration of the compound decreases in the organs until the 24 hour time point, reducing to near zero in the case of the intestine, heart and soft tissue. The concentration in the liver and kidneys also drops over this period, but the concentration in the tumour remains relatively elevated. This shows that accumulation of [Cu(L1)]Cl in the tumour is favourable, and the tumour is less able to excrete the compound. Uptake and retention of the compound in the tumour model is an exciting result for the study, it shows that the compound has potential for therapy and imaging *in vivo*. Table 7.5.2 summarises the percentage of the injected dose per gram in the five animals used in the study. The mean of this data is plotted in Figure 7.5.9.

Table 7.5.2: Biodistribution of [^{64}Cu(L1)]Cl in rats expressed in %ID/g 24 hours post injection (n = 5).

ORGAN	Rat 1 %ID/g	Rat 2 %ID/g	Rat 3 %ID/g	Rat 4 %ID/g	Rat 5 %ID/g	Average	Standard deviation
Blood	0.68	0.72	0.85	0.65	0.65	0.72	0.09
Plasma	1.85	2.00	2.24	1.83	1.47	1.85	0.31
Heart	1.34	1.18	1.41	1.13	1.15	1.23	0.13
Lungs	1.12	1.20	1.73	1.23	0.94	1.30	0.33
Large Intestine	1.94	2.59	2.19	2.82	1.85	2.29	0.40
Spleen	1.12	1.12	1.08	1.07	1.05	1.07	0.01
Left kidney	3.12	3.37	3.54	2.81	NA	3.18	0.37
Right kidney	2.99	3.51	3.54	2.89	NA	3.22	0.32
Tissue	0.27	0.24	0.28	0.19	0.18	0.22	0.05
Femur	0.51	0.55	0.64	0.46	0.54	0.55	0.07
Bladder	0.41	0.49	0.63	0.63	0.33	0.53	0.14
Ovaries	0.63	0.81	0.68	0.83	0.82	0.78	0.07
Thyroid	0.44	1.95	0.55	0.27	0.80	0.54	0.22
Brain	0.13	0.12	0.13	0.25	0.11	0.16	0.06
Skin	0.68	0.89	0.71	0.53	0.76	0.67	0.10
Tumour	4.42	4.80	18.81	4.98	7.27	10.35	6.05
Liver	0.25	0.27	0.29	0.26	0.28	0.28	0.01
Stomach	0.52	0.37	0.32	0.35	0.88	0.52	0.26
Small Intestine	0.86	0.63	0.90	0.97	1.26	1.04	0.16
Tail	0.85	0.98	0.60	0.43	1.08	0.70	0.28

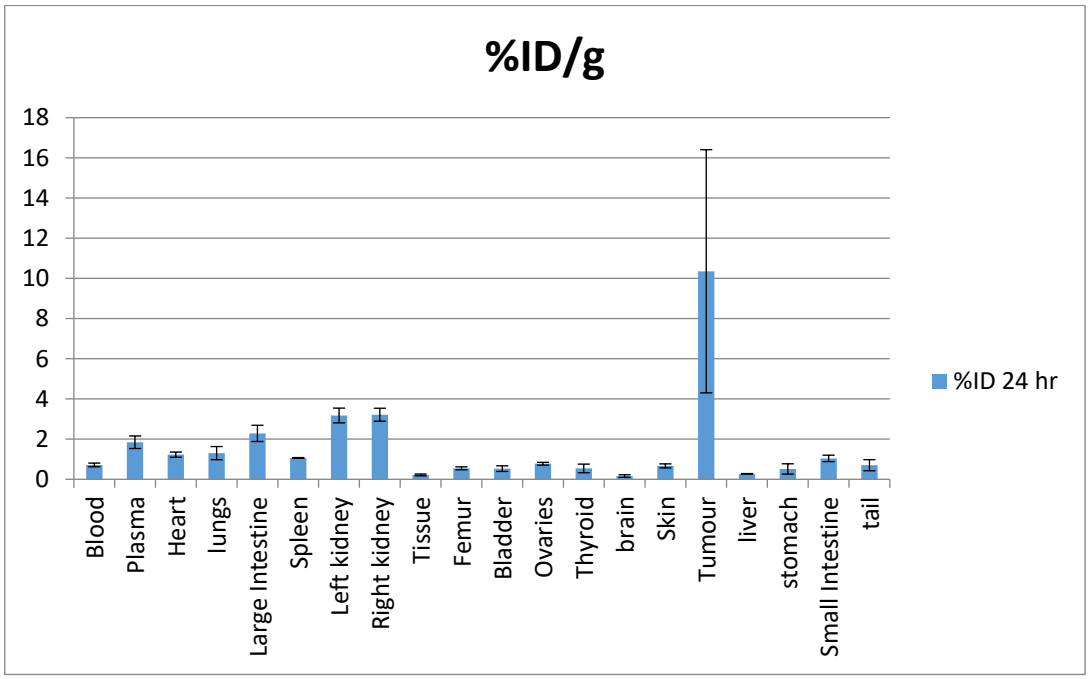

Figure 7.5.9: Biodistribution of [^{64}Cu(L1)]Cl in female Sprague Dawley rats after 24 hours, as determined by organ harvesting and well counting, measured in %ID/g. Note the elevated concentration of the compound in the tumour at the 24 hour time point.

The results of the biodistribution studies of [^{64}Cu(L1)]Cl are very encouraging. They show that the compound is stable *in vivo* (by lack of accumulation in the lungs or liver) and they show that there is uptake and retention of the complex in a non-small cell lung tumour model. The compound also seems to be excreted by the kidneys, although the rate of excretion is lower than some other metal chelates. An important next step in the process is to repeat the xenograft studies using another cell line, this will show whether the results are specific to the A549 cell line or whether they are more generally applicable. Considering the *in vitro* cell data, the compound is more effective in controlling the growth rate of other cell lines, such as U251. This will, hopefully, translate to increased uptake by the tumour with these cell lines.

7.6 Summary of Biological Studies

The cell screening data reported show that several of the novel amide-based and imine-based metal chelates synthesised in this work are promising anti-cancer agents. Based on these data, and previously reported studies, increasing the aromaticity of the chelates and the number of metal centres could improve the cytotoxicity further. This is discussed in Chapter 8. The structural properties of the chelates, especially [Cu(L1)](PF_6), have shown that the chelates are more hydrophilic, and there is minimal off-target binding to the HSA protein (off-target binding to serum proteins can be problematic with metal chelates, reducing the effective concentration of the cytotoxic agent in the blood). These properties suggest that the compounds have potential as antitumour agents. The *in vitro* results prompted further *in vivo* biodistribution studies using the ^{64}Cu radiolabelled analogue of [Cu(L1)]Cl. The initial biodistribution studies revealed that there is no problematic accumulation of [^{64}Cu(L1)]Cl in any organs. Based on this initial success, a xenograft model using the A549 cell line was used when a micro-PET-CT scanner became available. The micro-PET-CT scans showed that the compound initially accumulates in the small intestine, liver and kidneys and the tumour. The peak accumulation is reached at about three hours post-injection. The concentration of [^{64}Cu(L1)]Cl in these organs then begins to drop up to the 24 hour time point where the animals were sacrificed, but the concentration in the tumour drops by a smaller percentage than that of the other organs. This suggests that the lead compound is taken up and retained by the tumour model. Further studies are required to determine whether this uptake is specific to the A549 cell line, or is more generally applicable.

7.7 References

1. Barltrop, J. A.; Owen, T. C.; Cory, A. H.; Cory, J. G., *Bioorg. Med. Chem. Lett.* **1991,** *1* (11), 611-614.
2. Marques-Gallego, P.; den Dulk, H.; Backendorf, C.; Brouwer, J.; Reedijk, J.; Burke, J., *BMC Biotechnol.* **2010,** *10* (1), 43.
3. Hooi, D. S. W.; Bycroft, B. W.; Chhabra, S. R.; Williams, P.; Pritchard, D. I., *Infect. Immun.* **2004,** *72* (11), 6463-6470.
4. Shaakira, A.; Salerwe, M.; Muhammed, Q. F.; Maria, A. P.; Raymond, H., *South African Journal of Science* **2018,** *114* (3/4).
5. *OriginPro 8.0*, OriginLab Corporation, Northampton, MA, USA.
6. NCI DTP Database. http://dtp.nci.nih.gov/docs/dtp_search.html.
7. Fu, X.-B.; Liu, D.-D.; Lin, Y.; Hu, W.; Mao, Z.-W.; Le, X.-Y., *Dalton Trans.* **2014,** *43* (23), 8721-8737.
8. Zheng, K.; Liu, F.; Xu, X.-M.; Li, Y.-T.; Wu, Z.-Y.; Yan, C.-W., *New J. Chem.* **2014,** *38* (7), 2964-2978.
9. Zhao, J. a.; Peng, K.; Guo, Y.; Zhang, J.; Zhao, D.; Chen, S.; Hu, J., *J. Coord. Chem.* **2014,** *67* (13), 2344-2356.
10. Isbir, T.; Kirac, D.; Demircan, B.; Dalan, B., Gel Electrophoresis. In *Brenner's Encyclopedia of Genetics (Second Edition)*, Maloy, S.; Hughes, K., Eds. Academic Press: San Diego, 2013; pp 165-167.
11. YourGenome What is gel electrophoresis? https://www.yourgenome.org/facts/what-is-gel-electrophoresis (accessed 05 January 2021).
12. Manikandamathavan, V. M.; Parameswari, R. P.; Weyhermüller, T.; Vasanthi, H. R.; Nair, B. U., *European Journal of Medicinal Chemistry* **2011,** *46* (9), 4537-4547.
13. Moreno, E.; Gabano, E.; Torres, E.; Platts, J. A.; Ravera, M.; Aldana, I.; Monge, A.; Pérez-Silanes, S., *Molecules* **2011,** *16* (9), 7893-7908.
14. Wattanasin, P.; Saetear, P.; Wilairat, P.; Nacapricha, D.; Teerasong, S., *Anal. Chim. Acta In Press, Corrected Proof, Available online 16 August 2014*.
15. Lopes, J. C.; Botelho, F. V.; Barbosa Silva, M. J.; Silva, S. F.; Polloni, L.; Alves Machado, P. H.; Rodrigues de Souza, T.; Goulart, L. R.; Silva Caldeira, P. P.; Pereira Maia, E. C.; Morelli, S.; de Oliveira-Júnior, R. J., *Biochemical and Biophysical Research Communications* **2020,** *533* (4), 1021-1026.
16. Lipinski, C. A.; Lombardo, F.; Dominy, B. W.; Feeney, P. J., *Advanced Drug Delivery Reviews* **1997,** *23* (1), 3-25.
17. Ahmed-Ouameur, A.; Diamantoglou, S.; Sedaghat-Herati, M. R.; Nafisi, S.; Carpentier, R.; Tajmir-Riahi, H. A., *Cell Biochemistry and Biophysics* **2006,** *45* (2), 203-213.
18. Arms, L.; Smith, D. W.; Flynn, J.; Palmer, W.; Martin, A.; Woldu, A.; Hua, S., *Front Pharmacol* **2018,** *9*, 802-802.
19. Cheng, Y.; Ding, H.; Du, H.; Yan, H.; Zhao, J.; Zhang, W.; Zou, Y.; Liu, H.; Xiao, H., *Oncol. Rep.* **2014,** *32* (4), 1513 - 1520.

20. Shokeen, M.; Anderson, C. J., *Acc. Chem. Res.* **2009,** *42* (7), 832-841.
21. Banerjee, S. R.; Pullambhatla, M.; Foss, C. A.; Nimmagadda, S.; Ferdani, R.; Anderson, C. J.; Mease, R. C.; Pomper, M. G., *J. Med. Chem.* **2014,** *57* (6), 2657-2669.
22. Fournier, P.; Dumulon-Perreault, V.; Ait-Mohand, S.; Tremblay, S.; Bénard, F.; Lecomte, R.; Guérin, B., *Bioconjugate Chem.* **2012,** *23* (8), 1687-1693.
23. Boswell, C. A.; Sun, X.; Niu, W.; Weisman, G. R.; Wong, E. H.; Rheingold, A. L.; Anderson, C. J., *Journal of Medicinal Chemistry* **2004,** *47* (6), 1465-1474.
24. Philpott, G. W.; Schwarz, S. W.; Anderson, C. J.; Dehdashti, F.; Connett, J. M.; Zinn, K. R.; Meares, C. F.; Cutler, P. D.; Welch, M. J.; Siegel, B. A., *J Nucl Med* **1995,** *36* (10), 1818-24.
25. Ghosh, S. C.; Pinkston, K. L.; Robinson, H.; Harvey, B. R.; Wilganowski, N.; Gore, K.; Sevick-Muraca, E. M.; Azhdarinia, A., *Nuclear medicine and biology* **2015,** *42* (2), 177-183.
26. Tanzi, R. E.; Petrukhin, K.; Chernov, I.; Pellequer, J. L.; Wasco, W.; Ross, B.; Romano, D. M.; Parano, E.; Pavone, L.; Brzustowicz, L. M.; Devoto, M.; Peppercorn, J.; Bush, A. I.; Sternlieb, I.; Pirastu, M.; Gusella, J. F.; Evgrafov, O.; Penchaszadeh, G. K.; Honig, B.; Edelman, I. S.; Soares, M. B.; Scheinberg, I. H.; Gilliam, T. C., *Nature Genetics* **1993,** *5* (4), 344-350.
27. Brewer, G. J.; Yuzbasiyan-Gurkan, V., *Medicine* **1992,** *71* (3), 139-164.
28. Akerman, M. P.; Munro, O. Q.; Mongane, M.; van Staden, J. A.; Rae, W. I. D.; Bester, C. J.; Marjanovic-Painter, B.; Szucs, Z.; Zeevaart, J. R., *Journal of Labelled Compounds and Radiopharmaceuticals* **2013,** *56* (9-10), 530-535.
29. Bartholomä, M. D., *Inorganica Chimica Acta* **2012,** *389*, 36-51.

Chapter 8: Conclusions and Future Work

8.1 Conclusions

The key objectives for this work were the synthesis of two novel amide-bridged derivatised phenanthroline ligands, their copper(II), nickel(II), and palladium(II) chelates, as well as eight imine-bridged derivatised phenanthroline copper(II) chelates. These metal chelates were designed to intercalate DNA and inhibit the proliferation of cancerous tissue.

The synthesis of the metal chelates was broken down into two synthetic groups. These two groups differed by the functionalisation on the 2-position of phenanthroline. The first group were synthesised *via* an acid chloride group, at the 2-position of phenanthroline, which was further reacted with two amines, 8-aminoquinoline (forming HL1) and 2-picolylamine (forming HL2). The corresponding metal chelates were synthesised by reacting the ligands and respective metal salts in a 1:1 molar ratio, affording six novel monocationic amide-based chelates. The second group of compounds were synthesised in a one-pot reaction between 1,10-phenanthroline-2-ylmethanaminium chloride, various salicylaldehyde derivatives and copper(II) nitrate, in a 1:1:1 ratio, producing the eight imine-based copper(II) chelates. This group of chelates differed by the functional group on the 4-position of the phenol ring.

The IR, UV/Visible and, where possible, NMR data for the ligands and metal chelates confirmed the successful synthesis of the compounds. The effects of the different structural properties of the two ligands for the amide-based metal chelates were clearly evident in the UV/Visible spectra. The L1 chelates had more absorption bands than the L2 chelates due to the decrease in aromaticity from L1 to L2. The UV/Visible spectra of the eight imine-based copper(II) chelates suggest that there was a difference in the inner coordination sphere with chelates [Cu(L4)(NO_3)], [Cu(L5)(NO_3)], [Cu(L6)(NO_3)], and [Cu(L9)(NO_3)] seemingly having the nitrate counter ion coordinated to the copper(II) ion and [Cu(L7)](NO_3), [Cu(L8)](NO_3), while [Cu(L10)](NO_3) have a square planar geometry with the nitrate ion in the outer coordination sphere.

Ligand HL1 and chelates [Cu(L4)(NO_3)] and [Cu(L7)](NO_3) were studied by single crystal X-ray diffraction. HL1 showed that despite the extended aromatic nature of the ligand, the geometry was non-planar with a *ca.* 30° torsion angle between the phenanthroline and quinoline moieties. HL1 formed a polymer-like chain in the crystal lattice supported by intermolecular interactions between the carbonyl group of the amide and C–H groups of adjacent molecules. The two metal chelates showed two different coordination modes with respect to the position of the nitrate ion. [Cu(L4)(NO_3)] had the nitrate as part of the inner

coordination sphere and [Cu(L7)](NO_3) had the nitrate in the outer sphere. Both chelates had a square pyramidal geometry, with [Cu(L7)](NO_3) forming an inversion-symmetry dimer with the copper(II) ion coordinated to adjacent phenol oxygen as well as the tetradentate ligand. Compounds [Cu(L1)](PF_6) and [Ni(L1)](PF_6) were successfully crystallised, but the space group could not be reliably determined. For this reason, only low-resolution structures could be elucidated. The geometry of the two chelates was square planar, ideal for DNA intercalation.

DFT simulations at the B3LYP/6-311G (for the ligands, copper(II) and nickel(II) chelates) and B3LYP/LANL2DZ (for the palladium(II) chelates) level of theory were used to further understand the experimental data. The simulations showed that the solid-state structure of the ligand is *ca.* 10 kJ mol^{-1} higher in energy than the geometry-optimised structure, and for chelates [Cu(L4)(NO_3)] and [Cu(L7)](NO_3), 22.89 kJ mol^{-1} and 10.57 kJ mol^{-1} higher than the geometry-optimised structure, respectively. The vibrational frequencies of the ligands and metal chelates were calculated. A comparison with the experimental data showed these calculations to be fairly accurate. The calculated ^{1}H and ^{13}C NMR chemical shifts of the amide-based ligands were, in general, moderately accurate. The simulated chemical shifts were generally deshielded relative to the experimental data. The molecular orbital transitions responsible for the UV-visible spectra were predominantly of π-symmetry. The metal orbitals were extensively mixed.

The amide-based metal chelates were screened against four human cancer cell lines, and the imine-based copper(II) chelates were screened against a set of three different human cancer lines and one healthy cell line. The most cytotoxic amide-based metal chelate was found to be [Cu(L1)](PF_6) with a mean IC_{50} value of 12.02 µM. This significant cytotoxicity is attributed to the combination of a high DNA binding affinity and the ability of the metal centre to catalyse the production of hydroxyl radicals. The IC_{50} value of [Cu(L1)](PF_6) is similar to other copper(II) chelates and commercially available chemotherapeutic agents. The selectivity indices of the imine-based chelates were determined by using the healthy human cell line HEK293 as a reference. The selectivity index of these chelates showed that they generally have a higher affinity for neoplastic tissue, with the highest affinity for the triple-negative breast cancer cell line MDA-MB. The most cytotoxic of the imine-based chelates is an order of magnitude more toxic to tumour cells compared to healthy cells.

The lipophilicity and HSA affinity were determined for [Cu(L1)](NO_3) and showed that the compound is slightly hydrophilic with a log $P_{o/w}$ of -1.17(5) and an HSA binding constant of $2.01 \times 10^4\ M^{-1}$. The gel electrophoresis study on this chelate indicated the destruction of DNA at concentrations above 100 µM.

The biodistribution of [Cu(L1)]Cl was determined with the use of the copper-64 radiolabelled analogue of the chelate. The initial experiments showed that there was no problematic organ accumulation. The subsequent xenograft experiments with the A549 (non-small cell lung

carcinoma) cell line showed accumulation of the radiolabelled chelate in the tumour as well as (initially) in the small intestine, kidneys and liver, with the peak concentration in these organs at 3 hours. The concentration of the radiolabelled chelate in all organs decreased by 24 hours post-injection, but the tumour concentration remained relatively constant, indicating good tumour retention. These data suggest that the compound could find application as a theranostic agent.

8.2 Future Work

The initial work on this project has shown that the chelates have significant potential as chemotherapeutic agents. Several possible areas which should be further developed have been identified and are discussed below. In this work, it has been shown that the combination of a highly aromatic ligand and a copper(II) metal centre is effective in controlling the growth of tumour cells. This will, therefore, be the first area to develop.

Examples of possible derivatised phenanthroline ligands are shown in Figure 8.1. The range of ligands in Figure 8.1 show different structural features which could increase the efficacy of the chelates. The proposed ligands extend the aromatic region of the phenanthroline moiety or introduce functional groups into the system. The ligands will only be chelated to copper(II), as it has been shown that the redox activity of this metal ion is central to the success of the chemotherapeutics.

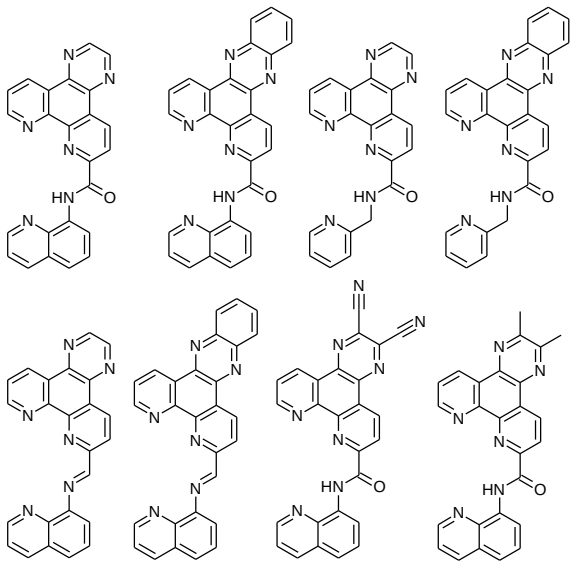

Figure 8.1: Proposed ligands for chelation to copper(II). These ligands will extend the aromaticity of the compounds, and possibly increase the cytotoxicity.

The X-ray structures of the metal chelates need to be elucidated so that structure-activity relationships can be better understood. To do this, better single crystals need to be grown. This could be done by changing the methods used to form the crystals, which include vapour diffusion, reducing the speed at which the chelate crystallises, and counter ion exchange, which changes the internal energy of the system and influences intermolecular interactions.

It has been shown that this class of metal chelates effectively bind DNA. The DNA binding mode is likely to be intercalation, based on the structures of the chelates. This hypothesis needs further testing to determine the exact DNA binding mode. Similarly, the copper(II) metal centre is thought to catalyse the production of hydroxyl radicals and induce DNA cleavage, this too needs further investigation. By using various radical scavenging agents, it is possible

to determine the species ROS that is being formed and whether it is responsible for DNA degradation

The metal chelates have been tested against four human tumour cell lines to determine a cross-section of the cytotoxicity profile. By increasing the number of cancer cell lines tested, a more accurate representation of the cytotoxicity profile can be achieved. The metal chelates could be tested against the National Cancer Institute's sixty human cell line panel (NCI 60). This will produce an activity profile for each chelate.[1] The activity profile of the metal chelates can be compared to other compounds with known modes of action, giving an indication of the likely mechanism of action.[1]

The current copper(II) complexes can be used for treating tumours, inducing cell death by binding to DNA and then causing DNA strand cleavage through the catalytic production of ROS. The radiolabelled analogues can also be used for the imaging of tumours, but the decay mode of ^{64}Cu is not suitable for radiotherapy. The same ligand could also be chelated to palladium(II). The rationale behind this is that palladium has an isotope which can be used for therapy: ^{103}Pd. This isotope falls in the category of Auger electron emitters, along with isotopes such ^{111}In (6.75 keV), ^{125}I (15.0 keV) and ^{67}Ga (6.26 keV), and is an exciting alternative to the more traditional beta-particle emitters for cancer therapy. The half-life of ^{103}Pd is relatively long at 17 days. As the range of Auger electrons is extremely short this form of therapy has the potential to be highly target-specific. The caveat to this is that to be effective a ^{103}Pd chelate must enter a tumour cell. Since the d^8 configuration of Pd(II) confines it to a square planar coordination geometry, the present tatradentate ligand is an ideal candidate for coordination to Pd(II). Currently, the applications of ^{103}Pd are limited to brachytherapy. Moving into the field of intracellular delivery and irradiation of tumour cells using this technique is thus an exciting prospect. The palladium(II) analogue, [Pd(L1)]Cl has been synthesised and extensively studied *in vitro*. These studies have shown a relatively good DNA binding constant of 5.25×10^6 M^{-1}. This binding constant also shows the similarity of the copper(II) and palladium(II) analogues, the binding constant for the former is 5.91×10^6 M^{-1}. This similarity would suggest that the structure of the compounds in solution is similar and that the tumour uptake noted for the copper(II) analogue may well be similar for the palladium(II) complex. Further to this, the similarity in the cytotoxicity profile (mean IC_{50} values of 4.92 and 4.65 for the copper(II) and palladium(II) analogues, respectively) would suggest that the tumour uptake demonstrated by the copper complex may well be extended to the palladium complex. This highlights the suitability of [Pd(L1)]Cl for radiolabelling with ^{103}Pd for the treatment of tumours *in vivo*.

8.3 References

1. N. K. Paul, M. Jha, K. S. Bhullar, H. P. V. Rupasinghe, J. Balzarini and A. Jha, *Euro. J. Med. Chem.* **2014,** *87*, 461 - 470.